GEOTECHNICAL CENTRIFUGE MODELLING OF CONTAMINANT TRANSPORT THROUGH FROZEN SOIL

MODELISATION PAR CENTRIFUGEUSE GEOTECHNIQUE DE TRANSPORT DE CONTAMINANT DANS DES SOLS GELES

A Thesis Submitted to the Division of Graduate Studies
of the Royal Military College of Canada
by

Patrick Joseph Albert Nadeau, B.Eng, rmc
Captain

In Partial Fulfillment of the Requirements for the Degree of
Master's of Applied Science

24 June, 2019

For Melissa, Rosalie and Arielle

ACKNOWLEDGEMENTS

I would like to thank the Department of National Defence, specifically 1 Engineer Support Unit for their financial support, which allowed me to attend the 5th European Conference on Permafrost. They also provided funding for me to attend the Symposium on Climate Change and its Impact on National Security at the Canadian Forces College, where a contact was made that was invaluable to this research.

Thank you to Joint Task Force North, specifically Pete Cott, who collected soil samples from Ellesmere Island to support my research. Thank you to the Environmental Sciences Group at RMC for facilitating the transport of the soil samples.

I would also like to thank the Natural Sciences and Engineering Research Council for funding the majority of the equipment that was procured to conduct this research.

The technical and administrative staff in the Department of Civil Engineering and the Department of Chemistry and Chemical Engineering was invaluable for the conduct of this research. Without their extensive expertise and assistance, this research would not have been possible.

To my wonderful supervisors, Dr. Ryley Beddoe and Dr. Sarah Creber, your mentorship and technical knowledge allowed me to conduct this research and grow as an academic and as a person. You both helped me overcome many technical and some personal challenges and get me to the finish line. The support you provided was above and beyond what I expected from my supervisors, especially while having to juggle my academic needs with your busy family lives.

To my amazing family, thank you for your patience, understanding and support during the last two years. Many evenings and weekends were spent labouring on this research instead of spending them with you. I promise that I am all yours from now on. To my wife, Melissa, your continued encouragement and support allowed me to achieve my goals, while also keeping a healthy work-life balance. I could not have done it without you and Rosalie.

ABSTRACT

Permafrost degradation due to climate change is a threat to the Canadian Arctic. A long-standing practice in cold regions is to use permafrost to contain contaminated soil because it was thought to be impermeable. Although not fully impermeable, frozen soil has been a reasonable containment option. However, the degradation of permafrost could lead to the release of previously contained contaminants, threatening the local ecosystems and communities. It is important to understand how contaminant transport will occur in a northern environment compared to temperate regions. The long-term study of contaminant transport is often a complex and expensive endeavour due to the isolation of most contaminated sites, the resources required and the short field season in the Arctic.

Geotechnical centrifuge modelling is one solution to the cost and complexities involved in performing in-situ field studies. With the scaling principles by which it is governed, centrifuge modelling has proven to be an effective tool to conduct research by simulating the behaviour of large-scale phenomena using benchtop sized models. The scaling effect of time also allows for the conduct of multiple experiments in a relatively short amount of time that simulates the behaviour of a prototype site over a long period of time.

The use of geotechnical centrifuge modelling for contaminant transport research was validated by conducting a modelling of models. Three centrifuge contaminant transport experiments were conducted at different acceleration ratios and another experiment was conducted in an acrylic column. Pumpkin seed oil was used as the contaminant for all experiments. The experiments proved that the scaling principle for the wetting front velocity of the oil was being followed, thereby validating the use of the centrifuge for contaminant transport research.

Centrifuge experiments were also conducted to observe and quantify the effects of moisture content on the advective and diffusive transport of the oil. The presence of moisture within the soil slowed the migration of the oil. Experiments with frozen soil were conducted to observe and quantify the effects of temperature on the migration of the oil. Decreased temperatures reduced the wetting front velocity of the oil due to the increased surface tension of the oil at lower temperatures. A centrifuge experiment was conducted with soil from an abandoned barrel cache on Ellesmere Island, NU. The wetting front velocity of the oil into the Arctic soil was calculated.

The results of this research demonstrate that the transport of contaminants through soil at contaminated sites can be calculated using centrifuge experiments. This would help to identify the contaminant source zone and plume based on the moisture conditions, soil, contaminant and recent climate of the site, thus increasing the effectiveness of remediation efforts.

RÉSUMÉ

La dégradation du pergélisol causé par les changements climatiques est un risque pour l’arctique Canadien. Une technique courante pour encapsuler du sol contaminé est l’utilisation du pergélisol puisqu’il est quasiment imperméable. La dégradation du pergélisol pourrait mener à la mobilisation de contaminants qui étaient immobilisés par le pergélisol. La recherche à long-terme de sites contaminés est très complexe et coûteuse en raison de l’isolation des sites, des ressources requises et de la courte période annuelle favorable pour la recherche dans le Nord.

La modélisation par centrifugeuse géotechnique est une solution aux coûts et aux complexités de la recherche à long-terme sur un site contaminé. Les principes d’échelle de la modélisation par centrifugeuse permettent l’étude du comportement de prototypes à grandes échelle avec des modèles de petite taille. Les principes d’échelle permettent la conduite de plusieurs essais dans un court délai qui simulent le comportement à long-terme d’un site prototype.

La validation de l’utilisation d’une centrifugeuse pour la recherche sur le transport de contaminants a été faite avec une modélisation de modèles. Trois essais ont été effectués dans la centrifugeuse à des accélérations différentes et un autre dans une colonne. De l’huile de graines de citrouille a été utilisée comme contaminant pour tous les essais. Les essais de validation ont prouvé que le principe d’échelle pour la vitesse d’infiltration est respecté. L’utilisation d’une centrifugeuse pour la recherche de transport de contaminant a été validée.

Plusieurs essais avec la centrifugeuse ont été effectués afin d’observer et de quantifier l’effet de la teneur en eau sur l’infiltration de l’huile dans le sol. Il a été observé qu’une augmentation de teneur en eau réduit le taux d’infiltration. Des essais avec du sol gelé ont aussi été effectués afin d’observer et quantifier l’effet de la température sur le taux d’infiltration. Les températures sous le point de congélation ont réduit le taux d’infiltration de l’huile. Ceci est causé par l’augmentation de la tension superficielle entre l’huile et les grains de sols à basse température.

Un essai a été effectué avec des échantillons de sol d’une cache de barils situé dans l’Arctique canadien sur Île d'Ellesmere, NU. Le taux d’infiltration de l’huile dans le sol arctique a été calculé. Les résultats de cette recherche ont prouvé que le taux d’infiltration des contaminants dans le sol du site contaminé peut être déterminé avec ces essais de centrifugeuse. Ceci aiderait à identifier la zone contaminé sous la surface du sol dépendant de la teneur en eau, du sol, des contaminants et le climat du site. Connaissant l’étendue de la zone contaminé aide à optimiser les efforts d’assainissement des sites contaminés dans l’Arctique canadien.

CO-AUTHORSHIP

The thesis, Geotechnical centrifuge modelling of contaminant transport through frozen soil, is the product of research conducted by the author, Patrick Nadeau. The development of the acrylic column and its experimental procedures was done with the collaboration of Ms. Brianna Bradley. The written content of Appendix F was co-authored by Ms. Bradley. While technical and editorial comments were made by Dr. Ryley Beddoe and Dr. Sarah Creber, the written content is solely that of the author.

TABLE OF CONTENTS

LIST OF TABLES

LIST OF FIGURES

LIST OF ACRONYMS AND SYMBOLS

α_i	Longitudinal Dispersivity (m)
α_j	Transverse Dispersivity (m)
θ	Angle (degree)
$\dot{\theta}$	Angular Velocity (rad/s)
η	Viscosity (Pa*s)
σ	Interfacial Tension (N/m)
$\boldsymbol{\psi}$	Elevation Head (m)
ω	Tortuosity (unitless)
ρ_w	Density of Water (g/ml)
ρ_o	Density of Oil (g/ml)
A	Soil Surface Area in Permeameter (m^2)
BTEX	Benzene, Toluene, Ethybenzene & Xylenes
C	Concentration of Contaminant (mg/kg)
CCME	Canadian Council of Ministers of the Environment
CFM	Cubic feet per minute
d	Average Soil Grain Diameter (m)
D_d	Diffusion Coefficient (m^2/s)
D^*	Effective Diffusion Coefficient (m^2/s)
D_L	Longitudinal Hydrodynamic Dispersion Coefficient (m^2/s)
D_T	Transverse Hydrodynamic Dispersion Coefficient (m^2/s)
dA	Cross Sectional Area (m^2)
DEW	Distant Early Warning
f	Fluidity (1/(m*s))
g	Gravitational Acceleration (m/s^2)
h	Total Hydraulic Head
∇h	Hydraulic Gradient (m/m)
J_d	Flux of Mass Transport by Diffusion (kg/s m^2)
K	Hydraulic Conductivity (cm/s)
k	Intrinsic Permeability (m^2)
L	Distance Between Manometers on Permeameter (m)
n	Porosity (unitless)
N	Acceleration Ratio
NAPL	Non-Aqueous Phase Liquid
- DNAPL	Dense Non-Aqueous Phase Liquid
- LNAPL	Light Non-Aqueous Phase Liquid
P	Peclet Number (unitless)
P_c^*	Dimensionless Capillary Pressure (unitless)
P_c	Capillary Pressure (Pa)
PFA	Perfluoroalkoxy
PHC	Petroleum Hydrocarbons
ppb	Parts per Billion
ppm	Parts per Million
Q	Water Discharged during Constant Head Test (ml)
r	Radius (m)
RMC	Royal Military College of Canada

SWCC	Soil Water Characteristic Curve
t	Time (s, min, h, d)
$v_{x,i}$	Average Linear Flow Velocity (cm/s, mm/min)
z	Pressure Head (m)

1 INTRODUCTION

1.1 Research Problem

Contaminated sites in Canada’s Arctic are common at former and current resource extraction sites as well as research and military facilities. One example of a contaminated site in the discontinuous permafrost zone of Canada’s Arctic was the former Colomac Mine in the Northwest Territories. The mine suffered several spills over its operating lifetime from 1989 to 1997, with a total of over 50,000 L of petroleum hydrocarbons (PHCs) reportedly spilled (Iwakun et al. 2010a). The remediation of the Colomac Mine took several years to complete and cost $70M. The complexity of the site, along with its location within the discontinuous permafrost zone contributed to the amount of time and money it took to remediate the site. The effects of the permafrost and the annual freeze-thaw cycles modified the expected behaviour of the spilled PHCs compared to PHC spills in temperate regions. An extensive site characterization was conducted in order to assess the extent of the contaminant migration at the site. Once the site was characterized, various methods were used to remove the PHCs that were found at the site. Most of the methods required that heavy equipment be transported to the site, which is typically the main contributor to the high costs of remediation projects in the Arctic (Filler et al. 2009).

Over the last few decades, the Canadian Armed Forces have been taking an active role in remediating their installations in the Arctic that have been contaminated over several decades. An example of this is the assessment and cleanup of barrel caches that are located on Ellesmere Island (Figure 1-1) as part of Operation NEVUS. Ellesmere Island is the most northern major island in the Canadian Arctic and home to CFS Alert, the most northern permanently inhabited location in Canada. Several barrel caches of arctic diesel, jet fuel, gasoline and heating oil were established to provide fuel to the military outposts on Ellesmere Island. Some of the caches contain thousands of barrels. Many of the caches were abandoned with no remediation or long-term monitoring plan put in place after their abandonment. Some of the barrels that were abandoned are empty, however many still contain PHCs that were mentioned above. Typically, the upright barrels still contain fuel while the ones stacked on their sides are empty (Figure 1-1 & Figure 1-2). The presence of these large quantities of petroleum hydrocarbons (PHCs) presents a significant environmental risk. Spills were observed at most of the locations during site visits.

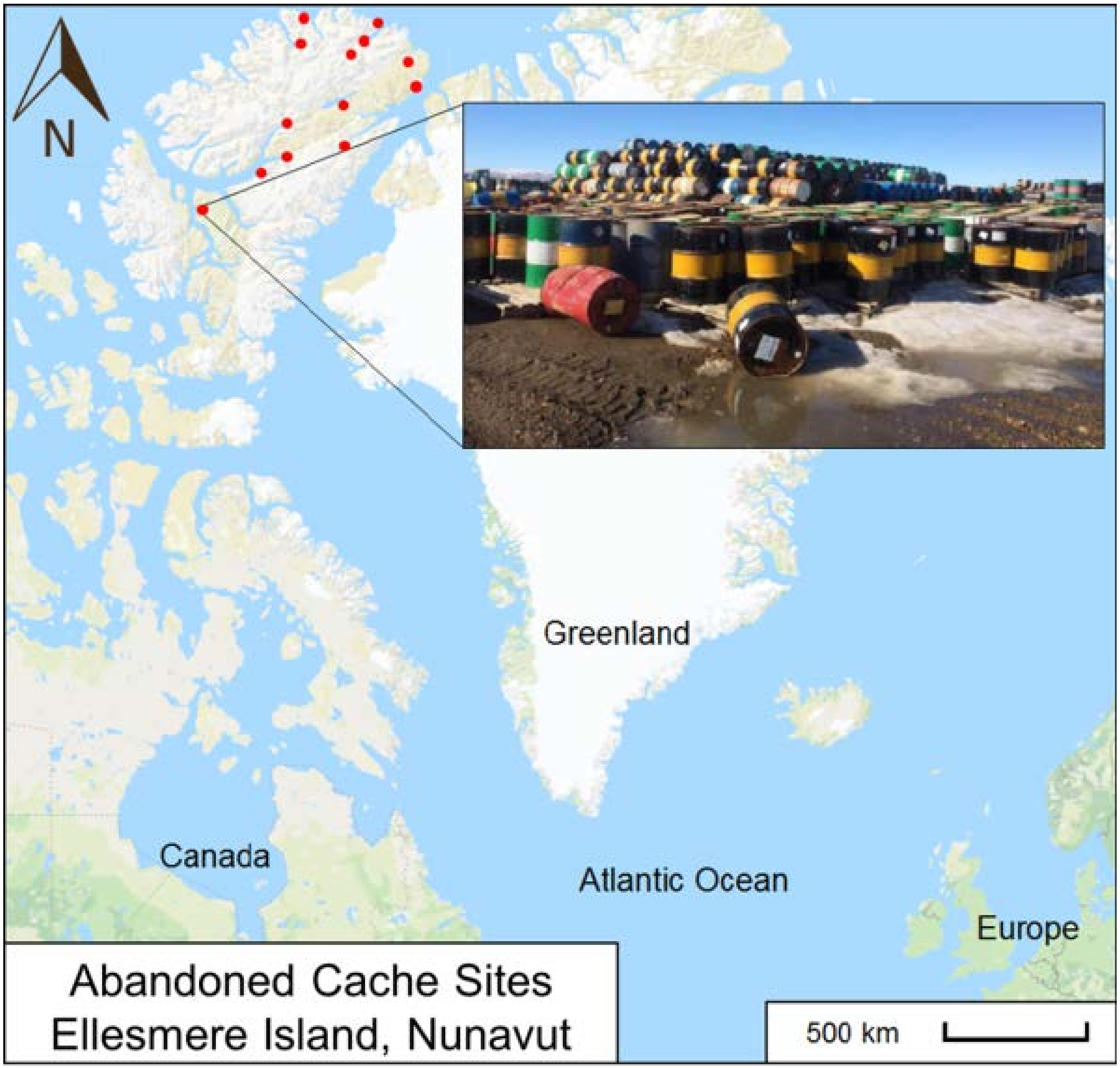

Figure 1-1: Abandoned barrel cache sites on Ellesmere Island.

The presence of petroleum hydrocarbons at those sites, especially without any contaminant monitoring, presents an environmental risk to the local communities and ecosystems. Their isolation and the limited understanding of where the contaminants may have migrated over their lifetime complicate the remediation of those sites. The study of contaminant transport in frozen soils will help to identify and delineate the source zones and the plumes of contaminants, which would make remediation efforts more efficient and allow to determine which ecosystems and communities could be at risk of contamination.

Using a geotechnical centrifuge is a possible solution in order to decrease the costs and time required to conduct the characterization and environmental assessment of the potentially contaminated sites. The geotechnical centrifuge allows for the simulation of large scale and long-term experiments over a short period of time and using a small-scale model of the field site being studied. The centrifuge is able to achieve this because of the scaling principles that govern centrifuge modelling.

Figure 1-2: Barrel cache at d’Iberville, Ellesmere Island.

1.2 Previous Research & Research Gaps

This thesis incorporated the research fields of contaminant transport, cold regions engineering and geotechnical centrifuge modelling. Some studies incorporated a combination of two of the three fields mentioned above (Table 1-1). Those studies were reviewed in order to determine which research gaps could be filled with this research. It was found that no studies incorporated all three research field into one study, thus this thesis is a starting point to fill this research gap. There were also no studies that investigated the effect of moisture content and temperature on the contaminant transport through soil in a geotechnical centrifuge. Some studies mentioned above were able to develop an apparatus that induce freeze-thaw cycles on the soil in a geotechnical centrifuge. However, an apparatus was not yet developed for use in the geotechnical centrifuge at RMC. Research was previously conducted using the geotechnical centrifuge at RMC (Kingswood et al. 2016a; Laporte and Siemens 2017). The procedures and some of the instrumentation used as part of this thesis were derived from the research mentioned above. Since the research field is different for this thesis, some new procedures, instrumentation and apparatus had to be developed.

Table 1-1: Examples of studies combining two of the three research fields that pertain to this thesis.

Research Fields	Publications
Contaminant Transport & Cold Regions Engineering	Konrad and Seto 1991 Tumeo and Davidson 1993 Biggar et al. 1998 Civan 2000 Chuvilin et al. 2001 Iwakun et al. 2008 (Chuvilin 2009) Iwakun et al. 2010a Iwakun et al. 2010b
Contaminant Transport & Geotechnical Centrifuge Modelling	Celorie et al. 1989 Kumar 2006 Kumar 2007 Bhatlu 2014 Qin 2019
Cold Regions Engineering & Geotechnical Centrifuge Modelling	Stone et al. 1996 Smith 2004 Kern-Luetschg and Harris 2008

1.3 Research Scope and Objectives

After identifying the gaps in the three research fields that this thesis will incorporate, the research objectives and scope were developed. The main objective of this research was to prove that a geotechnical centrifuge modelling could be used to conduct research on contaminant transport through frozen soil. The end goal of this research was to be able to conduct physical modelling of a contaminated site in the Canadian Arctic. In-situ soil and contaminants would be used to determine the behaviour and wetting front velocity of the contaminants. By determining this, the remediation of these sites could be facilitated by having a better understanding of where spilled contaminants would be located in the subsurface. To accomplish this, the following research objectives were established:

1. Develop the procedures for conducting contaminant transport experiments in the geotechnical centrifuge;

2. Design the instrumentation for contaminant transport experiments in the centrifuge;

3. Design an apparatus to create freeze-thaw cycles within the centrifuge cradle;

4. Validate the use of a geotechnical centrifuge for contaminant transport research, which includes the design and use of a column to conduct experiments;

5. Conduct experiments to determine the effects of moisture content on the wetting front velocity of contaminants;

6. Conduct experiments to determine the effects of temperature on the wetting front velocity of contaminants; and,

7. Develop the characterization requirements and experiment procedures to use samples collected from contaminated sites in order to conduct experiments in the geotechnical centrifuge. The centrifuge experiments will help determine the wetting front velocity of the contaminants at their respective sites.

The research as part of this thesis did not include an in depth thermal analysis of the experiments. It also did not include an analysis of the chemical processes of contaminant transport, such as the reactivity or adsorption of contaminants. The research focused on the physical macroscopic behaviour of the contaminants infiltrating through frozen soil.

1.4 Thesis Outline

Chapter 2 is a literature review on the topics of contaminant transport, cold regions engineering and geotechnical centrifuge modelling. It covers the important information that is required to understand how all three research fields are brought together in the scope of this research.

Chapter 3 explains how the experimental procedures were developed and explains the steps for conducting an experiment in the geotechnical centrifuge and in the acrylic column. Chapter 3 also presents the laboratory work that was done in order characterize the soils and contaminant used as part of this research.

Chapter 4 presents the results of the experiments that were conducted as part of this research. The experiments to validate the use of the geotechnical centrifuge are presented. Chapter 4 also presents the experiments conducted to determine the effects of moisture content and temperature on the wetting front velocity of pumpkin seed oil through soil in the centrifuge. Finally, Chapter 4 presents a centrifuge experiment that was conducted using soil from an abandoned barrel cache in Wrangle Bay, Ellesmere Island, Nunavut.

Chapter 5 concludes the thesis document, explains how the research field was advanced, and presents potential future research avenues to improve the experimental apparatus and methods in the geotechnical centrifuge for contaminant transport through frozen soil. It also explains how the research can help with the characterization and remediation of contaminated sites in cold regions.

Appendix A shows the laboratory work that was done to characterize the sand that was used for most of the centrifuge and all of the column experiments. Appendix B shows the laboratory work that was done to characterize the soil from Wrangle Bay, Nunavut that was used in one centrifuge experiment. Appendix C shows the laboratory work that was done to characterize the pumpkin seed oil that was used for all centrifuge and column experiments presented in this thesis. Appendix D lists the procedures to set up a centrifuge experiment and extract the raw data. Appendix E lists the materials and equipment required to build the thermistors used for the centrifuge experiments. It also lists the steps to build and calibrate the thermistors. Appendix F lists the steps to set up an experiment in the acrylic column. Appendix G lists the steps to run the code to analyze the images taken during centrifuge and column experiments.

2 LITERATURE REVIEW

2.1 Introduction

The study of contaminant transport in temperate and warm climates is well developed. However, the same cannot be said of contaminant transport in cold regions. Newfound interest in the topic is primarily driven by the requirement to remediate abandoned industrial installations such as mines and military outposts in Canada's Northern regions. Examples of facilities that were remediated in the Canadian Arctic are the Colomac mine (Iwakun et al. 2010a) and the Distant Early Warning (DEW) sites (Hyrd 2016), while the barrel caches on Ellesmere Island are in the process of being remediated. Because of the remoteness of most sites in the Arctic, it is often difficult and expensive to conduct long-term in-situ field studies on contaminant. To date, there have only been a handful of such types of studies completed such as Biggar et al. 1998a, Chuvilin 2009, Iwakun and Biggar 2007 and Kalinovich et al. 2008.

The barrel caches on Ellesmere Island are but one example of possibly contaminanted sites throughout the Canadian Arctic. A common remediation method is to use permafrost to contain contaminated soil. The hydraulic conductivity through permafrost is very low (Biggar et al. 1998a), which allows the permafrost to act as a barrier to contaminant transport. With global temperature predicted to rise even more over the next decades, the risk of permafrost degradation will creep further North. This means that the permafrost used to contain contaminanted soil could thaw and lead to the release of the contaminants into the environment which could pose an environmental risk for local communities and ecosystems. The complex problems that were encountered at these sites have shown that in order to effectively remediate these sites, it is critical to understand how the released contaminants will migrate through the soil based on the type of contaminant, the local geology or soil stratigraphy, the soil type, the hydrogeological conditions and the climate.

The advancement of the study of contaminant transport in frozen ground will help understand the behaviour of contaminants when they are released in cold regions and to understand where they might migrate after a spill. This would help remediation efforts since knowing where a contaminant is located is a critical portion of an environmental remediation plan.

2.2 Contaminant Transport

2.2.1 Introduction to Contaminant Transport

Contaminant transport is used to describe and quantify the migration of a contaminant through a given medium. Aromatic hydrocarbons, metals and radionuclides are examples of contaminants that can be present in the environment due to human activites. Air, water and soil are the most common mediums through which the contaminants will migrate. This research focuses on the contaminant transport of petroleum hydrocarbons (PHC) through soil, more specifically the #730 Silica sand used by Beddoe and Take (2016).

The concentration of a solute chemical in a given solvent can be expressed as mass concentration e.g. mg/kg, % of mass, parts per million (ppm) or ppb (parts per billion). It can also be expressed as volumetric concentration e.g. mg/L or moles/L. Load is the amount of chemicals transported per unit of time. The transport of contaminates through soil and water will be governed by the three following mechanisms: advection, diffusion and dispersion (van der Perk 2017).

Advection is the transportation of chemicals with the general flow of the medium (Figure 2-1), which is usually water in soil. Gravity and pressure will cause water to flow in a certain direction. The total force causing water flow is known as hydraulic head (Equation 1), where ‘ψ’ is the pressure head and ‘z’ is the elevation head (Figure 2-2).

$$\boldsymbol{h = \psi + z} \quad [1]$$

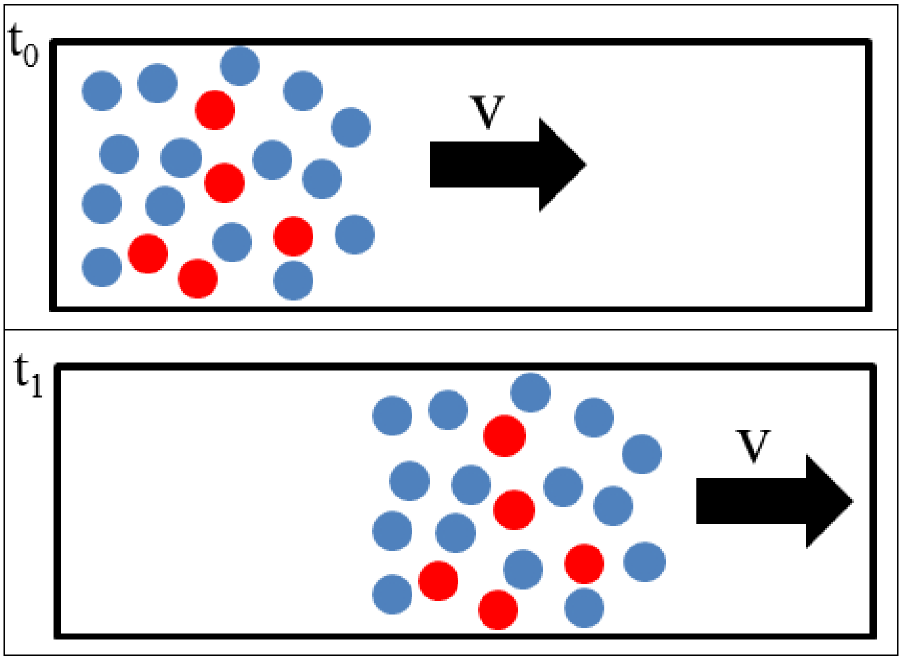

Figure 2-1: Advection of contaminant.

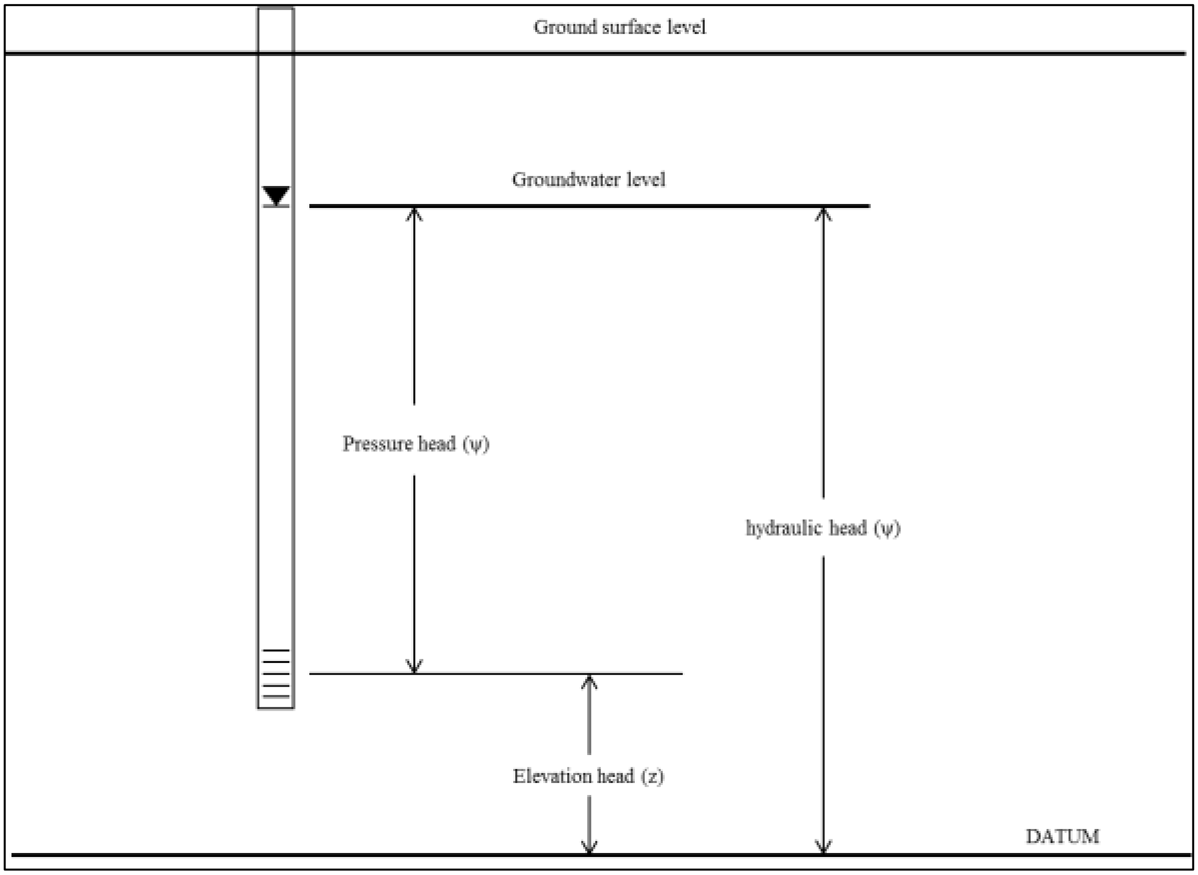

Figure 2-2: Visual representation of Equation 1 (after Fetter 2001).

The average linear flow velocity of a fluid through soil will be affected by the hydraulic head gradient (∇h), porosity of the soil (Equation 2), and the hydraulic conductivity of the soil (K). The average linear flow velocity in one direction can be calculated using Equation 3. The one-dimensional advective contaminant transport (Figure 2-3) would then be as shown in Equation 4. The derivation of Equation 4 would then be as shown in Equation 5.

$$n = \frac{volume\ of\ pores}{total\ volume} \text{ [2]}$$

$$v = \frac{K\ \nabla h}{n} \text{ [3]}$$

$$\frac{\partial C}{\partial t} = -v_x \frac{\partial C}{\partial x} \text{ [4]}$$

$$Advective\ Transport = v_i\ n\ C\ dA \text{ [5]}$$

Where:

v_i = Average linear velocity normal to the cross sectional area (dA) (m/s)
n = Porosity
C = Concentration of contaminant (mg/g)
dA = Cross-sectional area (m^2)

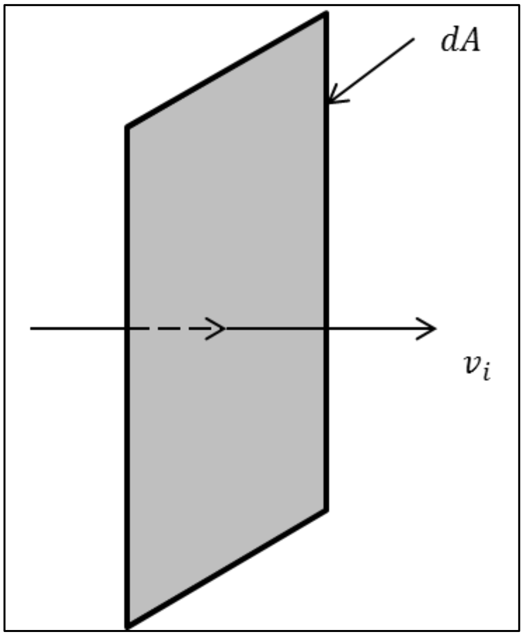

Figure 2-3: Advective transport through cross-sectional area.

Diffusion is the random movement of molecules through water from high solute concentration to low concentration (Figure 2-4). Fick's first law (Equation 6) describes the flux of mass transport. Diffusion will occur as long as there is a concentration gradient (van der Perk 2017).

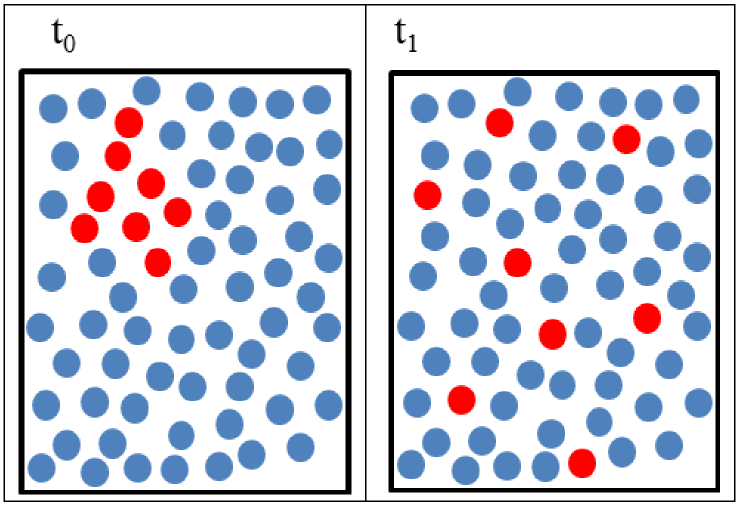

Figure 2-4: Diffusion of contaminant.

$$J = -D_d \frac{\partial c}{\partial x} \text{ [6]}$$

In that equation, D_d is the diffusion coefficient that will depend on the chemical and thermodynamic properties of the solute and the solvent being analyzed. The diffusion coefficient will also depend on the temperature at which diffusion is occurring. $\frac{\partial c}{\partial x}$ is the concentration gradient between two points. In a porous media, such as soil, diffusion cannot occur in a straight line because the molecules must travel around soil particles. This effect is known as tortuosity which ‘is a measure of the effect of the shape of the flow path followed by water molecules in a porous media’ (Fetter 2008). Tortuosity is taken into account by multiplying the diffusion coefficient, D_d, by a tortuosity coefficient, ω, (Equation 7) to get an effective diffusion coefficient.

$$D^* = \omega D \text{ [7]}$$

Because of soil’s heterogeneous nature, contaminants being transported by advective flow will spread and travel at different velocities. Dispersion occurring along the direction of flow is known as longitudinal dispersion. It is affected by the pore sizes in the soil, the flow path lengths and friction in the pores (Figure 2-5).

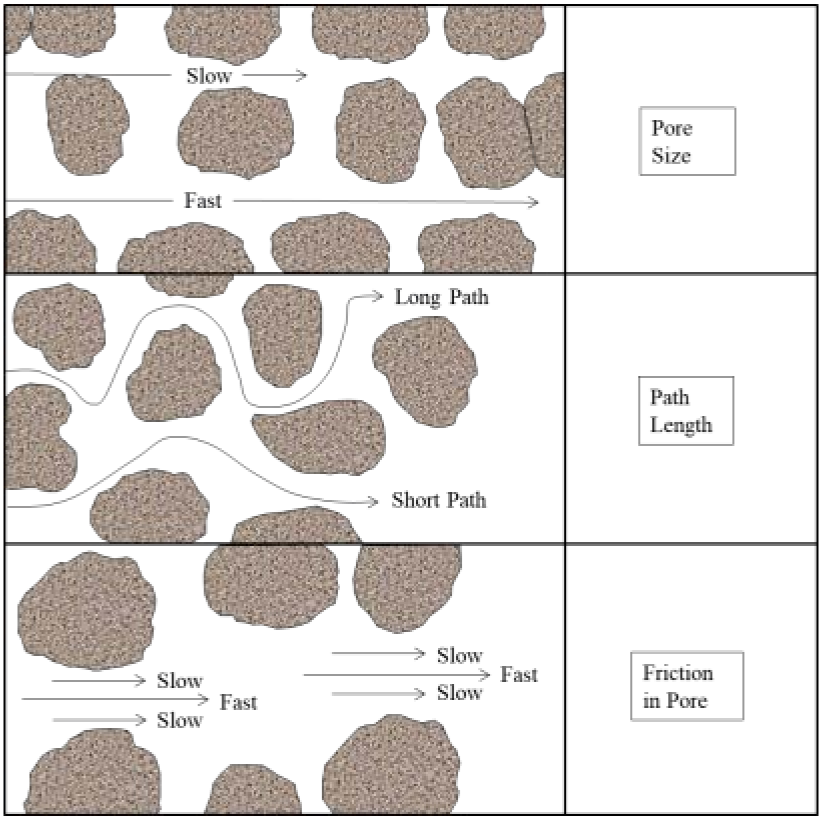

Figure 2-5: Mechanical dispersion in soil (after Fetter 2008).

Dispersion that is normal to the direction of flow is known as transverse dispersion. Transverse dispersion can be horizontal and vertical. Transverse dispersion is caused by the variation in flow path distances within soil. The amount of dispersion within soil is a function of the average velocity of advective flow (Fetter 2008). To quantify dispersion, a longitudinal and transverse coefficient of dispersion (Equation 8 & 9) is added to Fick's first law for diffusion (Equation 7).

$$Coefficient\ of\ longitudinal\ dispersion = \alpha_i v_i \quad [8]$$
$$Coefficient\ of\ transverse\ dispersion = \alpha_j v_i \quad [9]$$

In Equation 10 & 11, 'i' is the direction of flow, v_i is the average linear velocity in the 'i' direction, α_i is the longitudinal dispersivity and α_j is the transverse dispersivity. Since the process of dispersion and diffusion cannot be separated in flowing groundwater, and Fick's first law can be used for dispersion and diffusion, the coefficients for dispersion and diffusion can be added together to give what is called hydrodynamic dispersion (Fetter 2008). The hydrodynamic dispersion coefficients will then be:

$$D_L = \alpha_i v_i + D^* \quad [10] \text{ and;}$$
$$D_T = \alpha_j v_i + D^* \quad [11]$$

Where D_L is the longitudinal dispersion coefficient and D_T is the transverse dispersion coefficient. To determine if the contaminant transport is dominated by diffusion or advection, a Peclet number is calculated with Equation 12. The Peclet number is dimensionless (Fetter 2008).

$$P = \frac{v_x\, d}{D_d} \quad [12]$$

Where:

v_x = Advective velocity (m/s)
d = Average grain diameter (m)
D_d = Coefficient of molecular diffusion (m^2/s)

The curve in Figure 2-6 represents typical values of D_L/D_d versus the Peclet number, which helps to determine if contaminant transport is dominated by advection or diffusion. For Peclet numbers between 0.02 and 6, both diffusion and advection are contributing significantly.

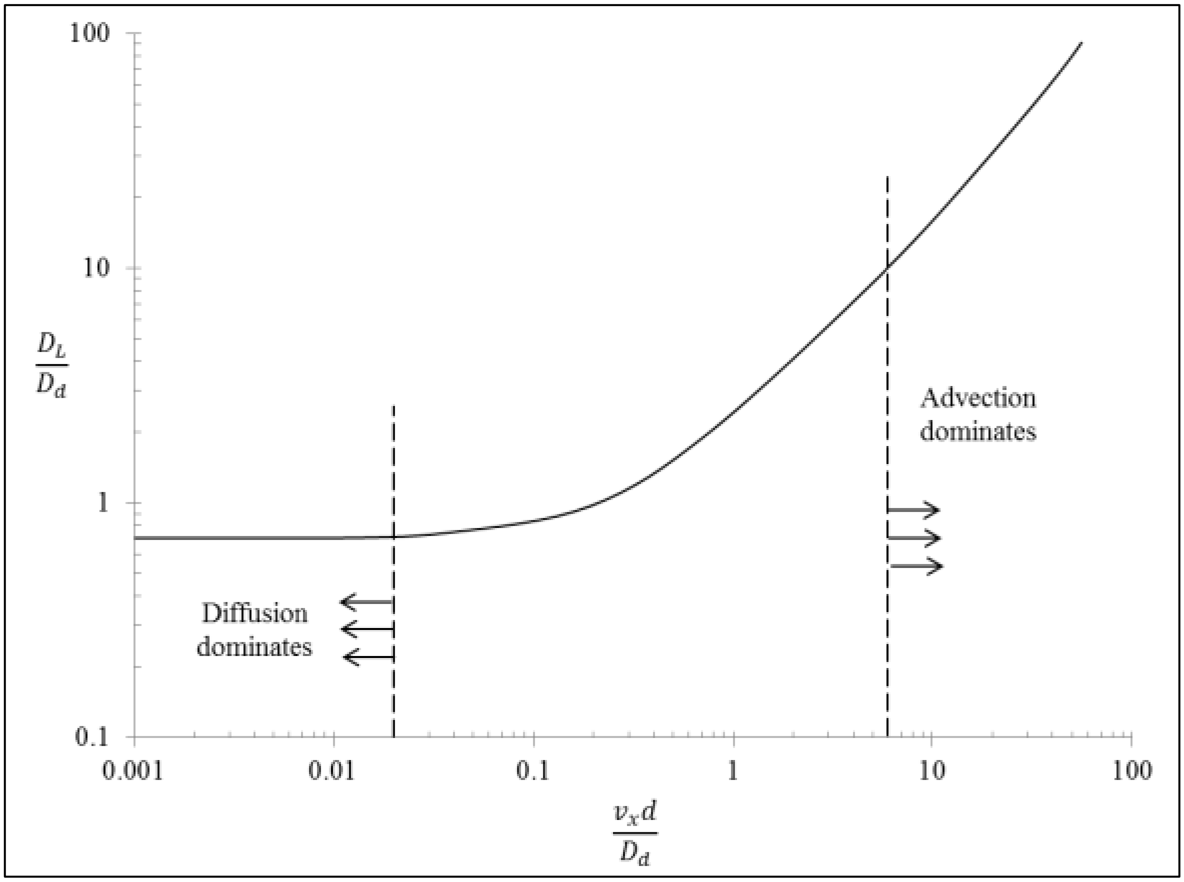

Figure 2-6: Graph of D_L/D_d versus Peclet number (after Fetter 2008).

When there is no flowing water within a soil, the transport of contaminants will occur by vertical advection due to the forces of gravity. From this point forward, that form of advection will be referred to as migration, while the speed at which the oil migrates through the soil will be referred to as wetting front velocity. When the force of gravity applied to the fluid is larger than the force of capillary tension, the fluid will migrate through the soil. If the opposite is true, the fluid will not be able to migrate through the soil and pool above it. If standing water within the soil is present, there will also be contaminant transport by diffusion once the contaminant reaches the water in the soil. Hydrodynamic dispersion also occurs during migration.

When a liquid is in contact with another material, such as soil particles, there is interfacial energy that keeps them attracted and in contact. Interfacial tension is the force required to separate the liquid from the surface to which it is attracted and it is expressed as Force/Length e.g. N/m (Fetter 2008). If more than two liquids are found in a soil, one of the two will preferentially coat the soil particles based on their respective interfacial tensions. This phenomenon is referred to as wettability and can be quantified with a contact angle (Figure 2-7). When a contaminant in fluid form and water are present in soil, their contact angle can be used to determine which of them will preferentially coat the soil particles (Table 2-1).

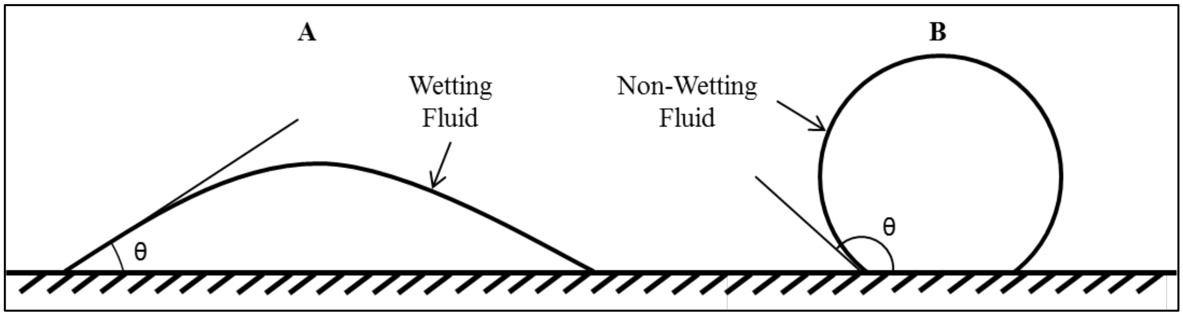

Figure 2-7: Contact angle for wetting (A) and non-wetting fluid (B) (after Fetter 2008).

Table 2-1: Wetting fluid based on the contact angle of water (Fetter 2008).

Contact Angle of Water (°)	Water	Contaminant
θ < 70°	Wetting Fluid	Non-Wetting Fluid
θ > 120°	Non-Wetting Fluid	Wetting Fluid
70°< θ < 120°	Intermediate Wetting	

When two fluids are present within a soil, the location of the fluids will be different based on the wettability. The wetting fluid will coat the soil particles and will be found in smaller pores and pore throats while the non-wetting fluid will be found in the larger pores (Figure 2-8) (Fetter 2008).

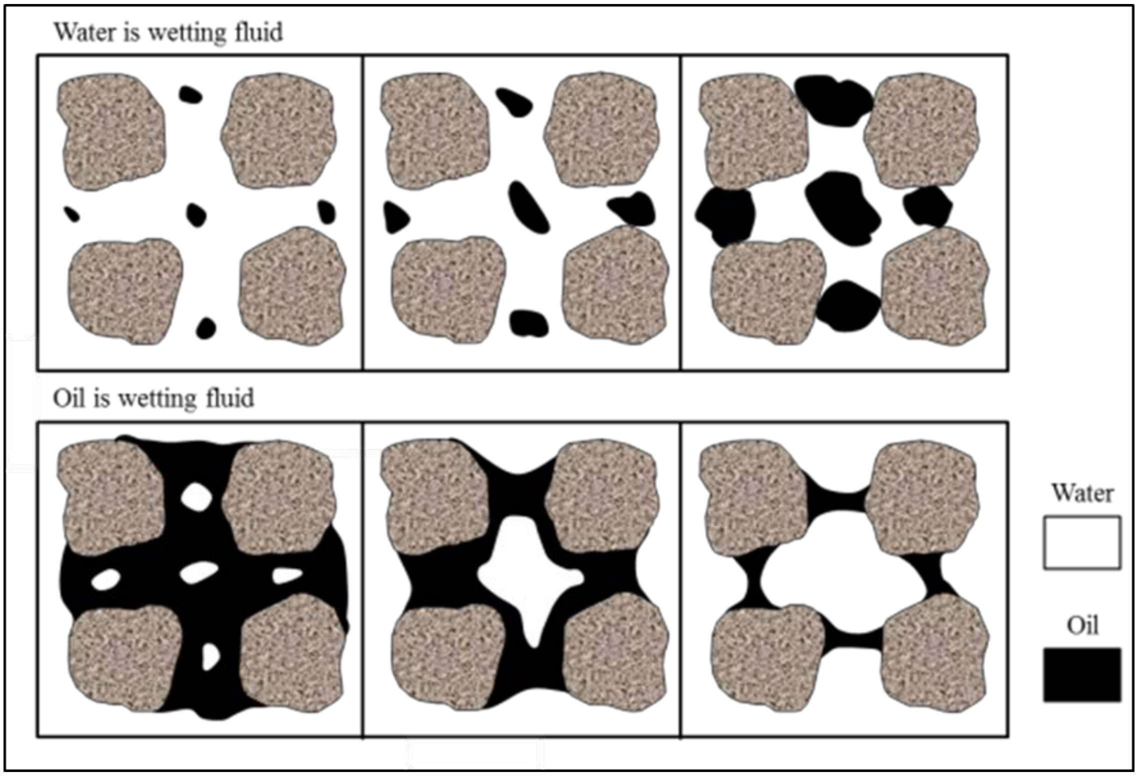

Figure 2-8: Distribution of water and oil as wetting fluid in soil at different saturation states (after Fetter 2008).

In unsaturated soils, capillary pressure is what allows water to be present above the water table. Depending on the soil type and its grain size distribution, the capillary fringe zone can extend from a few centimeters (sand) to 100 meters (clay) above the water table. In the capillary fringe zone, the degree of saturation range from 90 to 100% and can be mistaken for the water table (Fredlund et al. 2012). Capillary pressure will cause fluids to pool above soil if the entry pressure is not achieved. The air and water entry pressure can be extracted from the soil water characteristic curve (SWCC) of a given soil. The SWCC (Figure 2-9) is the plot of the degree of saturation versus the negative pore water pressure (or suction) (Fredlund et al. 2012). The degree of saturation at the water entry value is known as the irreducible degree of saturation. This is due to the water being held in the soil by the surface tension between the water and the soil particles. The surface tension also leads to residual contaminant being found in the contaminant's trail. The contaminant will remain in place until it is displaced by another fluid that is wetting relative to the contaminant or until it degrades naturally or it is actively remediated.

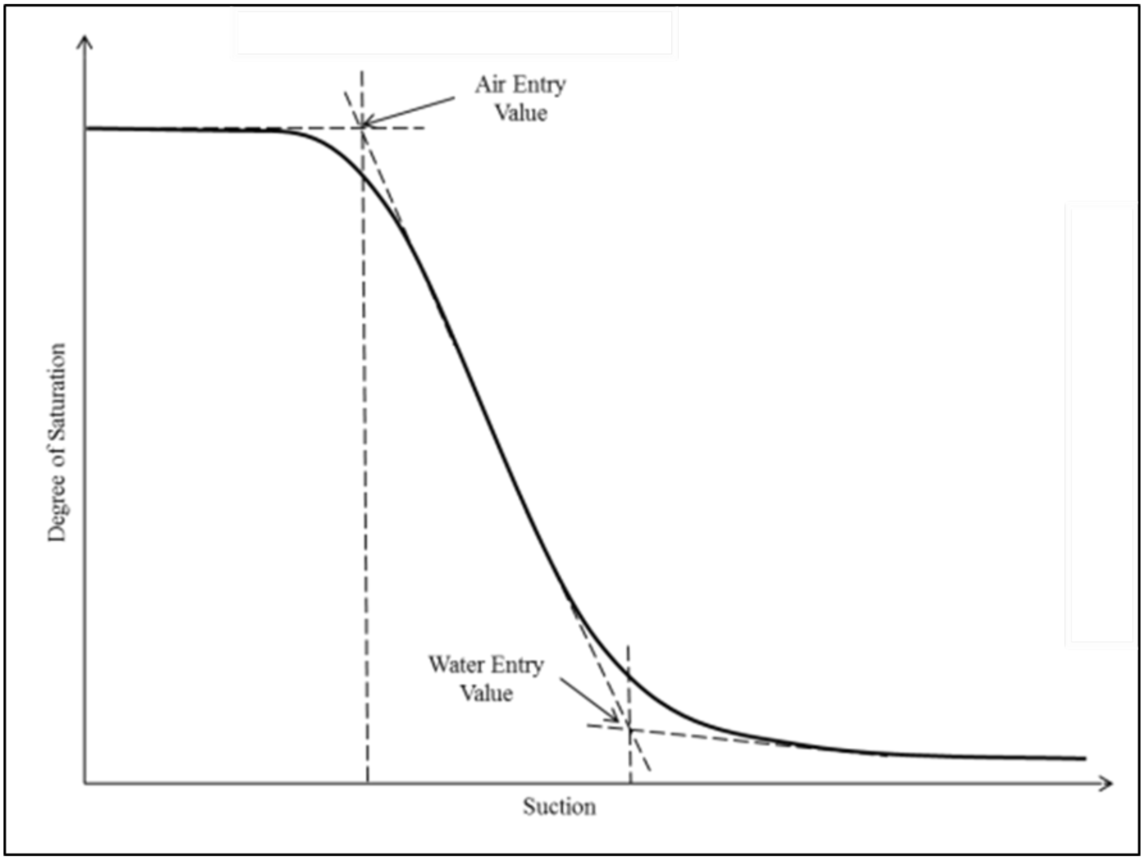

Figure 2-9: Generic soil water characteristic curve (after Fredlund et al. 2012).

It is possible to calculate the entry pressure of a contaminant fluid if the water's entry pressure into the soil is known because of the relationship between the entry pressure and the interfacial tension (Equation 13) (Fetter 2008).

$$P_c^* = \frac{P_c}{\sigma}\sqrt{\frac{k}{n}} \text{ [13]}$$

Where:

P_c^* = Dimensionless capillary pressure (unique to a given system)
P_c = Capillary pressure (Pa)
σ = Interfacial tension (N/m)
k = Hydraulic conductivity (cm/s)
n = Porosity

Since P_c^* is unique to every system we can assume that it will be the same number for the air-water, air-contaminant and oil-water interaction in a given system where both water and a contaminant are present. Equation 13 will then become Equation 14.

$$\frac{P_c^{air-water}}{\sigma^{air-water}}\sqrt{\frac{k}{n}} = \frac{P_c^{air-oil}}{\sigma^{air-oil}}\sqrt{\frac{k}{n}} \text{ [14]}$$

Also, since “k” and “n” are properties of the soil, they will remain the same on both sides of the equation in that system. Equation 14 can then be simplified to Equation 15.

$$\frac{P_c^{air-water}}{\sigma^{air-water}} = \frac{P_c^{air-oil}}{\sigma^{air-oil}} \text{ [15]}$$

A capillary rise experiment (Figure 2-10) can be conducted to determine the interfacial tension for both water and a contaminant of interest. The capillary rise experiment is governed by Equation 16.

$$h_c = \frac{2\sigma\cos\theta}{\rho_w g r} \text{ [16]}$$

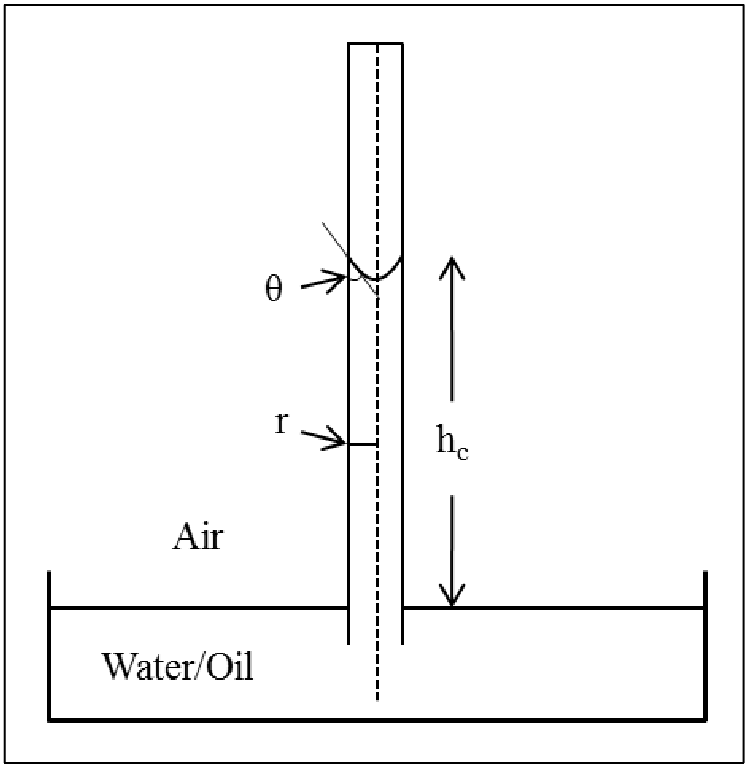

Figure 2-10: Capillary rise experiment (after Fetter 2008).

By conducting the experiment for both water and the contaminant of interest, it is possible to calculate the interfacial tension for each of them. The interfacial tensions can then be inputted into Equation 15 along with the known water entry pressure to calculate the entry pressure for the contaminant.

2.2.2 Light Non-Aqueous Phase Liquids

Non-aqueous phase liquids (NAPL) are liquids for which their compounds have extremely low solubility in water. Generally, the solubility of hydrocarbon compounds will decrease as the carbon number of the hydrocarbon increases. The solubility can range from 1780 mg/L for Benzene at 20°C to 32 mg/L for Naphthalene at 20°C (Larsen et al. 1992). Their freezing point is also generally lower than water, meaning that unfrozen free-phase NAPLs can persist in the soil in northern regions, even if temperatures are significantly below freezing. NAPLs are separated between light non-aqueous phase liquids (LNAPL) and dense non-aqueous phase liquids (DNAPL). LNAPs have a density lower than water while the density is higher than water for DNAPLs. NAPLs are composed of multiple organic compounds, with most of them being petroleum hydrocarbons. The focus of this research will be on contaminant transport of PHCs, which are LNAPLs, including gasoline, diesel, jet fuel, heating oil, etc. Since LNAPLs have a lower density than water, in the event of a spill, they will seep through the vadose zone until they reach the water table. At this point, the LNAPL will pool above the water table and begin to dissolve in the groundwater (Figure 2-11). The vadose zone is the area above the water table and below the ground surface (Fredlund et al. 2012).

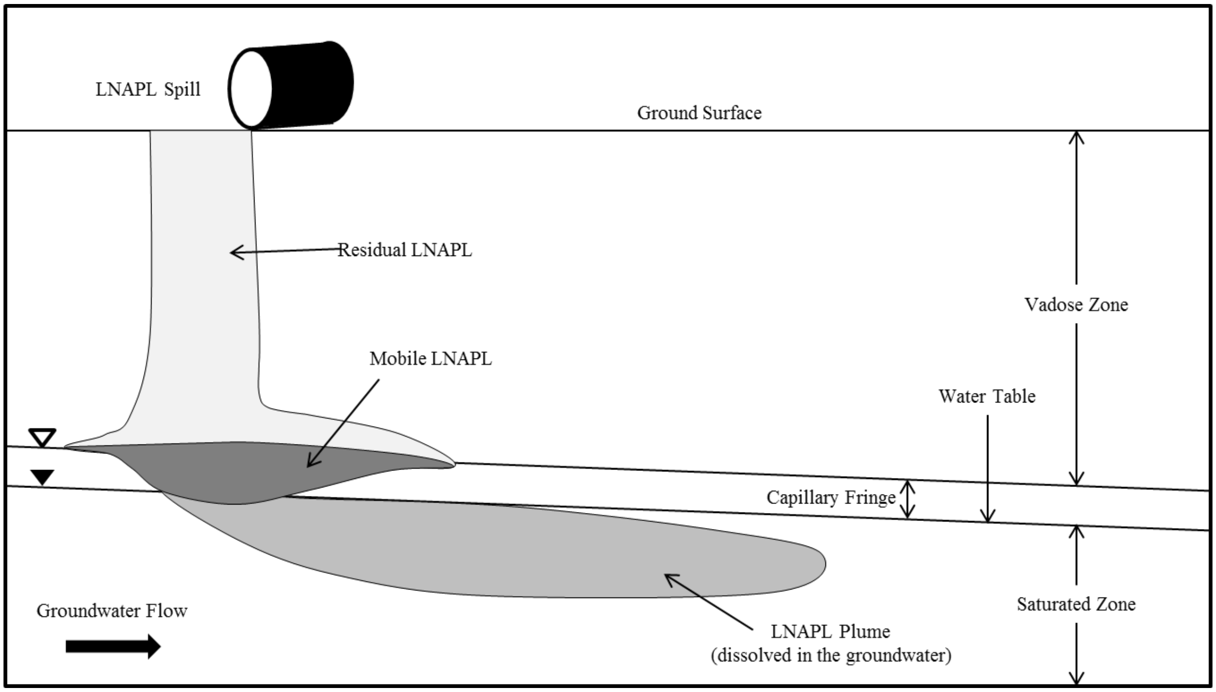

Figure 2-11: Subsurface LNAPL spill (after Fetter 2008).

BTEX, which are aromatic hydrocarbon compounds, are comprised of benzene, toluene, ethylbenzene and xylenes (Table 2-2), which are naturally found in crude oil. They will often be found at sites that have been contaminated with PHCs

Table 2-2: Chemical composition of BTEX compounds.

Compound	Chemical Composition
Benzene	C_6H_6
Toluene	C_7H_8
Ethylbenzene	C_8H_{10}
Xylenes	C_8H_{10}

2.2.3 PHC Standards in Canada

The Canadian Council of Ministers of the Environment (CCME), establishes concentration limits for petroleum hydrocarbons (PHC) in soil in Canada based on land use (CCME, 2008). PHCs are separated into four fractions (Table 2-3) based on the amount of carbon atoms present in each molecule of a given petroleum hydrocarbon. Gasoline mixtures, (Table 2-2), fall under the F1 fraction. Diesel, fuel oil and lubricating oil mixtures typically fall under the F2 and F3 fractions (Nyer and Skladany 1989).

Table 2-3: CCME PHC fractions (Canadian Council of Ministers of the Environment 2008).

F1	F2	F3	F4
C6-C10	C11-C16	C17-C34	>C34

Typically, lower carbon numbers for PHCs are associated with higher solubility in water and higher volatilization potential whereas higher carbon numbers are associated with lower solubility and lower volatilization potential (Biggar n.d.; Larsen et al. 1992).

The concentration limits are based on toxicological data and the expected exposure levels for the different land uses. The effects of PHCs on humans will depend on the compounds involved, the intensity, frequency and duration of the exposure and the exposure pathway. The concentration limits are different for fine and coarse-grained soil and different between surface and subsurface soils. (Canadian Council of Ministers of the Environment 2008).

2.3 Cold Regions Engineering

2.3.1 Introduction to Cold Regions Engineering

Cold regions is a relative concept that can be defined by multiple factors such as air temperature, snow depth, ice cover on lakes, or depth of frozen ground. For cold regions engineering, the most important aspect is frost penetration and the ground temperature, which must be below 0°C to be considered cold regions engineering. It is widely accepted that the southern boundary of cold regions in the northern hemisphere extends to about the 40^{th} parallel, which is where seasonal frost penetration generally reaches 300 mm (Andersland and Ladanyi 2004). The depth and rate of freezing within a soil will be affected by the type of soil, hydrogeological conditions, the presence of contaminants within a given soil, weather and soil cover (vegetation, snow, waterbody). The water within frozen ground acts as a bonding agent between the soil particles, which greatly improves soil strength and creates a near-impervious barrier to infiltration and groundwater flow (Andersland and Ladanyi 2004). Engineers have taken advantage of the increased soil strength when designing structures in cold regions. However, with climate change it is possible for normally frozen zones to thaw, which could put infrastructure at risk, especially in ice-rich soils. The near-impervious nature of permafrost, which has been extensively used to contain various contaminants, could also be lost. This could lead to the release of previously immobile contaminants into the environment.

Permafrost is defined as soil that is frozen (below 0°C) for at least two consecutive years. Cold regions are divided into three areas based on the prevalence of permafrost. An area with continuous permafrost is where permafrost is present all year and everywhere. An area with discontinuous permafrost is where permafrost is present, but only in certain areas. Sporadic permafrost is where the ground is seasonally frozen, and some permafrost may develop, but not permanently (Andersland and Ladanyi 2004). All three types of permafrost, in addition to mountain permafrost can be found in Canada (Figure 2-12).

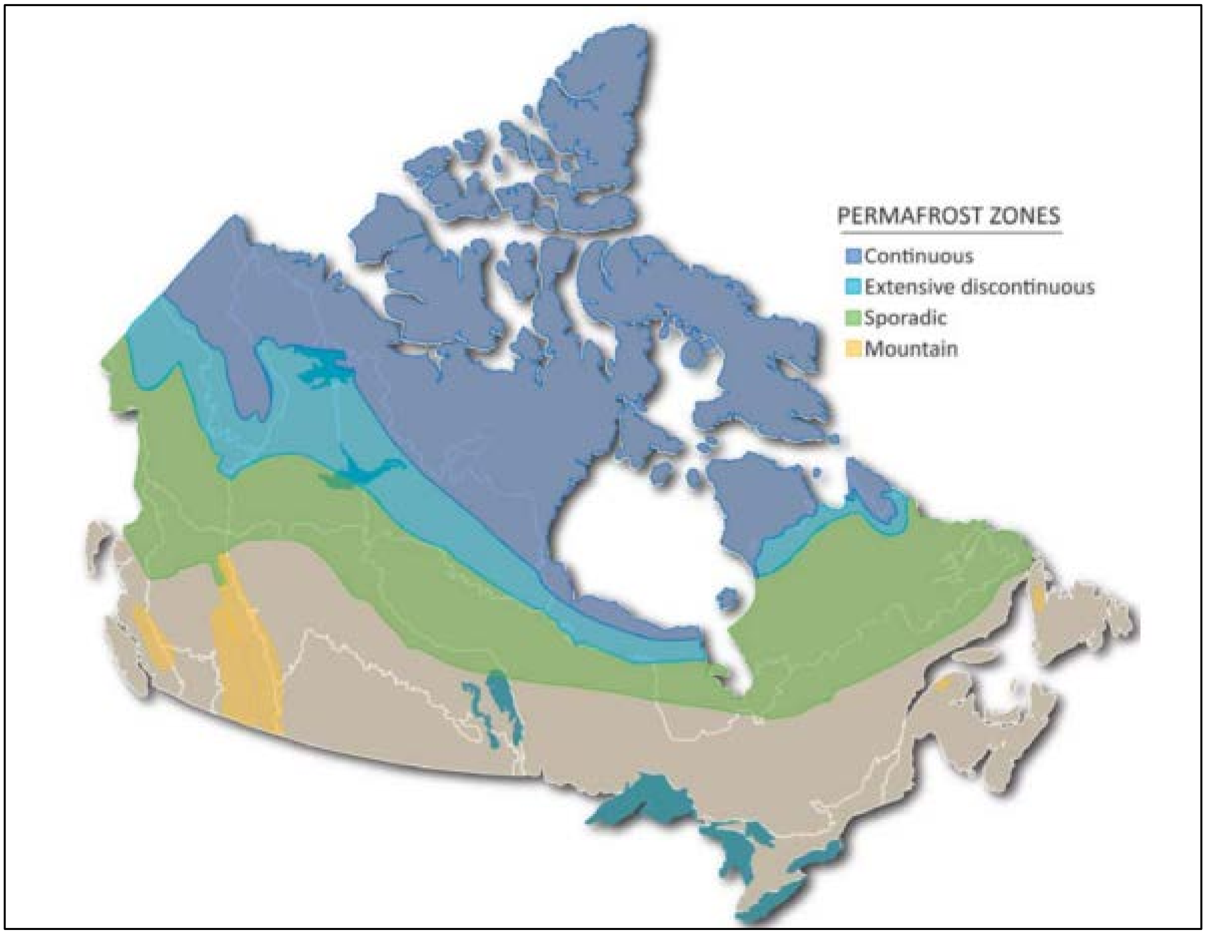

Figure 2-12: Permafrost map of Canada (Smith 2011)

It has been suggested by Gerdel (1969) that to have continuous permafrost, a freezing index of 3,900°C days is required. The freezing index is the cumulative degree-days that are below freezing temperatures. It is also widely accepted that the mean annual ground surface temperature must be at least -3°C for permafrost to exist (Andersland and Ladanyi 2004). The permafrost layer can range from a few meters to several hundred meters thick. The depth of the bottom of the permafrost will depend on the geothermal gradient from the heat originating from the Earth’s core. The active layer is the layer of ground which freezes during the winter and thaws during the summer. The active layer starts at the surface and generally extends to the permafrost. This layer experiences thaw during the summer and freezes back during the winter. The thickness of the active layer can be as little as 15 cm in the northernmost areas and can be several meters deep. Figure 2-13 represents the typical temperature profile in continuous permafrost zones and illustrates the active layer, the permafrost layer and the unfrozen layer beneath the permafrost layer. The depth of the active layer will be affected by the freezing index, soil and rock type, ground moisture content, snow cover, surface vegetation, drainage, and the degree and orientation of slopes (Andersland and Ladanyi 2004). In some areas, the active layer will not extend to the permafrost table. This is caused by permanently unfrozen zones within the soil, which occur because of lakes, rivers, or geothermal anomalies.

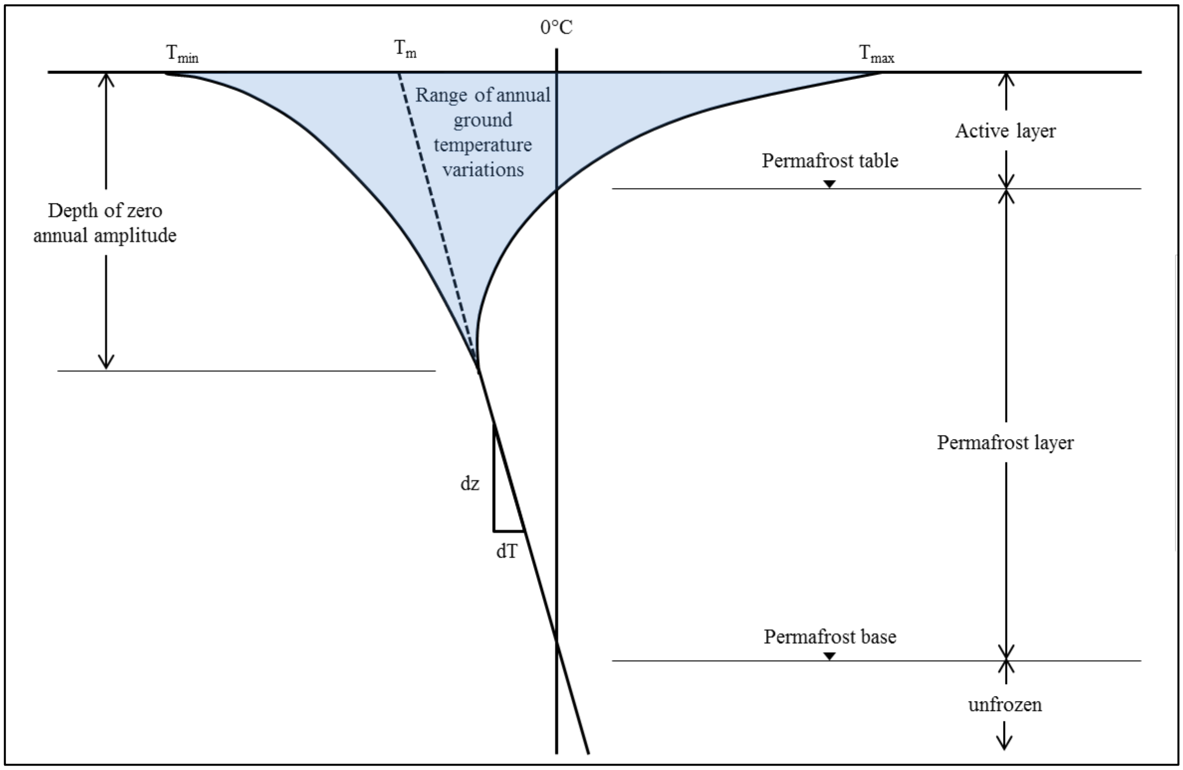

Figure 2-13: Typical temperature profile in continuous permafrost zones (after Andersland and Ladanyi 2004).

2.3.2 Contaminant Transport in Cold Regions

As mentioned previously, challenges were encountered during the remediation of contaminated sites in Canada's Arctic. The presence of permafrost and the low temperatures change the expected behaviour of spilled contaminants and their migration compared to temperate regions.

In northern regions, fill for construction pads is often unsaturated to reduce the impact of frost heave. The continuous air voids in unsaturated soil serve as a conduit for the migration of LNAPLs and other contaminants (Biggar et al. 1998). It has been documented by Grant and Bachmann (2013) that as temperature decreases, surface tension and capillarity increases in porous soils. An increase in capillary pressure will also increase the entry pressure of a fluid in a given soil. This would explain how some contaminants become trapped in frozen soils while migration would be possible if the soil was thawed. If particle sizes of the soil are small enough, the surface tension and small air voids will restrict the movement of LNAPLs. 'Frozen soil subject to decreasing temperatures will undergo thermal contraction, which may lead to the development of a network of fissures' (Biggar et al. 1998). The development of thermal fissures or cracks from annual freeze thaw cycles has been proven to be the mechanism behind the creation of ice lens in the soil (Azmatch et al. 2012). Ice lens are generally found in silty sands and sandy silts at a depth where the rate of frost penetration is slow enough and where the capillary movement of water towards the freeze front is rapid enough (Biggar n.d.). In the summer months, when ice lens are melted, contaminants may migrate through the voids occupied by the ice lens in the winter. This has been theorized to be a significant mechanism for the migration of contaminants through the active layer in cold regions (Iwakun et al. 2010). It is also possible that contaminants migrate at the interface between ice lenses and the soil. While conducting a site investigation of the Colomac gold mine in the Northwest Territories, which has been shut down and remediated, it was found that the seasonal fluctuation of the water table could have an effect on the migration of LNAPLs. Monitoring wells were placed throughout the site, with which it was observed that LNAPLs would be present just above the water table, regardless of the season (Iwakun et al. 2008). LNAPLs have a lower density that water, which is why it would float above it. In cold regions, the water table typically undergoes seasonal fluctuations that are more significant than in temperate climate. The fluctuation of the water table in areas where contaminants are present could help mobilize the contaminants and make it difficult to predict the extent of the contaminant migration after a spill. The task of determining the migration of the contaminant would also be more difficult for older spills.

While non-aqueous phase liquids have very low solubility in water, diffusion is still possible, albeit at very low rates. It has been documented that unfrozen water can be present in frozen soils due to the surface tension from soils particles. The amount of unfrozen water present at freezing temperatures is dependent on many factors such as temperature, soil grain surface, soil mineral composition and the presence of contaminants in the soil (Civan 2000). Unfrozen water exists as thin films adsorbed onto the surfaces of soils particles (Andersland and Ladanyi 2004; Biggar n.d.). Biggar, Nahir, and Haidar (1998) investigated diffusion rates for NAPLs through the unfrozen water of frozen soils. They concluded that although diffusion occurs through the unfrozen water, it is difficult to measure. The diffusion coefficient for petroleum hydrocarbons (PHC) into water has been estimated in the order of 10^{-8} to 10^{-9} cm^2/s.

Solute exclusion, also referred as solute rejection, is the process of rejection and concentration of solutes that is caused by nucleation during the freezing process (Chuvilin et al. 2001b; Konrad and Seto 1991b; Tumeo and Davidson 1993). This phenomenon can also be explained by the variability of the solubility of a contaminant at different temperatures. If a contaminant's concentration is near the maximum solubility, some contaminant will be excluded from the water as temperatures drop. Diffused contaminants have been observed to accumulate ahead of the freezing front due to solute exclusion (Iwakun et al. 2010). This means that the annual freeze-thaw cycles can also trigger the mobilization of contaminants due to solute exclusion. Due to the increased capillarity with decreasing temperatures, upward migration of contaminants have been observed, also by Iwakun et al. (2010) at the commencement of the freezing process.

The combination of both physical and chemical transport mechanism make it difficult to accurately predict the migration and transport rates of contaminants in cold regions.

2.4 Centrifuge Modelling

2.4.1 Introduction to Centrifuge Modelling

Centrifuge modelling has been used to analyze and solve geotechnical engineering problems for about 50 years (Corté 1988). The basic principle is that the rapid rotation of its payload simulates an increased gravitational field (Figure 2-14) as seen in Equation 17 below. 'N' is the acceleration ratio relative to Earth's gravitational pull 'g' while 'r' is the radius of the centrifuge and $\dot{\theta}$ is the angular velocity of the payload. The centrifuge's scaling laws for time, 1/N for dynamic problems and $1/N^2$ for consolidation problems allows for testing of long-term problems in a short period of time. The scaling law for dimensions is 1/N, which means that large-scale prototype areas can be tested using small-scale models in the geotechnical centrifuge (Madabhushi 2015). Centrifuge modelling has made geotechnical research more cost-effective and less time consuming thanks to the scaling laws that govern it (Table 2-4).

$$\mathrm{Ng} = \mathrm{r}\,\dot{\theta}^2 \quad [17]$$

Table 2-4: Centrifuge modelling scaling laws (Madabhushi 2015).

	Parameter	**Scaling law (model/prototype)**	**Units**
General Scaling Laws (slow events)	Length	1/N	m
	Area	$1/N^2$	m^2
	Volume	$1/N^3$	m^3
	Mass	$1/N^3$	$Nm^{-1}s^2$
	Stress	1	Nm^{-2}
	Strain	1	-
	Force	$1/N^2$	N
	Bending moment	$1/N^3$	Nm
	Work	$1/N^3$	Nm
	Energy	$1/N^3$	J
	Wetting Front Velocity	N	ms^{-1}
	Time (consolidation)	$1/N^2$	s
	Temperature	1	°C
Dynamic Events	Time (dynamic)	1/N	s
	Frequency	N	s^{-1}
	Displacement	1/N	m
	Velocity	1	ms^{-1}
	Acceleration/Acceleration due to gravity (g)	N	ms^{-2}

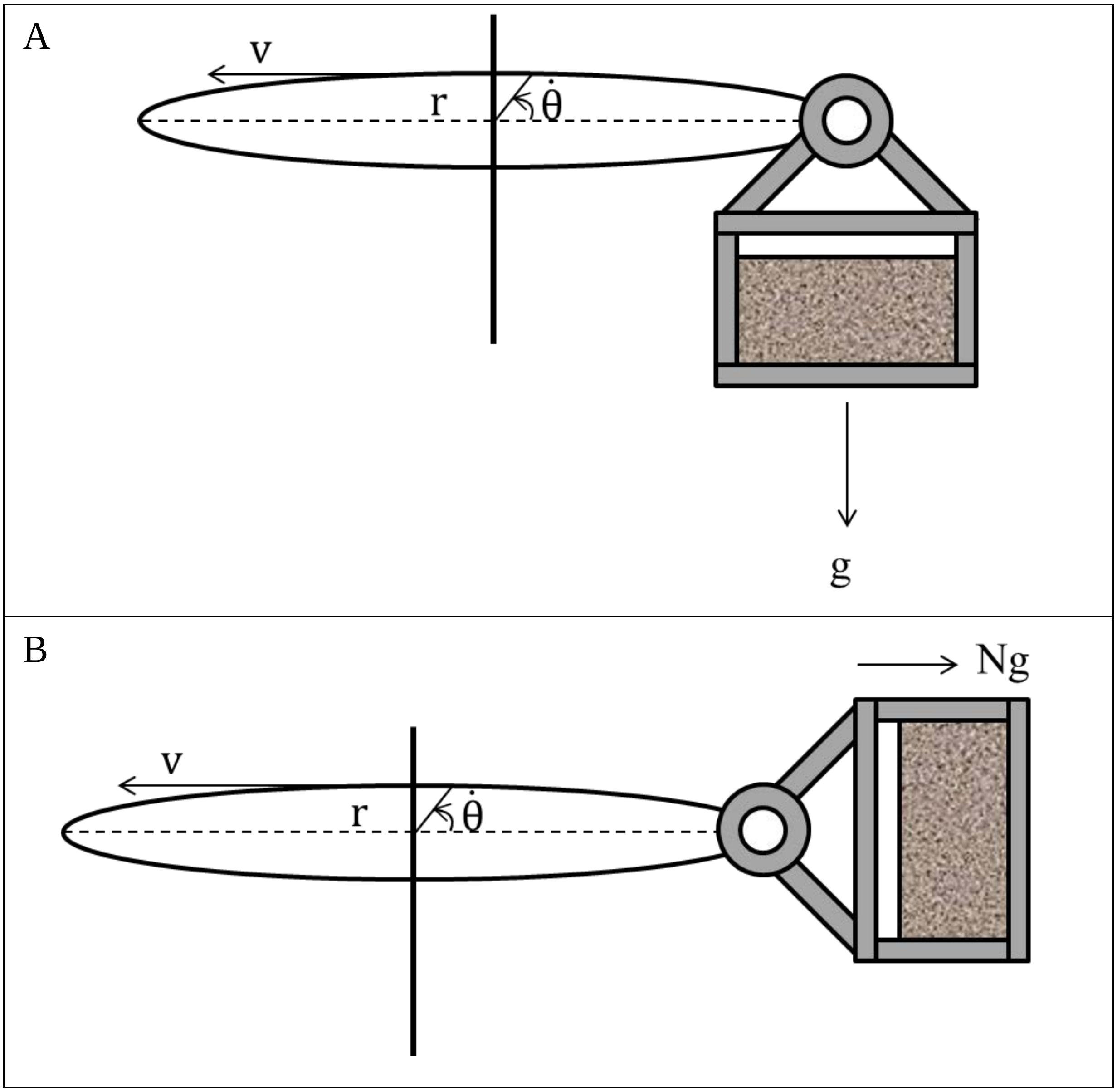

Figure 2-14: Geotechnical centrifuge at rest (A) and while running (B).

One of the methods to validate the scaling laws being applied is by conducting the modeling of models. The modelling of models can also be conducted to determine the scaling laws if they are not easily derived. (Madabhushi 2015). For this research, the scaling law of interest is the one for the wetting front velocity (Table 2-4). In the centrifuge, the contaminant will seep through the sand N times faster than at 1 g. When trying to determine the wetting front velocity of a prototype area (Figure 2-15), it is possible to scale down our model based on the acceleration of the centrifuge. When the model dimensions are converted to the prototype dimensions using the scaling laws in Table 2-4, we arrive at the same dimensions as the prototype. Similarly, when we measure the wetting front velocity experienced by the two models and convert them using the scaling laws they will be equal to the migration experienced by the prototype.

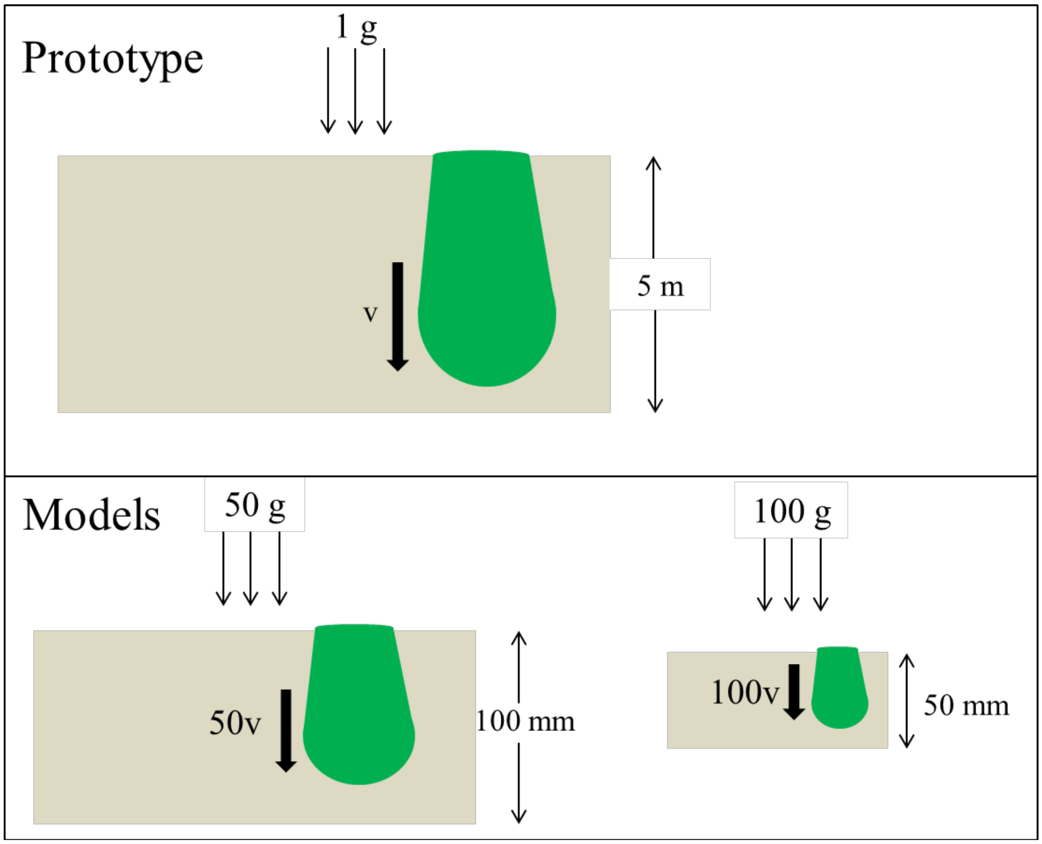

Figure 2-15: Modelling of models example (after Madabhushi 2015).

The Broadbent geotechnical beam centrifuge (Figure 2-16 & Figure 2-17) recently acquired by the Royal Military College was used for this research. It is able to rotate two payload cradles up to 638 rpm which would induce a force of 300 g at a radius of 0.66 m, which is the radius to the centroids of the cradles. The maximum payload is 90 kN (Broadbent 2015).

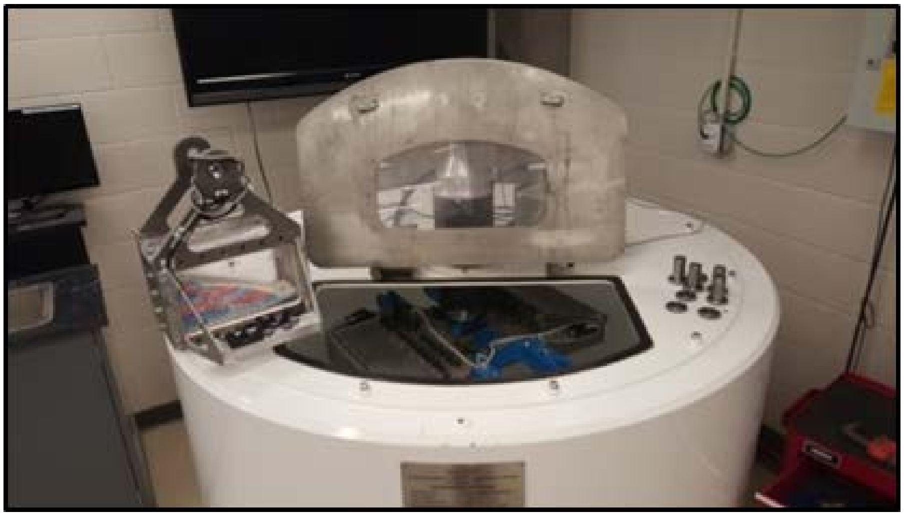

Figure 2-16: Broadbent geotechnical centrifuge at RMC.

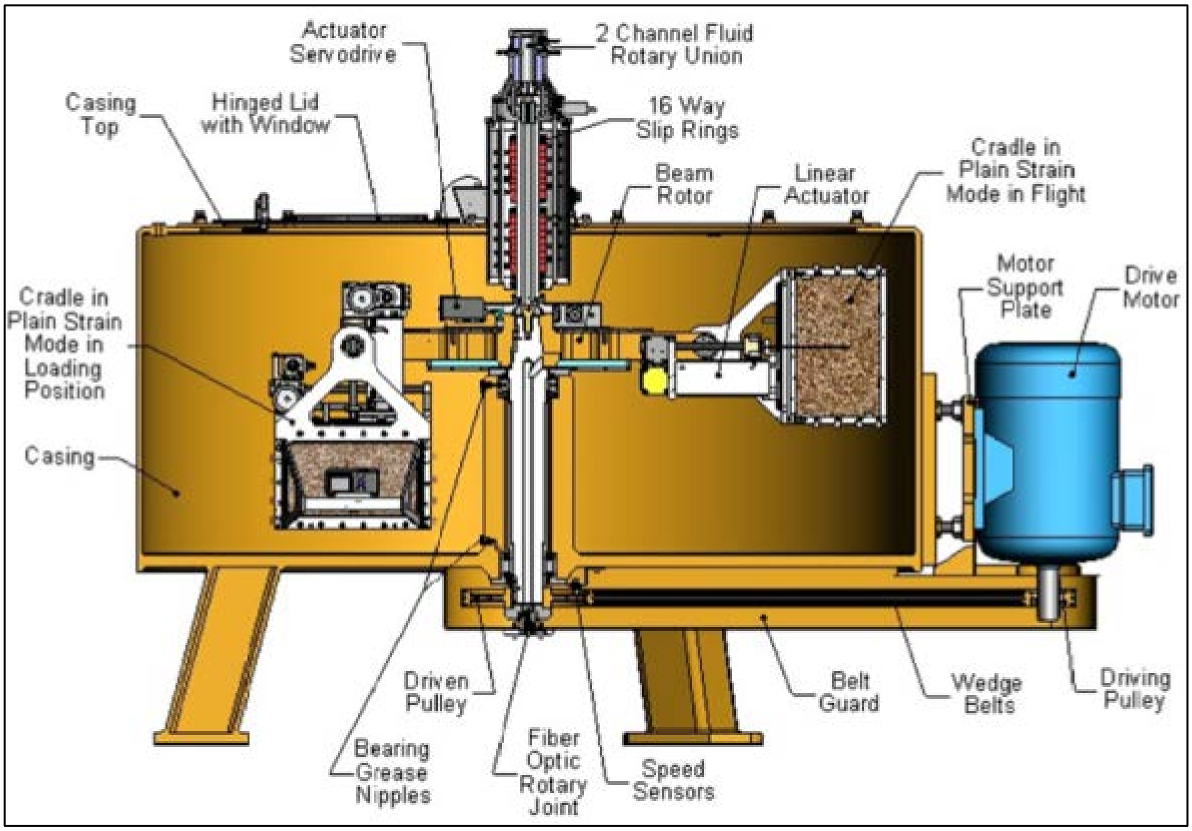

Figure 2-17: Sectional arrangement of RMC's geotechnical beam centrifuge (Broadbent 2015).

When analyzing structures on Earth, we assume a constant gravitational field and ignore the changes of the gravitational forces with depth. However, in a geotechnical centrifuge, the centrifugal forces applied to the prototype will vary with depth. This is because the centrifugal force is a function of the radius of the centrifuge, which varies throughout the prototype sample (Madabhushi 2015). As an example, the following graph shows the variation in the acceleration ratio for the geotechnical centrifuge at RMC (Figure 2-18). At the maximum speed of 638 rpm, the difference in acceleration ratio is quite significant: 259.36 at the top of the sample and 341.26 at the bottom, a difference of 81.9.

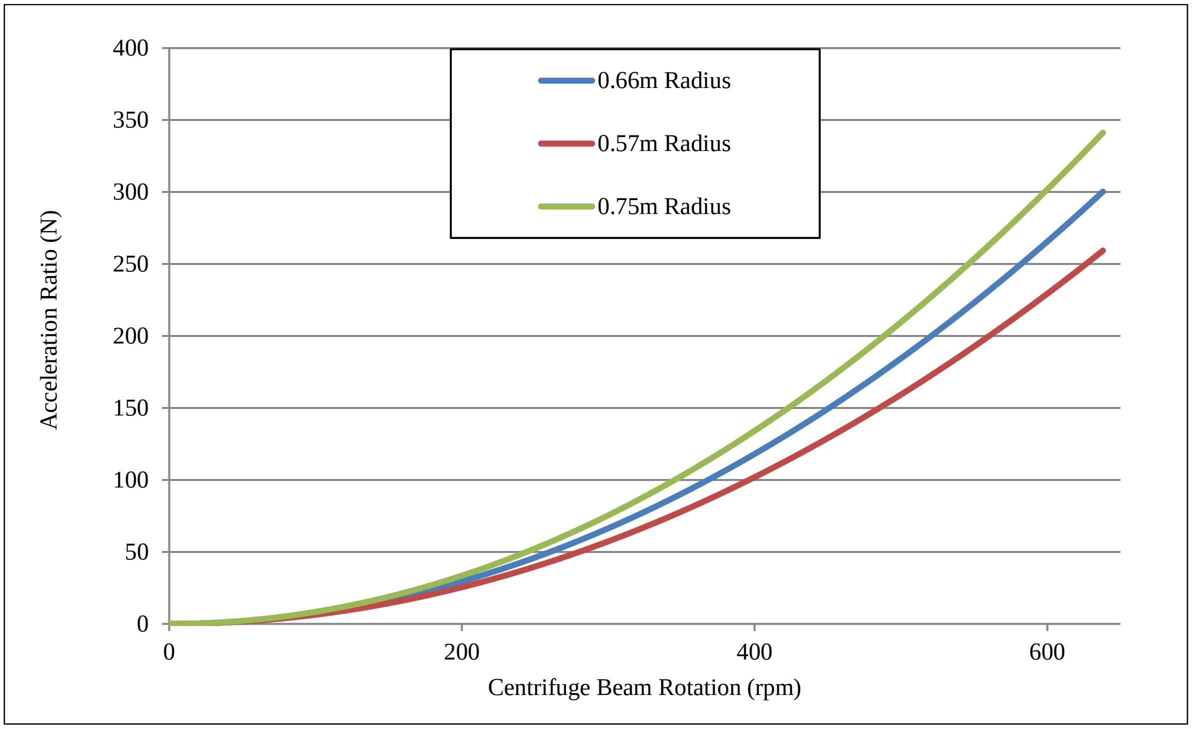

Figure 2-18: Variation of acceleration ratio at different radii.

The effect of the variation of the gravity field can be mitigated by a combination of the following factors: having a centrifuge with a larger radius, operating the centrifuge at lower speeds and setting the desired acceleration ratio based on the effective radius which would be the distance between the centre of the centrifuge and the vertical centroid of the sample. The variation in acceleration ratio throughout the sample will be reduced in those scenarios.

2.4.2 Geotechnical Centrifuge Modelling for Cold Regions Research

The goal of this research was to investigate the feasibility of using the Broadbent Centrifuge at the Royal Military college of Canada for modelling long-term studying of contaminant transport in cold regions. To simulate the annual freeze-thaw cycles to which Canada’s North is subject, an apparatus must be configured to induce cold and warm temperatures within the centrifuge’s cradle. Vortex tubes have been used with success to freeze samples while they are in flight (Harris et al. 2008; Kern-Luetschg and Harris 2008; Smith 2004; Stone et al. 1996). The basic principle of vortex tubes is that compressed air is fed into the tube and the air then enters the splitter cavity, at which point it is ejected into the spin chamber where is revolves rapidly inside the tube towards the warm end of the vortex tube (Figure 2-19).

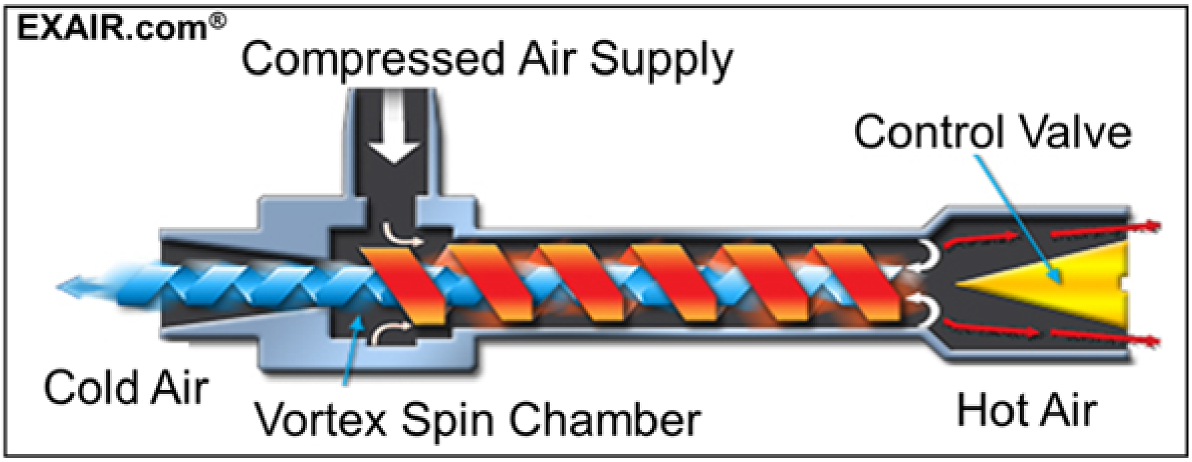

Figure 2-19: Sectional view of a vortex tube (Exair.com, 2018).

Some of the warm air escapes while the rest is directed back inside the tube with the help of a control valve. The returning air stream passes through the centre of the outer vortex flow while transferring heat to the outer flow. This process cools the inner vortex flow, which escapes through the cold end of the vortex tube. It is possible to control the temperature of both flows by adjusting the pressure of the compressed air and by adjusting the 'cold fraction' of the vortex tube. The cold fraction is the percentage of air that is directed towards the cold end of the vortex tube. A low cold fraction will produce the coldest air; however, flow will be sacrificed in that case. This is useful for spot cooling of parts or components, which is not the intended purpose of the vortex tubes for this research. By having a higher cold fraction, a greater percentage of air will escape through the cold end and this produces the best refrigeration, which is how the sample can be frozen in the centrifuge (Smith 2004). Harris et al. (2008) were able to lower the temperature inside the centrifuge cradle to -10°C while Stone et al. (1996) reached -20°C. Both also insulated their cradles to maintain lower temperatures.

2.5 Filling the Research Gap

The goal of this research is to investigate the feasibility of using a geotechnical centrifuge to simulate the long-term analysis of contaminant transport through various soils undergoing freeze-thaw cycles. The geotechnical centrifuge affords the opportunity to study long-term and large scale prototype models within a few days or even hours with benchtop-sized models (Madabhushi 2015). By developing the methods and designing the instrumentation and hardware required to conduct research on contaminant transport through frozen soil, it will help complement the field studies of contaminated site in the Canadian Arctic. The reduced cost of conducting research in a laboratory and the ability to control the experiment conditions based on the contaminated site being studied will help understand the extent at which the contaminant migrated since being spilled. Of the three main research fields (contaminant transport, cold regions engineering and geotechnical centrifuge modelling), some studies have combined two of them but no studies were found where all three were studies together. This thesis aims to address the identified gap, with the objective of helping with the remediation of contaminated sites in cold regions.

3 EXPERIMENTAL PROCEDURES

3.1 Introduction

The objective of this research is to analyze contaminant transport through frozen soil and to understand how the temperature and the water content of the soil will affect the wetting front velocity of the contaminants. Experiments were conducted in RMC’s geotechnical centrifuge and in an acrylic column. The two types of experiments were conducted in order to have a comparison of the wetting front velocities and the behaviour of the oil while subject to low temperatures. The experiments in the acrylic column were conducted in order to ensure that the scaling principle for wetting front velocity is being followed for the centrifuge experiments.

The procedures for the analysis of contaminant transport through frozen soil were developed in order to have controlled and repeatable results. This helps to understand how the different factors and conditions can affect the wetting front velocity of the oil during an experiment. The experimental procedures section will allow future users of the centrifuge the ability to repeat the experiments that were performed as part of this thesis. It also allows future users to implement improvements to the current experimental procedures and methods.

3.2 Material Properties

3.2.1 #730 Silica Sand

For all the experiments conducted as part of this thesis, except for one, the #730 silica sand was used (Beddoe and Take 2016). The #730 silica sand will now be simply referred to as sand from this point on. The soil properties of interest for this soil were its grain-size distribution, its hydraulic conductivity and its soil water characteristic curve from which we can extract the air and water entry pressure. The sand’s specific gravity was assumed to be 2.65 for all calculations. A sieve analysis following ASTM D422–63 (ASTM International 2003) was conducted to determine the grain-size distribution of the sand (Figure 3-1). The sand was poorly graded with the majority of the soil particles being retained by the #120 Sieve (0.125 mm).

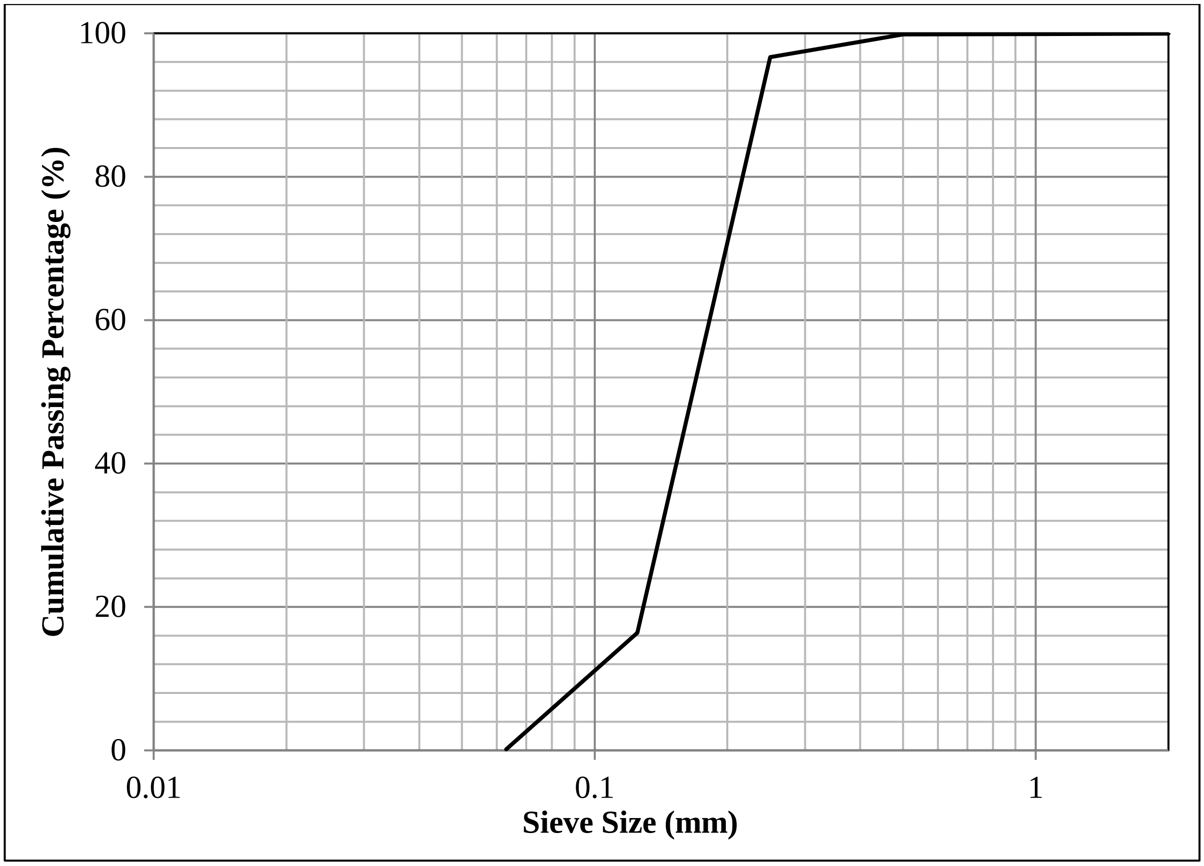

Figure 3-1: #730 silica sand grain size distribution.

The hydraulic conductivity of the sand was determined by following ASTM D2434-68 (ASTM International 1993) using a permeameter similar to the one illustrated in Appendix A. The hydraulic conductivity was calculated to be 8.88x10^{-3} cm/s by conducting two separate constant head tests of the sand. The air and water entry pressures for the sand were determined by using the soil water characteristic curve from Beddoe and Take (2016) (Figure 3-2). The air and water entry pressure were calculated to be 1.6 kPa and 4.1 kPA, respectively. Appendix A presents the detailed methods and calculations that were done to determine the soil properties mentioned above.

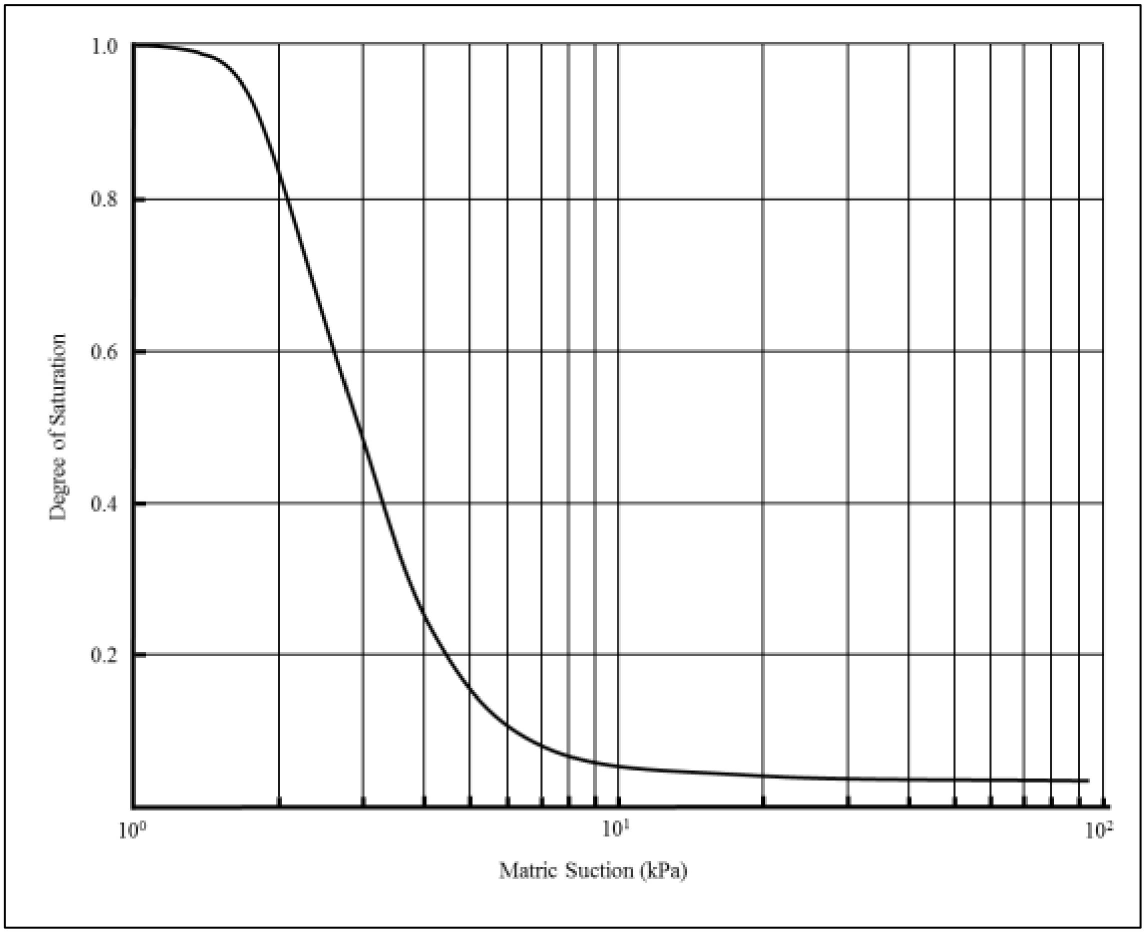

Figure 3-2: Soil water characteristic curve for the #730 silica sand (modified from Beddoe and Take 2016).

3.2.2 Wrangle Bay Soil

The soil from Wrangle Bay, NU was used for one centrifuge experiment. The soil properties of interest for this soil were its water content, grain-size distribution and its hydraulic conductivity. The soil's specific gravity was assumed to be 2.65 for all calculations. The soil from Wrangle Bay was transported back to RMC in sealed bags. It was then possible to calculate the in-situ moisture content of the soil. The two soil samples had a moisture content of 8.9 and 9.2%. A sieve analysis following ASTM D422–63 (ASTM International 2003) was conducted to determine the grain-size distribution of the sand (Figure 3-3). The soil was more well graded than the sand.

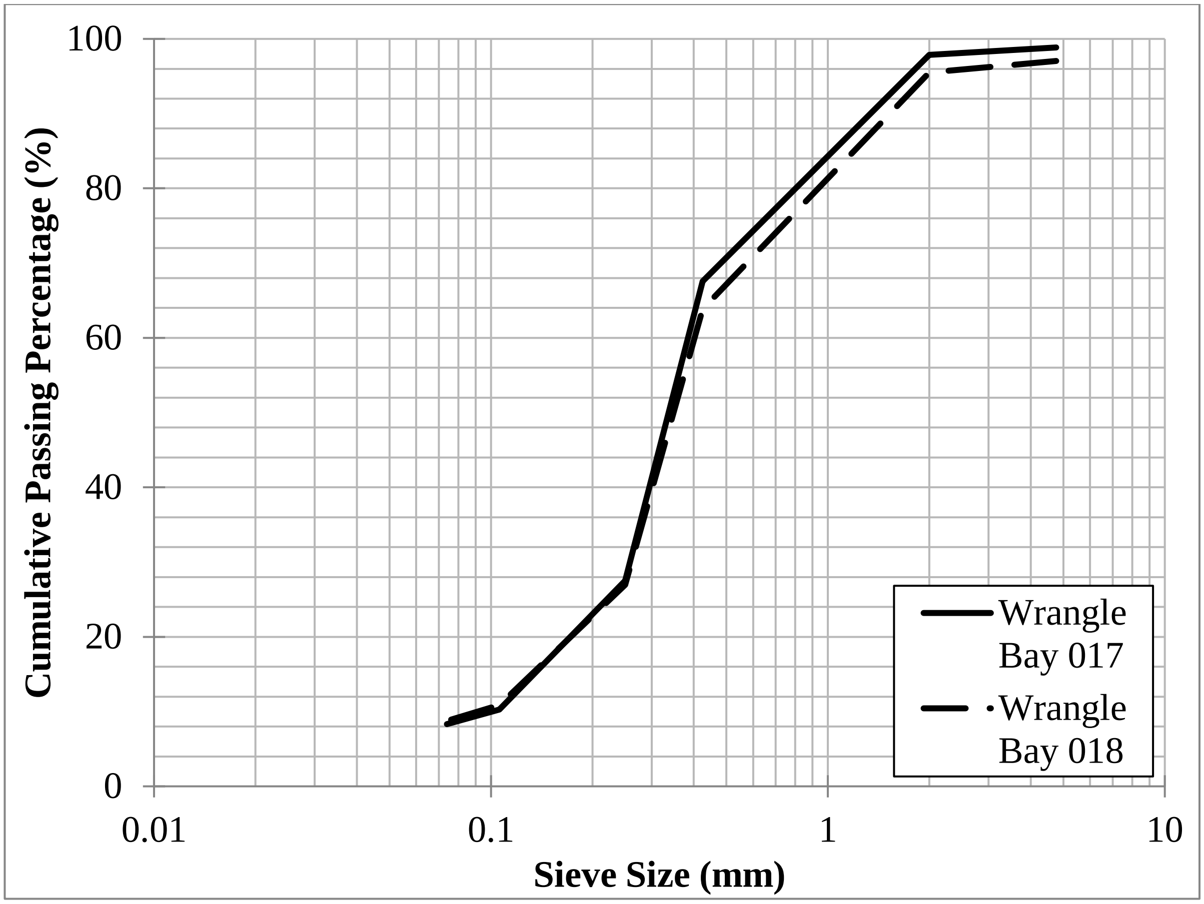

Figure 3-3: Wrangle Bay soil grain size distribution.

The hydraulic conductivity of the soil was determined by following ASTM D2434-68 (ASTM International 1993) using a permeameter as illustrated in Appendix B. The hydraulic conductivity was calculated to be 2.60x10^{-3} cm/s by conducting three separate constant head tests of the soil. Appendix B presents the detailed methods and calculations that were done to determine the soil properties mentioned above.

3.2.3 Pumpkin Seed Oil

Pumpkin seed oil was used as the contaminant for all column and centrifuge experiments. This oil was selected for several reasons. Firstly, using flammable materials within RMC's centrifuge is prohibited, as stated in the Operating Manual (Broadbent 2015). Secondly, exposure to pumpkin seed oil does not pose a health hazard while Petroleum Hydrocarbons (PHC) do (Canadian Council of Ministers of the Environment 2008). Lastly, the oil's physical properties were similar to PHC's properties (Table 3-5) and it was expected to behave similarly for the purpose of this research. Although there is a difference in the density of pumpkin seed oil compared to most PHCs, the pumpkin seed oil was chosen because it also has a density that is lower than that of water. Like Light Non-Aqueous Phase Liquids, the pumpkin seed oil will float above water. Although not as important as the density, the solubility for pumpkin seed oil is low, similar to PHCs. The solubility of pumpkin seed oil was not measured as part of this research, but could be determined by using various laboratory methods. It was also important to select a contaminant that has a freezing point that is lower than that of water, since most PHC have low freezing points. This allows for the analysis of the wetting front velocity at temperatures below 0°C. The physical properties of interest for the pumpkin seed oil that were determined were its density, its freezing point, its interfacial tension and its entry pressure (Table 3-6). The density was determined by gradually adding pumpkin seed oil to a graduated cylinder, weighting it, and calculating the density for different intervals. The freezing point was determined by placing pumpkin seed oil at freezing temperatures and taking measurements of its temperature with a thermocouple as it approached its freezing point. The ambient temperature would change until the freezing point for the oil was reached. The interfacial tension was determined by conducting a capillary rise experiment. With the interfacial tension of the air-water and air-oil interface, we are able to determine the entry pressure of the pumpkin seed oil since we already have the water entry pressure for the sand.

Table 3-5: Property differences between petroleum hydrocarbons and pumpkin seed oil.

Property	Petroleum Hydrocarbons	Pumpkin Seed Oil
Density (g/ml)	~ 0.8[1]	0.91
Freezing Point (°C)	<0[1]	~ -16.0
Solubility	Low[1,2]	Low[2]
Flammability	High[1,2]	Low[2]

[1] The exact property values will vary based on the compounds being analyzed.

[2] The qualitative values of these properties are simply to demonstrate the reasoning for selecting pumpkin seed oil to conduct experiments.

Table 3-6: Properties of pumpkin seed oil.

Temperature (°C)	Density (g/ml)	Freezing Point (°C)	Interfacial Tension (N/m)	Entry Pressure (kPa)
22	0.91	~ -16.0	0.019	1.1
5	0.91	~ -16.0	0.042	2.46

The viscosity of pumpkin seed oil at room temperature is approximately 70 mPa s (Tsaknis et al. 1997), while the viscosity for water is approximately 0.89 mPa s at room temperature. Since the hydraulic conductivity (with water) of the silica sand is 8.88x10^{-3} cm/s, it is possible to determine the hydraulic conductivity of the silica sand (with oil) with Equation 18 & 19, while using the viscosity values mentioned above.

$$K = kf \quad [18]$$

$$f = \frac{\rho g}{\eta} \quad [19]$$

Where:

K = Hydraulic Conductivity (m/s)
k = Intrinsic Permeability (m^2)
f = Fluidity (1/(m*s))
ρ = Density (kg/m^3)
g = Gravitational Acceleration (m/s^2)
η = Viscosity (Pa*s)

The hydraulic conductivity of the silica sand with pumpkin seed oil was determined to be 1.02×10^{-7} cm/s. Appendix C presents the detailed methods and calculations that were done to determine the properties of the pumpkin seed oil used for this research.

3.3 Geotechnical Centrifuge

Geotechnical centrifuge modelling can be used to solve and understand complex engineering problems. The concept of centrifuge modelling is that a simulated enhanced gravitational field is induced on a test sample by subjecting it to rapid rotation. Geotechnical centrifuge modelling offers the advantage of being able to conduct the analysis of large prototype samples with small benchtop-sized models in a relatively short amount of time. The expected behaviours at prototype size can be simulated with benchtop models that are scaled according to the acceleration ratio within the centrifuge. The 6 G-Tonne 0.75 m radius geotechnical beam centrifuge (Figure 3-4) used for this research was acquired in 2015 from Broadbent, a company based in of the United Kingdom. Its serial number is H83119.

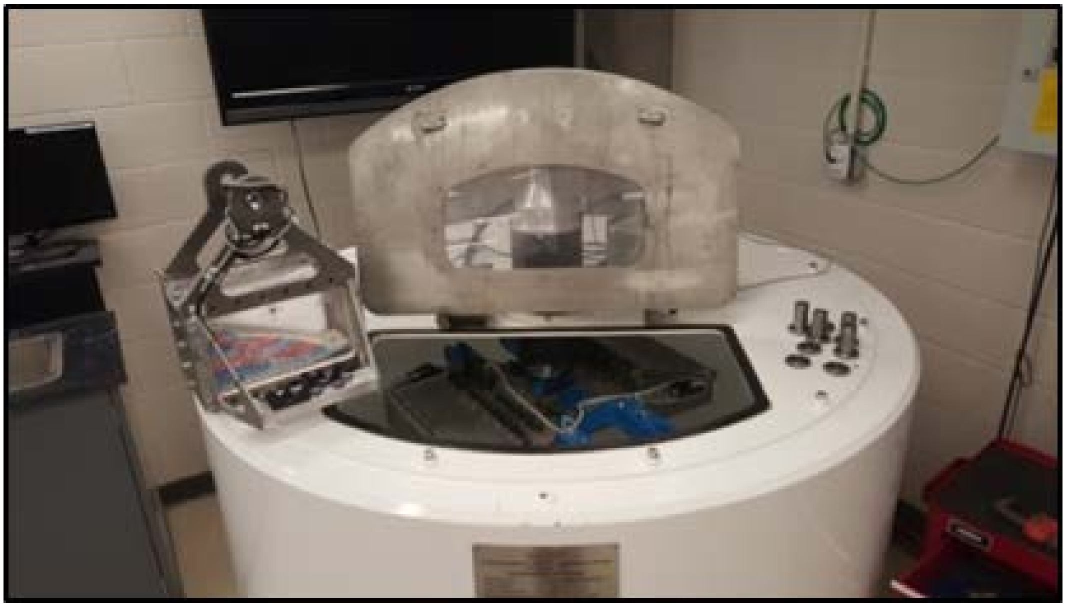

Figure 3-4: Broadbent geotechnical centrifuge at RMC.

The geotechnical centrifuge at RMC has been used to study a wide range of geotechnical problems such as slope stability (Kingswood et al. 2016) and expansive soils (Laporte and

Siemens 2017). The modelling of models method (Madabhushi 2015) was utilized to ensure that some of the scaling laws for the centrifuge were being followed in RMC's centrifuge as part of those studies.

3.3.1 Experimental Setup

The procedures for experiments in the centrifuge were developed in order to be able to observe and calculate the wetting front velocity of pumpkin seed oil through the sand. The models analyzed were setup in one of the centrifuge's two cradles (Figure 3-5). The maximum dimensions of the model that could be placed in the cradles were 300 x 100 x 180 mm (Figure 3-6). The steps to setup an experiment could be modified to change the experimental conditions. The other cradle was used as a balance weight for the primary cradle to reduce vibration while the centrifuge is running.

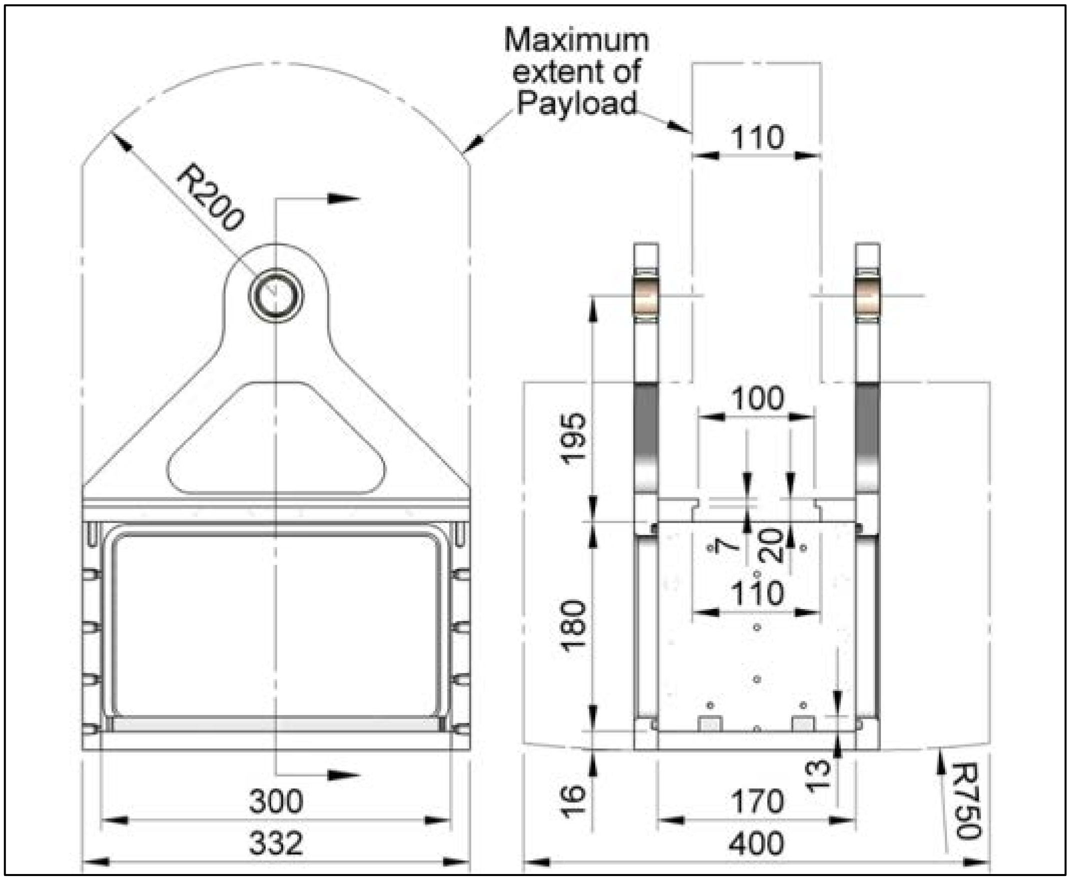

Figure 3-5: Centrifuge cradle (all dimensions in mm) (Broadbent 2015).

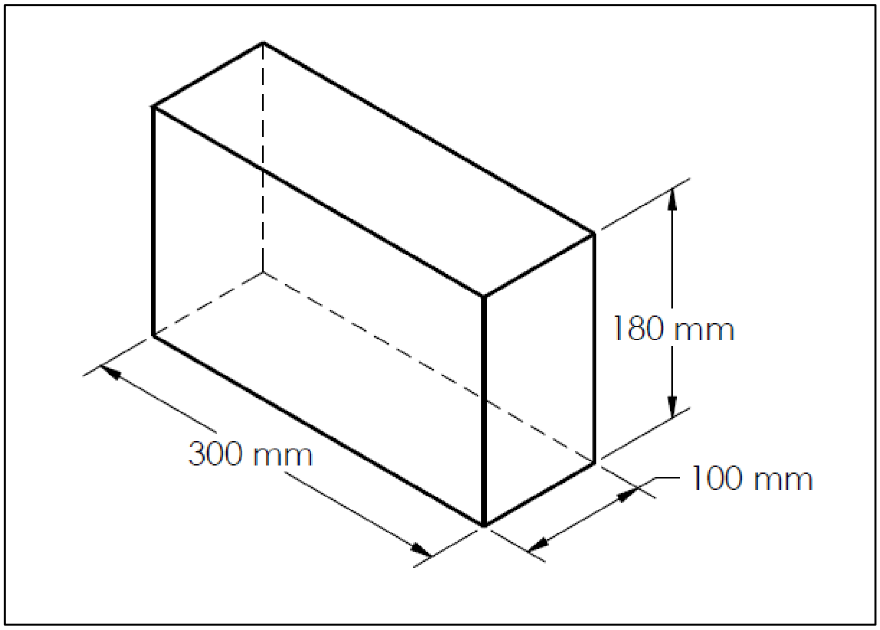

Figure 3-6: Maximum dimensions for model in the centrifuge cradle.

The sand selected for this research was used in order to create a baseline for future research on contaminant transport in the centrifuge. Since the void ratio and porosity of a soil will have an impact on the wetting front velocity through the sand, it was important to ensure that the soil compaction remained similar for every experiment. This was done by adding soil to the cradle and compacting it in layers of approximately 10 mm with a rubber tamper, as illustrated in Figure 3-7. The height of the soil was typically between 130 and 150 mm, which means that approximately 13 to 15 layers of sand were added to the cradle. The void ratio and porosity of the soil was calculated for each experiment. It was possible to calculate the void ratio and the porosity by collecting samples from the soil that was placed in the cradle and calculating the water content. The void ratio for all the experiments conducted varied from 0.58 to 0.71. The porosity varied from 37 to 42%. This range of void ratio and porosity was deemed acceptable for this research.

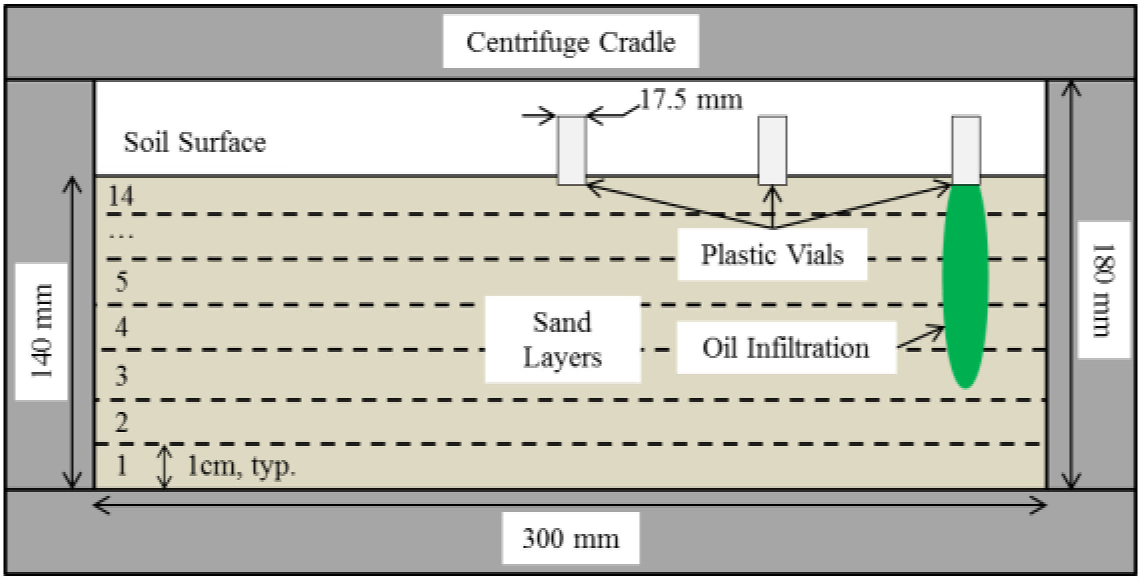

Figure 3-7: Layering of sand in the cradle.

Small plastic vials (Figure 3-8) were used as a delivery vessel for the oil. The vials contained approximately 6 ml of oil each. For most experiments, three separate vials were placed in the soil in order to maximize the number of results that can be obtained from each experiment. Approximately 6 ml of oil was added to each vial and they were placed in a freezer at a temperature of approximately -20°C for several hours until the oil froze. The oil was frozen because it took approximately 15 to 20 minutes to install the cradle and all the instrumentation to the centrifuge. If room-temperature oil was used, the infiltration would start immediately, before the cradle was installed and the centrifuge is running, which was not desired. Freezing the oil before allowed for the cradle and its instrumentation to be installed while the oil was thawing. The oil would be completely thawed only after the centrifuge started running.

Figure 3-8: Plastic vials used as delivery vessels for the oil.

Various methods for adding the vials to the soil were trialed. For the unfrozen experiments, the lids were removed from the vials and the vials were simply inserted into the soil upside-down. For the experiments when the cradle was frozen in the cold room, empty vials were inserted right side up to act as a spacer which could be removed prior to adding the oil-filled vials. The issue that was encountered with this method is that there usually wasn't enough space to add the oil-filled vials in the gap created by the empty vial because the fit was too tight. To remedy this issue, 3D printed spacers (Figure 3-9) that were slightly bigger than the plastic vials were designed and inserted into the sand prior to freezing. However, the printing method employed by the Maker Gear M2 3D printer consisted of layering of PLA plastic filament. The layering created a rough surface compared to the plastic vials, which makes it more difficult to remove the 3D printed spacers from the soil after it has frozen. The spacers would often break while attempting to remove them. The best solution trialed to date was a 3D printed sleeve for the plastic vials, which could be inserted into the sand along the acrylic window prior to freezing (Figure 3-10). The vials were then inserted into the sleeve when an experiment was about to start.

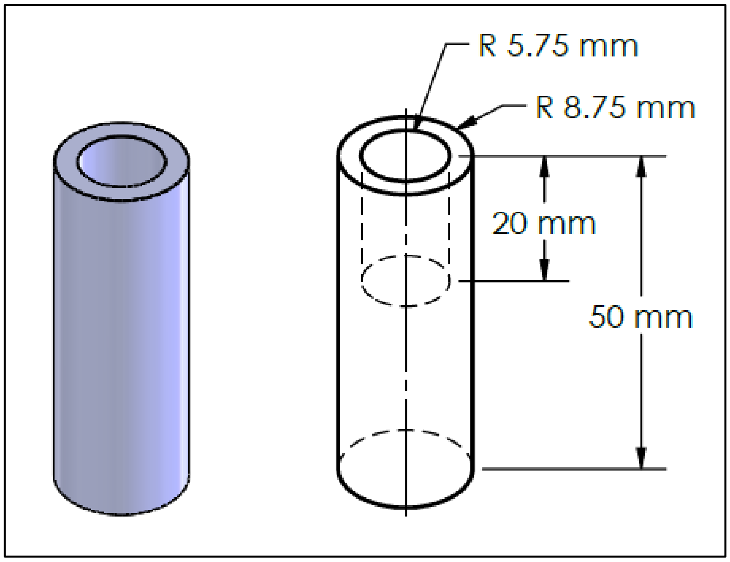

Figure 3-9: 3D printed vial spacers.

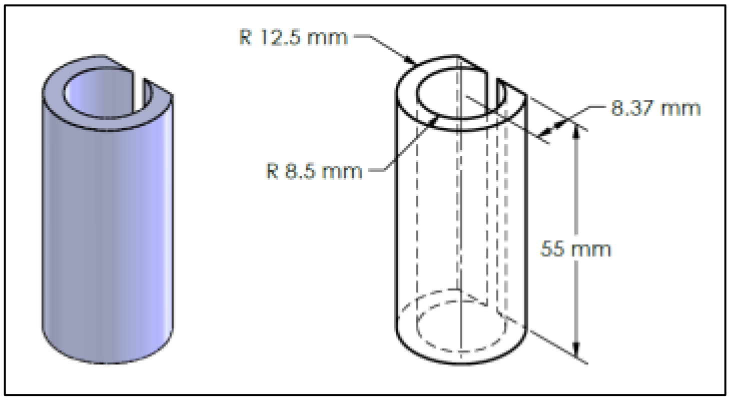

Figure 3-10: 3D printed vial sleeve.

It was noticed that if the oil-filled vial were inserted into the gaps created by the empty vials, the spacers or the sleeves, the pumpkin seed oil would have a preference for infiltrating along the face of the acrylic window instead of through the sand (Figure 3-11). This issue was resolved by filling the remaining volume of the oil-filled vials with sand. The sand was mixed with water to approximately to the same water content as the soil for the experiment. If the oil seeped along the acrylic window (Figure 3-11), the oil's colour was lighter than if the oil migrated through the sand (Figure 3-12). Results for which the oil seeps along the window were not analysed. For all methods of oil delivery trialed, it was important to insert the oil vials as close to the acrylic window as possible. If the oil vial was too far from the acrylic window, the oil migration could not be observed.

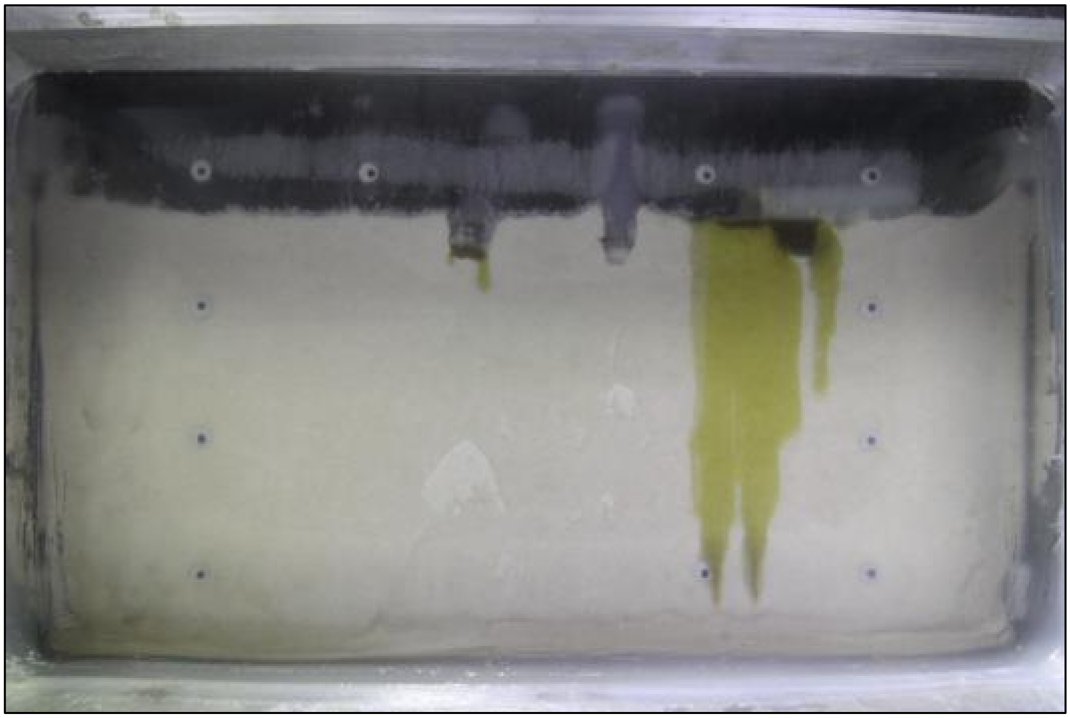

Figure 3-11: Example of oil seeping along the acrylic window.

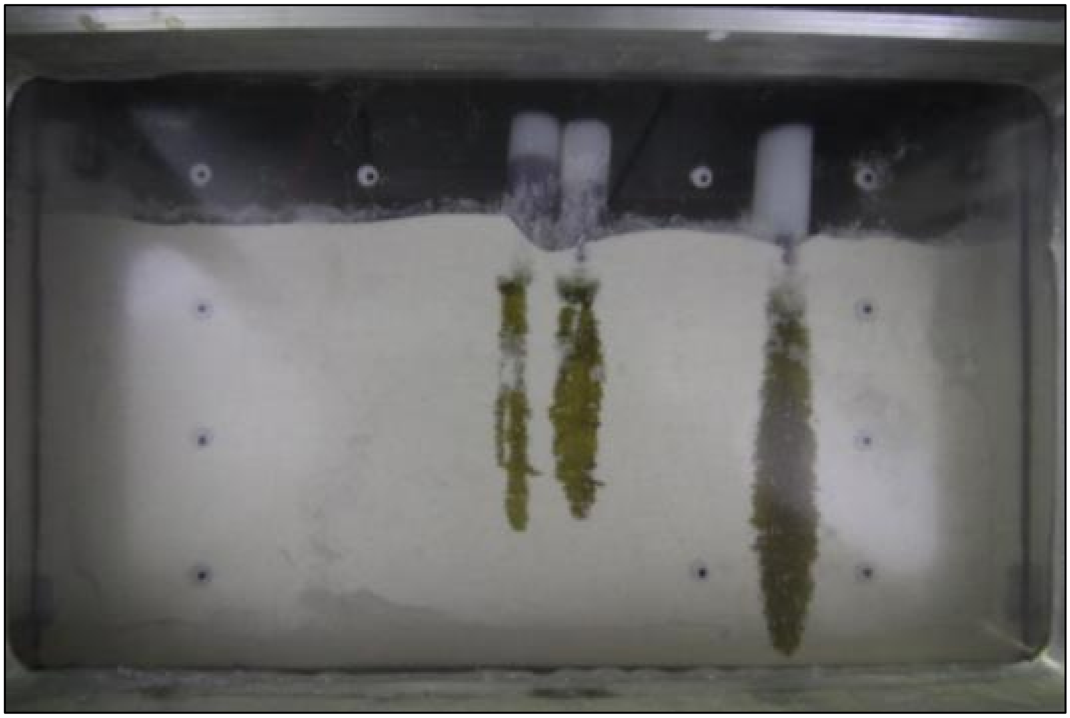

Figure 3-12: Example of oil infiltrating through the sand.

After an experiment was concluded, the water content of the sand at four different depths was recorded. Samples were taken from the surface and the bottom of the sand with two other sampling depths with equal spacing between the four sampling depths. Four samples of soil were taken for each layer of sand (Figure 3-13 & Figure 3-14) for a total of 16 samples from which the water content was measured. The intent of the experiments is to replicate a surface spill like the one illustrated in Figure 2-11. Depending on the experiment setup and the initial moisture conditions, the experiment would be able to simulate all phases of the spill: the initial infiltration, the migration of the contaminant through the vadose zone, the pooling of the contaminant above the water table and the diffusion of the oil into the saturated soil layer. Appendix D details the step-by-step procedures to setup a typical experiment in the centrifuge.

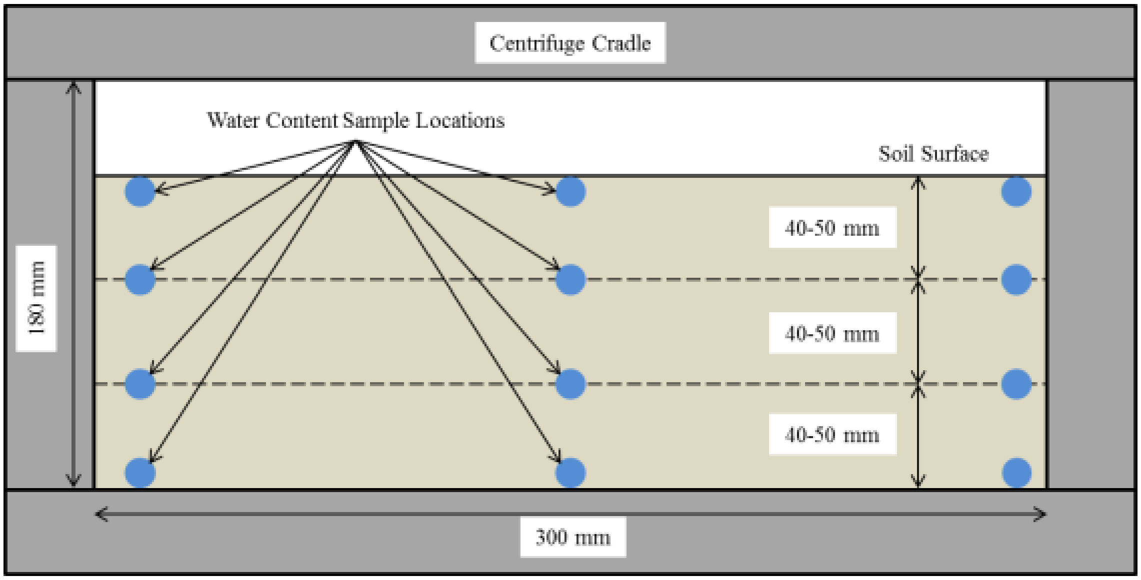

Figure 3-13: Water content sample locations (side view).

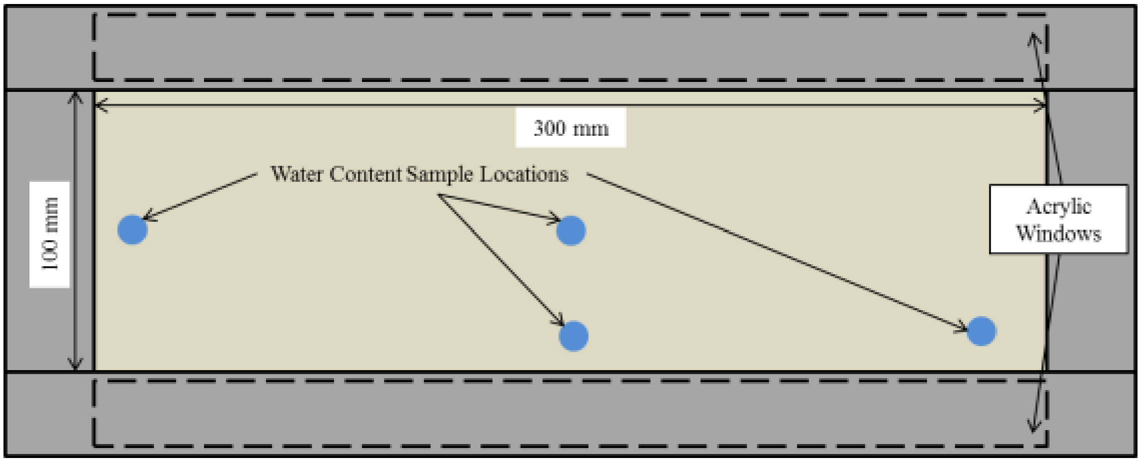

Figure 3-14: Water content sample location for each layer of sand (top view).

3.3.2 Instrumentation

The instrumentation used to analyze the behaviour of the oil during the experiments were a digital camera for image analysis and thermistors to record temperature throughout the soil model while the centrifuge is running.

3.3.2.1 Digital Camera

The Canon Rebel XSI (Figure 3-15) was used to take pictures of the cradle during experiments (Figure 3-16).

Figure 3-15: Canon Rebel XSI used to take pictures in the centrifuge.

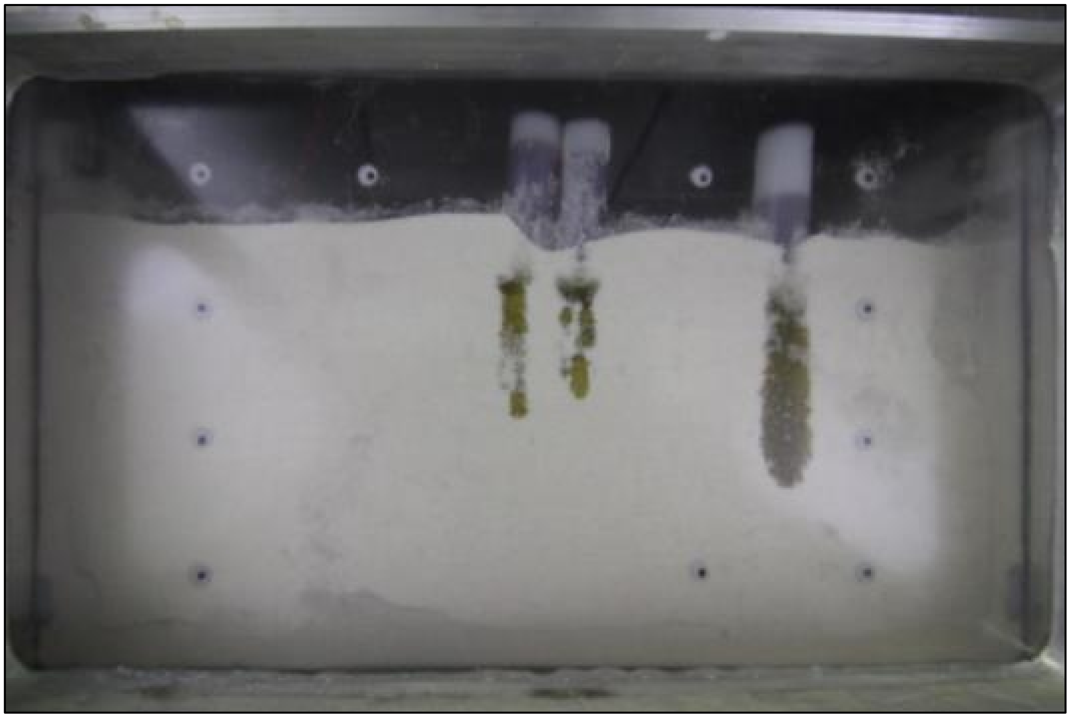

Figure 3-16: Example of a picture from the camera's viewpoint.

The camera was mounted on the cradle's camera bracket that was previously fitted with a 3D printed attachment to secure the camera while the centrifuge is running. The camera's battery could be used but its life was only seven to eight hours. For longer experiments, a hardwired power source was connected to the camera. The camera was connected to the centrifuge's in-flight computer through a USB cable. Canon’s EOS Utility software allowed for remote shooting with the camera at the desired time intervals. It was found that a 15 second period was adequate for the experiments through dry sand while a period of one to two minutes was best for the frozen experiments. It was important to optimize the picture frequency in order to reduce the amount of unnecessary data being produced for each experiment. While conducting their research, Kingswood et al. (2016) and Laporte and Siemens (2017) tried various cameras in the centrifuge to record their experiments. Many of them were not able to withstand the forces of the increased acceleration. It was found that the Canon Rebel XSI was able to withstand the forces of an acceleration ratio of up to 60g and was able to function properly if the camera shutter is glued to remain open at all times. No experiments were conducted above 60g to avoid damaging the camera.

A webcam was also inserted into the 3D printed camera mount. The webcam allowed for real-time observation of the experiment however, it couldn’t record video. Pictures could be taken with the webcam, but the field of view did not cover the entire acrylic window and the image resolution was poor. The pictures taken with the Canon camera could be strung together to create a video. The webcam was useful to observe the experiments in real time between image recordings.

3.3.2.2 Thermistors

Thermistors were designed for use inside the centrifuge (Figure 3-17). The thermistors were built using analog connectors to connect to the centrifuge’s in-flight computer through a total of 16 analog ports. This means that a maximum of 16 thermistors could be placed inside the cradle during an experiment, although the maximum was never used for the experiments as part of this thesis. Typically, five to eight thermistors were used during an experiment. Silicone conformal coating was applied to the ends of the thermistors in order to waterproof them. This prevented the thermistors from shorting when exposed to water. Thermistors that shorted during an experiment produced highly variable temperature data that was discarded from the experimental analysis.

The thermistors were calibrated by placing them in a saline solution which was cooled to a temperature of -15°C (Figure 3-18). The Acqlipse software would then be run to record the voltage every 10 seconds. The temperature of the solution near the thermistors would be recorded at each voltage recording with a thermocouple. The addition of salt to the water enabled its freezing point to drop to approximately -20°C. A better calibration was achieved by using a saline solution versus simply using frozen water because the thermistor bead was in constant contact with the saline solution.

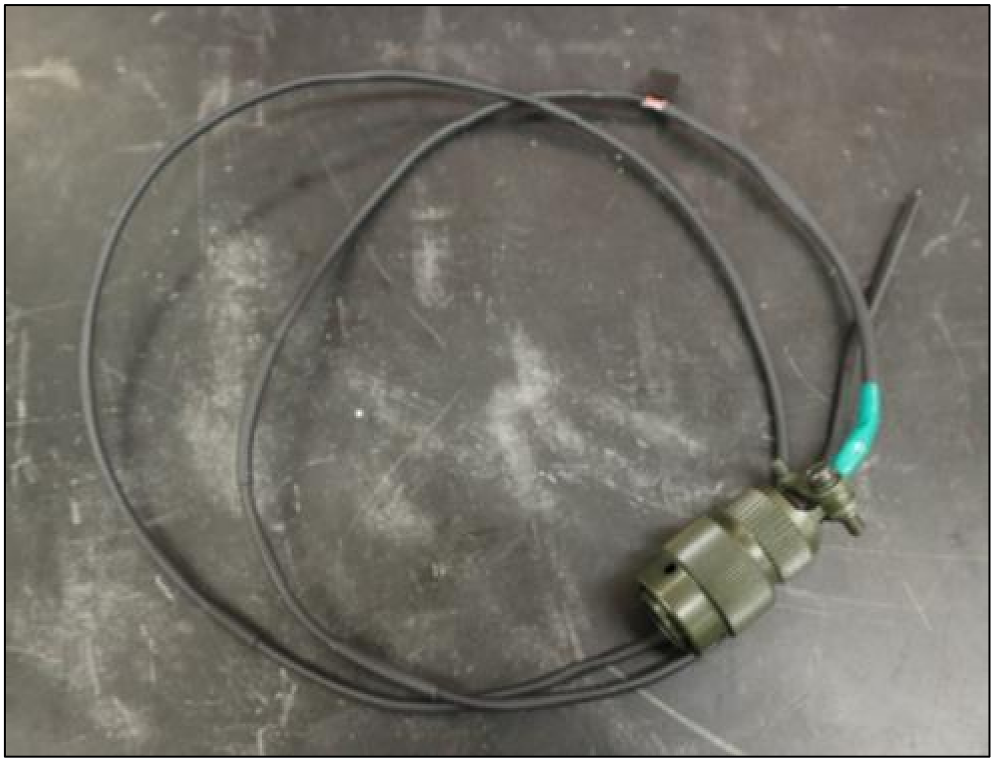

Figure 3-17: Assembled thermistor.

Figure 3-18: Thermistor calibration in saline solution.

Thermistors were placed throughout the soil in order to have a good representation of the temperature during an experiment and to be able to properly analyze the temperature data. Two thermistor layouts were used (Figure 3-19 & Figure 3-20 versus Figure 3-21 & Figure 3-22) as part of this research. The thermistor locations for the initial layout ensured that the temperature of the soil could be recorded at various depths. A thermistor was also placed along the acrylic window closest to the camera. This was done in order to observe the difference in thawing rate between the middle of the soil and the edge of the acrylic windows. The final layout was developed to improve upon the first layout, which had a significant flaw. Although the thermistors were spaced equally at various depths, they were not at equal distances from the edge of the cradle. Since the soil would be thawing from all directions, the thermistors closer to the edge of the cradle would experience thawing sooner. For the final layout, the thermistors were attached to a 3D printed plastic rod, which was inserted vertically into the sand.

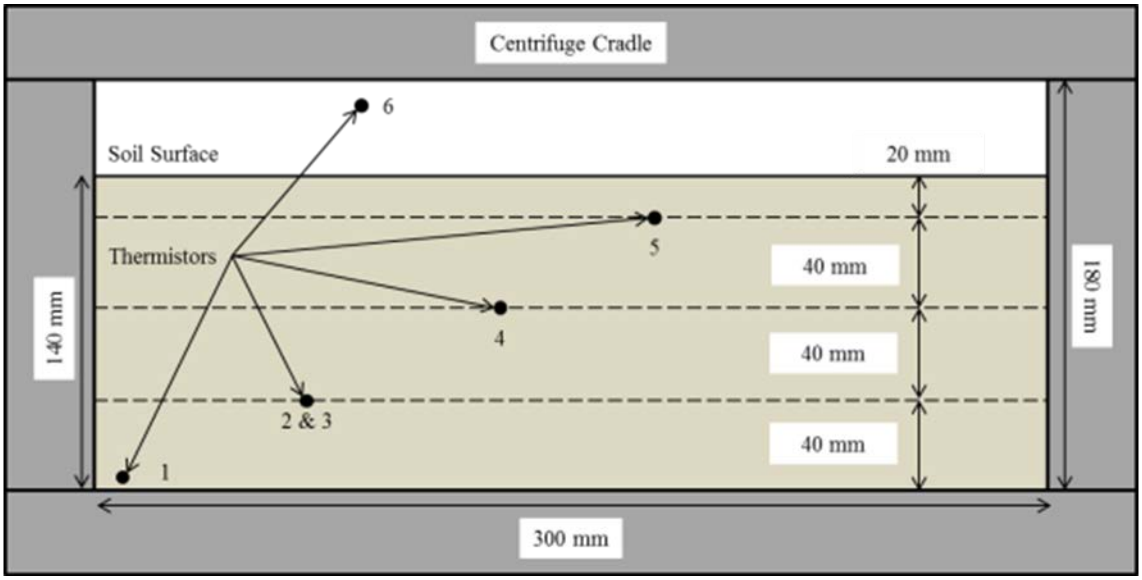

Figure 3-19: Initial thermistor layout side view.

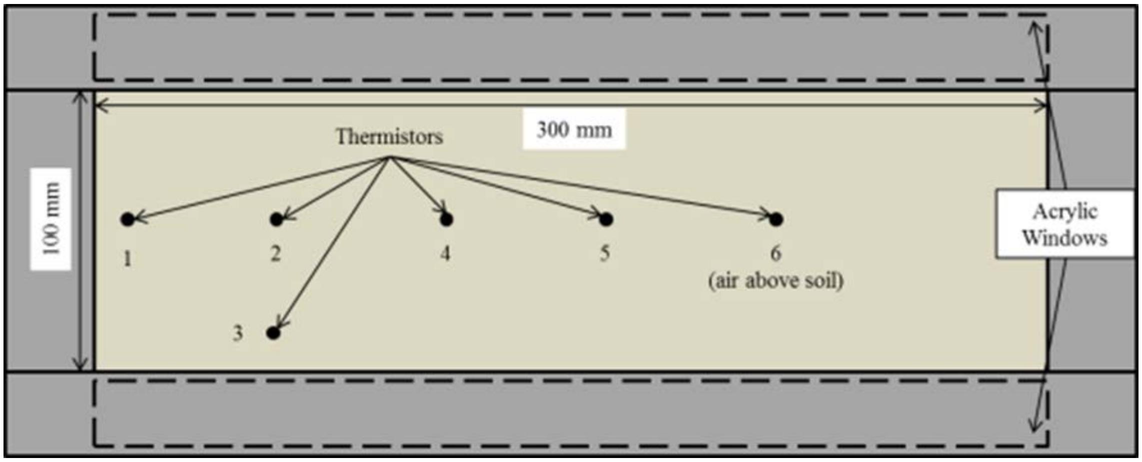

Figure 3-20: Initial thermistor layout top view.

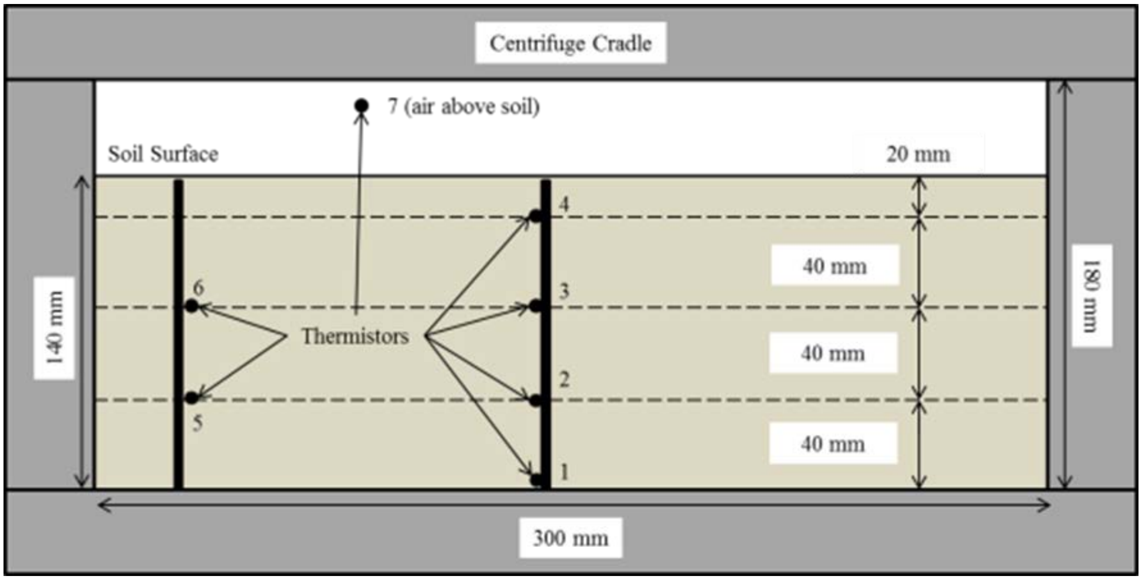

Figure 3-21: Final thermistor layout side view.

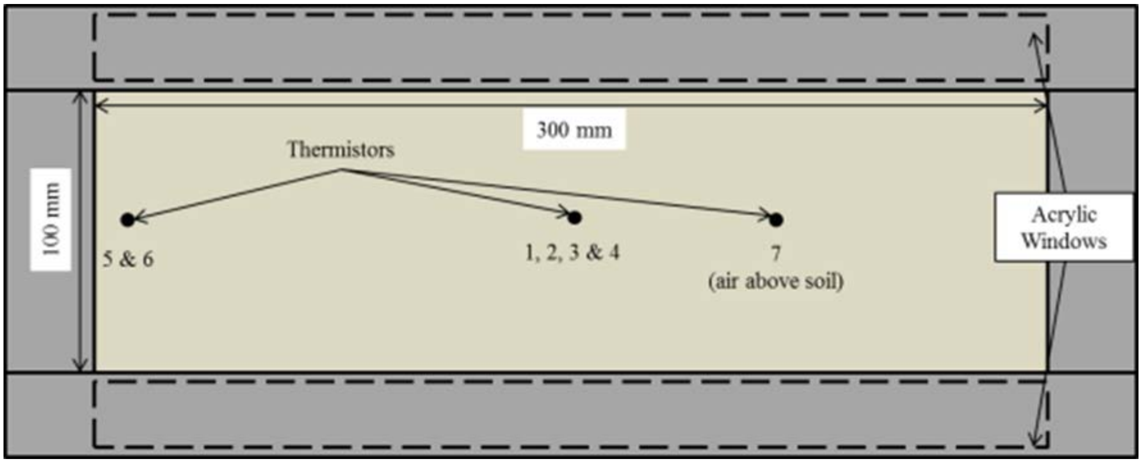

Figure 3-22: Final thermistor layout top view.

For most experiments, the temperature was recorded every minute. The recordings for the pictures and temperatures were started within a few seconds of each other to ensure that the temperature data and the images were synchronized. The Acqlipse software from which the thermistors were controlled produced voltage data based on the thermistor’s response to changing temperatures. The voltage data was converted to temperature data using the calibration factors as specified in Appendix E. The temperature was then plotted versus time. Below (Figure 3-23) is an example of a graph produced from an experiment where the cradle is frozen overnight prior to being accelerated in the centrifuge. The experiment used thermistor layout #1 (Figure 3-19 & Figure 3-20). The materials and equipment required as well as the assembly and calibration instructions for the thermistors are located in Appendix E.

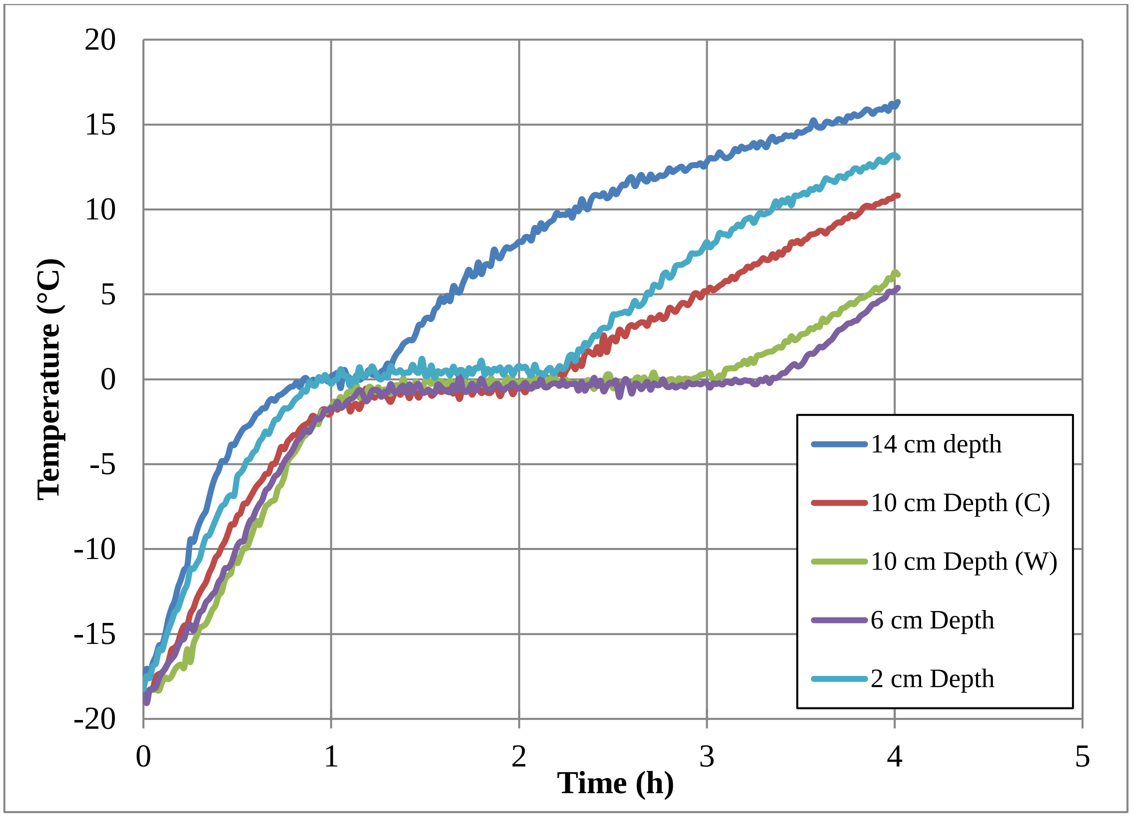

Figure 3-23: Example of temperature data from a frozen experiment (C denotes a thermistor placed in the middle of the cradle and W denotes a thermistor that is placed close to the acrylic window).

3.3.3 Freeze-Thaw Mechanism

3.3.3.1 Cold Room

Two methods were tested to freeze the soil in the cradle. The first one consisted of setting up the cradle with the compacted soil at the desired water content and then placing the whole cradle in a freezer or cold room overnight prior to running an experiment. The frozen cradle was then installed onto the centrifuge and would thaw while the centrifuge was spinning. The cold room was used the most for this research. The temperature inside the cold room was set at between -18°C and -20°C. The soil could maintain frozen temperatures for over two hours when this method was used. The moisture content of the soil, the ambient temperature, the amount of insulation used and the use of the climate box had an effect of the time for which the soil would remain frozen.

3.3.3.2 Insulation

While using the cold room freezing method, it was noticed that the soil within the cradle was thawing from all directions. Ideally, the thaw front would penetrate from the top of the soil surface. The fastest thawing was experienced for the soil at the bottom of the cradle (Figure 3-24). Figure 3-24 shows the temperature data for a frozen experiment that uses the initial thermistor layout (Figure 3-19 & Figure 3-20). The thermistor at a depth of 140 mm (bottom of the cradle) experienced the quickest thaw while the top of the soil experienced the slowest thaw. This happened because the cradle is made of aluminium, which has very high heat conductivity. This causes the aluminium cradle to transfer a lot of heat to the soil with which it was in contact.

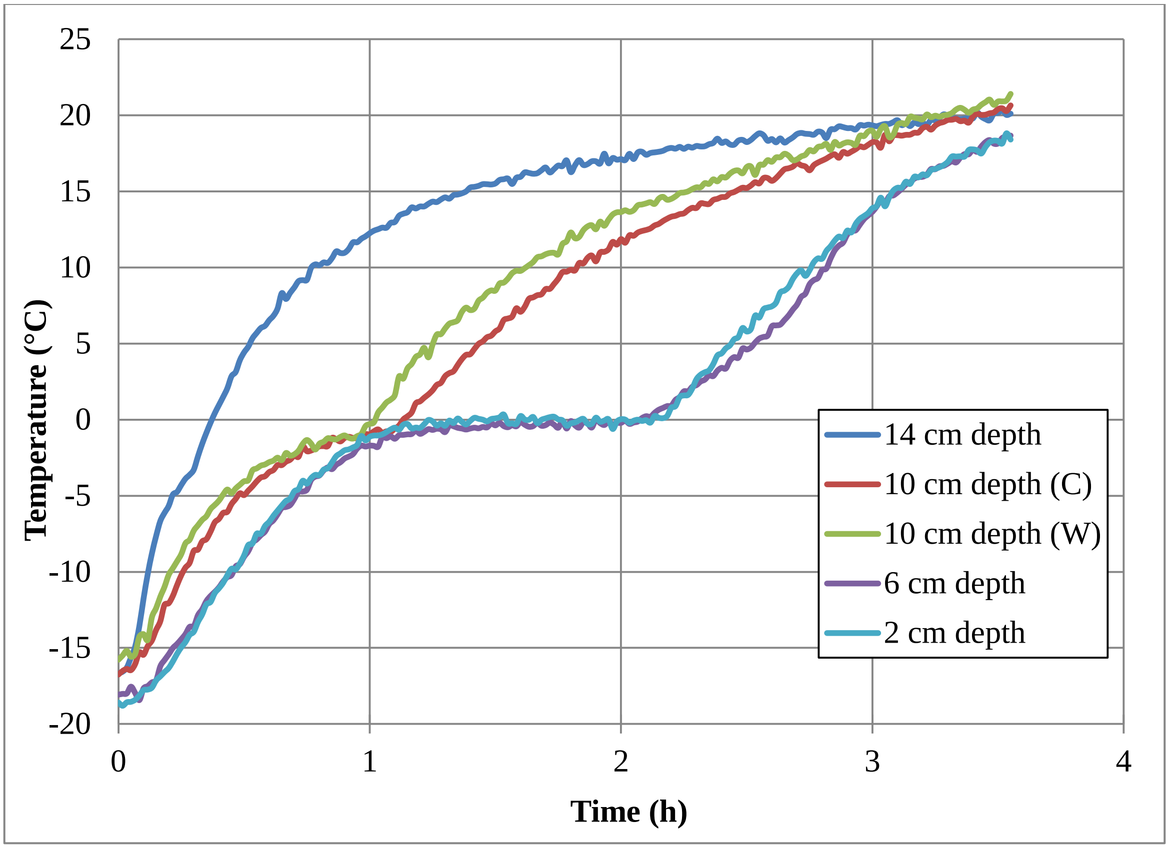

Figure 3-24: Temperature data for a frozen experiment with no insulation.

Soft foam insulation was placed at the bottom of the cradle to fix the issue of the rapid thawing from the bottom of the cradle (Figure 3-25). Initially, one layer of insulation was placed at the bottom of the cradle. This improved the issue, however the fastest thawing was still being experienced at the bottom of the cradle (Figure 3-26). With no insulation in the cradle, the bottom thermistor maintained frozen temperature for approximately 20 minutes. By adding a single layer of insulation, that time was increased to approximately one hour. Another experiment was conducted where three layers of insulation were added at the bottom of the cradle. In this case, the bottom of the soil maintained frozen temperature for approximately 80 minutes (Figure 3-27). It was decided that all subsequent experiments would be conducted using two layers of insulation at the bottom of the soil. Two layers was sufficient to improve the thermal conditions of the soil while also reducing the space taken by the insulation at the bottom of the cradle. Each layer of insulation had a thickness of approximately 2.5 mm after the soil above it was compacted.

Figure 3-25: Foam insulation at the bottom of the centrifuge cradle.

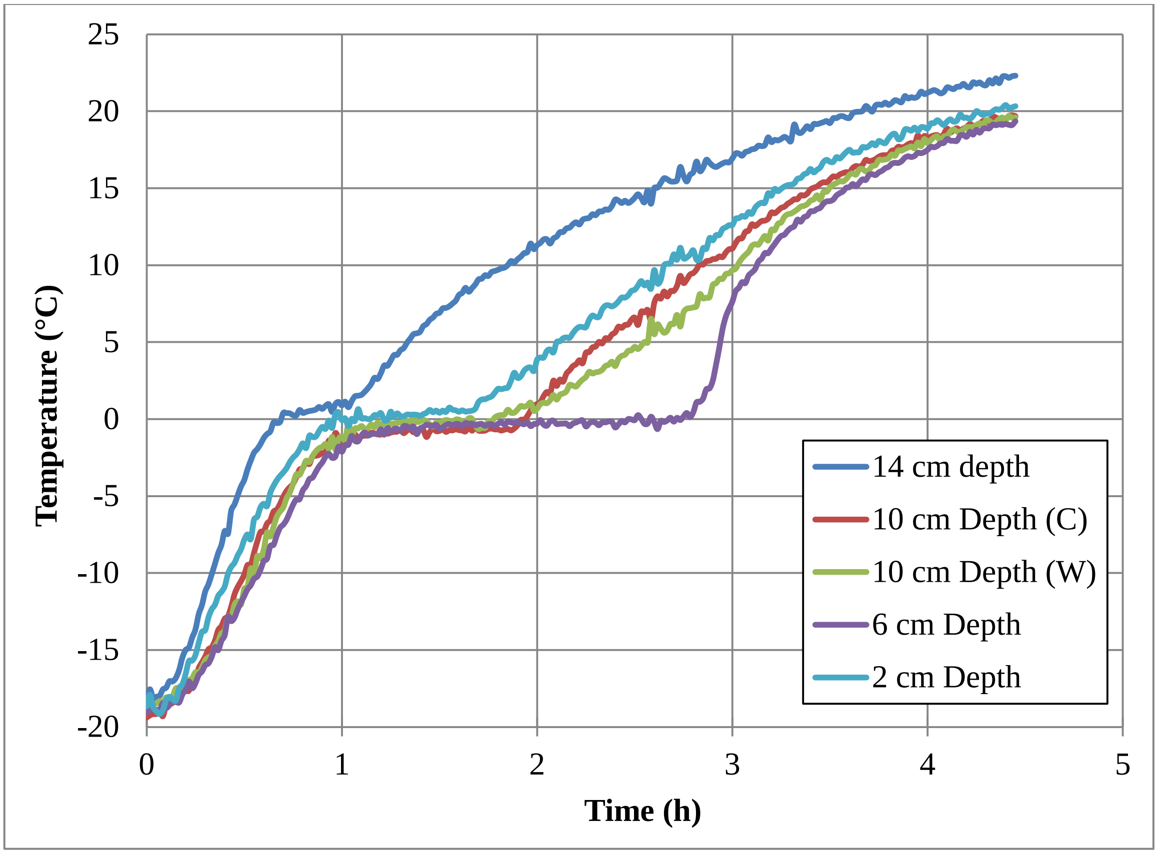

Figure 3-26: Temperature data for a frozen experiment with one layer of insulation.

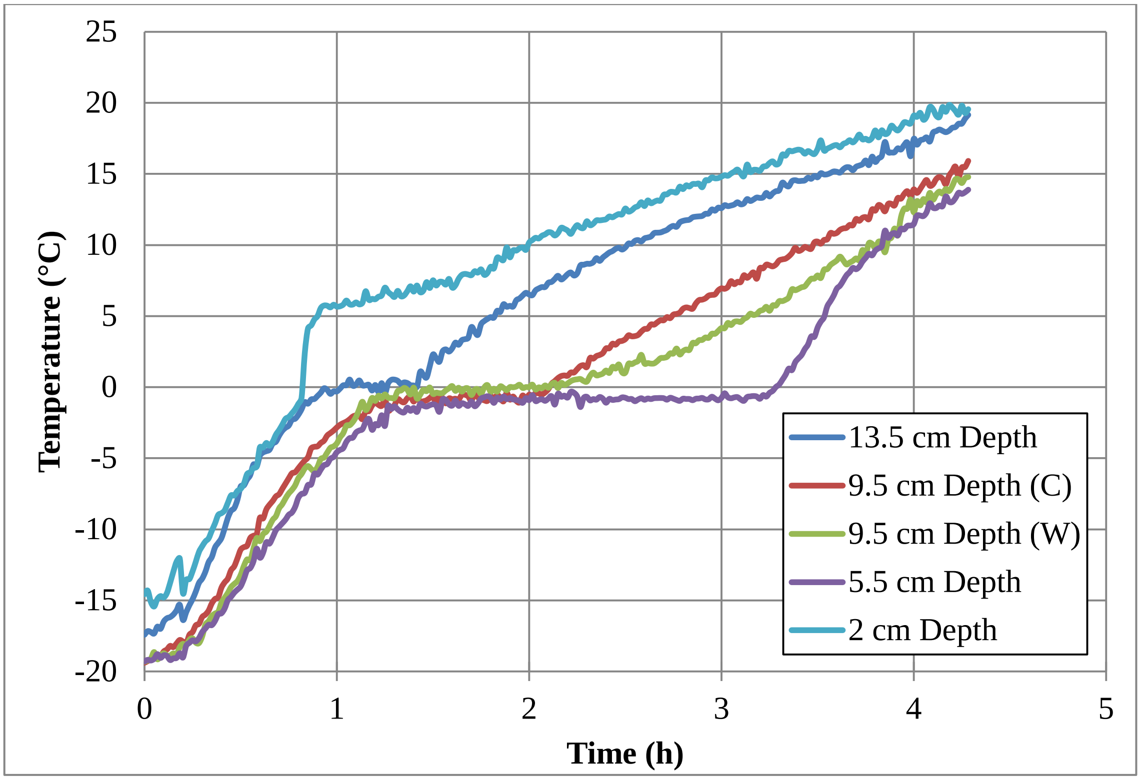

Figure 3-27: Temperature for a frozen experiment with three layers of insulation.

3.3.3.3 Vortex Tubes

Vortex tubes supplying cold air to the cradle was the second method that was used to attempt to freeze the sample during an experiment. The basic principle of vortex tubes is that they are supplied with compressed air then push out two separate streams of air, one hot and the other cold. The cold air stream was diverted into the centrifuge cradle through the climate box. Two compressed air lines with a maximum pressure of 7 BAR and a flow of approximately 7 CFM were available for use in the centrifuge. The temperature of both streams varied based on the temperature and pressure of the compressed air as well as the cold fraction setting of the vortex tube. The cold fraction was adjusted by turning the screw on the hot air stream exhaust. A higher cold fraction increased the flow of air towards the cold end of the vortex tube and decreased the flow out of the hot end of the vortex tube; however it sacrificed the temperature drop at the cold end. Maximum refrigeration performance was usually achieved with the lowest desirable temperature drop from the compressed air. Table 3-7 shows the temperature drop and increase from the supplied air temperature for the cold and hot flows for various cold fractions and supply pressures. Prior to each experiment with the vortex tube, the flow and pressure of the air into the vortex tube as well as the temperature of the air coming out of the cold end were recorded. The vortex tubes were usually adjusted to have a cold flow at a temperature of -6 to -8°C with a compressed air supply of 7 BAR and a cold fraction of approximately 80%. Approximately 6.8 CFM of compressed air was supplied to each vortex tube.

Table 3-7: Vortex tube performance chart (Exair, 2018)

	Cold Fraction (%)						
Supply Pressure (bar)	**20**	**30**	**40**	**50**	**60**	**70**	**80**
1.4	34.4	33.3	31.1	28.3	24.4	20	15.6
	8.3	13.9	20	28.3	35.6	46.1	59.4
2	40.9	39.6	37.1	33.8	29.2	24	18.1
	9.8	16.4	24	33.3	42.6	54.6	69.5
3	50.4	48.7	45.7	41.6	36	29.7	21.9
	12	19.9	29.6	40.3	52.3	66.5	83.5
4	56.9	54.7	50.9	46.1	40	32.9	25.1
	13.2	21.9	32.4	43.9	57.1	72.5	91.2
5	61.6	59	54.8	49.4	43	35.4	26.9
	13.7	23.3	34.2	46.5	60.9	77.2	97.1
6	65.4	62.7	58.2	52.7	45.6	37.6	28.6
	14.1	24.3	35.8	48.6	63.9	81	102.1
7	68.6	65.8	61.4	55.7	48	39.6	30
	14.4	25.1	37.3	50.2	66.3	84.2	106.3
8	71.1	68.2	63.8	57.3	50	40.8	30.4
	14.4	25.4	38.1	51.8	67.9	86.1	107.9

Numbers in shaded area give the temperature drop of the cold air (°C)
Numbers in white area give the temperature rise of the hot air (°C)

The vortex tubes were mounted on an aluminium climate box (Figure 3-28) which could be mounted onto the centrifuge cradle. The climate box was assembled using socket head screws. The climate box was designed to slide onto the cradle with a tight fit. Five new aluminium plates were fabricated and assembled based on the original design by Laporte and Siemens (2017). Since the climate box was designed to fit tightly onto the cradle, air could only pass through the holes that were drilled at the top of the climate box. The thermistors were inserted into those holes before being inserted into the sand (Figure 3-29).

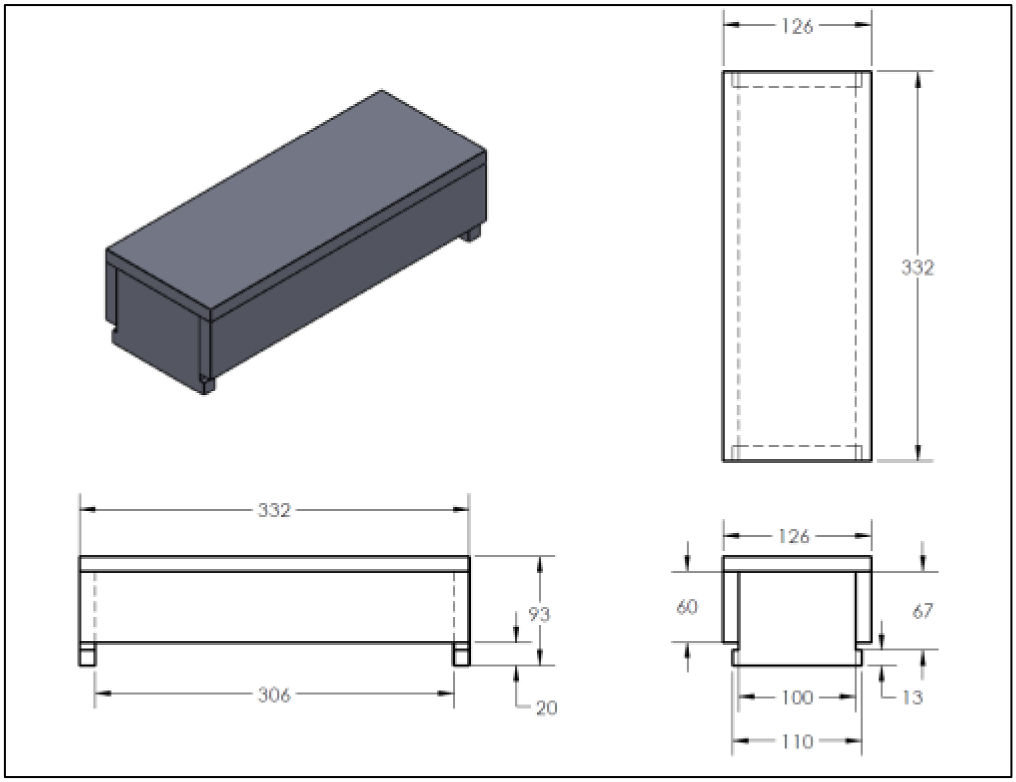

Figure 3-28: Climate box for the centrifuge cradle (dimensions in mm).

The vortex tubes were mounted onto the climate box with 3D printed parts (Figure 3-29). The vortex tubes could be turned on or off with the supply valve in the laboratory and also with a solenoid valve mounted on the climate box that could be controlled from a power source outside the centrifuge. The solenoid valve was mounted onto the climate box with a 3D printed part (Figure 3-30). PFA (Perfluoroalkoxy) tubing and stainless steel fittings were used to supply the vortex tubes in the centrifuge. R2 rated insulation was also installed in the cradle to improve the thermal performance of the climate box. The current apparatus would need to be improved in order to reach freezing temperatures in the cradle.

Figure 3-29: Vortex tubes mounted on the climate box.

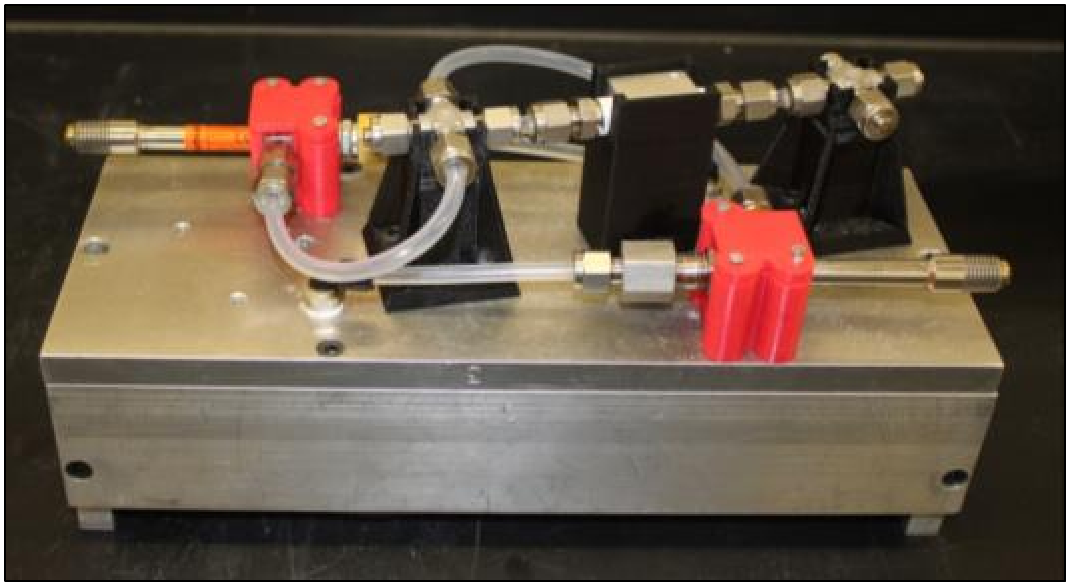

Figure 3-30: Climate box with solenoid valve.

In order to keep the bottom of the soil frozen, an aluminium plate (Figure 3-31) with air channels was designed and milled from a solid aluminium plate. The plate was installed at the bottom of the cradle with the channels facing towards the bottom of the cradle. A third vortex tube (Figure 3-32) supplied cold air at the entrance of the plate with the air exiting at the other end of the cradle (Figure 3-33). High vacuum grease was applied to ensure that no water or oil seeps between the acrylic windows and the air channel plate. With the current climate box and vortex tubes, temperatures of 2°C were achieved (Figure 3-34) while the sand started at room temperature (approximately 22°C)

Figure 3-31: Aluminium air channel plate.

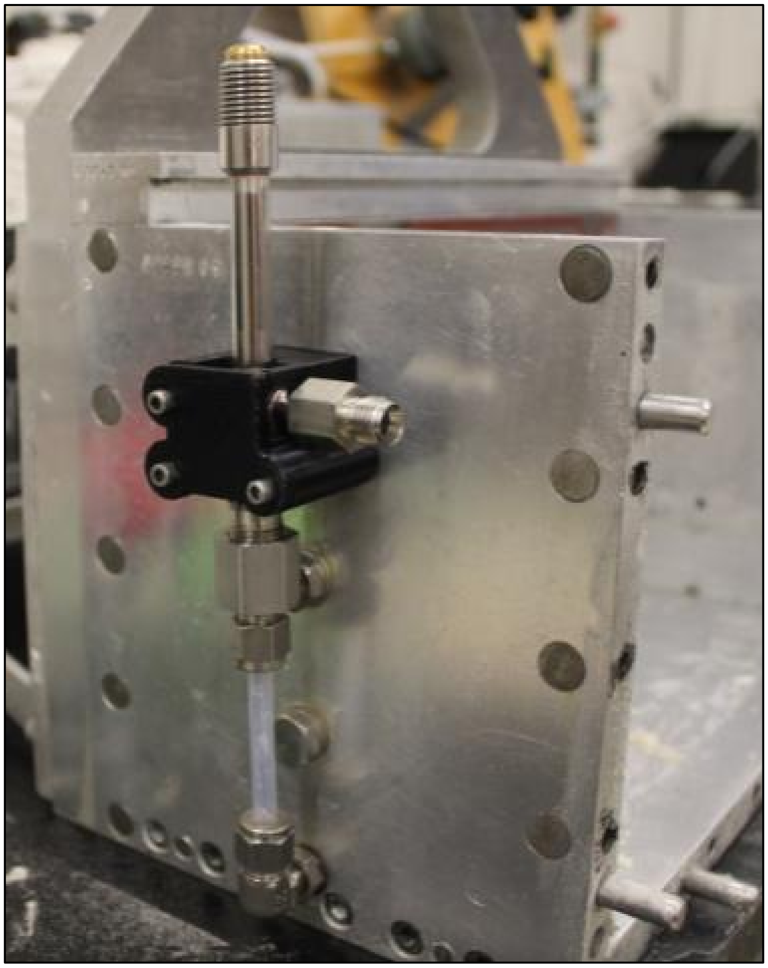

Figure 3-32: Vortex tube mounted to provide cold air to the bottom of the cradle through the air channel plate.

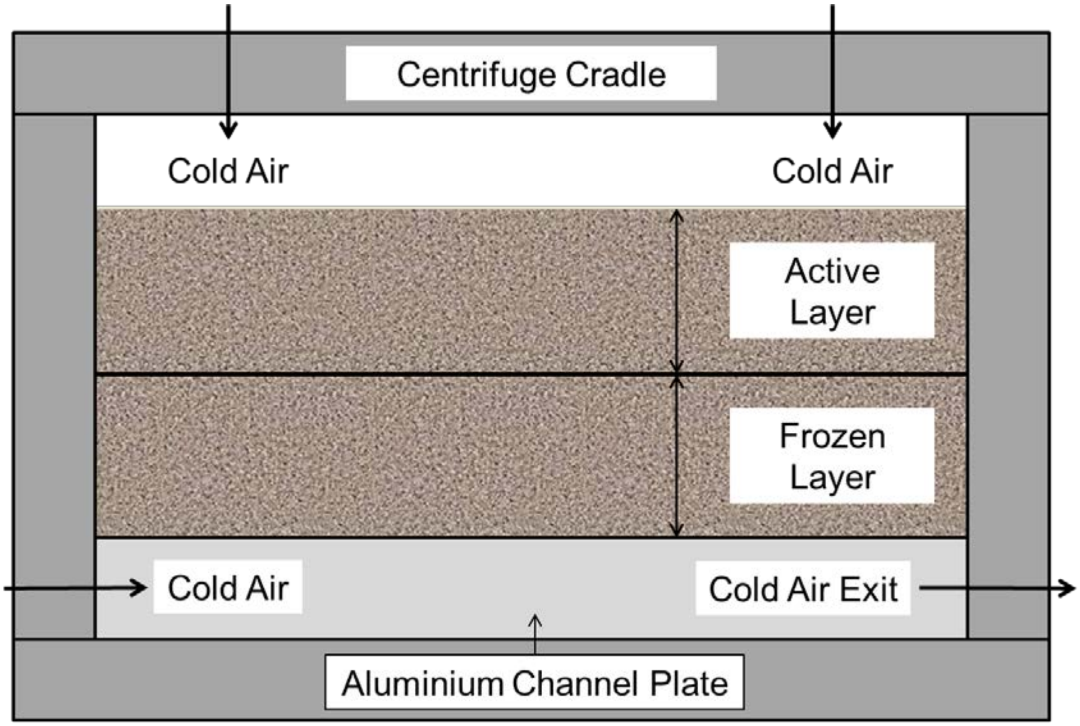

Figure 3-33: Centrifuge cradle cooling.

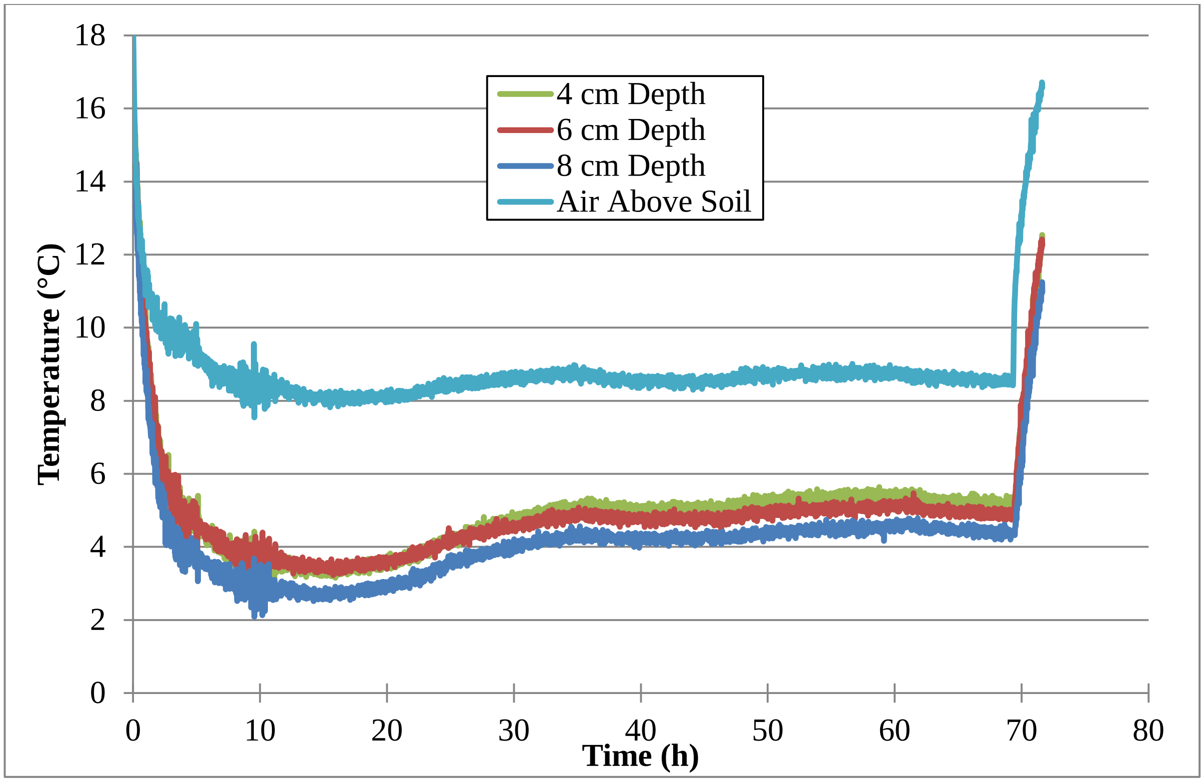

Figure 3-34: Temperature data from a vortex tube trial.

3.4 Column Experiments

An acrylic column (Figure 3-35) was designed in order to conduct experiments with the same sand and pumpkin seed oil as the centrifuge experiments. The results from both experiments were then compared to ensure that the scaling principles for wetting front velocity were being followed in the geotechnical centrifuge. The validation of the scaling principles ensured that further experiments could be conducted in the geotechnical centrifuge. The experiments within the column were also used as the baseline results from which the centrifuge experiments could be compared. The column was placed in a chest freezer to freeze the soil during experiments. Thermocouples were placed in the sand to monitor and record the temperature during an experiment and a camera was placed in front of the column to take pictures of the migration of the oil. The column had inner dimensions of 533.4 x 342.9 x 177.8 mm (Figure 3-36).

Figure 3-35: Column used for oil migration experiments.

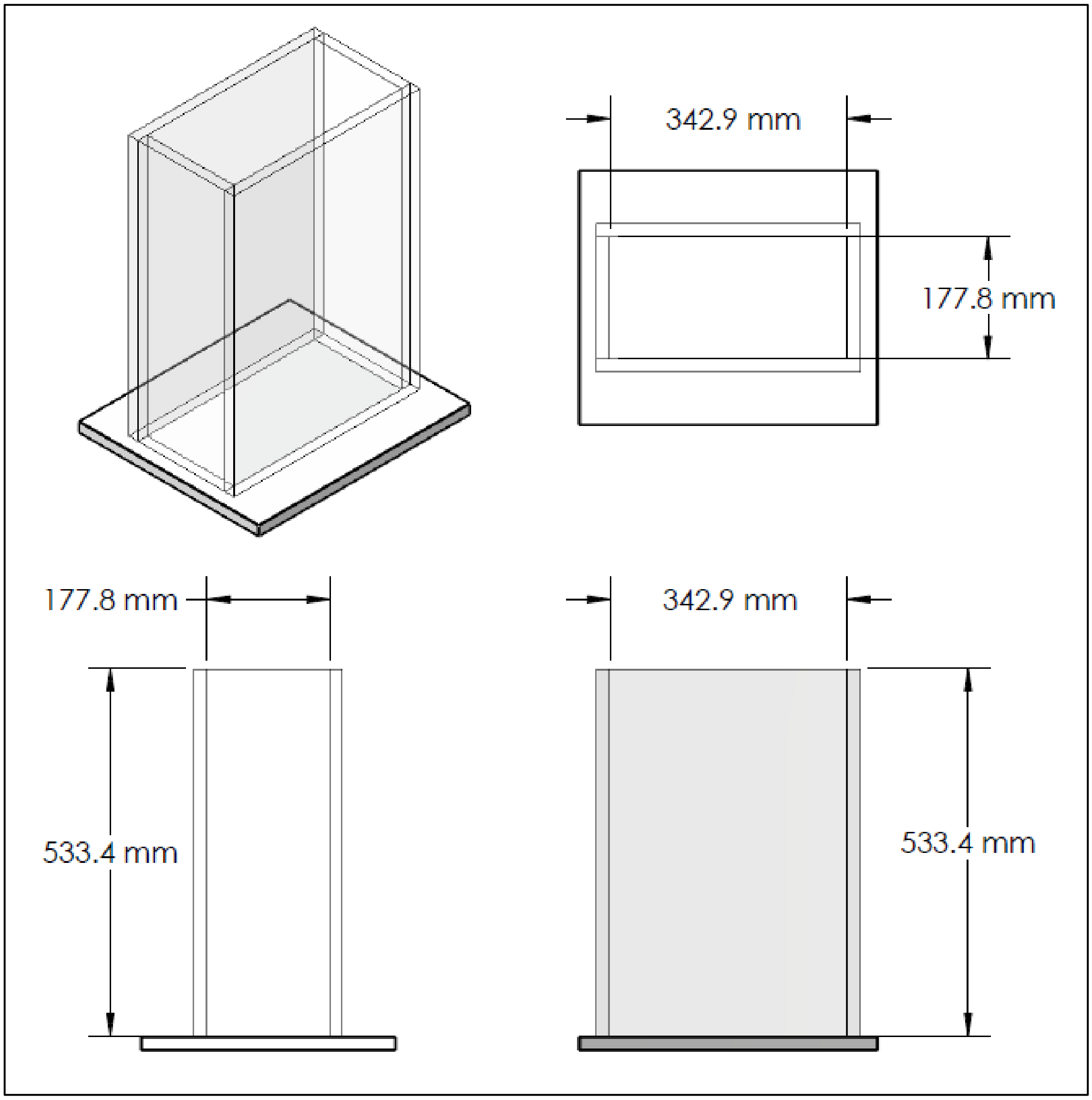

Figure 3-36: Acrylic column inner dimensions.

3.4.1 Experimental Setup

The sand was used for all the column experiments as part of this research. The sand was mixed with water to the desired moisture content in batches of 3 kg of soil. The soil and water mix was then added to the column in layers of approximately 10 mm. Each 10 mm layer of sand would be tamped down. Once the 3 kg batch of soil was completely added to the column, weights were placed above the sand and the column would be vibrated using a shaker table (Figure 3-37). The vibratory compaction ensured that the void ratios and porosities between different experiments were consistent. The compaction was done for each batch of 3 kg of soil until the desired height of sand was reached. Once the column was filled to the desired height, the column was lowered onto a scissor jack (Figure 3-38), which was placed at the bottom of the freezer. Jeep lights were also placed at the bottom of the freezer to provide lighting. The position of the lights (Figure 3-38) was chosen because it produced the least amount of glare from the camera’s viewpoint.

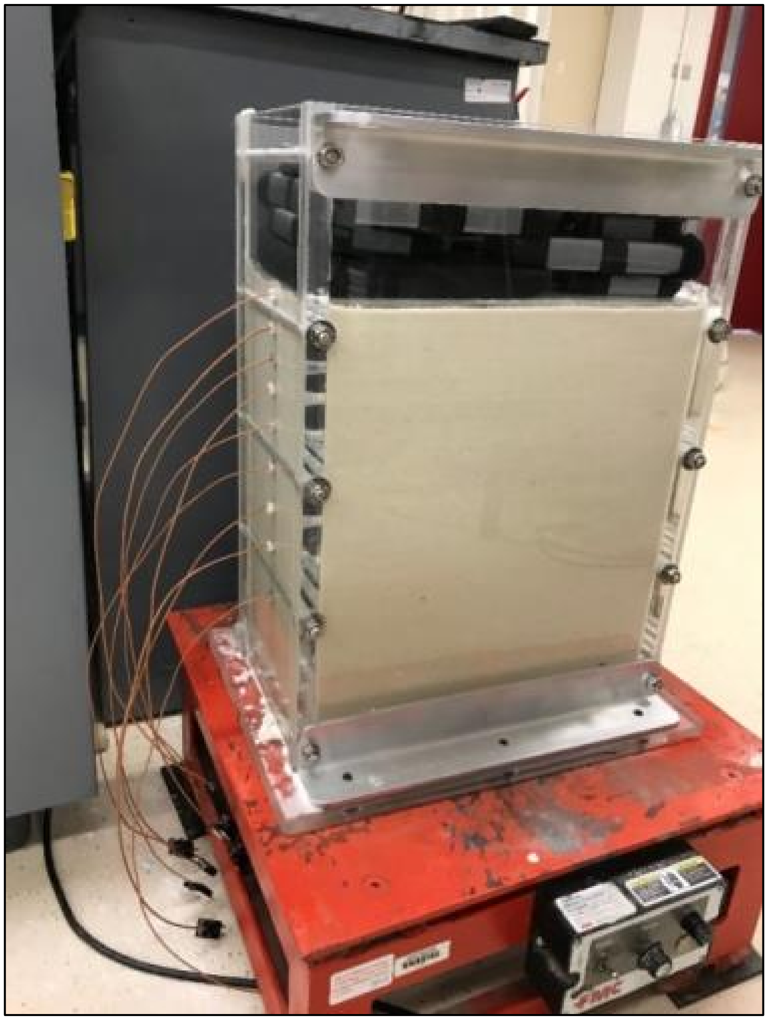

Figure 3-37: Vibratory compaction of the sand.

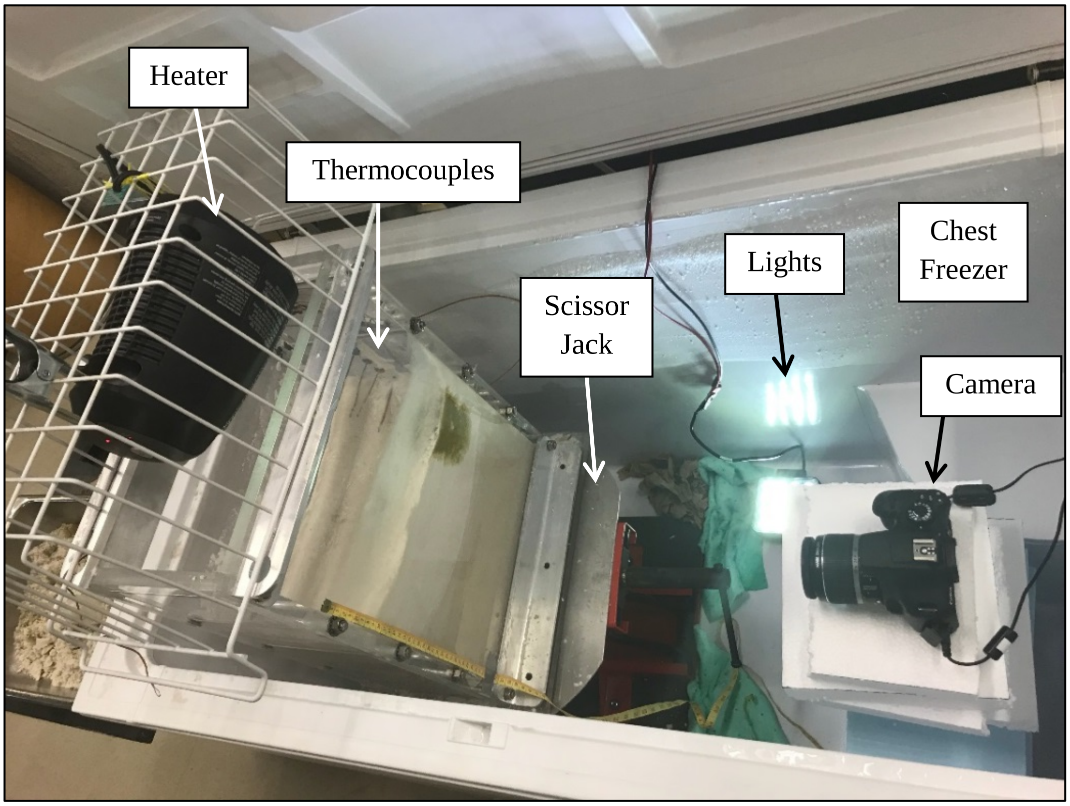

Figure 3-38: Column experiment setup.

Various methods were trialed to deliver the oil to the sand for an experiment. For the initial experiments, the pumpkin seed oil was added to the column by drilling a vertical hole into the sand with a drill bit. The oil would then be added to the hole with a plastic syringe in order to add the exact amount of oil desired. Using a peristatic pump with the hose inserted in the sand was also trialed unsuccessfully. Even on the lowest setting, the pressure from the oil was too high and the oil would rise to the surface and displace sand on its way up. Similar to the centrifuge experiments, it was found that freezing the oil in vials and placing them in the sand at the beginning of an experiment was the most effective method for delivering the oil. This allowed the oil to infiltrate the sand at the maximum wetting front velocity permitted by the sand and it would also be easier to follow the depth of the oil front compared to drilling a hole and adding the oil with a syringe. Appendix F provides detailed step-by-step instructions to set up a column experiment.

3.4.2 Instrumentation

A Canon Rebel T6 camera and thermocouples were used to monitor and record data during column experiments. The camera was placed in front of the column to take pictures of the oil infiltrating the sand (Figure 3-39).

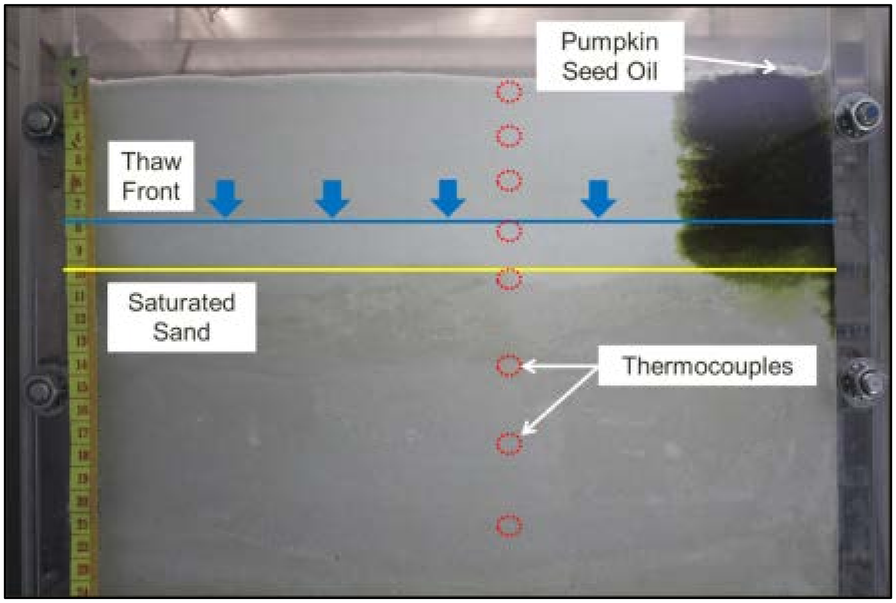

Figure 3-39: Example image from the camera.

The pictures were analyzed using the code described in Appendix G. The thermocouples were installed throughout the column at various depths to record the temperature during an experiment. They were inserted into the sand as the column was being filled. A thermocouple was also typically placed above the soil in the column and one was placed at the bottom of the freezer. The camera and the thermocouples were connected to a laptop from where they could be controlled. EOS Utility was used to control the remote shooting for the camera and Labview was used to control the thermocouples and record temperature. The interval for taking pictures and thermocouple readings was typically between three and five minutes. As with the centrifuge experiments, the temperature and image recordings were synchronized to within a few seconds of each other.

3.4.3 Freeze-Thaw Mechanism

A chest freezer was used to freeze the soil within the column during an experiment. The freezer used was able to reach temperatures of -20°C. When completely frozen soil was desired for an experiment, the whole column was lowered into the freezer overnight with the lid closed (Figure 3-40). When it was time to thaw, the column was raised to approximately 100 mm above the edge of the freezer (Figure 3-41). The column was lowered and raised with a scissor jack. Styrofoam insulation was used to cover the opening of the freezer so that only the top of the column was exposed to room-temperature air. This also allowed the bottom of the column to stay frozen during the thaw cycles. A space heater was suspended above the column from one of the freezer’s basket to thaw the soil from the top down (Figure 3-41). The basket from which the heater is suspended was raised on one side with foam insulation since the heater’s face was angled. This ensured that the heat distribution would be even across the sand surface.

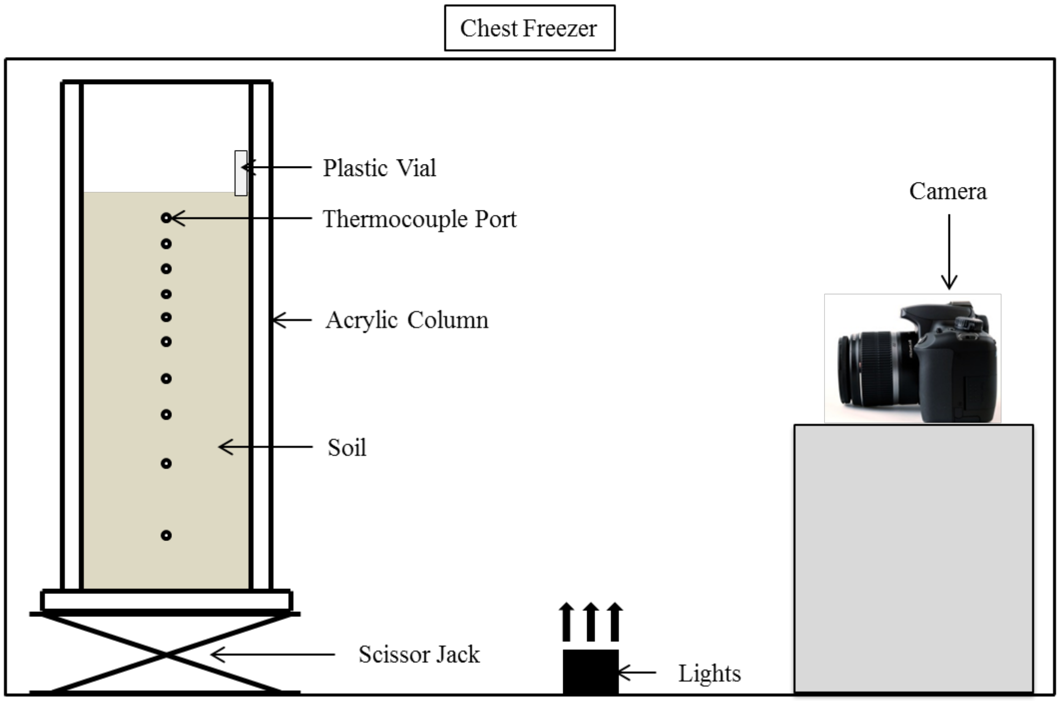

Figure 3-40: Column in the freezing position in the freezer.

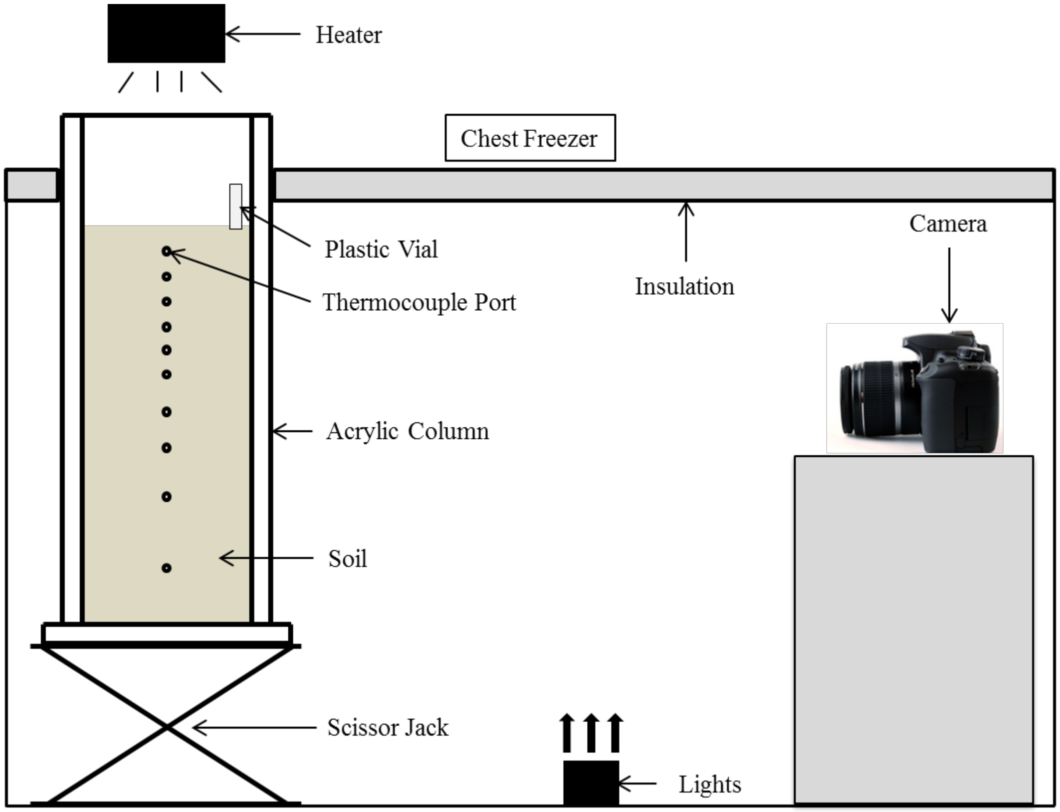

Figure 3-41: Column raised in the thaw position in the freezer.

3.5 Image Analysis

In order to quantify the results of the contaminant transport experiments, code was developed to track the depth of the oil front over time. The code took images from an experiment and the depth of the oil front was manually tagged for each picture. The code then plotted the depth of the oil front versus time. The code used a manually inputted pixel to mm ratio to transform the tagged pixel locations to distances between the tagged points. The pixel to mm ratio was determined by determining the pixel location of two points with a known distance from each other. The vertical or horizontal difference in pixels was divided by the known distance to get the pixel to mm ratio. In this study, the pixel to mm ratio was determined to be 11.3 for the column experiments and 12.8 for the centrifuge experiments. The interval between the pictures used for the analysis was also manually inputted when the code was running. For all the experiments shown in this thesis, the times presented are model times, unless specified. Appendix G lists the detailed instructions to use the code in order to quantify the results of an experiment.

3.6 Experimental Data Analysis

At the end of each experiment, three sources of data were extracted: the voltage recordings of each thermistor, the raw images taken from the digital camera and the soil samples that were collected throughout the cradle. In the case of the column experiment, it would be thermocouple data instead of the thermistor voltage recordings. Figure 3-42 shows the steps required to process the raw data acquired during an experiment to get the final data.

For the temperature data, the raw output from the centrifuge experiment was the voltage that was recorded every minute for each thermistor. The voltage was then converted to temperature data using the calibration parameters. Each thermistor had its own calibration parameters, which were obtained using the methods described in Appendix E. The temperature data would then be plotted versus time. A quick observation was done of the graph to ensure that all the temperature data was valid. Some thermistors were damaged during experiments and would stop recording the voltage or would produce data that was inconsistent. The data that was faulty would then be removed from the graph. The final temperature graph was then produced.

A digital camera was used to capture images of the soil model during experiments. Once all the images were downloaded from the centrifuge on-flight computer, the images to be used for analysis were selected. The image analysis process is described in Appendix G. The images were selected in order to have a thorough representation of the oil migration. Images where no migration was occurring were not analyzed. In some cases, only every second, third or fourth, etc image was selected for analysis in order to reduce the time required for analysis. Since the oil front for every image must be tagged manually, optimizing the number of pictures analyzed saved many hours of image analysis. Once the images were analyzed, the depth of the oil front was plotted versus time. The data where the oil front was immobile were removed for each individual vial. After this was done, the migration data would then be zeroed so that the beginning of the infiltration for each vial would start at $t = 0$. The data would also be zeroed so that the depth of the oil front at $t = 0$ would also be 0. The final migration data could then be produced. The zeroing of time and depth allowed for all experiments to be compared more efficiently.

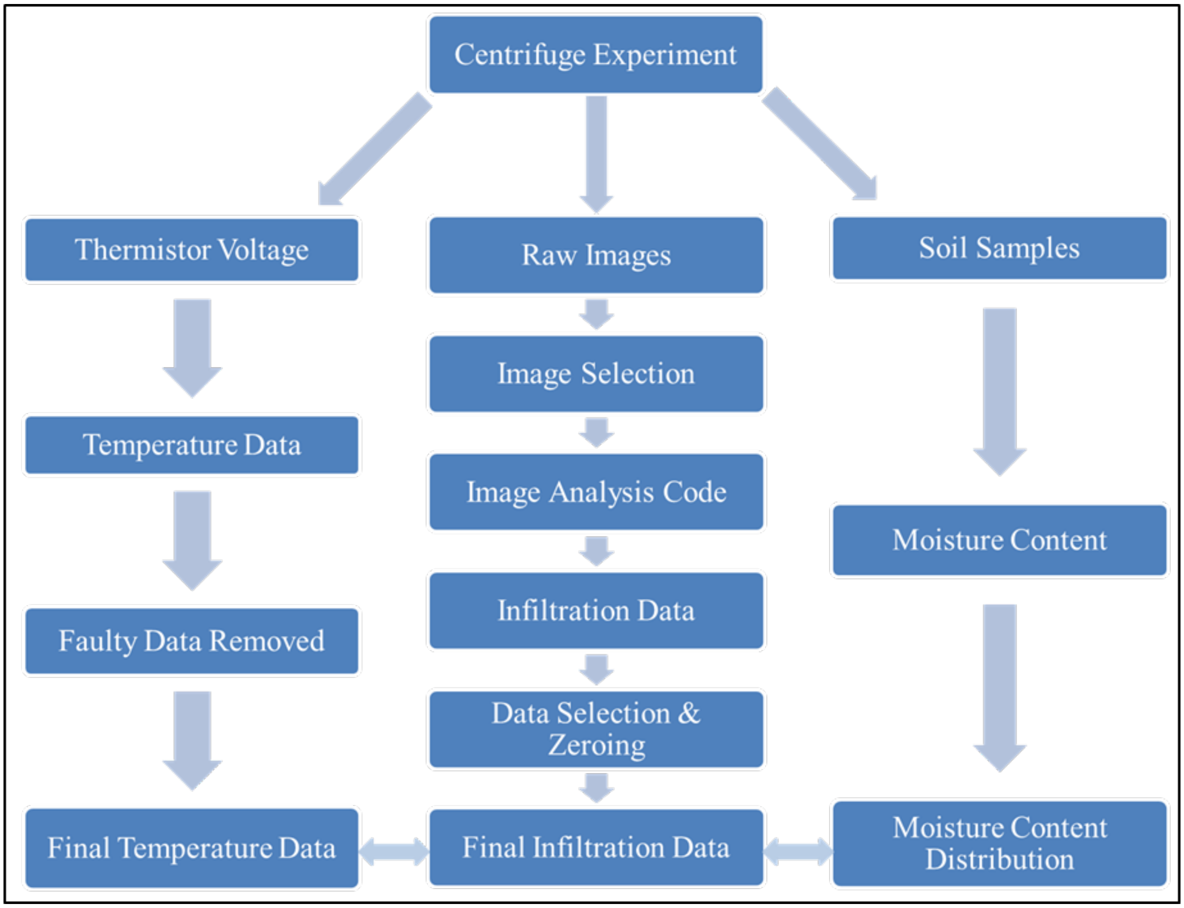

Figure 3-42: Experiment data processing.

After every experiment, soil samples were collected throughout the cradle in order to measure the moisture content. The final temperature data, the final migration data and the moisture content distribution were then compared in order to analyze the relationship between the three types of data.

4 EXPERIMENTAL RESULTS & ANALYSIS

4.1 Introduction

Chapter 4 presents the results from the experiments conducted in the acrylic column and in the geotechnical centrifuge. The results analyzed and presented in this chapter encompass the experiments with variations of the moisture content, temperature and acceleration ratio. The objective was to change the conditions for the three factors mentioned above to determine their individual and collaborative effect on the wetting front velocity of pumpkin seed oil through the #730 silica sand. Four of the experiments, one in the column and three in the centrifuge at different acceleration ratios, were conducted to validate the centrifuge experiment and ensure that the scaling laws for wetting front velocity were being followed. The modelling of models concept explained in Chapter 2 was used to validate the use of the centrifuge for contaminant transport experiments (Madabhushi 2015). This ensured that further experiments could be conducted in the centrifuge with the confidence that the results would be valid.

The following experiments were analyzed using the image analysis code described in Appendix G. The code allows for the calculation of the wetting front velocity of the pumpkin seed oil, which would be the v_x term (average linear advective velocity) in Equation 4. This equation was presented in Chapter 2.

4.1.1 Experiment Nomenclature

The experiments that were conducted in the centrifuge were classified using the following nomenclature (Figure 4-1).

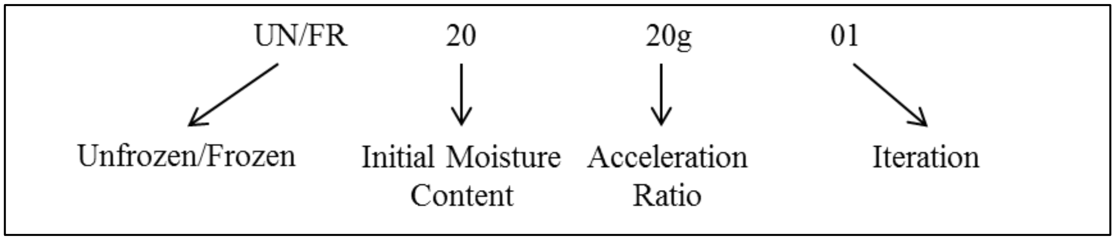

Figure 4-1: Experiment nomenclature.

The first term denoted the difference between experiments that had room-temperature soil and experiments that were frozen overnight prior to the experiment. The term FRV was used once to denote the experiment that used vortex tubes, while FRWB denotes the experiment where the soil from Wrangle Bay was used. The second term denotes the initial moisture content of the soil. The moisture content in nomenclature was rounded to the nearest full number. The third term denoted the acceleration ratio for the experiment. The centrifuge experiments were conducted at acceleration ratios of 20, 40 and 60g. The experiments in the column had an acceleration ratio of 1. Different iteration of a given experiment series, moisture conditions and acceleration ratios were conducted when an experiment needed to be redone because of unsatisfactory results, to change the amount of insulation used and/or to change if the climate box was installed or not. Table 4-1 shows the list of all the experiments that were conducted and presented in this chapter.

Table 4-1: List of all experiments.

Experiment #	Frozen/Unfrozen	Moisture Content	Acceleration Ratio	Experiment Name
Section 4.2 Experiments – Unfrozen Dry Sand				
1	UN	0%	1g	UN-0-1g-01
2	UN	0%	20g	UN-0-20g
3	UN	0%	40g	UN-0-40g
4	UN	0%	60g	UN-0-60g
Section 4.3 Experiments – Unfrozen Wet Sand				
5	UN	9%	1g	UN-9-1g
6	UN	10%	20g	UN-10-20g
7	UN	17%	20g	UN-17-20g-01
8	UN	17%	20g	UN-17-20g-02
9	UN	0/18%	20g	UN-0/18-20g
Section 4.4 Experiments – Frozen Sand				
10	FR	0%	20g	FR-0-20g
11	FR	0%	40g	FR-0-40g
12	FR	0%	60g	FR-0-60g
13	FR	10%	20g	FR-10-20g-01
14	FR	10%	20g	FR-10-20g-02
15	FR	18%	20g	FR-18-20g
16	FRV	10%	20g	FRV-10-20g
Section 4.5 Experiment – Column Freeze-Thaw				
17	FR	0/18%	1g	FR-0/18-1g
Section 4.6 Experiment – Wrangle Bay Soil				
18	FRWB	8%	20g	FRWB-8-20g

4.2 Centrifuge Experiment Validation

4.2.1 Dry Sand Experiments

In order to validate the centrifuge experiments and verify that the scaling law for wetting front velocity was being followed, a modelling of models was conducted. The scaling law for wetting front velocity is N, which means that it will increase linearly with increasing acceleration ratio. The modelling of models was done by conducting three experiments at different acceleration ratios in the centrifuge and one experiment in the acrylic column. The acrylic column's acceleration ratio was 1 while the three centrifuge experiments were run at acceleration ratios of 20, 40 and 60g. All four experiments were done with dry sand at room temperature to have a baseline from which all experiments with changing moisture content and temperature could be compared. The wetting front velocities were determined by calculating the slope of the depth of the oil front versus time, which was plotted using the code described in Appendix G.

Figure 4-2 shows the layout for the dry sand column experiment. Dry sand was compacted to a height of 365 mm. Two vials containing 50 ml of oil each were used for the dry sand experiment in the column (Figure 4-3). The vials, containing frozen oil, were simply inserted into the sand at the beginning of the experiment.

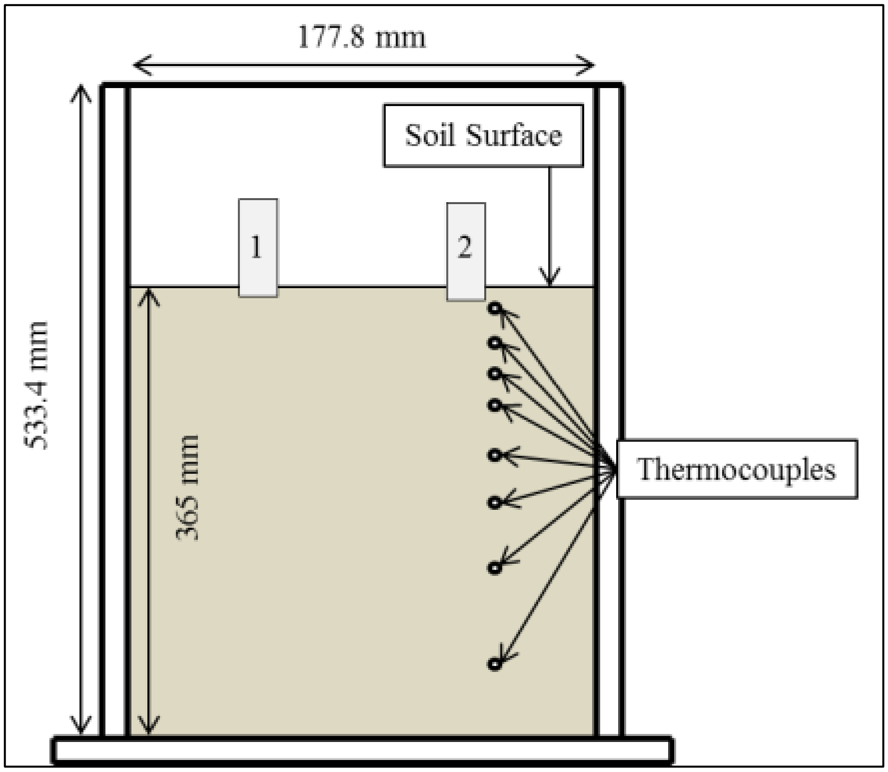

Figure 4-2: Dry sand column experiment layout (UN-0-1g).

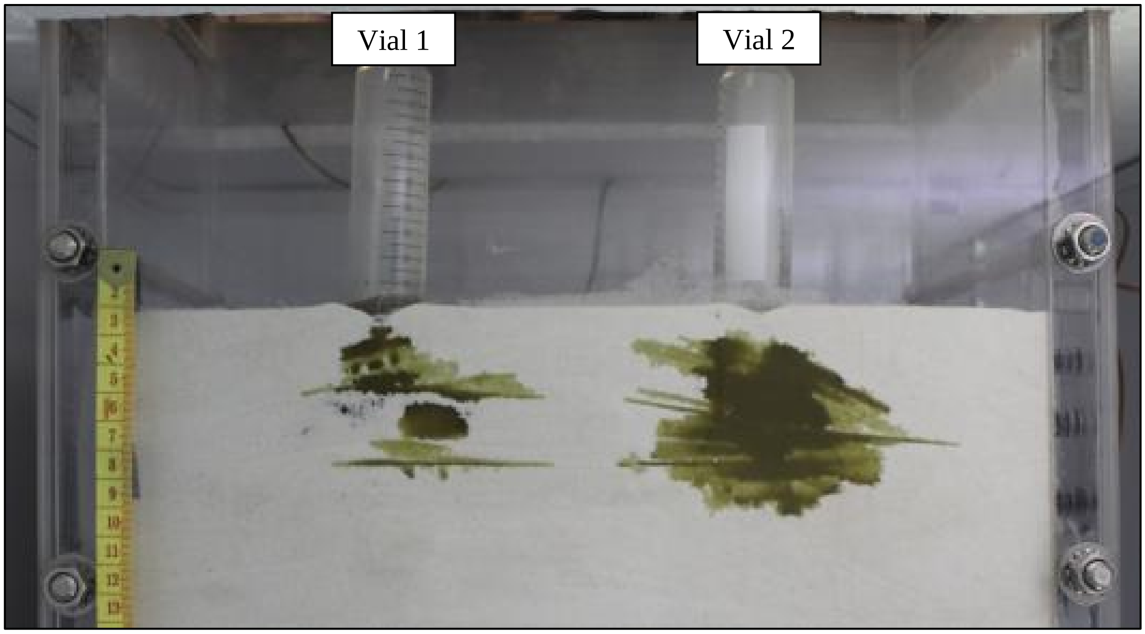

Figure 4-3: Sample image from the dry sand column experiment (UN-0-1g).

The migration data was zeroed so that the time when infiltration begins is set at 0. It took 25 minutes for the oil to melt from its original frozen state after it was placed in the sand and so, by zeroing the data, easier comparisons could be made. The initial depth of the oil front was also zeroed because the depth of the vials had slight variations between them. The zeroing of depth and time was conducted for all subsequent experiments. The average wetting front velocity for the two vials for the dry sand column experiment was calculated to be 0.21 mm/min (Figure 4-4). The wetting front velocity was relatively linear with a few areas where the migration would plateau. This plateau phenomenon could be attributed to the layering effect from compacting the soil in layers. Some of the layers became clearly visible when the oil migrated through them, as seen in Figure 4-3. The oil also had a tendency to migrate laterally along the interface between two layers once it reached another layer. In this case, the oil was moving along the path of least resistance. It is also possible that the oil would be moving laterally, and in some cases, slightly upwards because of the capillary effect of the soil.

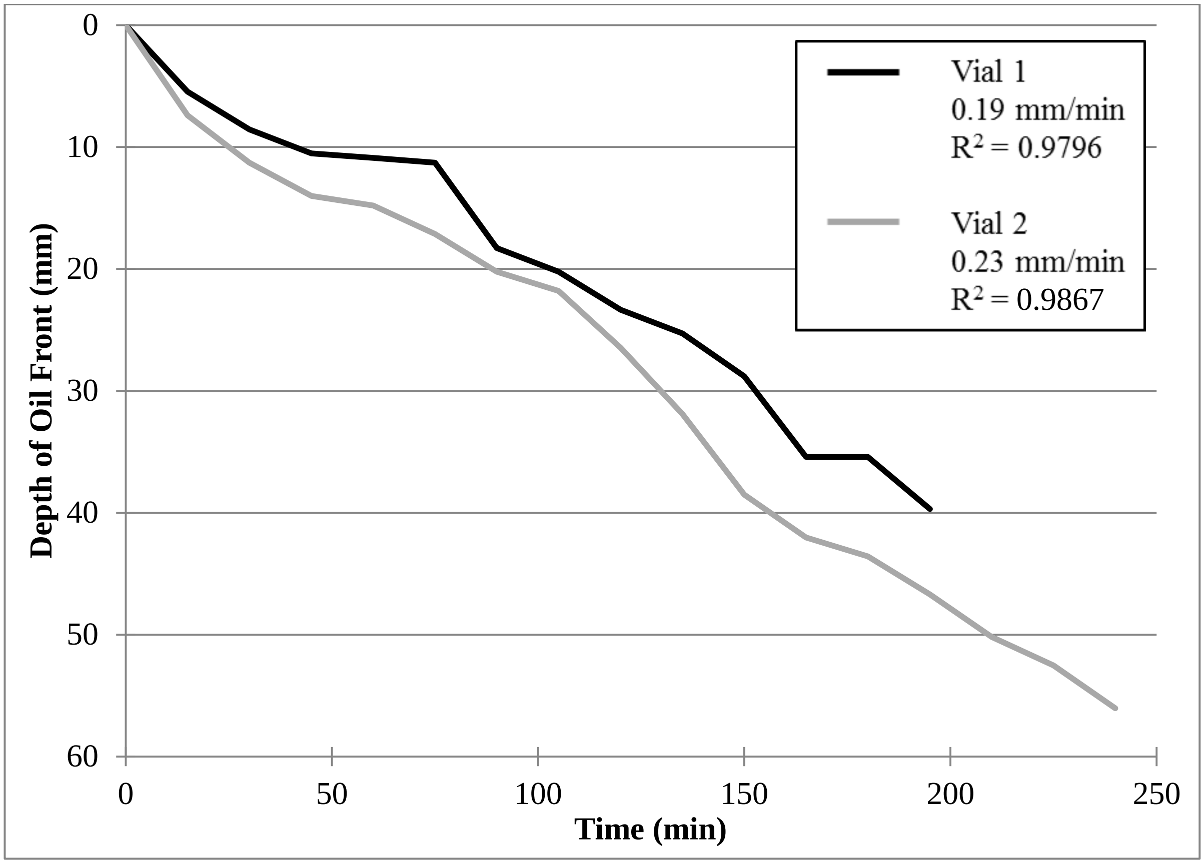

Figure 4-4: Oil migration through dry sand in the column (UN-0-1g).

For the centrifuge experiments (UN-0-20g, UN-0-40g& UN-0-60g), three vials containing approximately 6 ml of oil each were placed in the sand (Figure 4-5). The depth of the oil front from each vial was plotted versus time. The wetting front velocities were determined by calculating the slope of each of the oil front versus time. The average wetting front velocity was then calculated for each experiment at the different acceleration ratios. The average wetting front velocities for the 20, 40 and 60g experiments as well as the column experiment average wetting front velocity are shown in Table 4-2. The method to determine the wetting front velocity was accurate to one decimal point e.g. 0.2 mm/min, which is why the significant digits vary within some of the tables shown below, including Table 4-2. It was observed that the layering effect was also present for the centrifuge experiments, especially for the 20g experiment. For the 40 and 60g experiments, the layering effect was minimal (Figure 4-6). It was also noticed that more transverse dispersion was occurring during the column experiment compared to the centrifuge experiments. Transverse or longitudinal dispersion coefficient were not calculated as part of this research. The dispersion coefficient, which includes mechanical and diffusion dispersion, could be calculated if the diffusion coefficient for pumpkin seed oil in water was calculated. It would also require a calculation of the tortuosity of the soil.

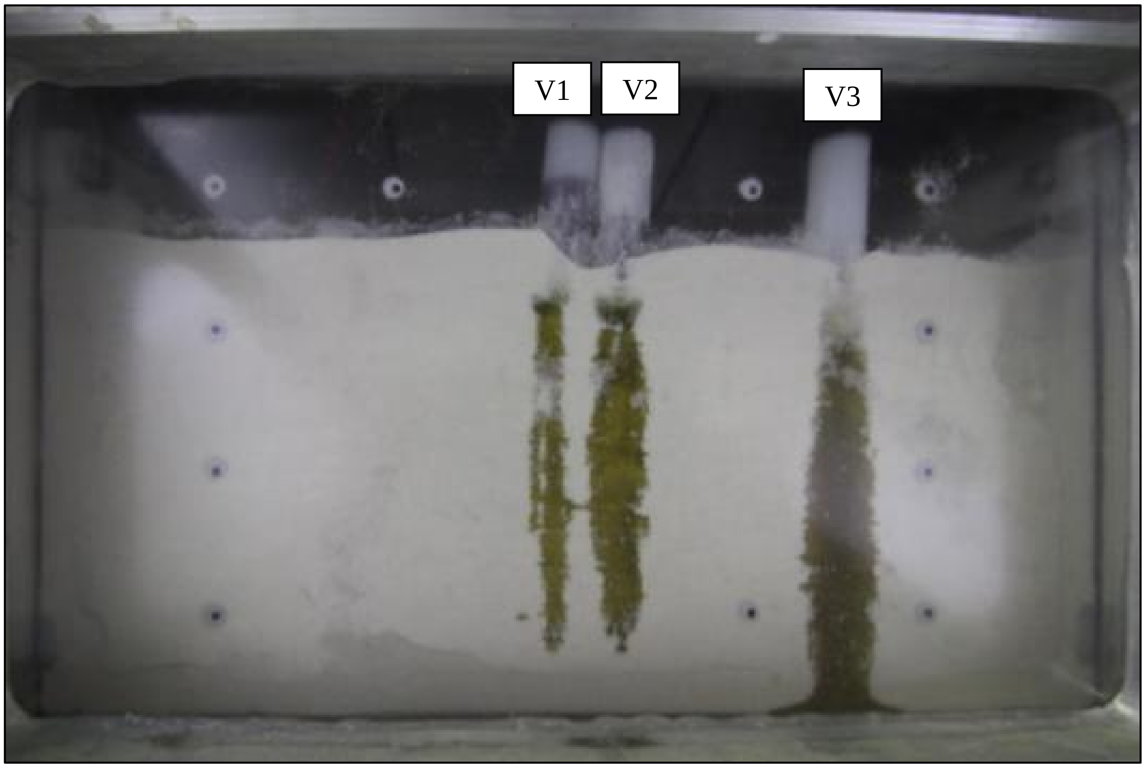

Figure 4-5: Sample image of a centrifuge dry sand experiment (UN-0-20g) at 30 minutes.

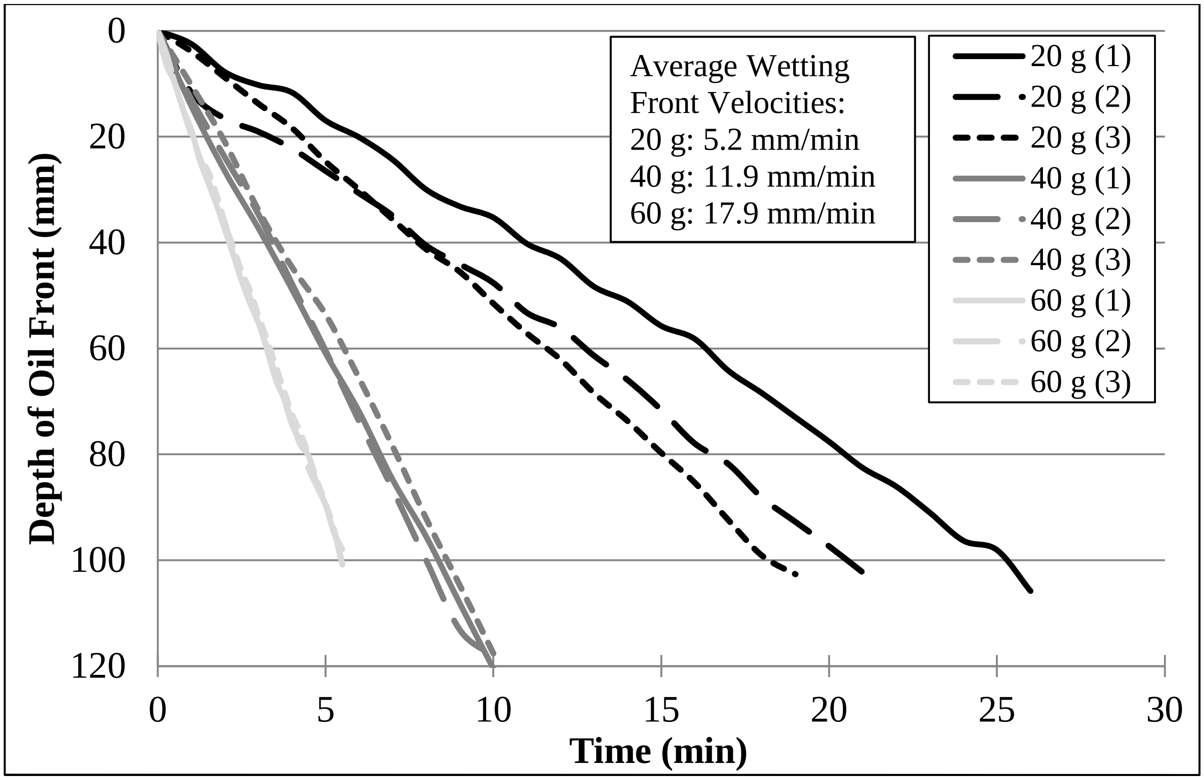

Figure 4-6: Oil migration through dry sand in centrifuge.

Table 4-2: Centrifuge validation results.

Experiment	Acceleration Ratio	Average Wetting Front Velocity (mm/min)
UN-0-1g	1	0.2
UN-0-20g	20	5.2
UN-0-40g	40	11.9
UN-0-60g	60	17.9

When the average wetting front velocities were plotted versus their respective acceleration ratios (Figure 4-7), it was observable that the wetting front velocities increased linearly with increasing acceleration ratio. This confirms that the wetting front velocity scaling law (N) was being followed for the centrifuge experiments. After completing this validation of the centrifuge experiments, it then seemed reasonable to continue subsequent experiments with confidence.

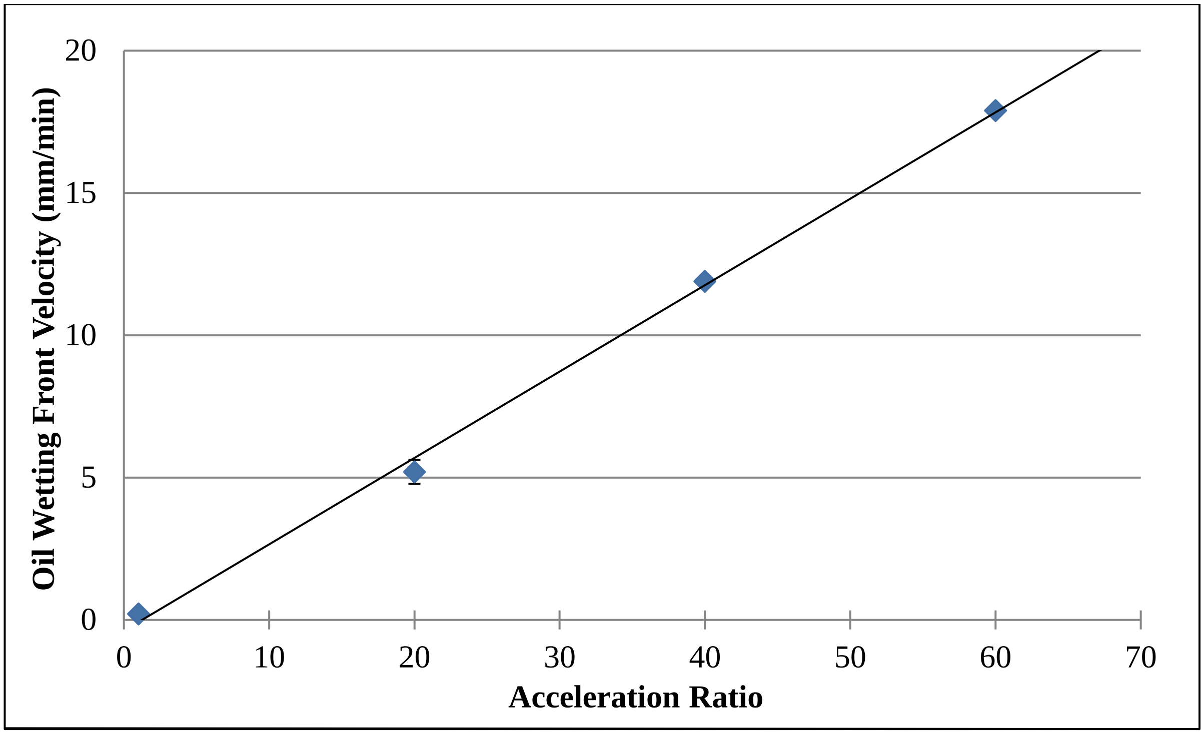

Figure 4-7: Wetting front velocity versus acceleration ratio (error bars show standard error).

When conducting the characterization of the sand as part of Appendix A, constant head tests were done to determine its hydraulic conductivity. The hydraulic conductivity of the sand was calculated to be 8.88x10^{-3} cm/s or 5.33 mm/min. Experiments UN-0-1g had wetting front velocities lower than the hydraulic conductivity (0.21 mm/min). However, experiments UN-0-40g and UN-0-60g had wetting front velocities (11.9 and 17.9 mm/min) above the hydraulic conductivity of the sand. This was because the hydraulic conductivity of the sand is also scaled in the geotechnical centrifuge. The scaling factor for hydraulic conductivity is N, which means that the hydraulic conductivity will increase linearly with increasing acceleration ratio (Qin 2019). In that case, the maximum flow through the sand was never achieved by the oil (Table 4-3).

Table 4-3: Hydraulic conductivity and wetting front velocities of oil at different acceleration ratios (model).

	Acceleration Ratio			
	1g	20g	40g	60g
Hydraulic Conductivity (mm/min)	5.3	106.6	213.1	319.7
Wetting Front Velocity (mm/min)	0.2	5.2	11.9	17.9

4.3 Effect of Moisture Content on Wetting Front Velocity

Experiments were conducted in the column and in the centrifuge where water was added to the sand. The goal of the addition of water to the sand was to observe and quantify the effects of the moisture content on the wetting front velocity of the oil through the sand. This will help to understand how contaminated sites with various moisture conditions will experience different wetting front velocities of their local contaminants. All the experiments were conducted at moisture contents near 10 or 18%. The saturation moisture content for the #730 silica sand was approximately 18%.

4.3.1 Oil Migration Results

An experiment (UN-9-1g) was conducted in the column where the sand had a uniform initial moisture content of 9% (Figure 4-8). The objective of this experiment was to set a baseline from which the centrifuge experiments with wet sand could be compared. This was also previously done for the dry sand experiments as part of the centrifuge validation process. The sand was added and compacted to the column, then two vials containing 50 ml of frozen pumpkin seed oil each were added to the sand. When conducting the experiments in the column, migration due to advection by gravity and migration by diffusion were both observed (Figure 4-9). The oil that is infiltrating due to gravity is visibly darker than the oil that is infiltrating through the sand by diffusion. The diffusion rate and the wetting front velocity were both calculated by using the image analysis method described in Appendix G. Only the dark oil was considered for the oil front to determine the wetting front velocity by advection. The wetting front velocity was calculated for the time that the oil was moving through the soil only. The time when the oil was still frozen in the vial and the time after which the oil was immobilized in the sand was not considered for the calculation of the oil infiltrating through advection by gravity. Migration of the oil into the sand by diffusion started almost immediately after the initially frozen oil was thawed. The oil that was diffusing through the water in the soil had a distinctly lighter colour than the oil that migrated by advection. The front of the oil infiltrating through diffusion was ahead of the front of the oil infiltrating through advection because of the time it took for the free-phase oil to enter the sand. Free-phase oil is a continuous mass of oil which can flow in the presence of a hydraulic gradient and that has not diffused in the water. Figure 4-11 shows the migration of the oil from the second vial through four images for experiment UN-9-1g, taken at 24 minute intervals.

The wetting front velocity of the oil through the wet sand through advection (Figure 4-10) was slower when compared to the migration through the dry sand (Figure 4-4). The wetting front velocity in the sand at 9% was 0.14 mm/min compared to 0.21 mm/min in the dry sand experiment, a reduction of 33%. Only the results from Vial 2 were used for analysis because the results for the other vial were unsatisfactory. It seemed like the vial was not inserted close enough to the window, which caused most of the migration to not be visible. At a moisture content of 9%, the sand was halfway to saturation, thus half of the pore space was occupied by water. The reduction of the wetting front velocity could be attributable to the water occupying pore space within the sand and reducing the amount of possible flow paths that the oil can take to seep by gravity through the sand.

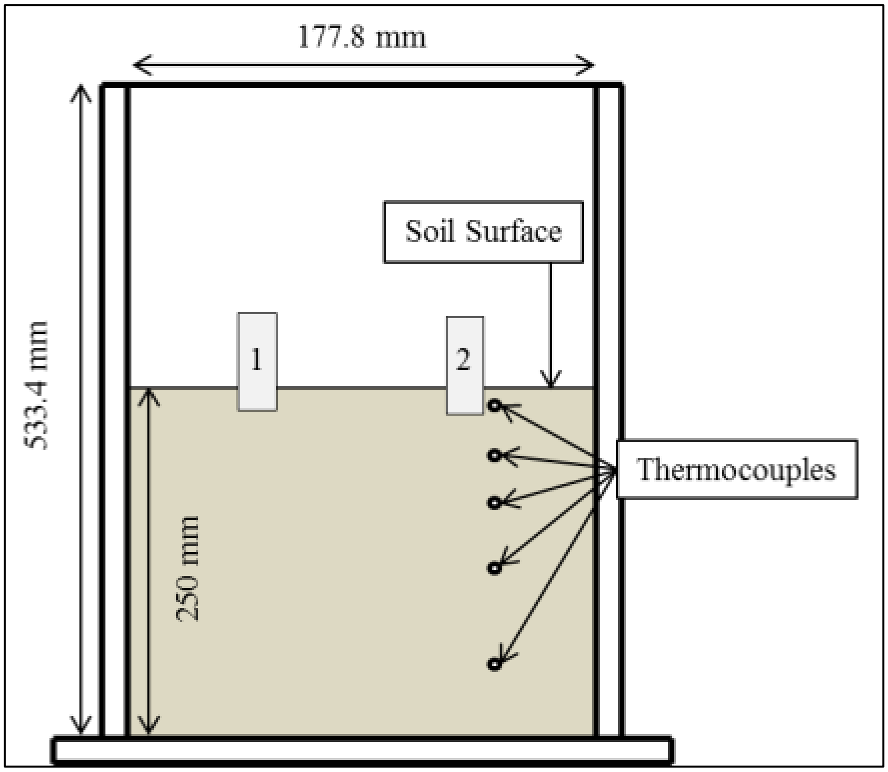

Figure 4-8: Layout for unfrozen wet sand experiment in the column (UN-9-1g)

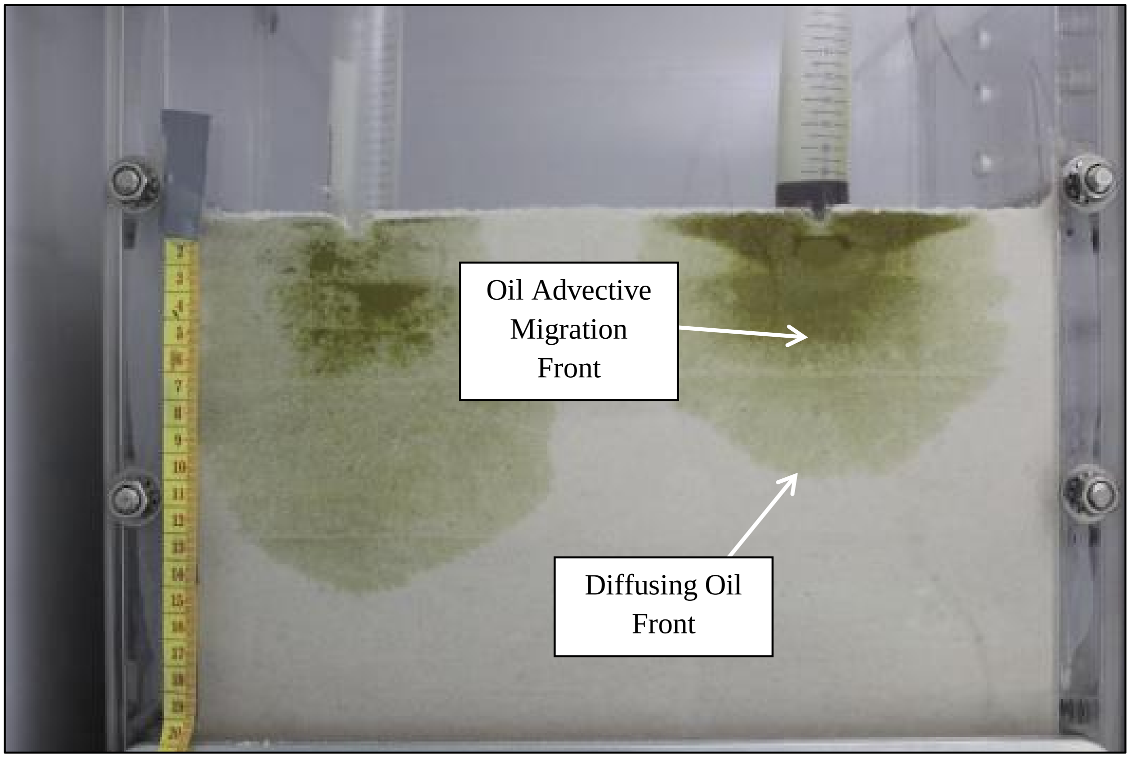

Figure 4-9: Diffusion and advective transport of oil in a column experiment (UN-9%-1g).

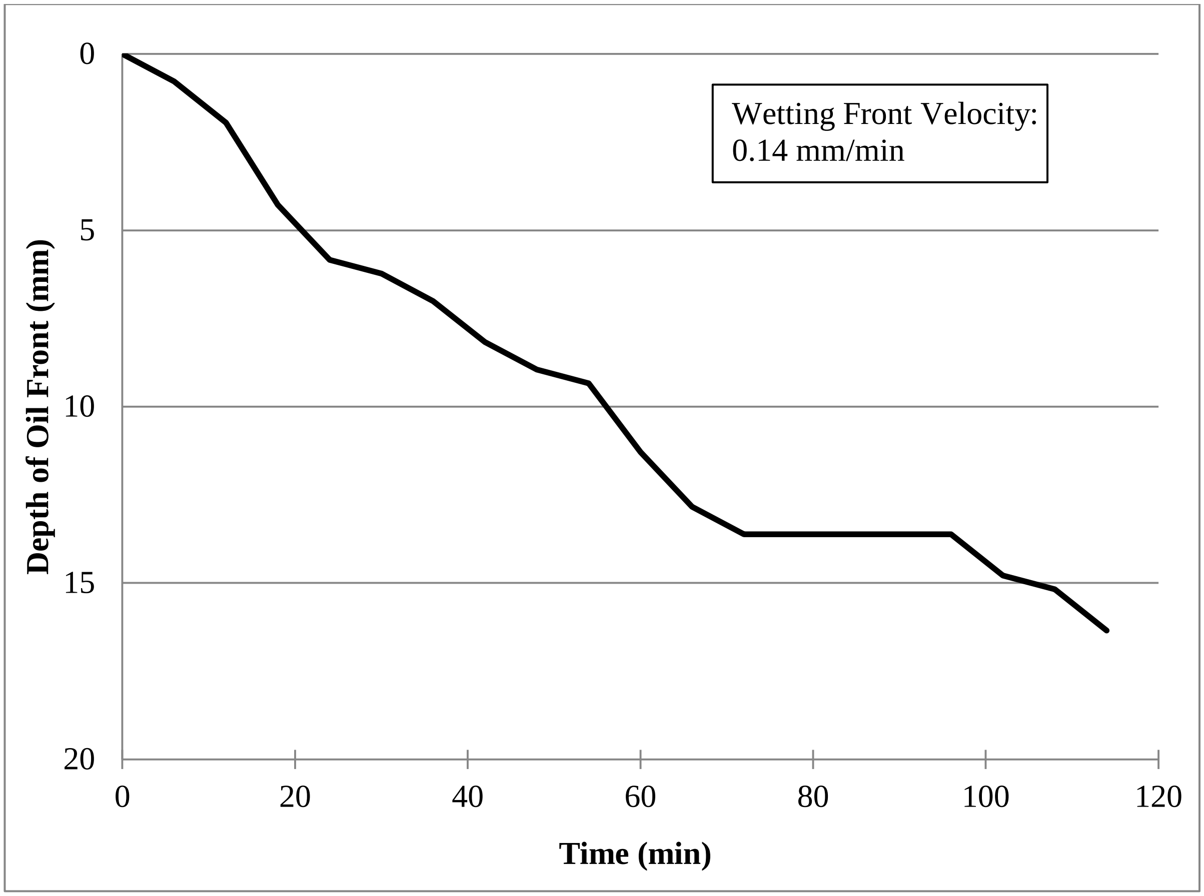

Figure 4-10: Oil migration through wet sand (10% moisture content) in the column (UN-9-1g).

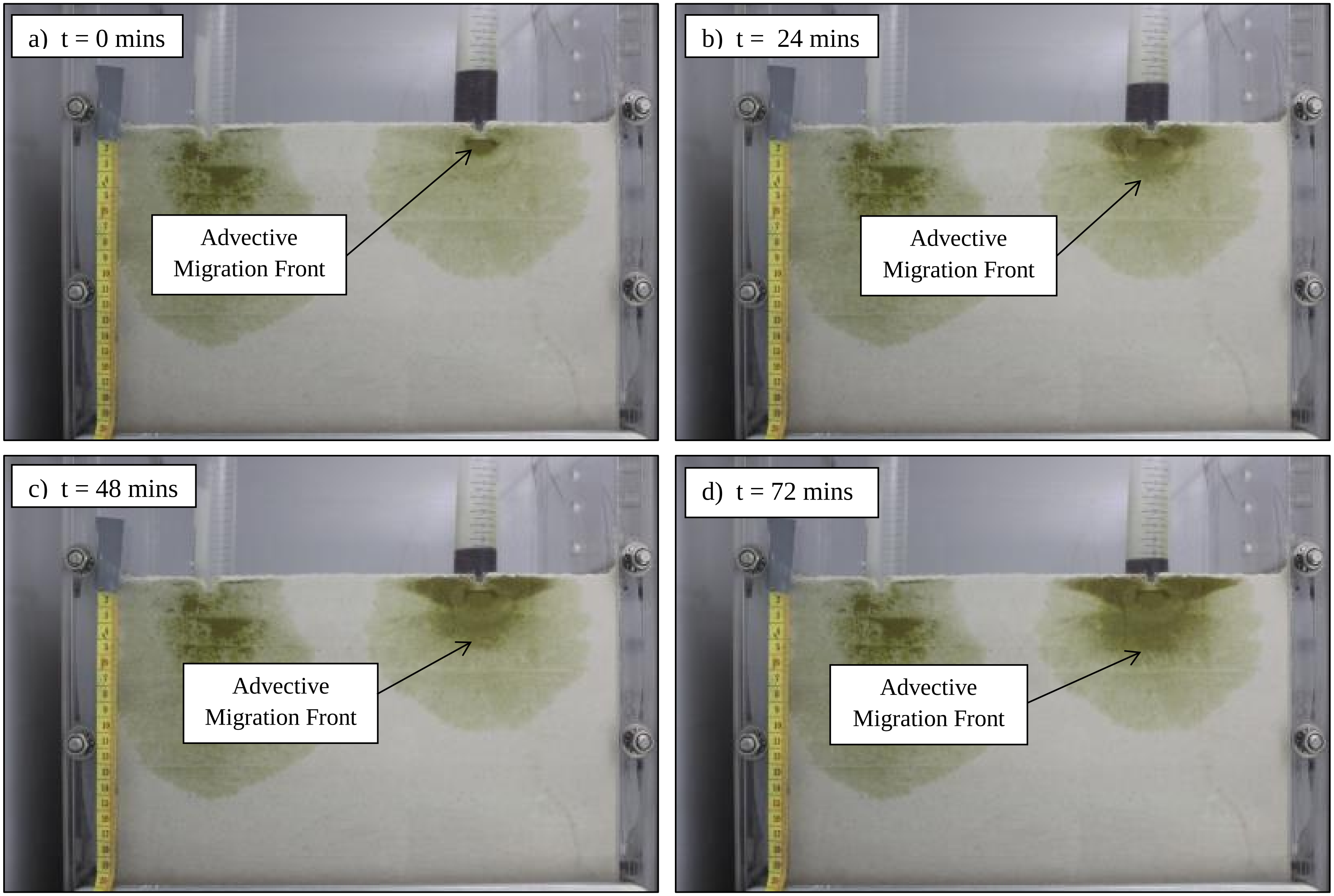

Figure 4-11: Advective migration of the oil during experiment UN-9-1g.

It should be reasonable to expect the wetting front velocity due to gravity to be approximately half that of the dry experiment (Fredlund et al. 2012), since half the pore space was initially occupied by water. However, that was not the case for this experiment. The wetting front velocity was reduced by 33% compared to the wetting front velocity of the oil through dry sand. At the end of the experiment, soil samples were collected at different depths in order to measure the moisture content. It was observed that the moisture content was progressively higher with increasing depth (Figure 4-12). Drying of the sand over the course of the experiment was evident since all the samples collected had a moisture content below the initial moisture content of 9%. The water in the sand also migrated through the sand during the experiment. However, it was not possible to measure the separate contributions of drying and migration of moisture within the sand to the variation of moisture content at various depths. Since moisture content was not recorded over the course of the experiment, it was not possible to determine the moisture content of the sand when and where the migration of the oil was occurring. However, we can deduce that when infiltration began, the moisture content was lower than the initial moisture content of 9%. It was also observed that the second vial took nearly 5 days to start infiltrating through the soil by advection. The oil from the first vial began to infiltrate through advection immediately after the oil thawed. This is because the pressure caused by the height of the oil was not high enough to overcome the entry pressure of the sand under those moisture conditions. The equation (Equation 20) to calculate the pressure due to the height of the oil is shown below:

$$P = \rho g h \quad [20]$$

Where:

P = Pressure (Pa)
ρ = Density of the fluid (kg/m^3)
g = Gravitational acceleration (m/s^2)
h = Height of the fluid (m)

The pressure caused by the height of the oil was 1,027 Pa (ρ = 910 kg/m^3, g = 9.81 m/s^2 and h = 0.115 m), while the entry pressure of the oil through the sand was estimated to be 1,100 Pa. With the error in the estimation of the entry pressure, it was possible that the entry pressure was slightly lower than 1,100 Pa since the pumpkin seed oil eventually entered the sand. The time it took for the oil to enter the sand could be caused by the water within the soil. As the experiment progressed, the water content near the surface decreased, which allowed the oil to move into the sand. This also shows that the water was the wetting fluid, while the pumpkin seed oil was the non-wetting fluid within the sand. The concept of wetting/non-wetting fluid was explained earlier, in Chapter 2. The entry pressure was also affected by the compaction of the sand, which could have been slightly different at the two vial locations. This is why the oil in the two vials did not enter the sand at the same time.

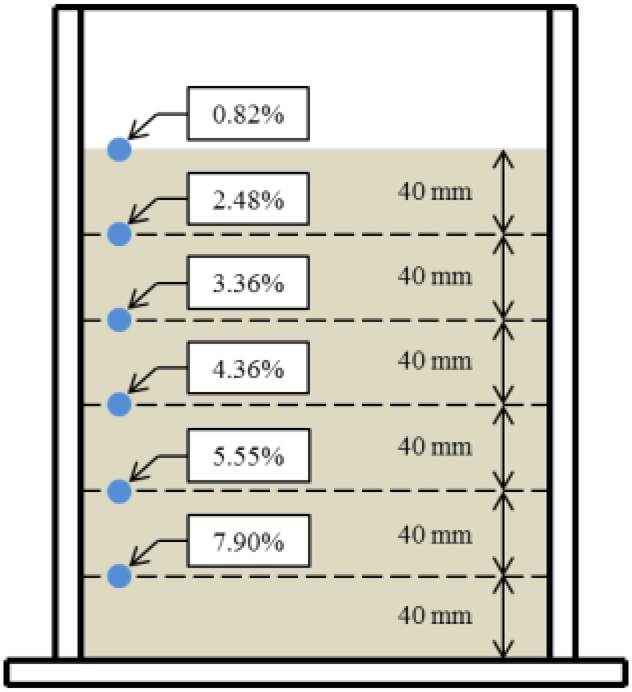

Figure 4-12: Moisture content at various depths for the column experiment (UN-9-1g).

After analyzing the images from experiment UN-9-1g, it was observed that the oil was also infiltrating the soil by diffusion of the pumpkin seed oil through the water in the soil .Two separate image analyses were conducted in order to quantify the rate of diffusion through the sand in addition to the wetting front velocity due to gravity. The diffused oil front was tracked using the image analysis code (Figure 4-13). From the image analysis code results, the rate of advancement of the diffused oil was calculated. The average rate was calculated to be 0.0085 mm/min, which was nearly two orders of magnitude slower than the migration by advection. The diffused oil was identifiable by its light colour compared to the free phase pumpkin seed oil, which was darker. Since the advection rate of the oil through gravity migration was nearly two orders of magnitude higher than the rate of migration by diffusion, it is safe to assume that advection is the dominant form of contaminant transport for this experiment. This means that its Peclet number would be close to 100, placing it well into the advection-dominated spectrum. As mentioned in Chapter 2, a Peclet number between 0.02 and 6 means that both advection and diffusion are contributing significantly to contaminant transport, while anything below that range is diffusion dominated and anything above the range is advection dominated. The Peclet number was not calculated since the coefficient of molecular diffusion was not calculated as part of this research.

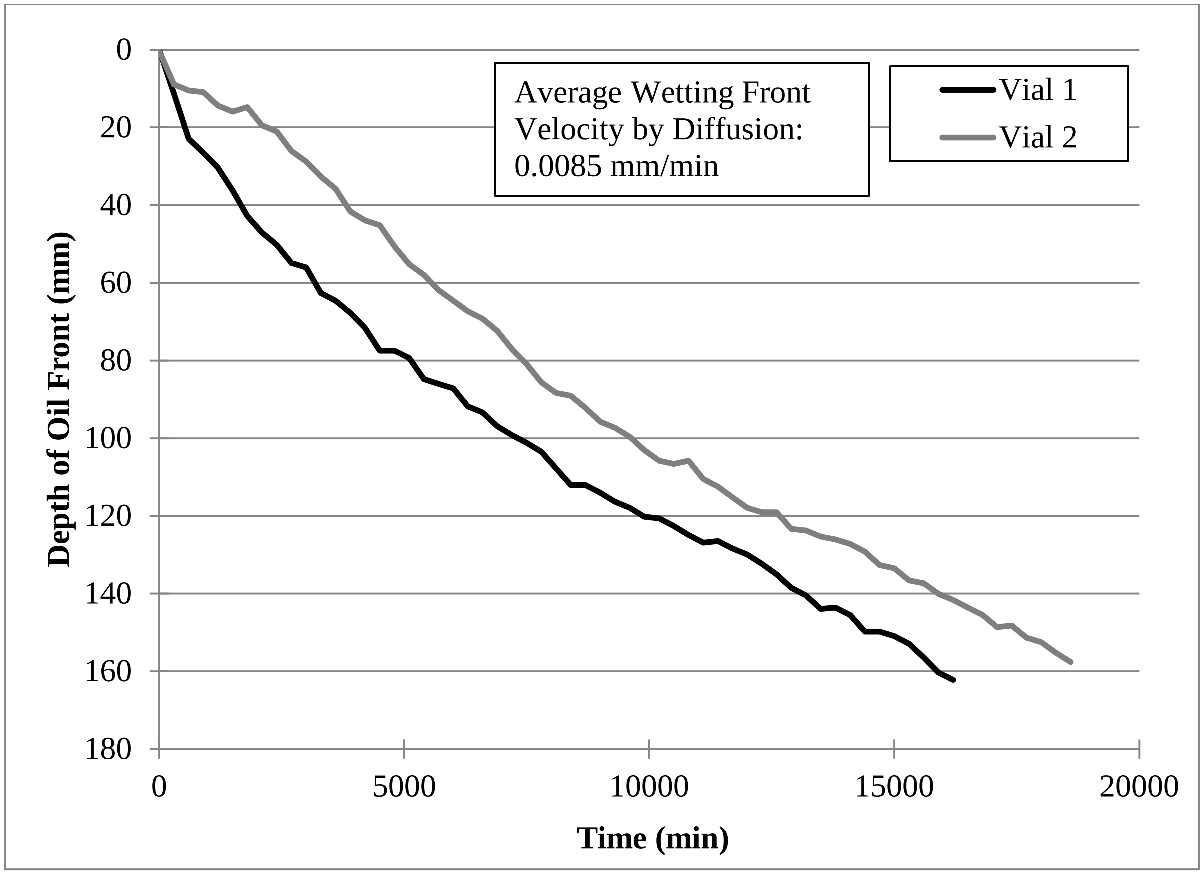

Figure 4-13: Diffusion of oil through water during a column experiment (UN-9-1g).

After conducting the experiment with 9% moisture content in the acrylic column (UN-9-1g), the same thing was done in the centrifuge (UN-10-20g). The initial moisture content in the centrifuge experiment was 9.7%. The average wetting front velocity was calculated to be 4.2 mm/min, which was a reduction of approximately 20% compared to the 5.2 mm/min wetting front velocity of the 20g experiment with dry sand (UN-0-20g).

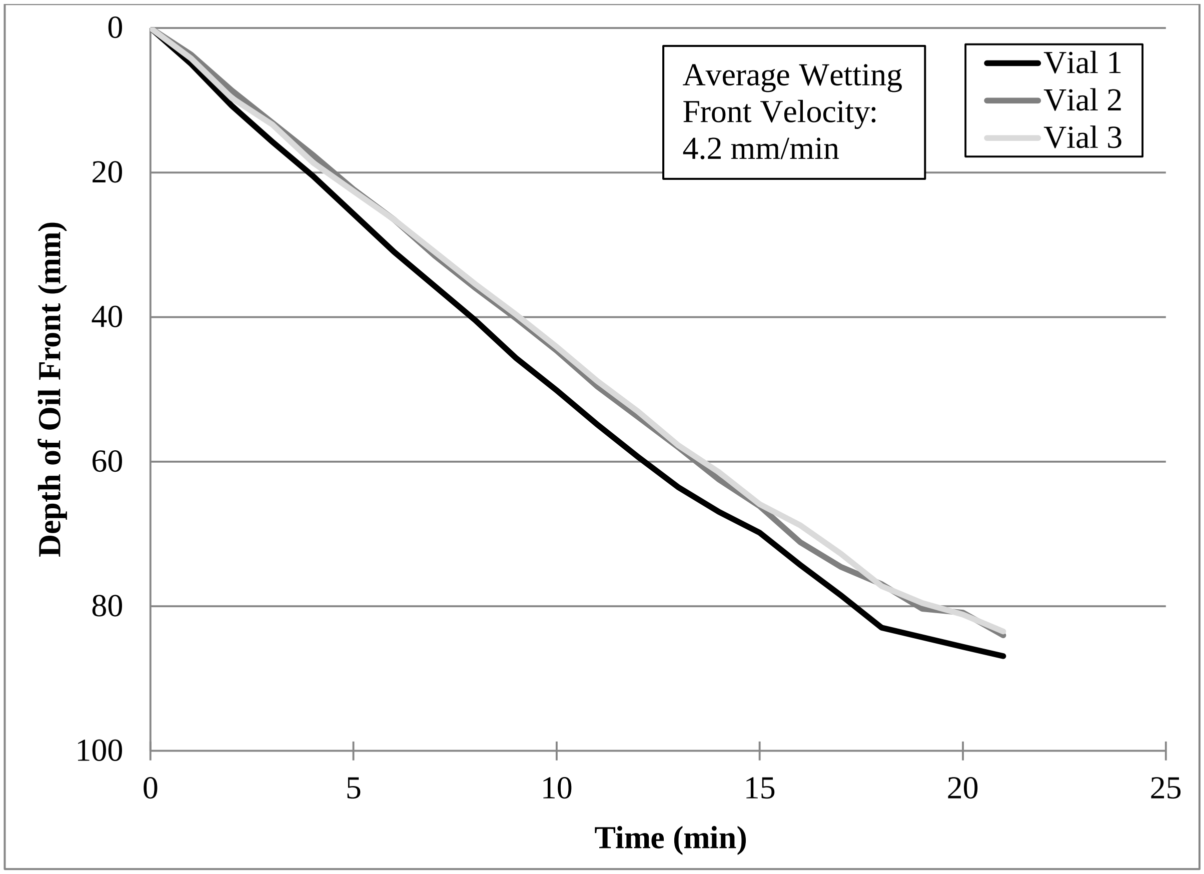

Figure 4-14: Oil migration through wet sand (10% moisture content) at 20g (UN-10-20g).

A smaller reduction of the wetting front velocity was observed (20% versus 33%) for the centrifuge than for the column experiments. Because of the centrifugal forces being applied to the model in the centrifuge experiment, the migration of the water through the sand was more pronounced and occurred faster than in the column. The difference in the moisture content distribution could be seen between Figure 4-15 and Figure 4-16. In only five minutes, water had clearly pooled at the bottom of the sand and created a saturated layer. The sand where the migration was occurring had likely lost most of its moisture, thus allowing the oil to seep faster than it would if the moisture content hadn’t changed from the initial moisture content. After the experiment was finished, the moisture content was measured at four different depths in the sand (Figure 4-17). Similarly to the column experiment (UN-9-1g), the moisture content was higher at the bottom of the sand. However, because of the time difference between the experiments (14 days for the column experiment versus less than two hours for the centrifuge experiment), the drying of the sand contributed less to the moisture content distribution change. Water loss occurred during the experiment due to inadequate sealing of the cradle. This was why the moisture content at the bottom of the sand was not near saturation.

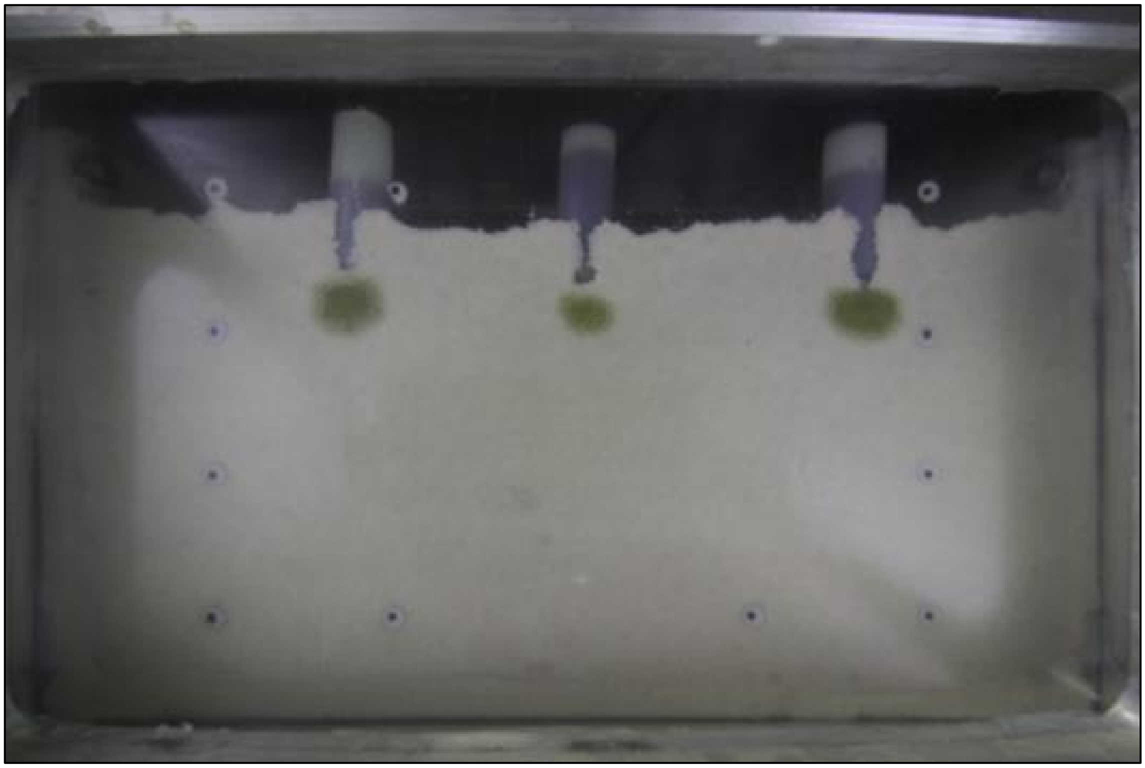

Figure 4-15: Initial image used for analysis from experiment UN-10-20g.

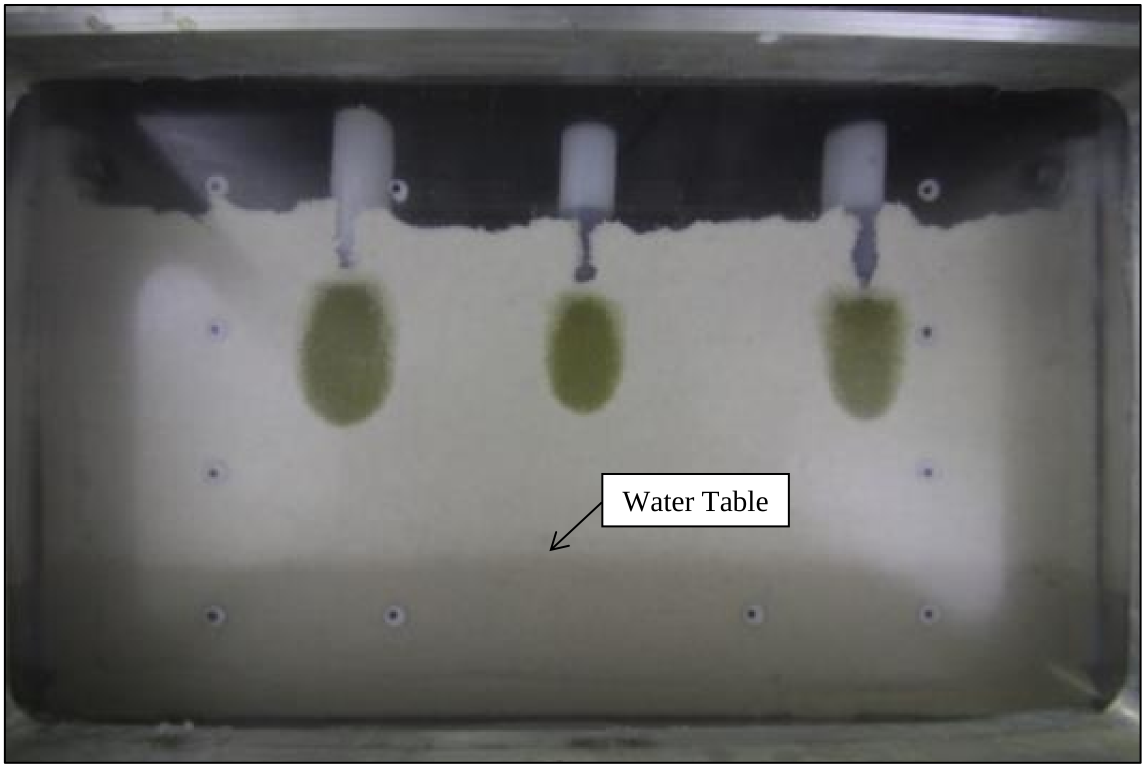

Figure 4-16: Image taken five minutes after the image above (Figure 4-15).

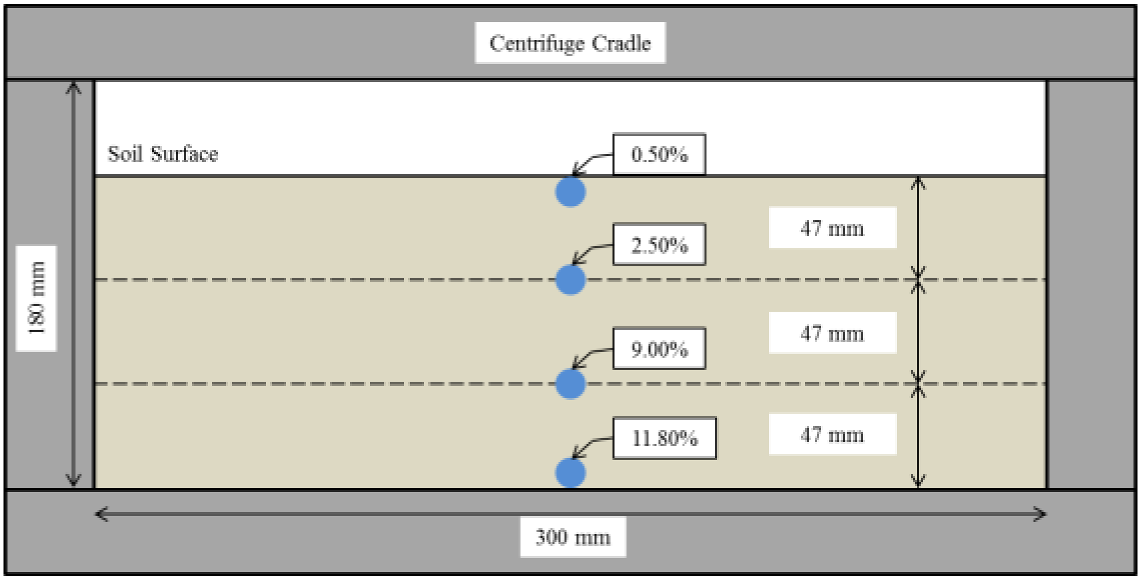

Figure 4-17: Water content distribution at the end of experiment UN-10-20g.

Experiment UN-17-20g-01 had an initial moisture content of 16.15%, which was near saturation. The objective of this experiment was to determine if saturated sand would completely block the infiltration of the oil, even at an increased acceleration ratio. No infiltration into the sand occurred during the experiment as shown in Figure 4-18 where the depth of the oil front vs time has been plotted. The experiment was conducted for 18 hours at 20g. The oil migrated by diffusion only through the water over the course of the experiment. Some diffusion was observed during this experiment (Figure 4-19 & Figure 4-20), however the diffusion rate did not increase due to the increase in the acceleration ratio. The rate of diffusion was very close to the rate observed during the column experiment. This proves that diffusion did not scale in the centrifuge, giving it scaling factor of 1, as previous studies have also proven (Qin 2019). The variations in the depth of the oil front in Figure 4-18 were within the margin of error of the tagging process while running the image analysis code. The depth of the oil front was within 1 mm for the three vials. Thus, the migration measured from the image analysis process was negligible, demonstrating that saturated soil blocks the infiltration of oil into the soil, even at an enhanced acceleration ratio. Since the diffusion coefficient of the oil remained the same even while subject to an increased acceleration field, the contaminant transport will be dominated by advection, but more significantly than in the column test since the advection through gravity migration will increase linearly with increasing acceleration ratio. However, if the sand is saturated, the contaminant transport process will be dominated by diffusion since no advection by gravity migration will occur.

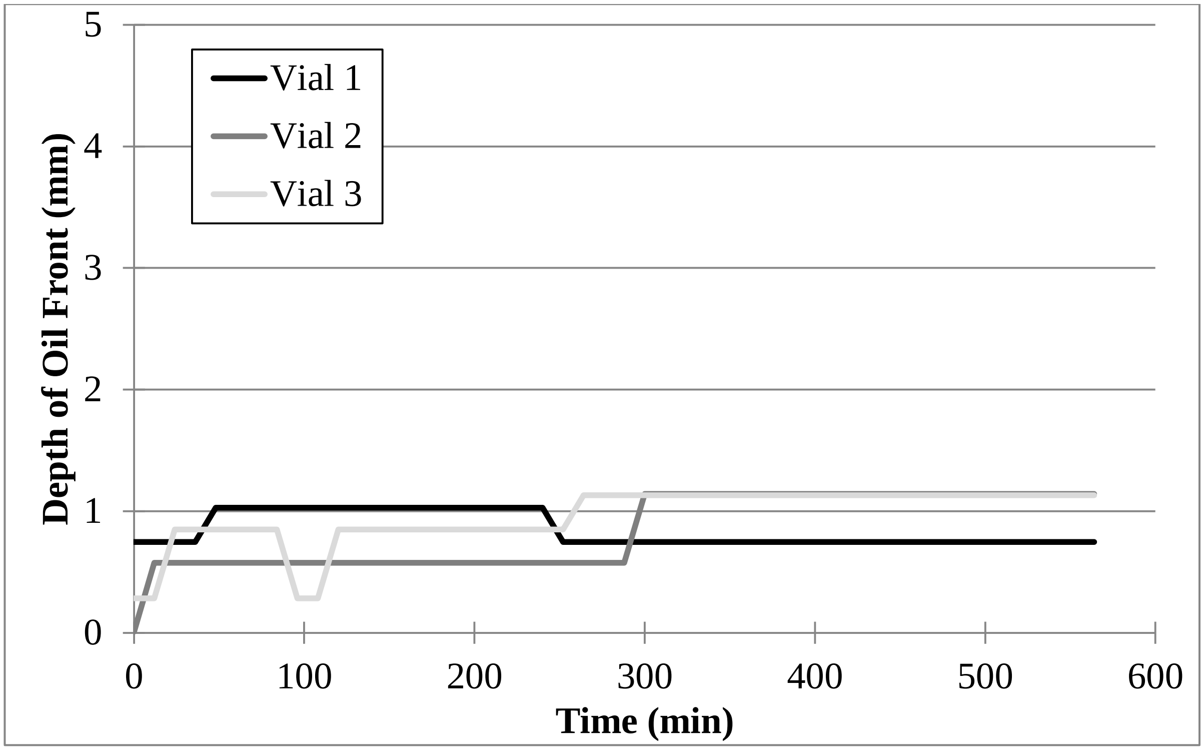

Figure 4-18: Oil migration through saturated sand at 20g (UN-17-20g-01).

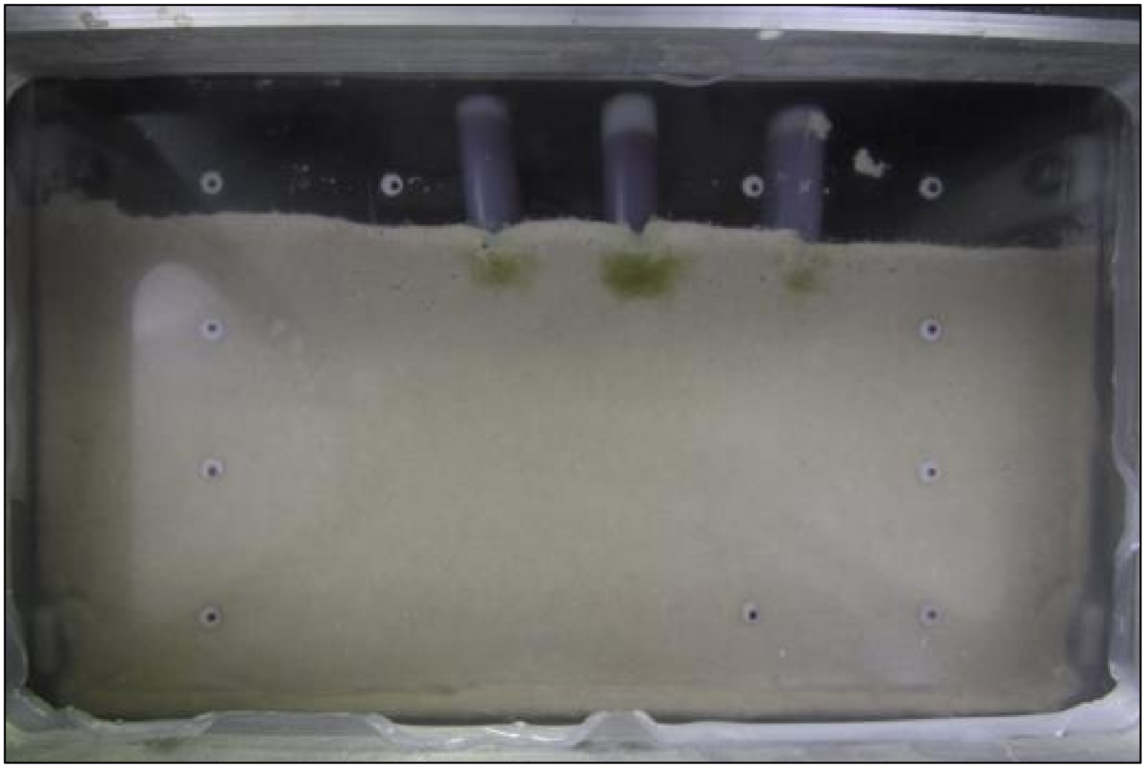

Figure 4-19: Image at the beginning of experiment UN-17-20g-01.

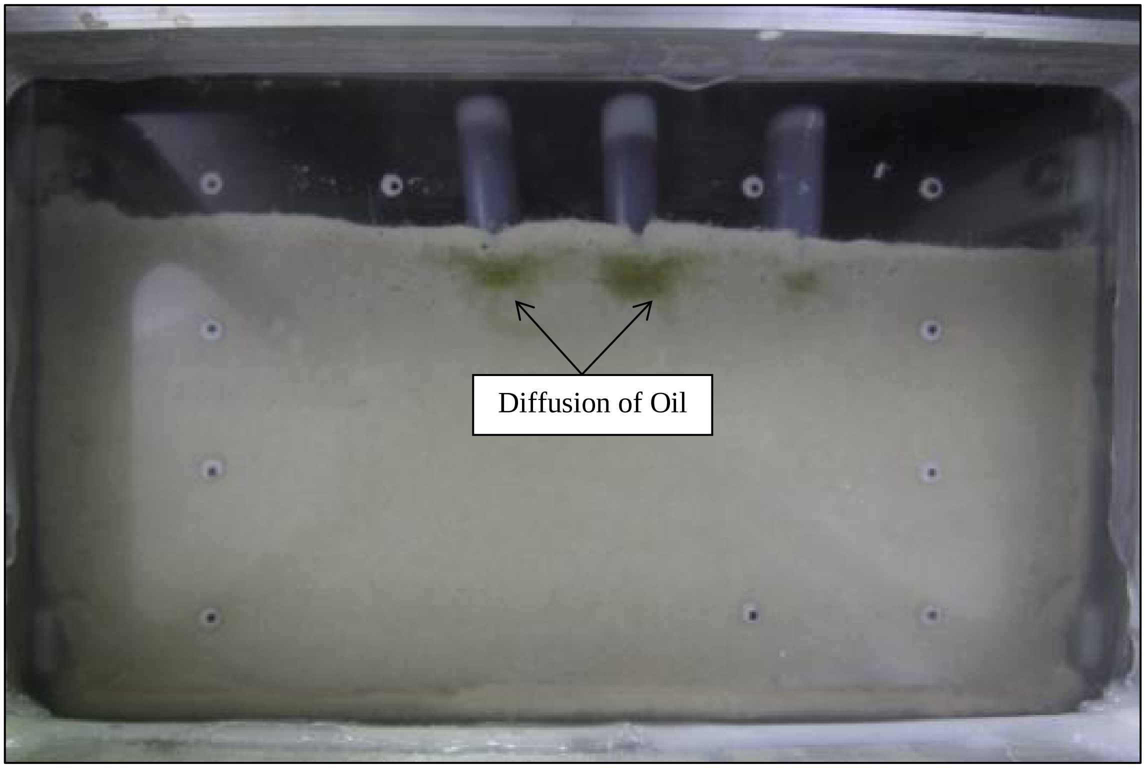

Figure 4-20: Last image taken for experiment UN-17-20g-01 (18 hours later) .

Another experiment (UN-17-20g-02) was conducted where the initial moisture content was close to saturation. The initial moisture content was 16.7%. However, water loss occurred over the course of this experiment because of an inadequate seal of the cradle. Before the observation of water loss, the oil did not seep through the soil (Figure 4-21). As soon as the water began escaping the cradle, the oil front followed the water table of the sand (Figure 4-22). The average wetting front velocity of the oil after the water begins to escape was 1.9 mm/min (Figure 4-23), which is a decrease of 63% compared to the migration through dry sand at 20g. The behaviour of petroleum hydrocarbons (PHC) increasing and decreasing in depth along with the water table was also observed during the site characterization of the Colomac Mine in the Northwest Territories (Iwakun et al. 2008). The observation of this behaviour is further validation that a geotechnical centrifuge can be used to model the contaminant transport of PHCs.

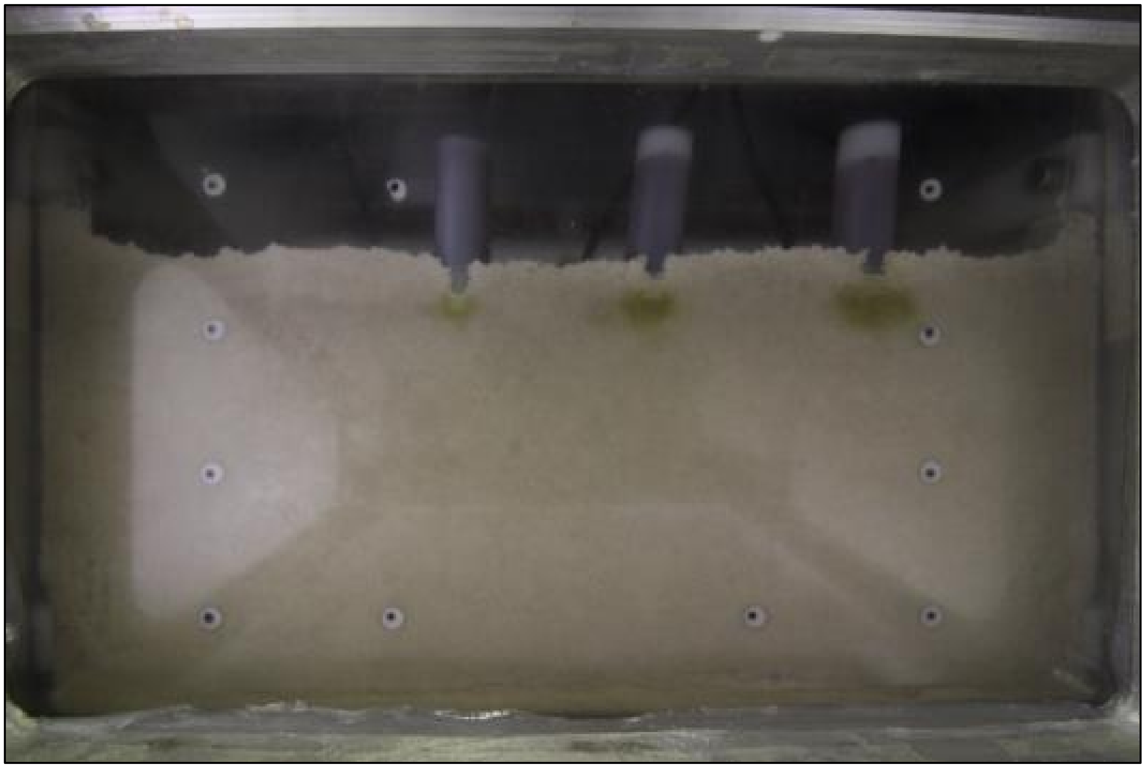

Figure 4-21: Beginning of experiment UN-17-20g-02.

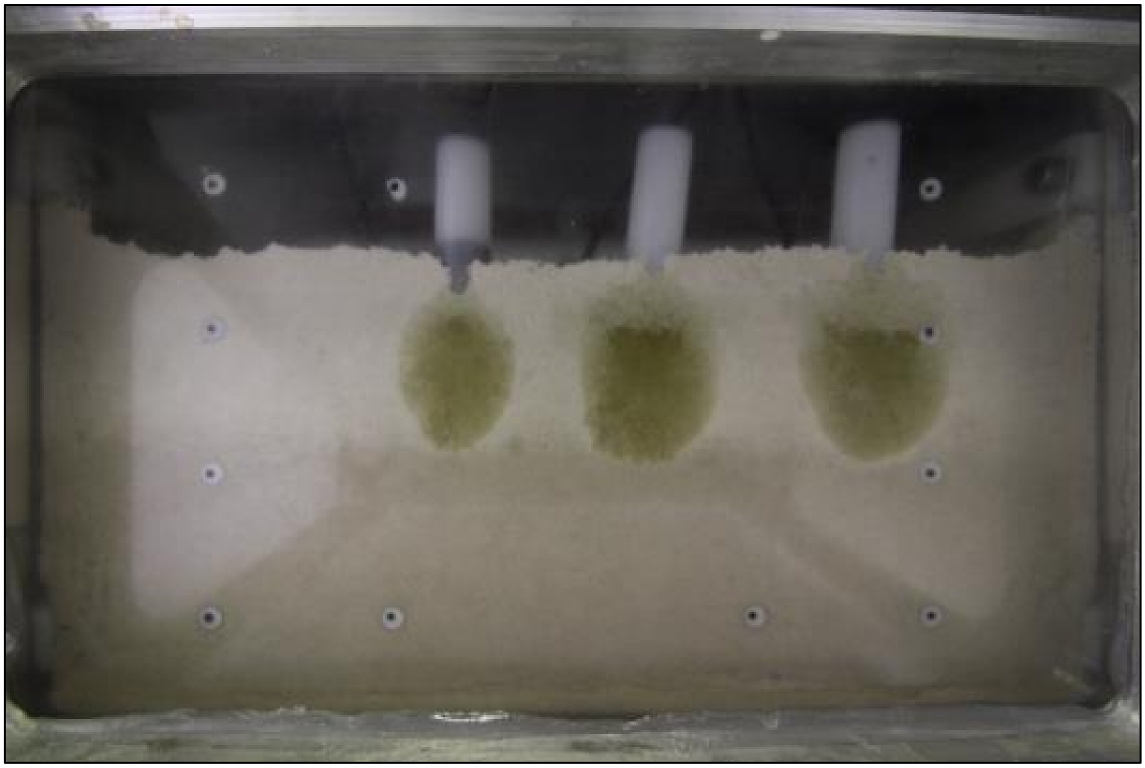

Figure 4-22: Oil front following the water table during experiment UN-17-20g-02.

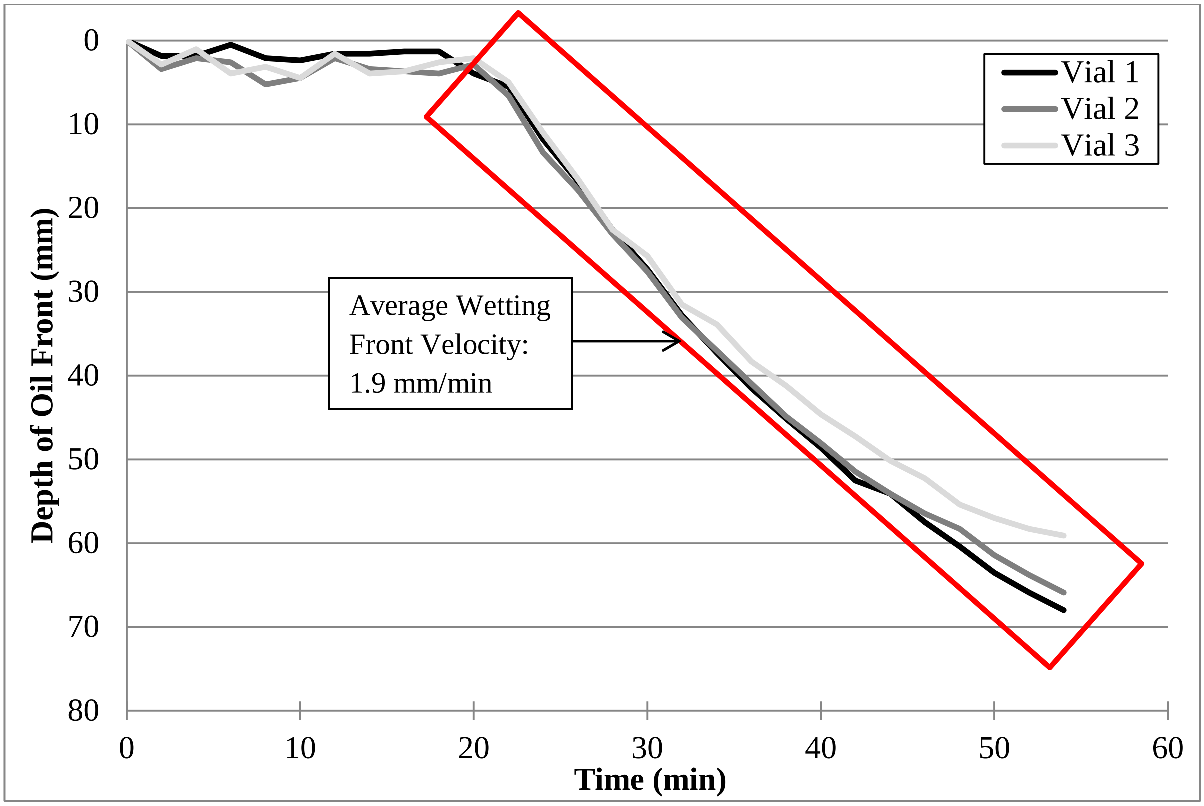

Figure 4-23: Oil migration through initially saturated sand that loses water during experiment (UN-17-20g-02).

Experiment UN-0/18-20g (Figure 4-24) is the last experiment presented that demonstrated the effects of moisture content on the wetting front velocity of pumpkin seed oil through the #730 silica sand. A 47.5 mm thick layer of sand with a moisture content of 17.5% was added to the cradle. A 92.5 mm thick layer of dry sand was then added on top of the saturated layer. The objective of the experiment was to observe the slowdown or stopping of the migration of the oil once it hits the saturated layer. As was observed in the three centrifuge validation experiments, it was expected that the oil would seep at a linear rate. Experiment UN-17-20g-01 demonstrated that saturated sand completely restricts the migration of oil. As was expected the oil migrated through the dry sand at a similar rate to experiment UN-0-20g. The wetting front velocity through the dry sand was 5.9 mm/min (Figure 4-25). In addition, once the oil reached the saturated layer, the wetting front velocity drastically slowed before completely stopping (Figure 4-26). The oil penetrated approximately 15 mm into the saturated layer before stopping. This behaviour was not observed in experiment UN-17-20g-01.

Figure 4-24: First image from experiment UN-0/18-20g.

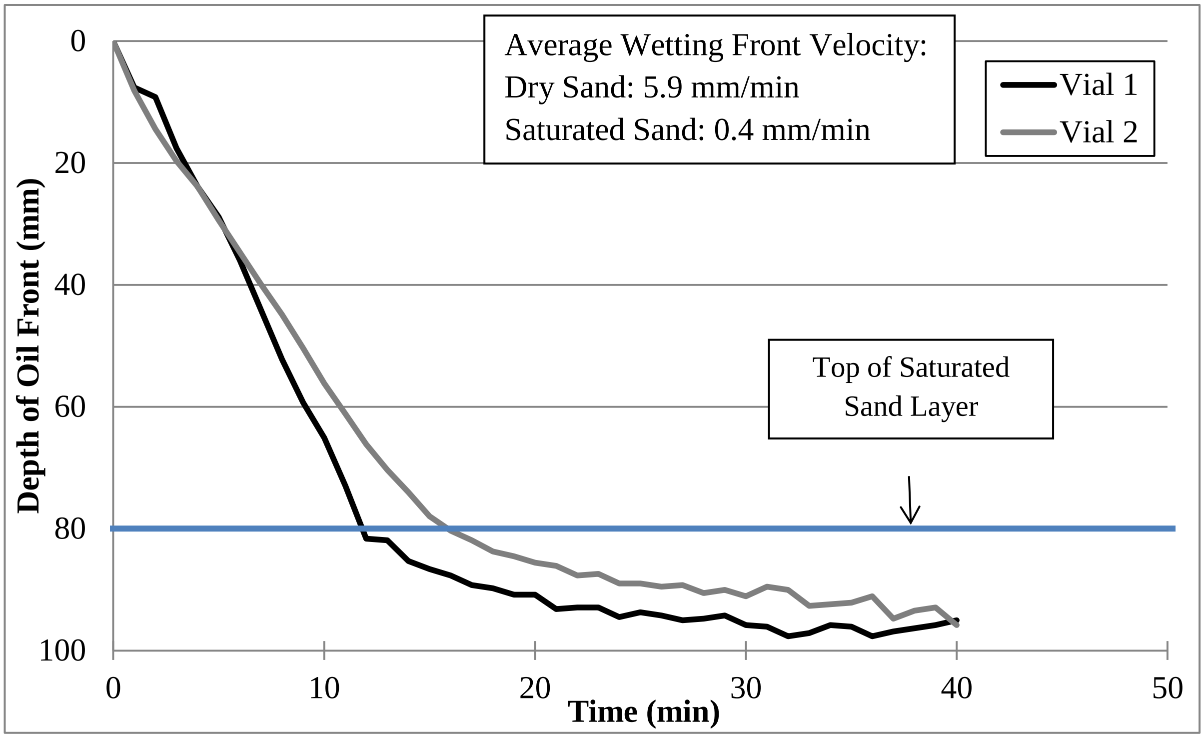

Figure 4-25: Oil migration through dry and saturated sand at 20g (UN-0/18-20g).

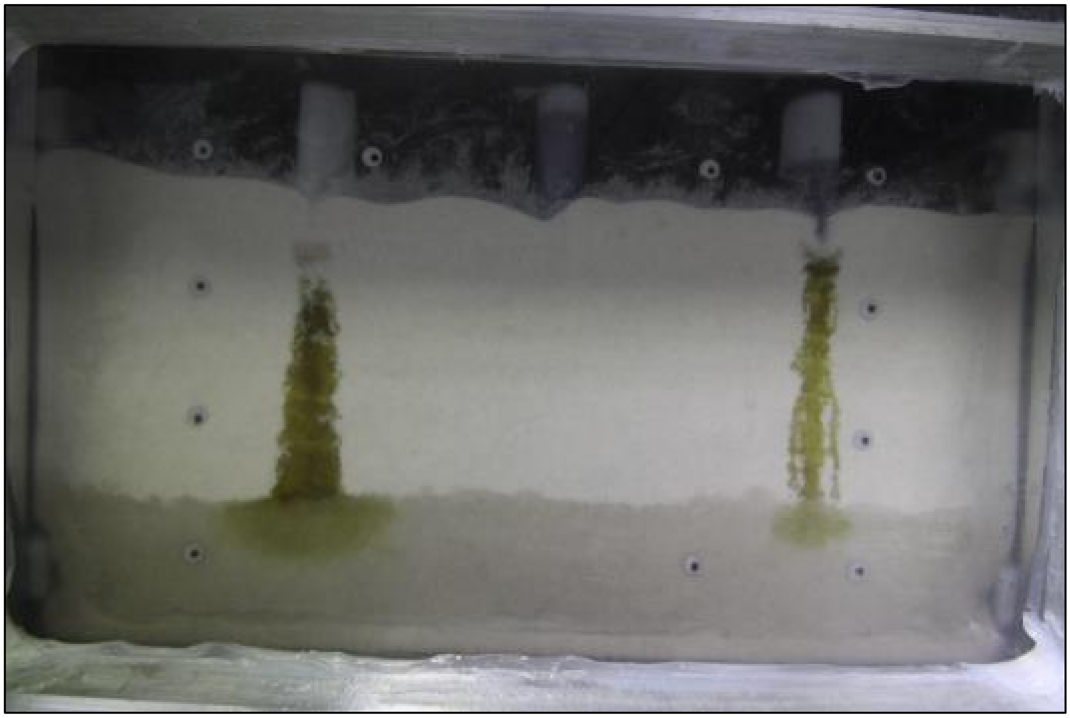
Figure 4-26: Pumpkin seed oil reaching the saturated layer in experiment UN-0/18-20g.

The previous experiments demonstrated the effects of moisture content within the soil on the wetting front velocity of pumpkin seed oil. Baseline wetting front velocities through dry sand were also established with the experiments used for the validation of the centrifuge. Experiments at half and full saturation showed that the presence of water within the soil pores affected the wetting front velocity of the oil. The wetting front velocities were reduced with increasing moisture content in the sand. Although this information was previously known in the literature (Fetter 2008), it is important because the same behaviour is being observed in the geotechnical centrifuge.

4.4 Effect of Temperature on Wetting Front Velocity

After conducting the validation of the centrifuge experiments and conducting experiments with wet sand, it was possible to move forward with conducting centrifuge experiments with initially frozen soil. By conducting experiments with initially frozen soil, it was possible to observe and quantify the effects of temperature on the wetting front velocity of pumpkin seed oil through the sand.

4.4.1 Frozen Dry Sand Experiments

Similarly to the experiments presented in Section 4.2, three experiments were conducted using dry sand at three different acceleration ratios (FR-0-20g, FR-0-40g and FR-0-60g). However, the entire cradle was frozen prior to starting the experiments. The depth of the oil front was plotted versus time for each of the experiments (Figure 4-27). The wetting front velocities were then calculated and compared to the experiments presented in Section 4.2 (Figure 4-28 & Table 4-4). Wetting front velocity reductions of 48, 54 and 47% were observed between the room temperature and frozen experiments at acceleration ratios of 20, 40 and 60, respectively. Figure 4-29 & Figure 4-30 show the layout for the oil vials and the thermistors for experiment FR-0-20g.

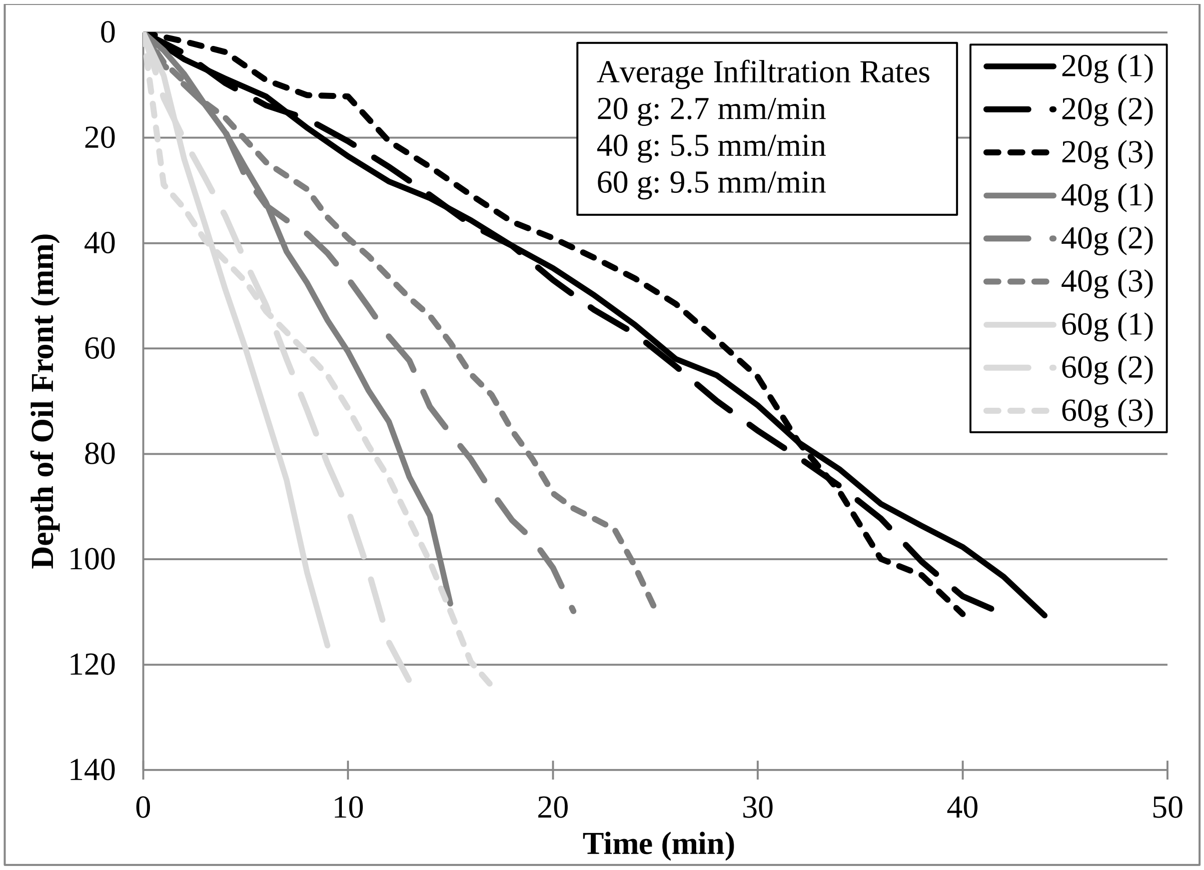

Figure 4-27: Oil migration through frozen dry sand at various acceleration ratios.

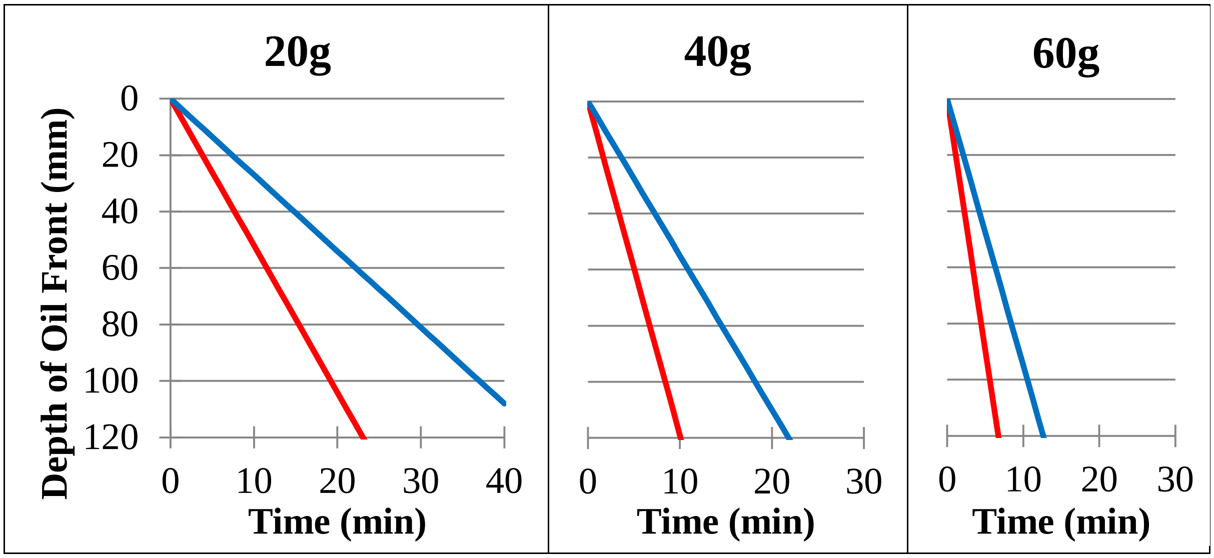

Figure 4-28: Migration difference between unfrozen (red) and frozen (blue) at different acceleration ratios with dry sand.

Table 4-4: Wetting front velocity decrease between room temperature and frozen soil.

Acceleration Ratio	**Room Temperature Soil Wetting Front Velocity (mm/min)**	**Frozen Soil Wetting Front Velocity (mm/min)**	**Wetting Front Velocity Decrease (%)**
20	5.2	2.7	48
40	11.9	5.5	54
60	17.9	9.5	47

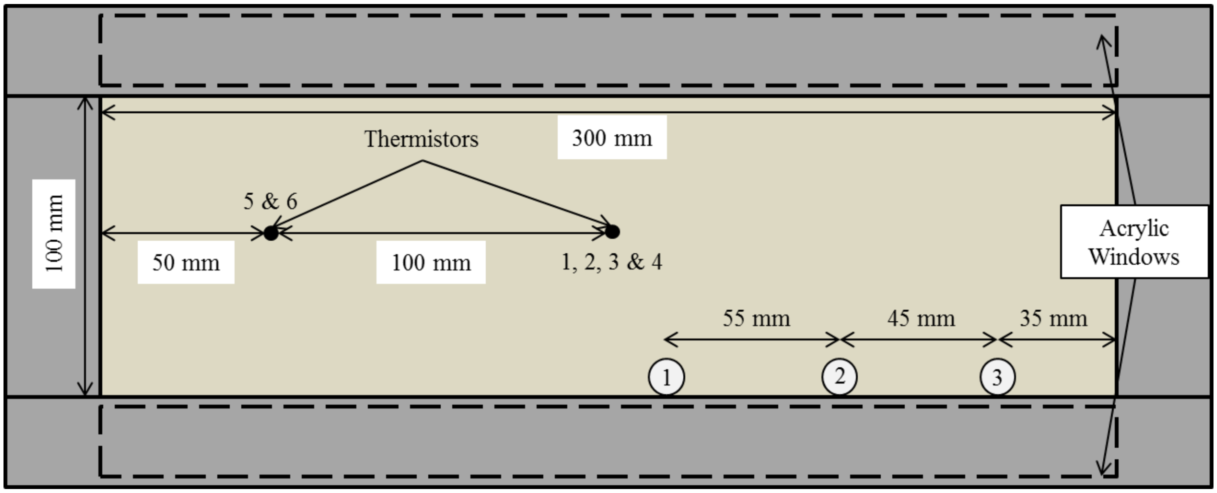

Figure 4-29: Thermistor and vial layout (top view) for experiment FR-0-20g.

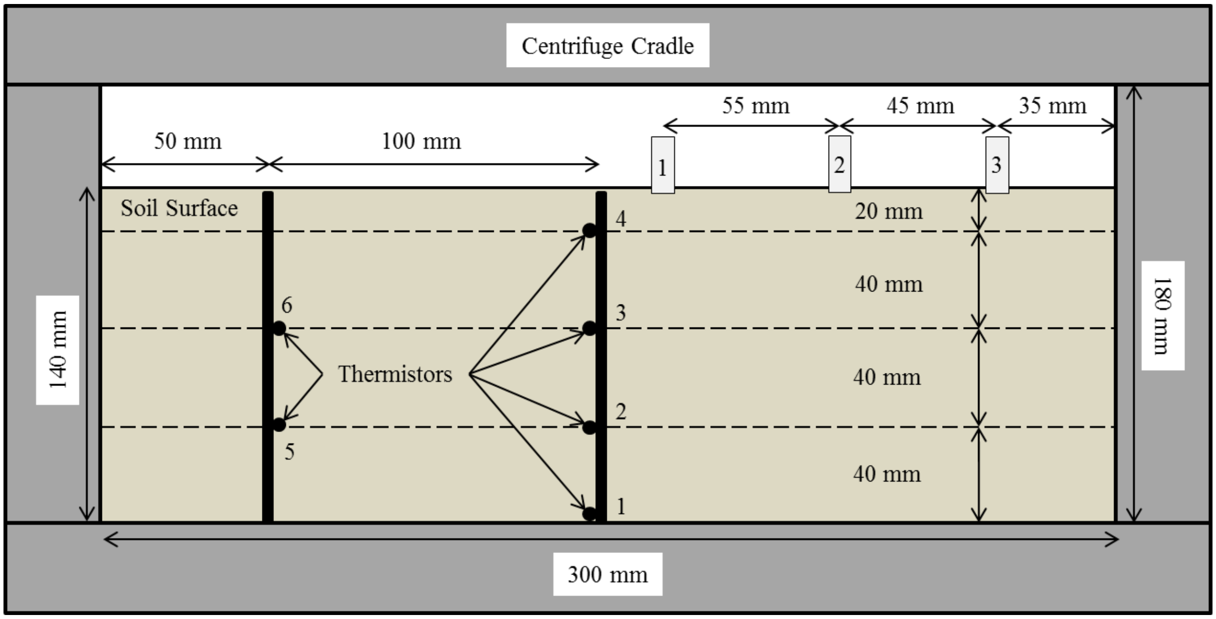

Figure 4-30: Thermistor and vial layout (side view) for experiment FR-0-20g.

Figure 4-31 presents the depth of the oil front versus time and the temperature recorded for each thermistor versus time. The recorded temperature when infiltration starts for each vial is presented in Table 4-5. The average temperature when infiltration of the oil into the sand begins was calculated for each vial using the recorded temperature from the thermistors at that time. An average temperature for each thermistor was also calculated using the temperature at which each oil vial began to infiltrate. An overall temperature average was also calculated.

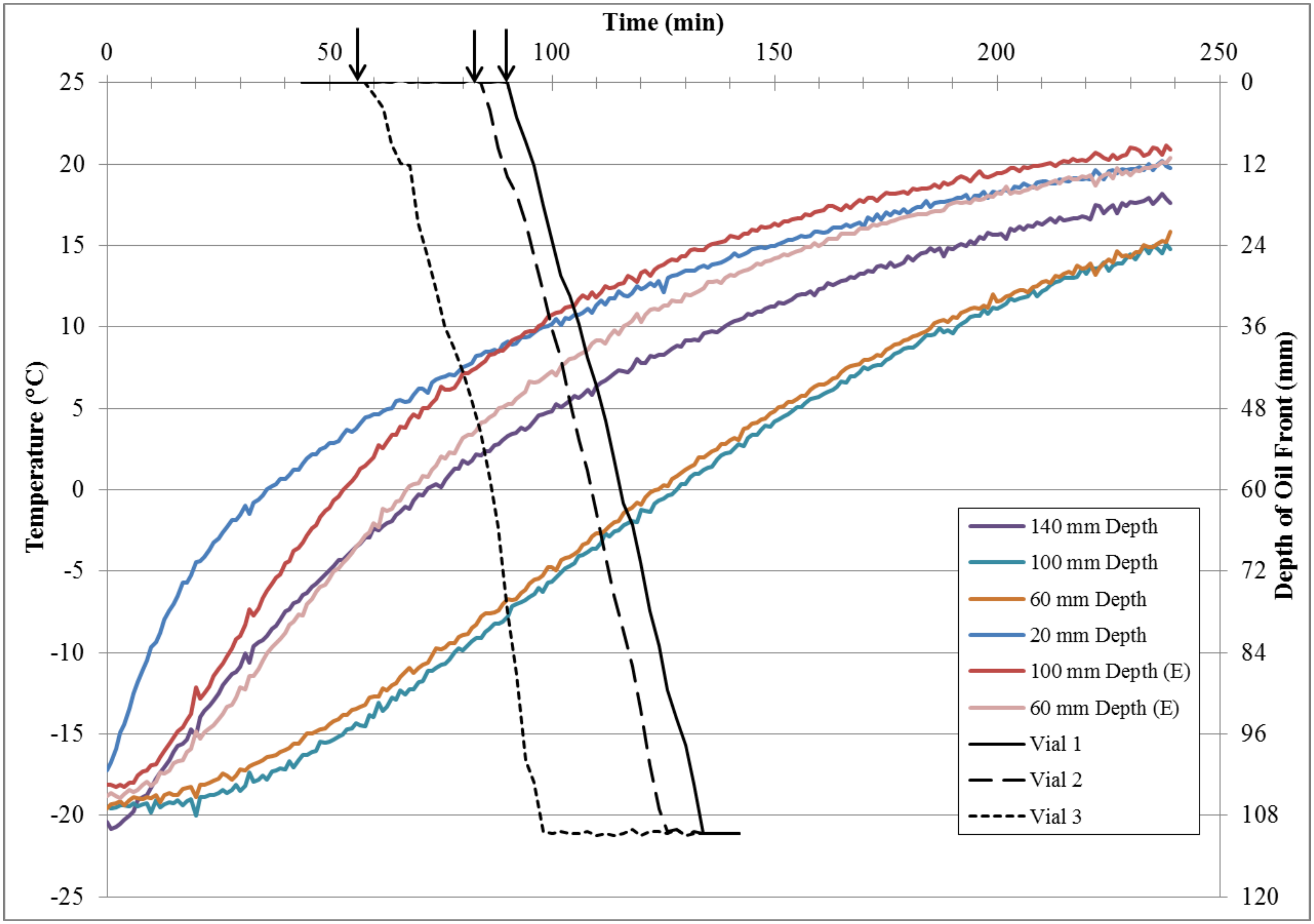

Figure 4-31: Temperature and oil migration for experiment FR-0-20g (arrows show the time at which infiltration begins for each oil vial).

Table 4-5: Temperature at the start of oil infiltration for experiment FR-0-20g.

Temperature at Start of Infiltration (°C)							
Vials	140 mm Depth (1)	100 mm Depth (2)	60 mm Depth (3)	20 mm Depth (4)	100 mm Depth (5)	60 mm Depth (6)	Average
1	3.3	-7.8	-6.7	9.1	8.9	5.3	2.0
2	2.1	-9.1	-7.8	8.3	7.7	4.1	0.9
3	-3.0	-14.5	-13.2	4.5	1.5	-2.8	-4.6
All	0.8	-10.5	-9.2	7.3	6.0	2.2	-0.6

Experiments FR-0-40g and FR-0-60g had the same thermistor layout as experiment FR-0-20g. However the positioning of the vials was different (Figure 4-32 & Figure 4-33). Since the vial layout mirrors the layout from the previous experiment, the effect of temperature on the oil vials was expected to be the same. A graph with the depth of the oil front and the temperature versus time was also created for FR-0-40g and FR-0-60g (Figure 4-34 &Figure 4-35). Table 4-6 & Table 4-7 present the same information presented in Table 4-5, except it presents the temperatures for experiments FR-0-40g and FR-0-60g, respectively.

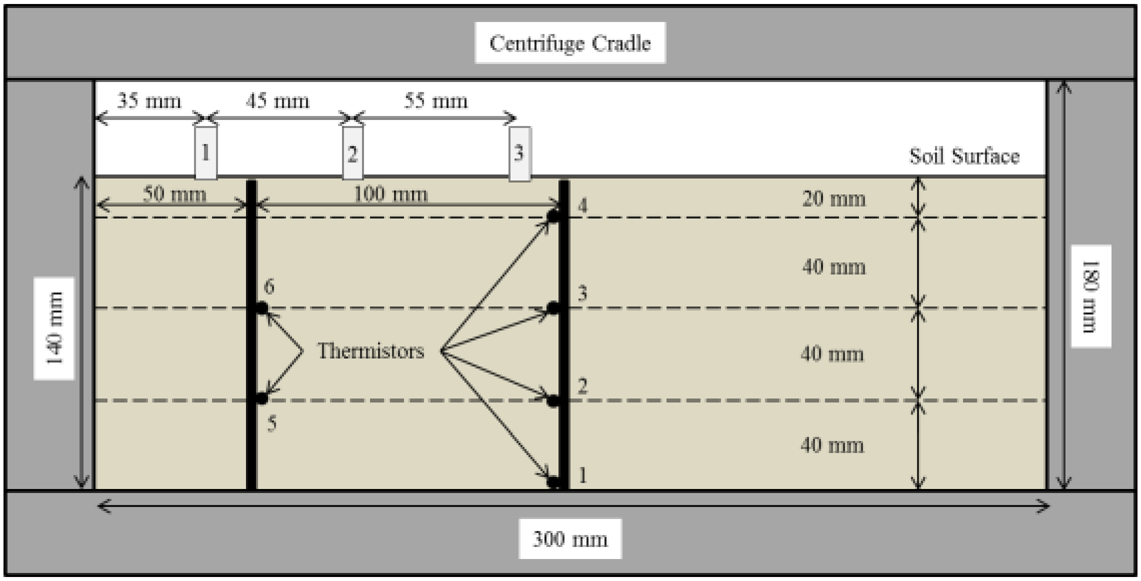

Figure 4-32: Thermistor and vial layout (Front View) for experiments FR-0-40g and FR-0-60g.

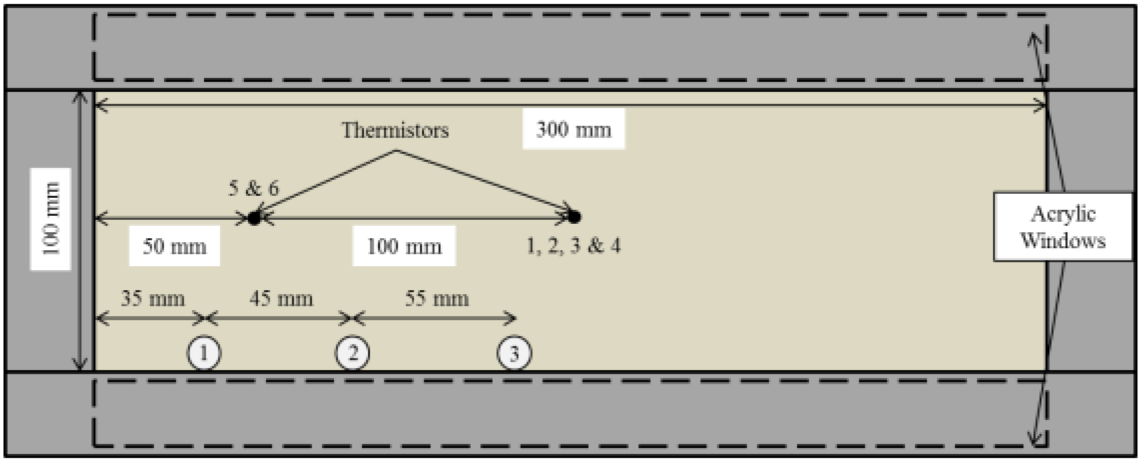

Figure 4-33: Thermistor and vial layout (Top View) for experiments FR-0-40g and FR-0-60g.

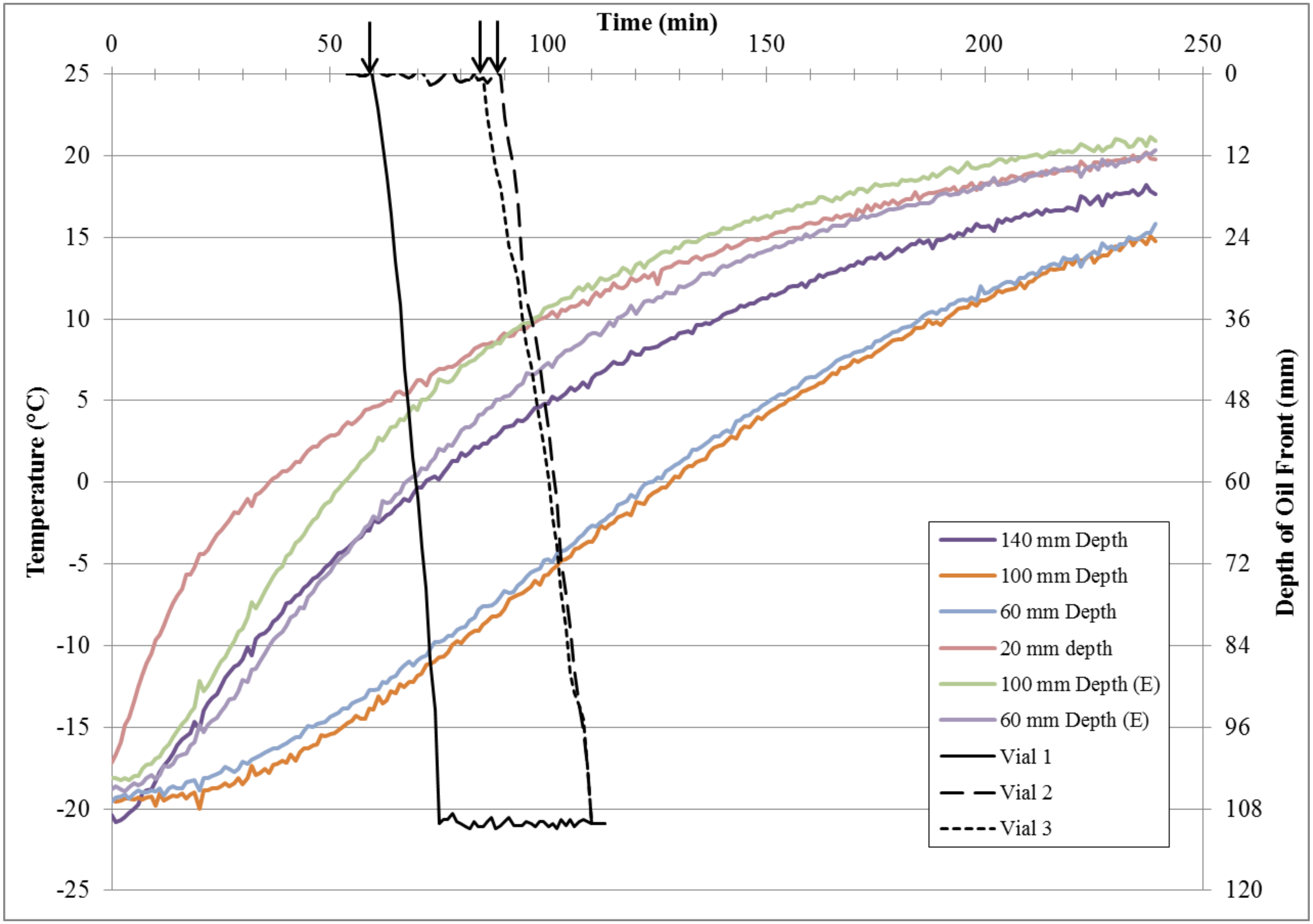

Figure 4-34: Oil migration and temperature for experiment FR-0-40g (arrows show the time at which infiltration begins for each oil vial).

Table 4-6: Temperature at the start of oil infiltration for experiment FR-0-40g.

Temperature at Start of Infiltration (°C)							
Vials	140 mm Depth (1)	100 mm Depth (2)	60 mm Depth (3)	20 mm Depth (4)	100 mm Depth (5)	60 mm Depth (6)	Average
1	-5.5	-15.5	-14.7	2.5	-1.6	-6.0	-6.8
2	0.3	-11.0	-9.8	6.8	5.6	1.5	-1.1
3	1.3	-10.0	-9.4	7.0	6.3	2.2	-0.4
All	-1.3	-12.2	-11.3	5.4	3.4	-0.8	-2.8

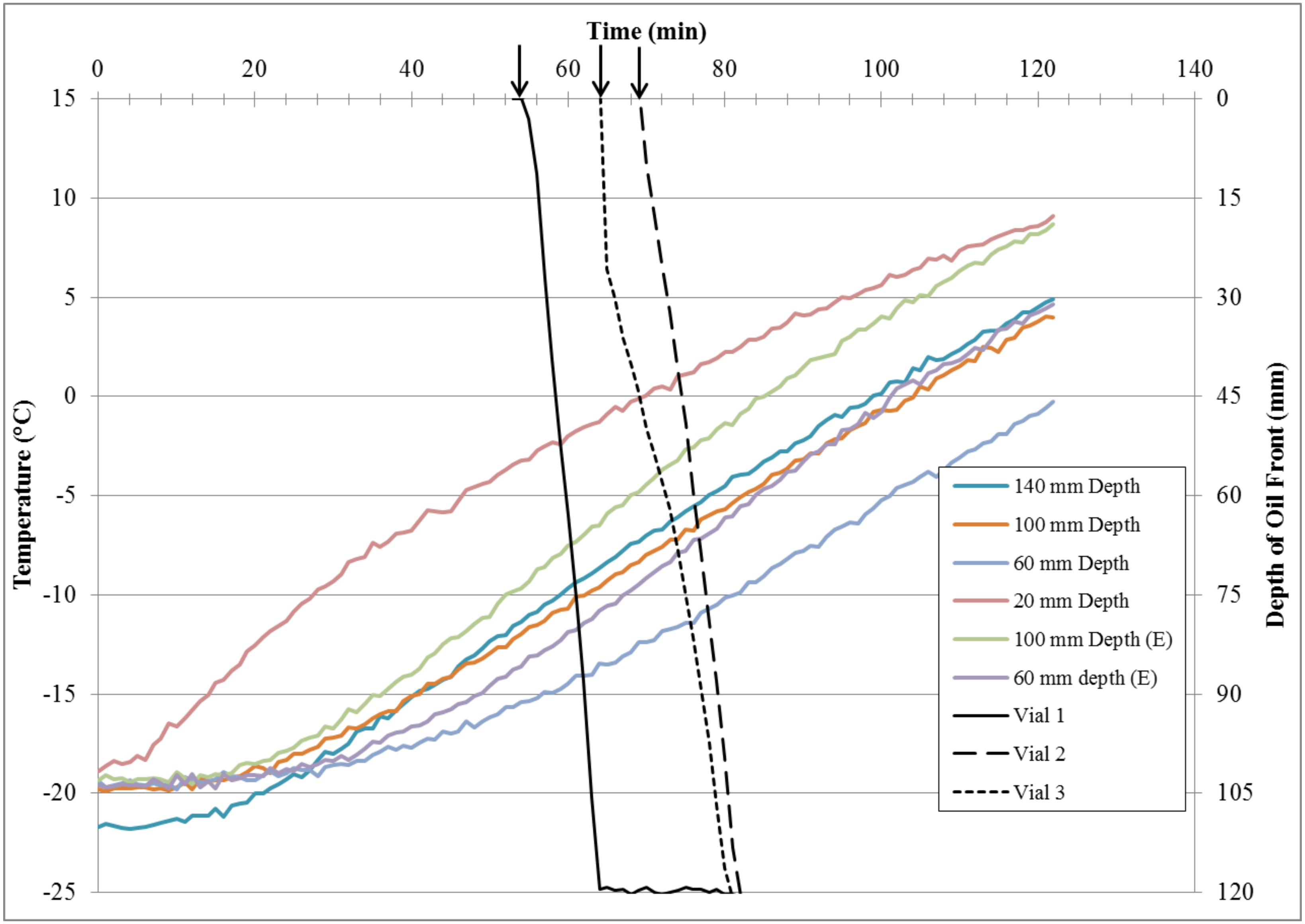

Figure 4-35: Oil wetting front depth and temperature for experiment FR-0-60g (arrows show the time at which infiltration begins for each oil vial).

Table 4-7: Temperature at the start of oil infiltration for experiment FR-0-60g.

Temperature at Start of Infiltration (°C)							
Vials	140 mm Depth (1)	100 mm Depth (2)	60 mm Depth (3)	20 mm Depth (4)	100 mm Depth (5)	60 mm Depth (6)	Average
1	-11.3	-12.0	-15.4	-3.2	-9.7	-13.6	-10.9
2	-8.7	-9.6	-13.4	-1.3	-6.5	-10.8	-8.4
3	-7.3	-8.3	-12.4	-0.1	-4.8	-9.5	-7.1
All	-9.1	-10.0	-13.7	-1.5	-7.0	-11.3	-8.8

The temperature at which infiltration started was lower for each subsequent increase in the acceleration ratio. The overall average temperature at which oil infiltration started was -0.6, -2.8 and -8.8°C for the initially frozen experiments at acceleration ratios of 20, 40 and 60g, respectively. Regardless of this, the increase in the wetting front velocity with increasing acceleration ratio was still linear, just as it was for the unfrozen experiments (Figure 4-36). The rate at which the wetting front velocity increased with increasing acceleration ratio was reduced for the initially frozen experiments compared to the room temperature experiments, as was shown in Table 4-4. It is also interesting to note that the trend line of the average wetting front velocity versus acceleration ratio intersects the x-axis at an acceleration ratio of 5.5. The cause of this will be explained below.

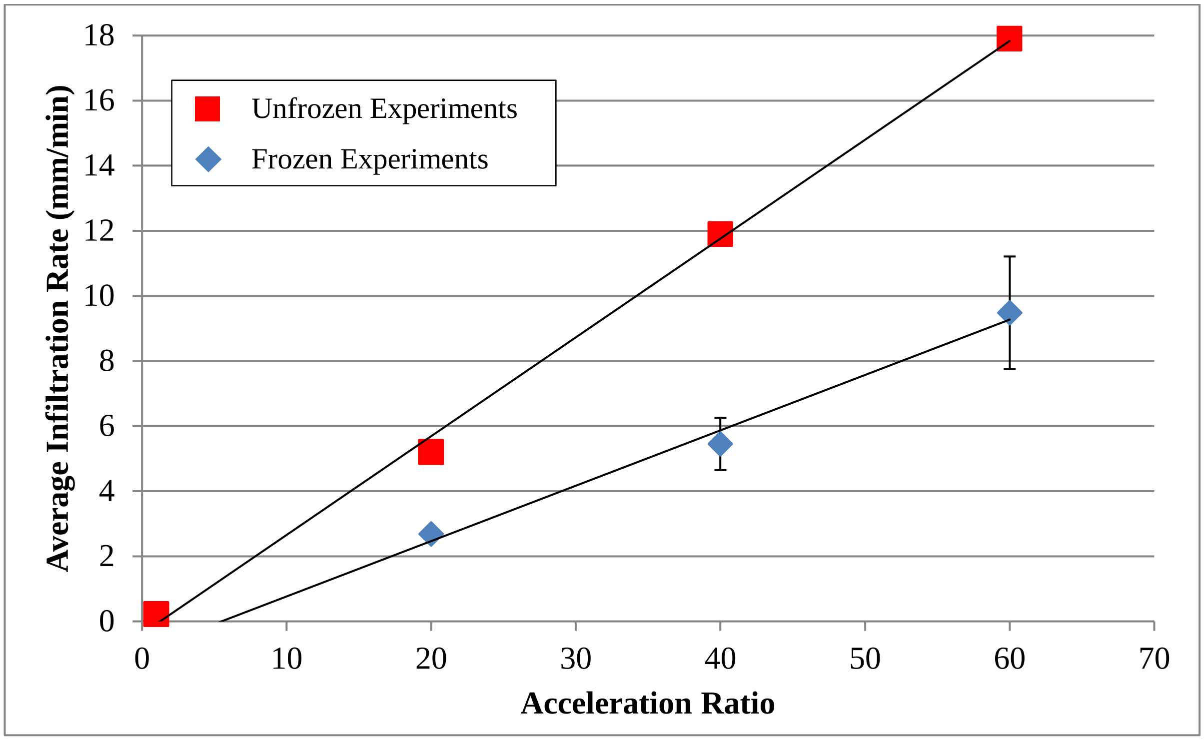

Figure 4-36: Wetting front velocity versus acceleration ratio for unfrozen and frozen dry sand experiments (error bars show standard error).

Since the temperature of the soil did not seem to have a proportional impact on the wetting front velocity of the oil, another factor must be causing the reduction of the wetting front velocity in the frozen soil. As was calculated as part of the characterization of the pumpkin seed oil in Appendix C, the surface tension of the oil did see variations with changing temperature. It was possible that the increased surface tension at lower temperatures could be causing the reduction of the wetting front velocity. The relationship between the surface tension of the oil and the wetting front velocity reduction seems to be inversely proportional. When the surface tension is slightly more than doubled (0.019 N/m to 0.042 N/m), there is an average decrease of 49.6% of the wetting front velocity between room temperature and frozen experiments. Further experiments are required to determine the exact relationship between surface tension and the decrease of the wetting front velocity since the surface tension for the oil was only calculated at two different temperatures. If the surface tension of the oil was the factor leading to a decrease in the wetting front velocity, it means that the temperature of the oil would have an effect on the wetting front velocity. Since the temperature of the oil was not recorded during the experiments, it is not possible to determine the surface tension of the oil while it was infiltrating the soil. It is also important to note that the entry pressure of the pumpkin seed oil into the #730 silica sand will change based on the temperature of the oil. However, the pressure caused by the height of the oil will increase with increasing acceleration ratio. To calculate the pressure at the oil-soil interface, Equation 21 as used (Fetter 2008).

$$P = \rho g h \; [21]$$

Where:

P = Pressure (Pa)
ρ = Density of the fluid (kg/m^3)
g = Gravitational acceleration (m/s^2)
h = Height of the fluid (m)

Since the gravitational acceleration will be increased in the centrifuge, the pressure caused by the height of the oil in the vial will also increase. This can counter-act the increased surface tension of the oil at lower temperatures and help maintain the linear increase of the wetting front velocity with increasing acceleration ratio, even when the temperature of the soil is colder. Table 4-8 shows the pressure caused by the height of the pumpkin seed oil in the vial at 20, 40 and 60g. By determining the surface tension of the oil at lower temperatures, it would be possible to determine the entry pressure of the oil at lower temperatures. As it was presented in Chapter 2, the entry pressure of a given fluid is dependent on its surface tension. The increased surface tension at lower temperatures can explain why the trend line of the wetting front velocity versus acceleration intersects the x-axis at 5.5. It shows that at freezing temperatures, the pumpkin seed oil’s surface tension would be higher, thus increasing the entry pressure into the soil. This means that under freezing conditions no infiltration would occur unless the forces of gravity would be 5.5 times higher than normal. This shows that in freezing conditions, contaminants could be perched above soil lenses where in temperate regions, the contaminant would be able to infiltrate through a soil lens of the same soil type.

Table 4-8: Pressure caused by height of oil at different acceleration ratios.

Variable	20g	40g	60g
ρ (kg/m^3)	910	910	910
g (m/s^2)	196.2	392.4	588.6
h (m)	0.05	0.05	0.05
P (kPa)	8.9	17.9	26.8

4.4.2 Frozen Wet Sand Experiments

Experiments FR-10-20g-01 and FR-10-20g-02 were conducted to verify the effectiveness of insulation at the bottom of the cradle. The experiments were also used to verify the effects of having moisture content in the soil while having soil that was frozen. Both the experiments mentioned above had an initial moisture content of 9.5%. The cradles, with the wet sand added and compacted, were frozen overnight prior to conducting the experiment. The two experiments had average wetting front velocities of 1.5 mm/min (Figure 4-37) and 1.3 mm/min (Figure 4-38). When compared to the average wetting front velocity of 2.7 mm/min of the initially frozen dry sand experiment, the wetting front velocity reduction observed was 44 and 52%. In Section 4.3, it was shown that the effect of a moisture content of approximately 10% at room temperature reduced the wetting front velocity by 20%. Thus, the presence of moisture within the soil had a more pronounced effect on the wetting front velocity when the soil was frozen. It was also mentioned previously that while the centrifuge is running, the centrifugal forces brought some moisture to the bottom of the cradle. When the soil was still frozen, the ice within the soil was subject to the same forces, but remained immobile because it was frozen within the soil. Because of that, the presence of ice within the soil reduced the wetting front velocity of the oil even more than at room temperature, as it was observed for experiments FR-10-20g-01 and FR-10-20g-02.

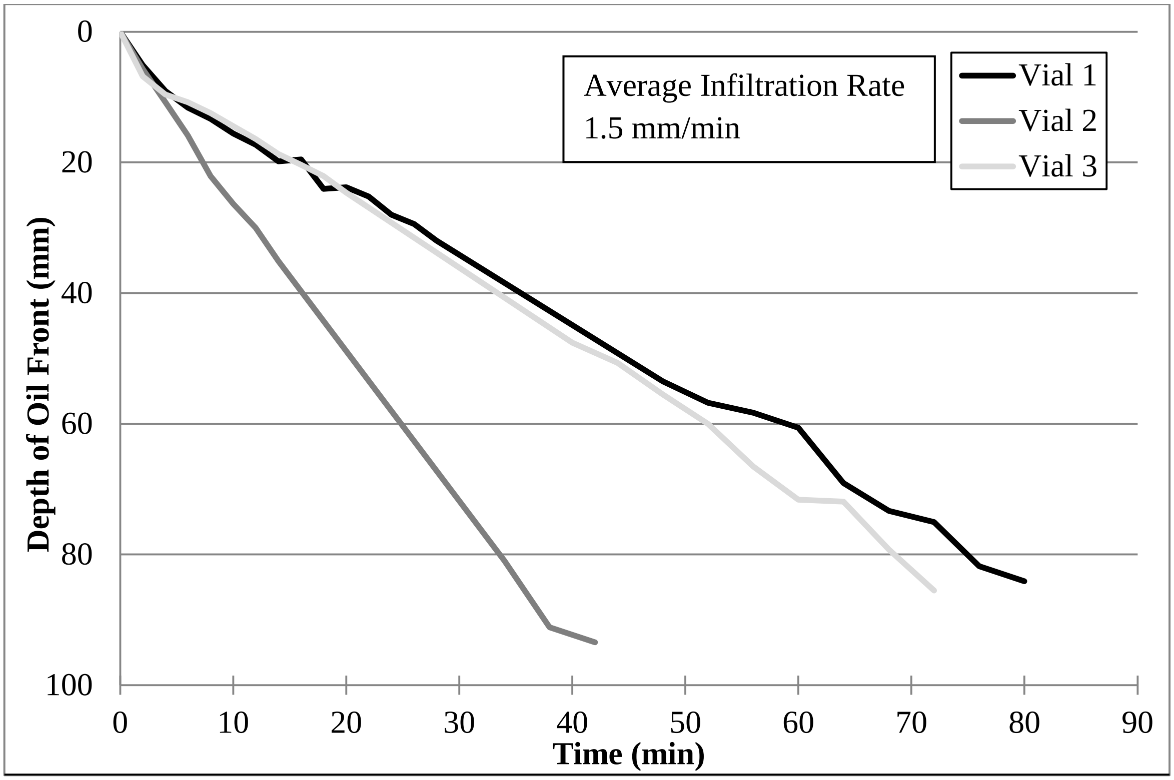

Figure 4-37: Oil migration through initially frozen 10% moisture content sand at 20g (FR-10-20g-01).

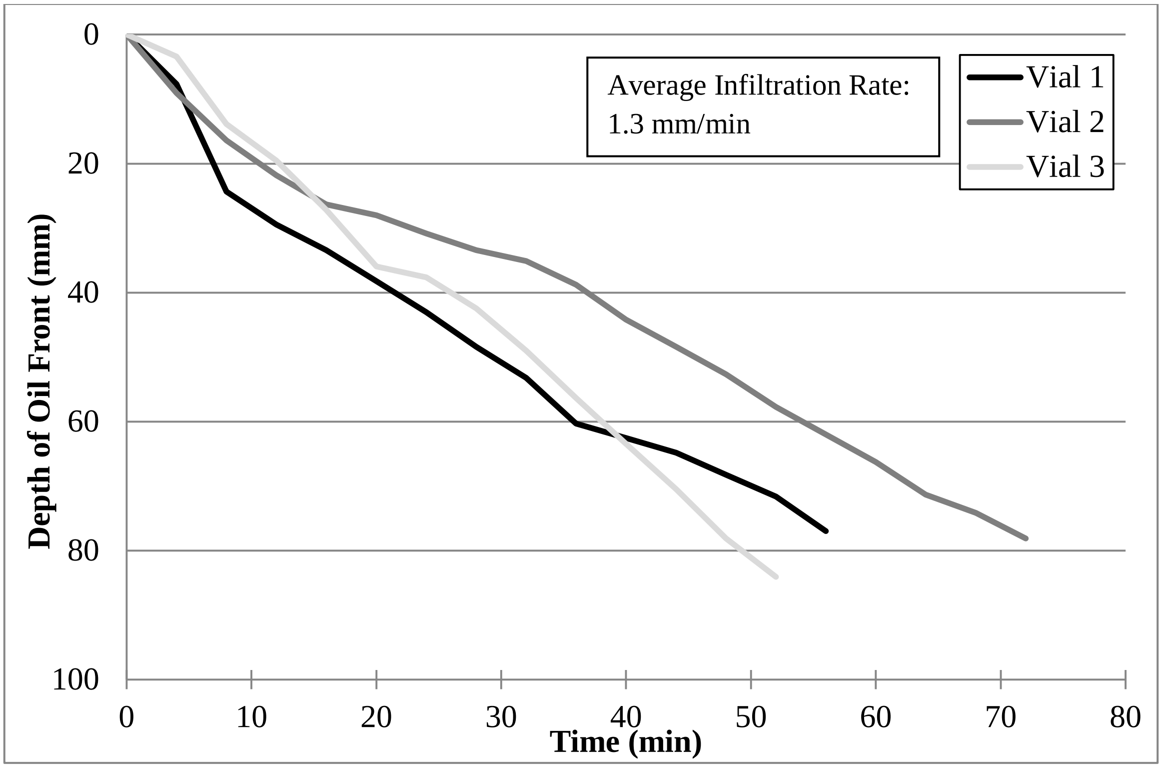

Figure 4-38: Oil migration through initially frozen 10% moisture content sand at 20g (FR-10-20g-02).

Experiment FR-18-20g was conducted in order to observe the effects of having frozen saturated soil on the wetting front velocity of oil. The soil for this experiment had a moisture content of 18% and was frozen overnight in the cradle before running it in the centrifuge. It was noticed that oil was seeping along the acrylic window before the migration of the oil began (Figure 4-39). This shows that the oil had melted enough to begin infiltration but was being blocked by the frozen saturated sand. This behaviour of blocking the infiltration of oil by advection resembled the behaviour observed during experiment UN-17-20g-01 where the saturated sand would not allow for the infiltration of the oil. The frozen soil did not settle as the room temperature soil did when subject to the centrifugal forces in the centrifuge. Because of this, small paths along the window/soil interface were present through which the oil could move. After the majority of the soil reached 0°C, infiltration through the soil started because the cradle was leaking water, similarly to experiment UN-17-20g-02. The average wetting front velocity of the oil from the three vials was calculated to be 0.7 mm/min. The reduction of the wetting front velocity compared to the frozen dry sand experiment was 74%. The reduction was slightly more pronounced in the frozen experiment (74%) compared to the reduction with the room temperature experiments (63%) as presented in Section 4.3 (Figure 4-41).

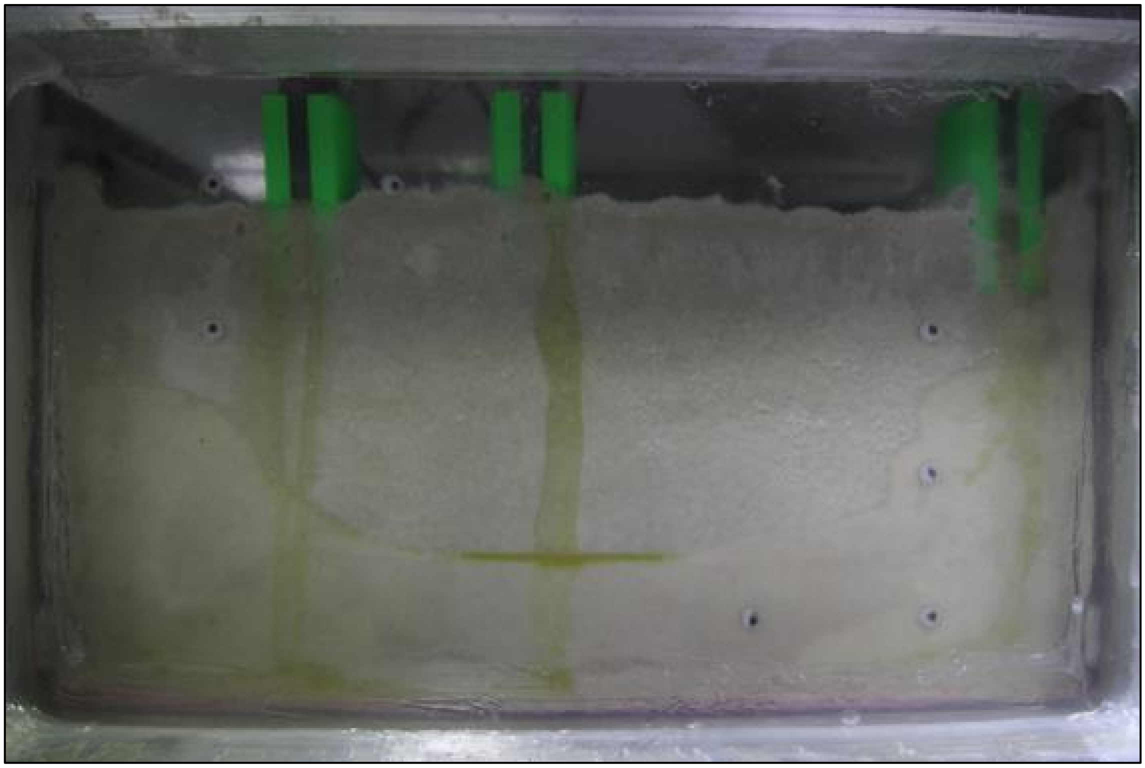

Figure 4-39: Oil seeping along acrylic window during experiment FR-18-20g.

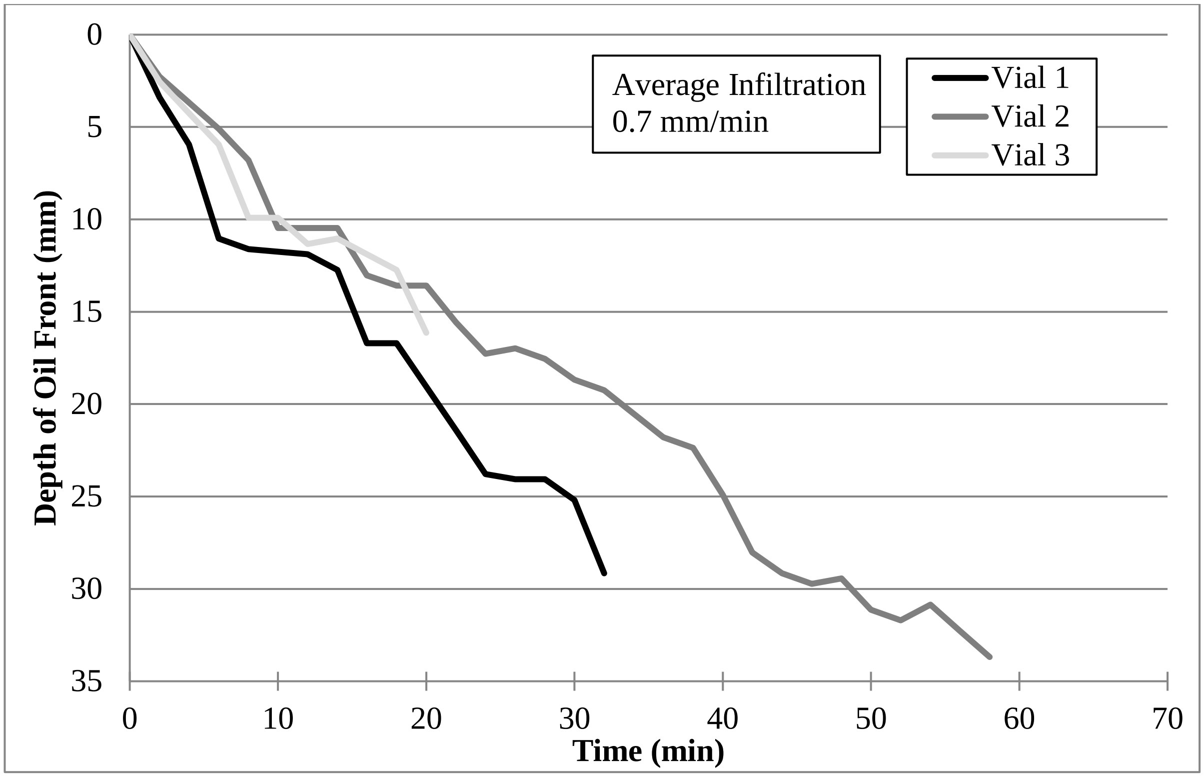

Figure 4-40: Oil wetting front velocity through initially frozen 18% moisture content sand at 20g (FR-18-20g).

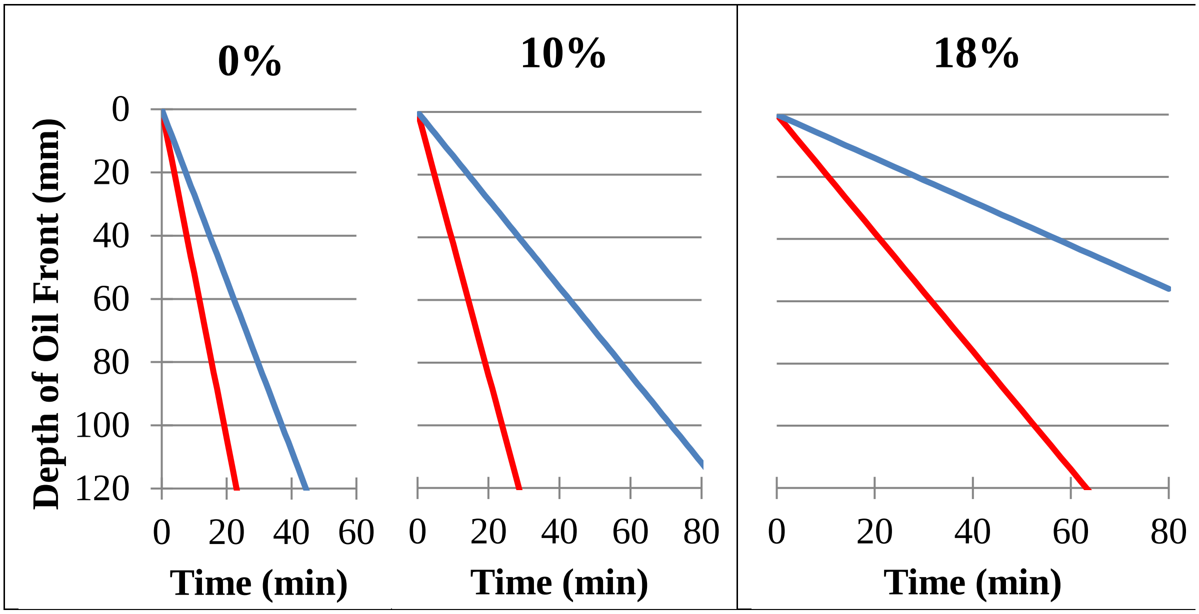

Figure 4-41: Migration difference between unfrozen (red) and frozen (blue) at different acceleration ratios with wet sand.

Experiment FRV-9-20g was the only one presented in this thesis that used vortex tubes while the cradle was in flight. Two vortex tubes provided cold air to the soil within the cradle. The first vortex tube had an airflow of 6.3 CFM (2.97×10^{-3} m^3/s) with an exit air temperature of -6.0°C. The second vortex tube had an airflow of 6.6 CFM ($2.97\text{x}10^{-3}$ m^3/s) with an exit air temperature of -6.8°C. The vortex tubes did not seem to have a significant impact on the time it took to reach temperature above freezing (Figure 4-42). It took approximately 1h20 for the first thermistor (the one at the bottom of the cradle) to register temperature above freezing. This is similar to the previous experiments with 10% moisture content that did not use the vortex tubes. The vortex tubes did help maintain freezing temperatures throughout the sand for a longer period. It took nearly 4 hours for all thermistors to be recording temperatures above freezing. When vortex tubes were not used, it took approximately 2.5 hours. Towards the end of the experiment, it seemed like the temperature of the air above the soil was stabilizing at around 10°C. The wetting front velocity of the oil occurred while most of the soil was still frozen (Figure 4-43). Compared to the other experiments with a water content near 10% and initially frozen soil, it took longer for the oil to start infiltrating in the experiment with the vortex tubes. It took approximately 2h for the oil to start infiltrating in the vortex tube experiment compared to approximately 1h for the experiments without vortex tubes. The delay in the infiltration seems to be caused by the vortex tubes blowing cold air on the oil vials and keeping them frozen for longer. It was noticed that when moisture is added to the sand, the latent heat effect from the transition between solid and liquid water is observable. For the vortex tube experiment, it took between approximately 30 minutes and three hours for the water to transition from solid to liquid.

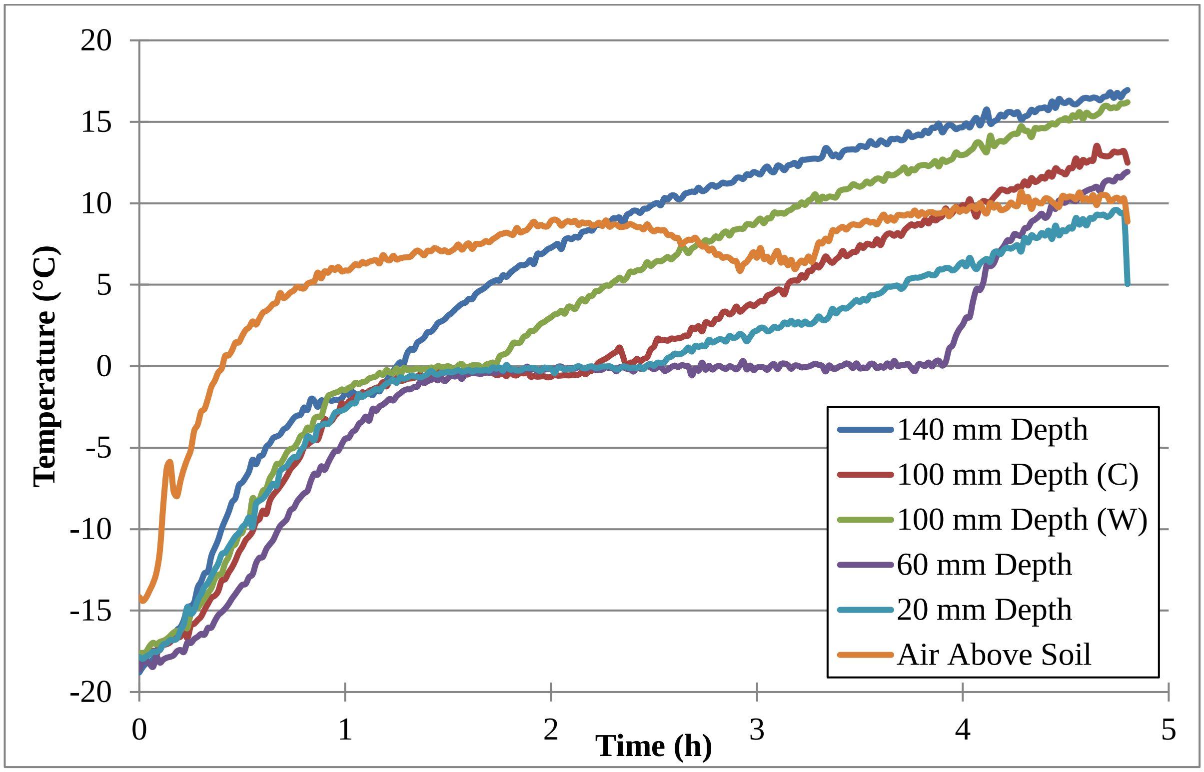

Figure 4-42: Temperature data for experiment FRV-9-20g.

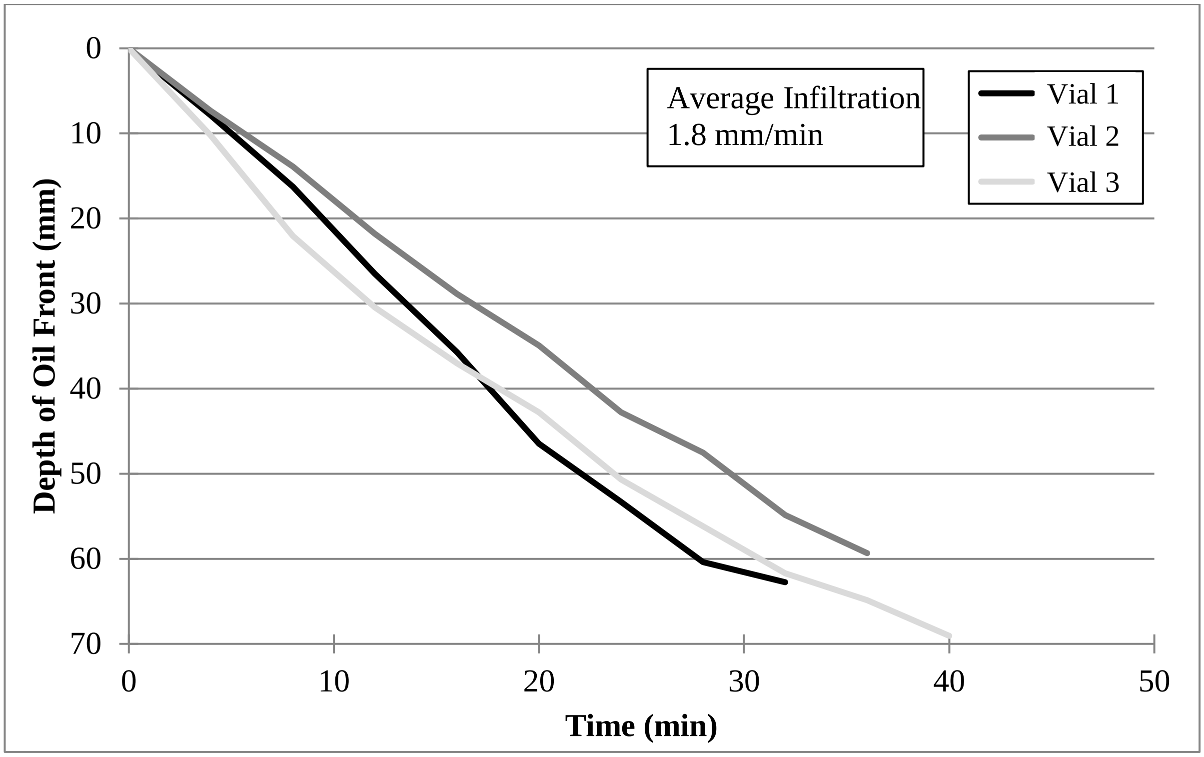

Figure 4-43: Oil migration through initially frozen 10% moisture content sand using vortex tubes (FRV-9-20g).

4.5 Effect of Freeze-Thaw Cycles on Wetting Front Velocity

The effects of moisture content and temperature on the wetting front velocity of pumpkin seed oil through the sand in the centrifuge have been observed and quantified. It is now important to move forward with understanding how the oil will seep through the soil when subject to freeze-thaw cycles. This would represent a more accurate modelling of the migration of petroleum hydrocarbons through frozen soil in the Canadian Arctic. Unfortunately, the development of a freeze-thaw apparatus for the centrifuge cradle was started as part of this research but the apparatus developed could not achieve freezing temperatures. The freeze-thaw apparatus that was developed was capable of cooling the sand to a temperature of 2°C. Improvements to the apparatus would need to be made in order to create freeze-thaw cycles in the centrifuge cradle during flight. Although freeze-thaw cycles were not achieved in the centrifuge, the column experiment apparatus allowed for the freezing and thawing of the soil and the infiltrating oil. An experiment (FR-0/18-1g) was conducted where the whole column was frozen to -17°C overnight prior to adding the oil. The sand was comprised of a saturated layer and a dry sand layer. The dry sand layer was at the top of the column and had a thickness of approximately 90 mm (Figure 4-44a). The rest of the column was filled with saturated sand.

For this experiment, two holes were drilled along the acrylic face. The first one was drilled and filled with oil in the morning, at approximately 09:30 am (Figure 4-44b) while the other was drilled and filled with oil in the afternoon of the same day at approximately 03:30 pm (Figure 4-44c). Both holes were drilled to the saturated layer. 100 ml was added with a syringe to each hole. During that day, the column was being thawed with the top of the column being exposed to heat from a block heater. When the second hole was drilled the thaw front was at the saturated layer. The column was lowered into the freezer to freeze overnight. One thaw cycle that lasted seven hours was done the next day. Figure 4-44d shows the column at the end of that thaw cycle. The column was then lowered back into the freezer for 2.5 days.

While the column was kept frozen for 2.5 days, there was minimal movement of the oil through the soil as can be seen between Figure 4-44d and Figure 4-44e. The oil was prevented from infiltrating by the saturated sand layer. A common assumption is that saturated frozen soil will act as an impermeable barrier to the migration of contaminants (Biggar et al. 1998a).

A thaw cycle was then started to observe if the oil would be mobilized by the thaw front. The column was thawed for 49h48min and the thaw front reached a depth of approximately 180 mm. It was observed that the thaw front did indeed cause the oil to mobilize. Interestingly the infiltrating oil front mirrored that of the thaw front. Figure 4-44f shows the final image of the experiment with the oil that migrated nearly 100 mm into the saturated layer. This experiment demonstrated that petroleum hydrocarbons could infiltrate through saturated frozen soil under certain conditions. At room temperature, it was expected that the oil would simply float above the water table and diffuse into the water. However, when freeze-thaw cycles were introduced, it allowed the oil to infiltrate into the water table. More research would be required to determine the microscale factors that allow for the oil to infiltrate into the saturated sand layer. However, it was possible that when the ice within the saturated layer thawed, it created temporary gaps within the pore spaces that could then be filled with either more water or whatever contaminant may be present above the water table.

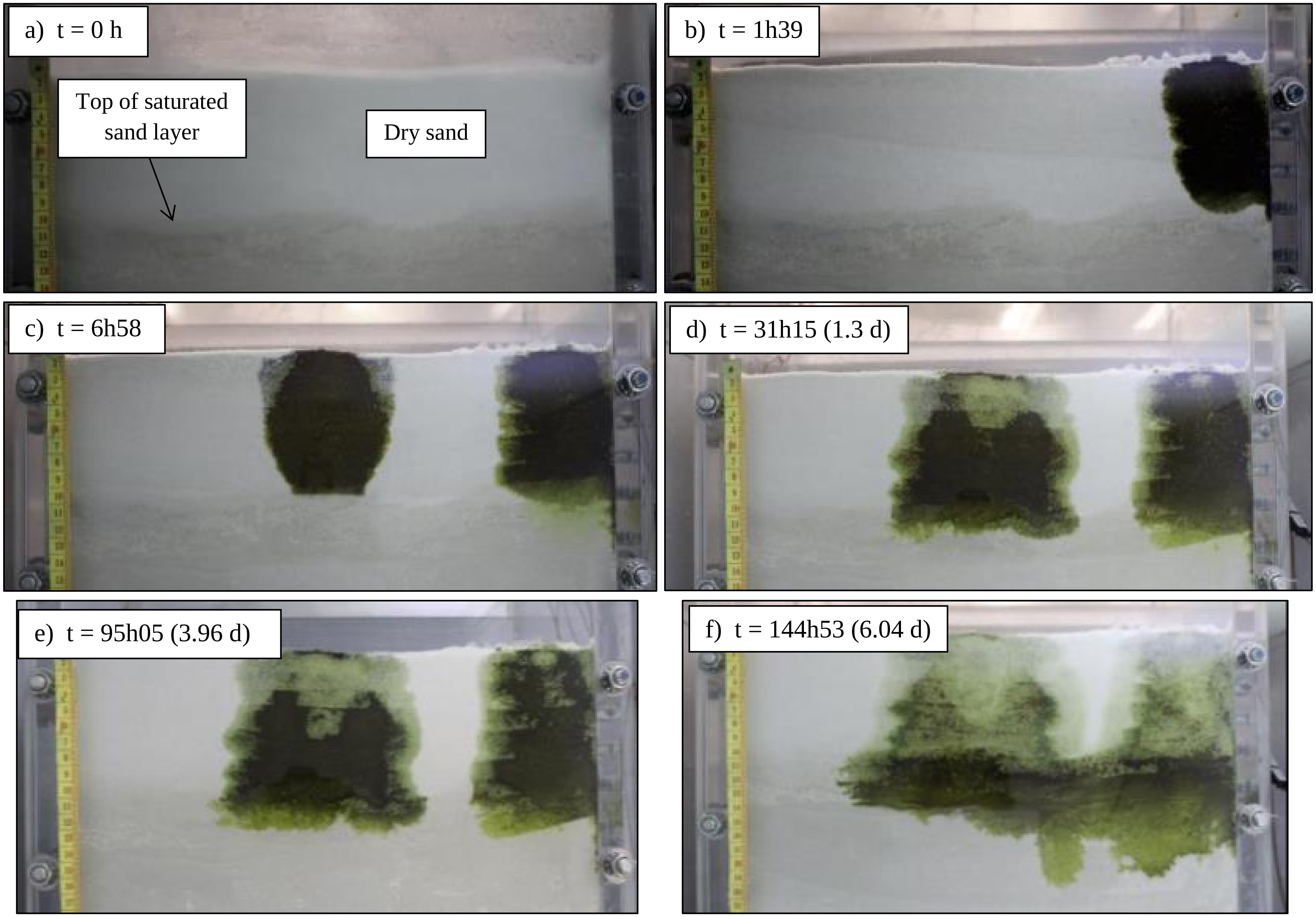

Figure 4-44: Migration of oil during experiment FR-0/18-1g.

4.6 Oil Migration through Arctic Soil

Soil samples were collected from several sites on Ellesmere Island where abandoned fuel barrels are located. An experiment (FRWB-8-20g) was conducted using sand from Wrangle Bay, Nunavut. Since only approximately 1 kg was sampled from this site, a mold was 3D printed in order to conduct an experiment with the limited amount of soil. The mold created a small column against the middle of the acrylic window (Figure 4-45 & Figure 4-46). The space around the mold was backfilled with sand (Figure 4-47). The soil from Wrangle Bay was mixed to an initial moisture content of 8.1%. This was similar to the moisture content of the soil when it was sampled in Wrangle Bay as shown in Appendix B. This experiment was conducted in order to demonstrate that soil collected from contaminated sites could be used in a centrifuge experiment. The results of the experiment could be used to determine the wetting front velocity of the contaminants found at the site. The soil from Wrangle Bay was significantly darker (Figure 4-48) than the sand that had been used for all the other centrifuge experiments. Nonetheless, migrating oil was still visible during the experiment.

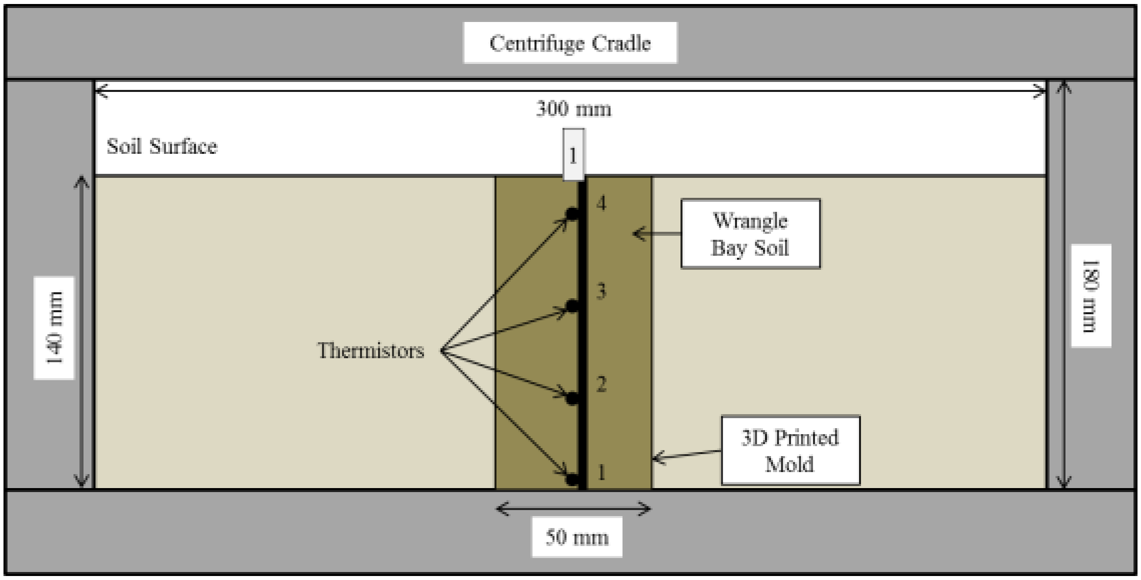

Figure 4-45: Experiment layout with soil from Wrangle Bay (Front View).

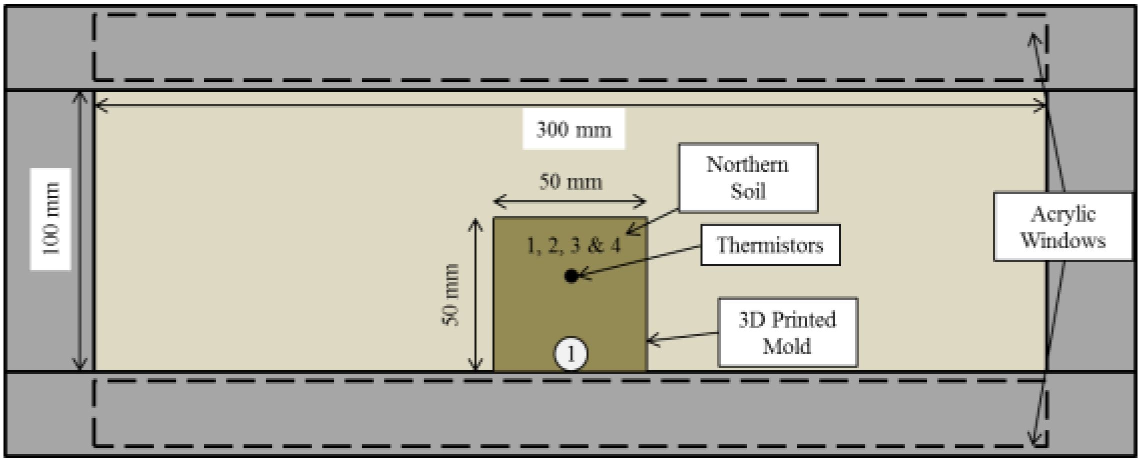

Figure 4-46: Experiment layout with soil from Wrangle Bay (Top View).

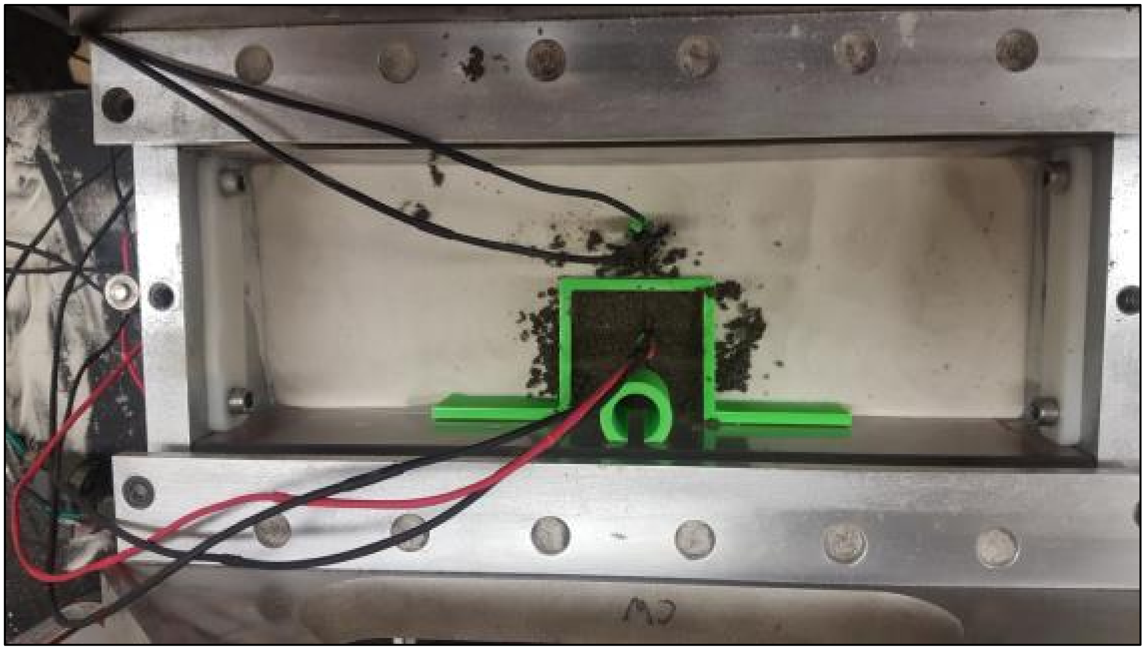

Figure 4-47: Overhead view of the cradle with the soil from Wrangle Bay.

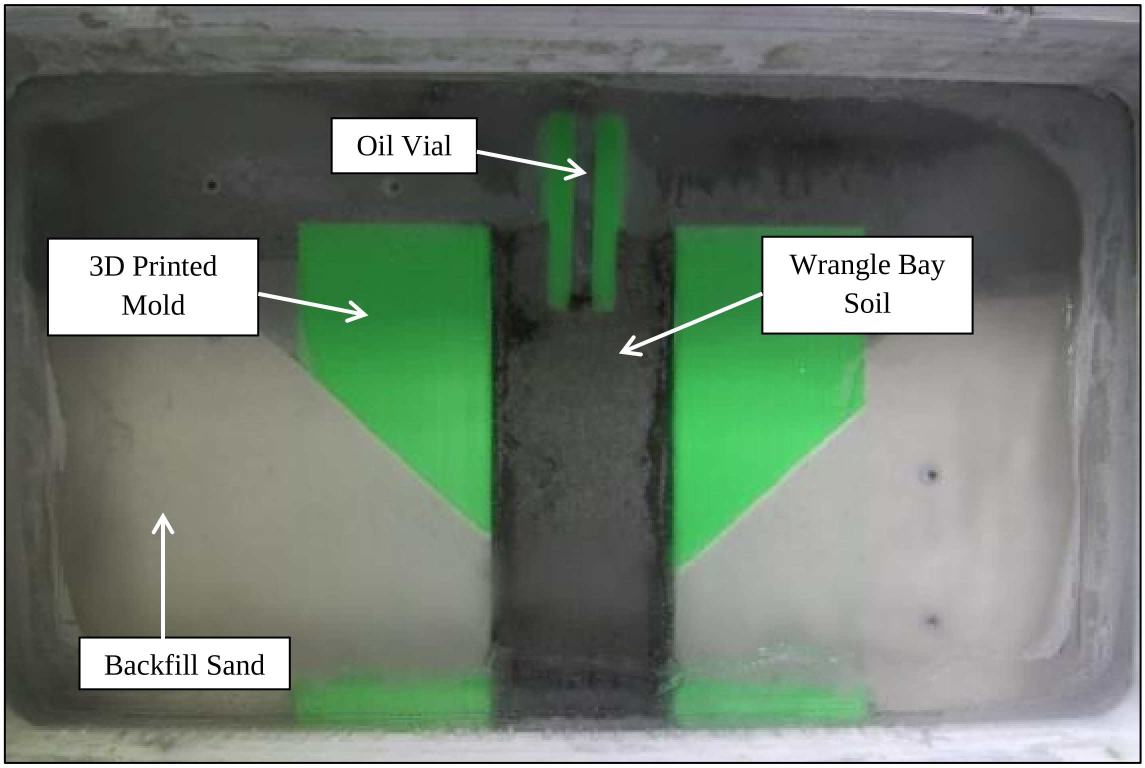

Figure 4-48: First image taken as part of experiment FRWB-8-20g.

While the centrifuge experiments using sand had a distinct oil front, the same was not the case for the experiment with the soil from Wrangle Bay. The oil took multiple paths to seep through the soil (Figure 4-49). Because of this, an average wetting front velocity of the multiple migration paths was calculated (Figure 4-50). The average wetting front velocity was calculated to be 2.4 mm/min. When the wetting front velocity was scaled back to 1g, the wetting front velocity was 0.12 mm/min or 2.0x10^{-4} cm/s. That would be the wetting front velocity of a contaminant with similar properties to pumpkin seed oil at Wrangle Bay under thawing conditions. It is important to note that this soil was collected from the active layer, which means that migration through thawing permafrost would most likely occur at a different rate. That is due to the typical difference in composition and moisture content between the active layer and permafrost. Like the first three centrifuge experiments with dry sand, the wetting front velocity of the oil did not surpass the hydraulic conductivity of the soil. The hydraulic conductivity of the soil from Wrangle Bay was 2.60x10^{-3} cm/s or 1.56 mm/min. At an acceleration ratio of 20g, the hydraulic conductivity was 31.2 mm/min. This was significantly higher than the wetting front velocity, which was calculated to be 2.4 mm/min. Similarly, to the sand, the soil from Wrangle Bay recorded the first thawing after approximately one hour in the centrifuge, although no insulation was used for this experiment. The insulation wasn't used to reduce the risk of water seeping into the sand between the 3D printed mold and the insulation. The infiltration of the oil started after 1h25. The Wrangle Bay soil thawed at a similar rate to the sand that was used to backfill the 3D printed mold (Figure 4-51).

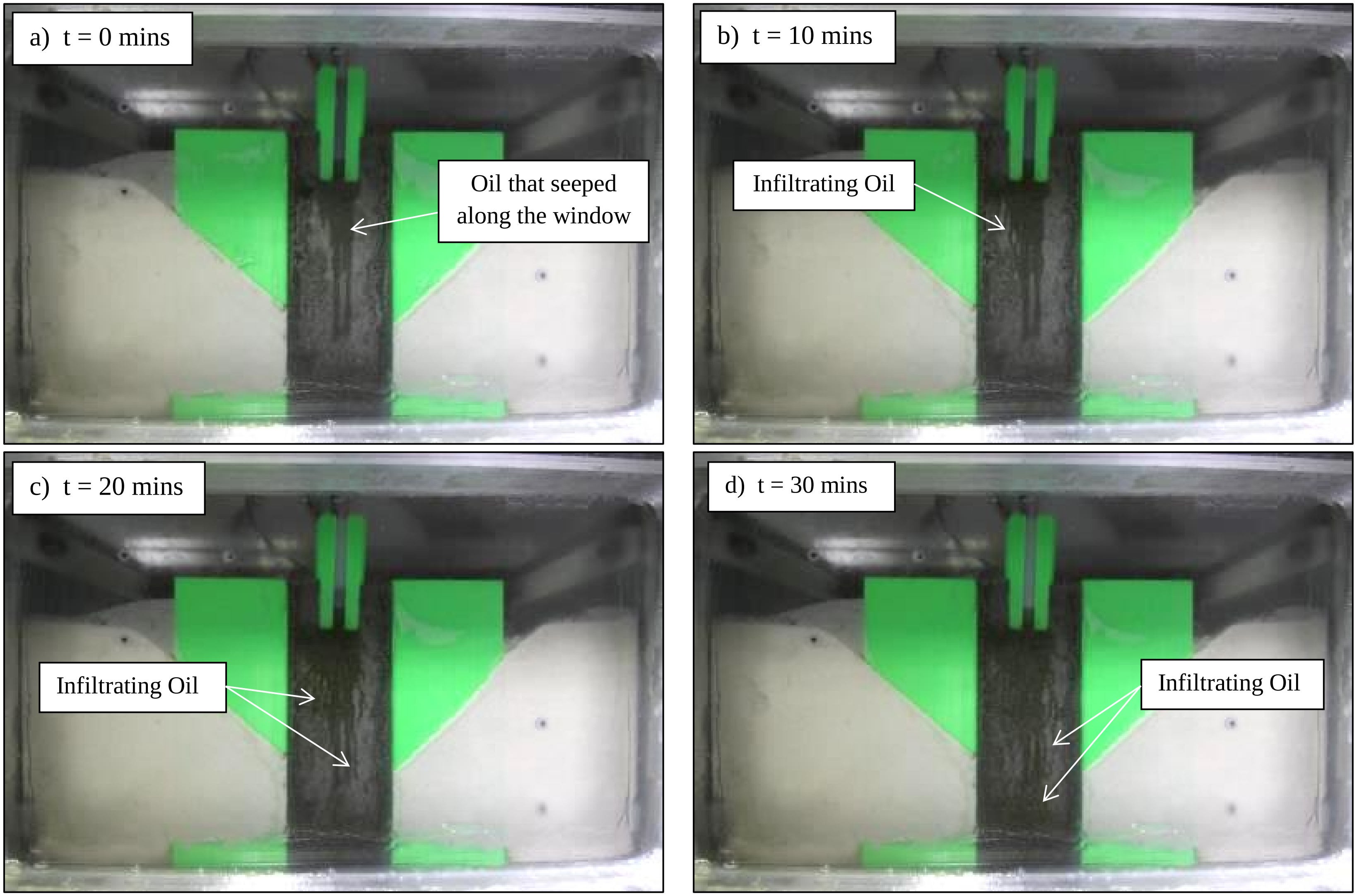

Figure 4-49: Migration of oil through Wrangle Bay soil during experiment FRWB-8-20g.

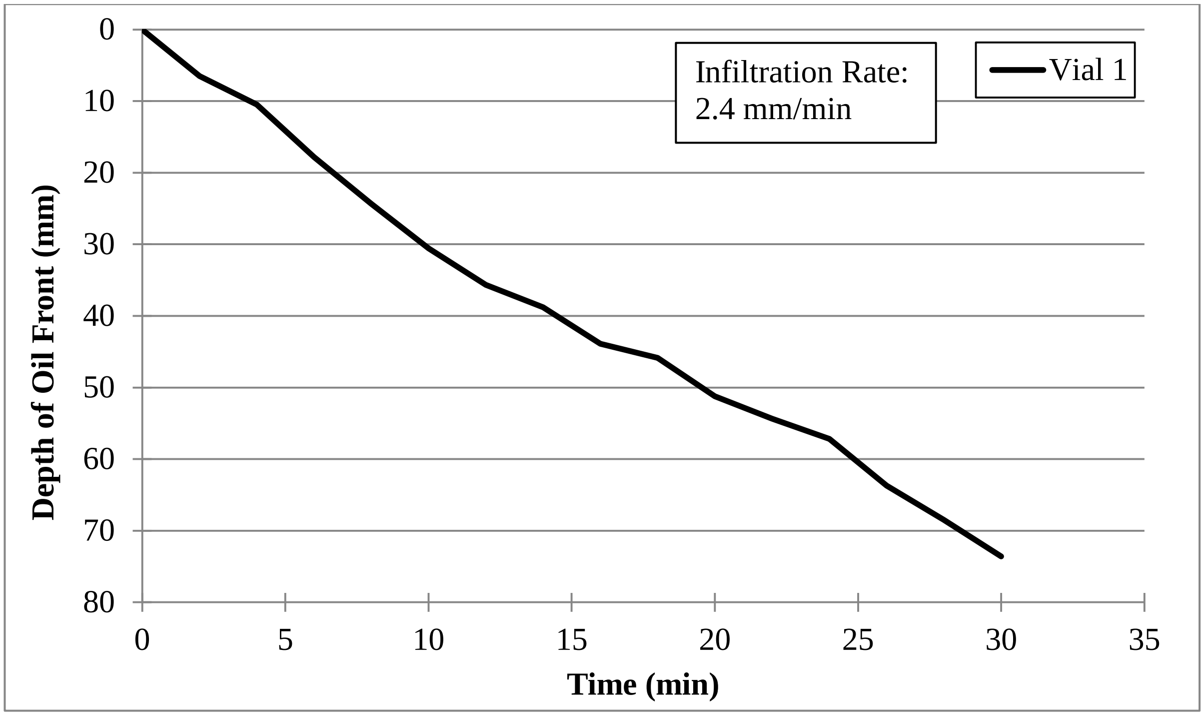

Figure 4-50: Oil migration through initially frozen soil from Wrangle Bay (FRWB-8-20g).

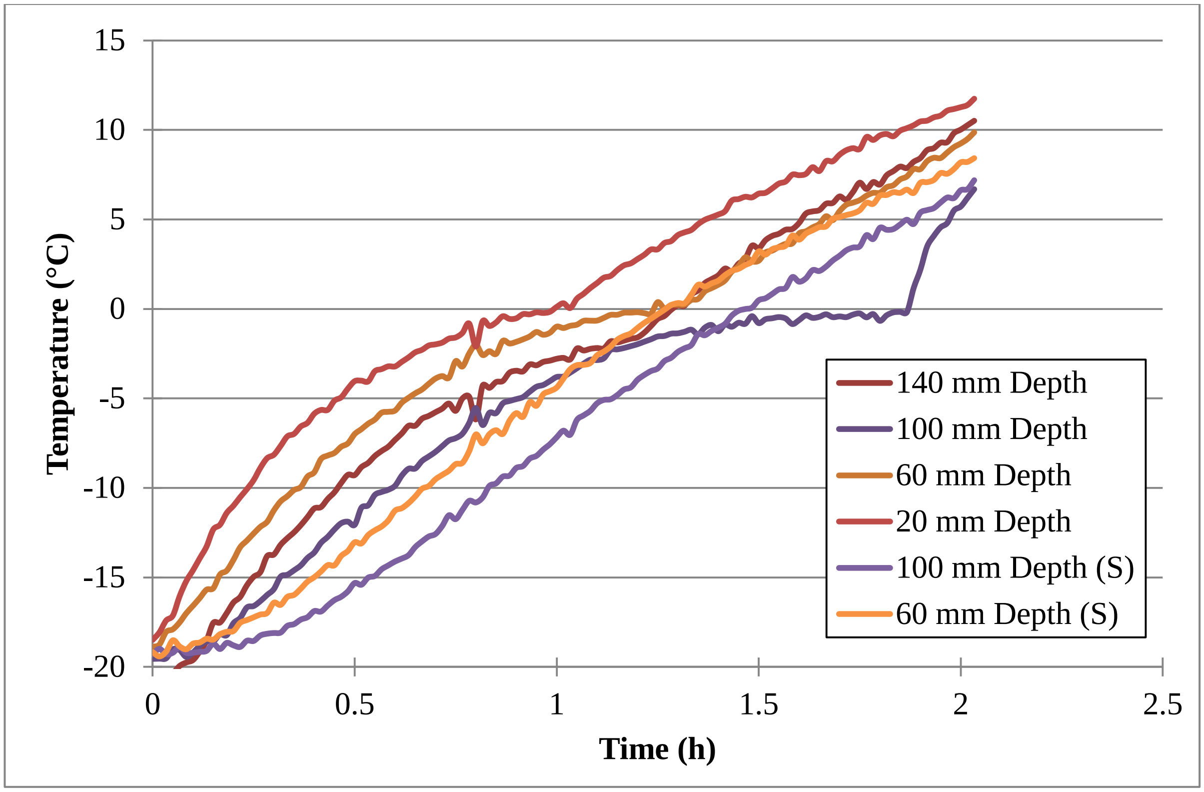

Figure 4-51: Temperature data for experiment FRWB-8-20g.

The wetting front velocity of the oil during experiment FRWB-8-20g was higher than the average wetting front velocity for the similar experiments (FR-10-20g-01 & FR-10-20g-02) using initially frozen sand and with a moisture content at 10% (Figure 4-52). The experiment using the soil from Wrangle Bay had a slightly lower moisture content (8% versus 10%), which could partially explain why the migration was faster. For the Wrangle Bay soil experiment, the infiltration of the oil started after 1h26, when the average soil temperature was 2.3°C. For the two experiments using frozen sand at 10% moisture content, the average soil temperature when the oil started to infiltrate was -3.2°C and 1°C. The lower temperatures, especially around freezing temperatures, could mean that more moisture within the sand was still frozen. This could also explain why the wetting front velocity was higher for the Wrangle Bay soil Experiment. Some other factors, such as the microscale interaction between the oil and the soil particles, could be affecting the wetting front velocity. Future research to determine how the soil properties affect the wetting front velocity of various contaminants would be beneficial.

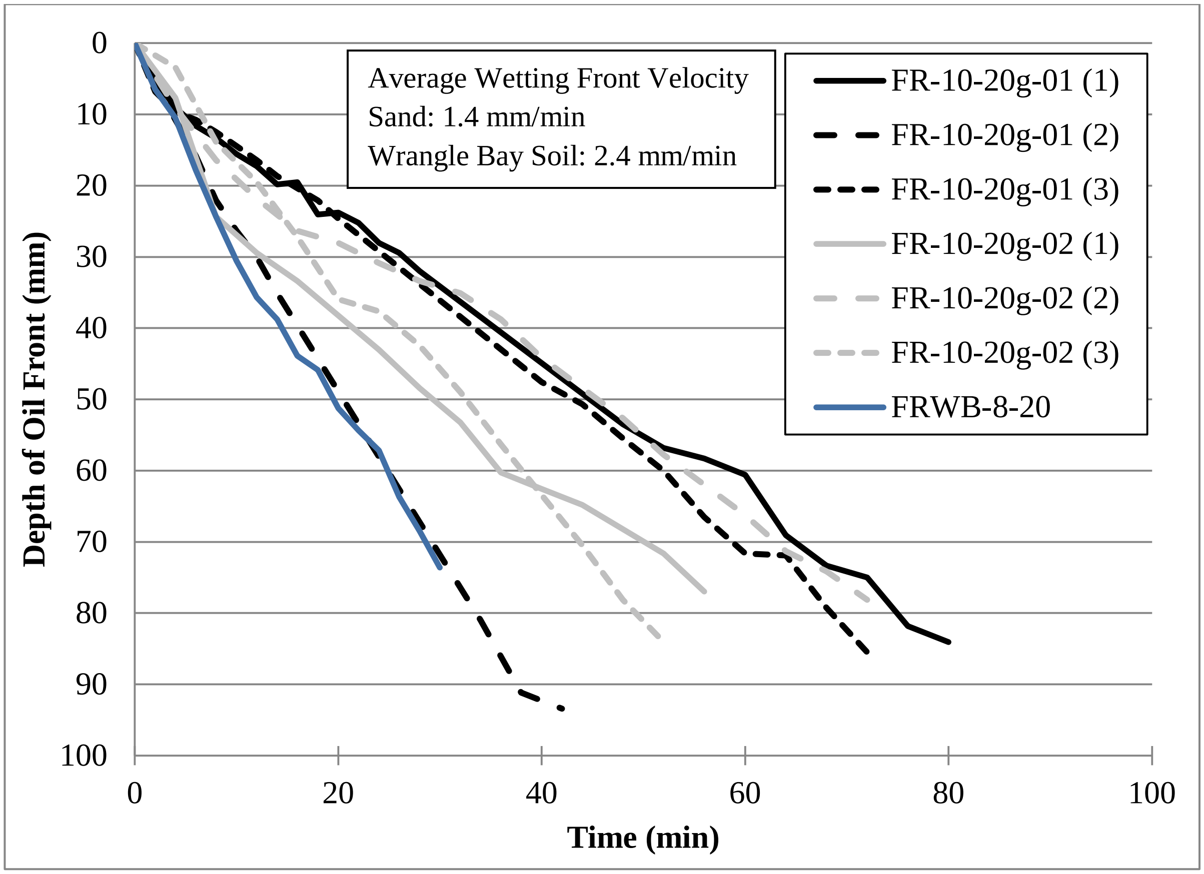

Figure 4-52: Migration comparison between experiments FR-10-20g-01, FR-10-20g-02 and FRWB-8-20g.

4.7 Outcomes and Findings

Several centrifuge experiments were presented in this chapter along with three column experiments. The experiments were conducted using different moisture contents and different initial temperature conditions. The thermistor, oil vial and insulation layouts were also changed between some experiments. The wetting front velocities for the experiments presented above are shown in Table 4-9.

Table 4-9: Summary of wetting front velocities for the experiments presented in this chapter (in mm/min).

<table>
<tr><th colspan="5">Unfrozen Experiments</th></tr>
<tr><th rowspan="2">Moisture Content (%)</th><th colspan="4">Wetting Front Velocity (mm/min) at</th></tr>
<tr><th>1g</th><th>20g</th><th>40g</th><th>60g</th></tr>
<tr><td>0</td><td>0.21</td><td>5.2</td><td>11.9</td><td>17.9</td></tr>
<tr><td>10</td><td>0.14</td><td>4.2</td><td>-</td><td>-</td></tr>
<tr><td>18
(with water loss)</td><td>-</td><td>1.9</td><td>-</td><td>-</td></tr>
<tr><td>18</td><td>-</td><td>0</td><td>-</td><td>-</td></tr>
<tr><th colspan="5">Frozen Experiments</th></tr>
<tr><th>Moisture Content (%)</th><th>1g</th><th>20g</th><th>40g</th><th>60g</th></tr>
<tr><td>0</td><td>-</td><td>2.7</td><td>5.5</td><td>9.5</td></tr>
<tr><td>10</td><td>-</td><td>1.5</td><td>-</td><td>-</td></tr>
<tr><td>10</td><td>-</td><td>1.3</td><td>-</td><td>-</td></tr>
<tr><td>10
(vortex tubes)</td><td>-</td><td>1.8</td><td>-</td><td>-</td></tr>
<tr><td>18
(with water loss)</td><td>-</td><td>0.7</td><td>-</td><td>-</td></tr>
</table>

4.7.1 Effect of Moisture Content on Wetting Front Velocity

For all experiments presented above, it was found that the presence of moisture within the soil reduced the wetting front velocity of the oil. Increasing moisture content led to decreasing wetting front velocities for the oil. Although it is counter-intuitive to think that increasing moisture content would reduce the contaminant transport, but it is important to remember that the contaminant transport mechanism for all experiments is advection due to gravity migration, with a few having migration by diffusion. If there was water flow within the soil during an experiment, we would most likely see the opposite effect where increasing water content would increase the rate of contaminant transport, but in the horizontal direction instead of vertical (Fetter 2008). Table 4-10 shows the percentage decrease of the wetting front velocity compared to the dry experiments. All unfrozen experiments with moisture added were compared to the dry unfrozen experiments and all initially frozen experiments with moisture added were compared to the dry initially frozen experiments.

Table 4-10: Wetting front velocity reduction between wet and dry sand experiments.

	Unfrozen Experiments		**Frozen Experiment**
	Acceleration Ratio		
Moisture Content (%)	1g	20g	20g
10	33%	20%	44%
10	-	-	52%
10 (vortex tubes)	-	-	33%
18 (with water loss)	-	63%	74%
18	-	100%	-

4.7.2 Effect of Temperature on Wetting Front Velocity

It was also found that the wetting front velocities for the initially frozen experiments were lower than their corresponding unfrozen experiments. As discussed earlier, the decreased temperature increased the surface tension of the pumpkin seed oil, which made it stick more to the soil particles due to interfacial tension and thus reducing its wetting front velocity. Table 4-11 shows the decrease in wetting front velocity between the initially frozen experiment and their corresponding unfrozen experiments e.g. FR-0-20g is compared to UN-0-20g or FR-18-20g- is compared to UN-18-20g-01. It was observed that the temperature effect on the wetting front velocity of the oil was more pronounced when moisture was added to the sand. This may be caused by ice within the soil that is still present while the oil is infiltrating. Since water expands as it turns to ice, the ice would take up more pore space than if liquid water was present within the soil. The ice within the soil blocks potential pathways through which the oil would migrate.

Table 4-11: Wetting front velocity reduction between unfrozen and initially frozen experiments.

Moisture Content (%)	20g	40g	60g
0	48%	54%	47%
10 (1)	64%	-	-
10 (2)	69%	-	-
18 (with water loss)	63%	-	-

The effects of freeze-thaw cycles on the migration of pumpkin seed oil through sand was observed by conducting a column experiment and making it go through freeze-thaw cycles. It was found that freezing the soil immobilized the oil within the soil. It was also observed that a thaw cycle could induce the migration of the oil through sand even though it was saturated.

4.7.3 Implications for the Canadian Arctic

A centrifuge experiment was conducted with soil from Wrangle Bay, one of the abandoned barrel caches located in the Canadian Arctic. This demonstrated that using a geotechnical centrifuge can help determine the wetting front velocity of contaminants found at these sites. The centrifuge experiments would be tailored to reflect the conditions of the site. Soil and contaminant samples would have to be collected at a site and brought back to a laboratory to be able to determine their properties. The properties of interest for the soil would be its moisture content, as sampled from the site, its grain size distribution, its hydraulic conductivity and its air and water entry pressure. The properties of interest for the contaminant would be its density, its freezing point, its surface tension at various temperatures, along with its entry pressure into the soil at the site being analyzed. Since most contaminants at Arctic sites are flammable and/or pose a health hazard, a fluid with similar properties to the contaminant would have to be used for the centrifuge experiments.

5 CONCLUSION

5.1 Thesis Overview

Contaminated sites are found throughout the Canadian Arctic at mines, military bases and research stations. It is important to have the capability to study the long-term contaminant transport behaviour at those sites in order to determine where the contaminants have migrated in the subsurface since being spilled. Field work in the Arctic is complex, expensive and typically limited to a few months throughout the year. Having laboratory based methods to complement the field research can help reduce the costs and time required to characterize a site before remediation. The capability for researching contaminant transport in cold regions was developed for the geotechnical centrifuge at RMC. This capability did not exist prior to undertaking this research project.

The use of a geotechnical centrifuge for contaminant transport research was validated by conducting three centrifuge experiments at different acceleration ratios and one experiment in an acrylic column. The experiments proved that the scaling principle for wetting front velocity was being followed. The wetting front velocity increases linearly with increasing acceleration ratio in the centrifuge. The validation of using RMC's centrifuge for contaminant transport research means that future research can be conducted to better understand the factors affecting contaminant transport in cold regions.

The various experiments conducted also allowed for the observation and quantification of the effects of moisture content and temperature on the wetting front velocity of the oil. It was found that increasing moisture content would slow the wetting front velocity of the oil. Wetting front velocity decreases of 20 and 44% were observed for unfrozen and frozen experiments at 20g with a moisture content of 10%. An experiment with saturated sand at room temperature showed that saturated soil could completely block the advective migration of oil. However, migration of the oil by diffusion through the water was observed and advanced at a rate similar to that observed in the column experiment. This demonstrated that the migration of oil by diffusion does not scale in the centrifuge.

It was also found that decreasing the temperature of the soil slowed the migration of the oil. Wetting front velocity decreases of approximately 50% were observed for centrifuge experiments using initially frozen dry sand. The wetting front velocity decrease was even more pronounced for frozen experiment when water was added to the sand due to the ice filling the pore spaces, which blocked possible flow paths for the oil. Quantifying the effects of moisture content and temperature on the wetting front velocity of the oil provides a good starting point for estimating the wetting front velocity of contaminants at contaminated sites based on the local hydrological conditions and climate.

Soil collected from the abandoned barrel cache in Wrangle Bay, Nunavut was used to conduct a contaminant transport experiment in the centrifuge. This demonstrated that centrifuge experiments can now be conducted using soil and a contaminant from a contaminated site in the Arctic. The centrifuge experiments can help to understand where spilled contaminants may have migrated based on the moisture and temperature conditions of the site. This would ultimately improve the effectiveness of site remediations.

5.2 How Research was Advanced

This research combined the fields of contaminant transport, cold regions engineering and geotechnical centrifuge modelling. The combination of these three research fields has not been well documented in the literature to date. The development of the centrifuge experiment methods along with the validation of the use of a centrifuge created a novel way to conduct research on contaminant transport in cold regions. The centrifuge experiments were validated by conducting a modelling of models (Madabhushi 2015) to prove that the scaling laws for wetting front velocity and diffusion was being followed. The centrifuge experiment methods along with the apparatus and instrumentation developed is a good starting point to conduct future contaminant transport research. The potential for improvements is very high since most of the methods and apparatus were developed without any reliance on past methods for contaminant transport or cold regions research within the RMC centrifuge. No contaminant transport or cold regions research had been previously conducted in the RMC centrifuge. This research investigated the effects of moisture content and temperature on the migration of oil through soil in the geotechnical centrifuge. This research also created a baseline for wetting front velocities of pumpkin seed oil through the #730 silica sand. The results could be used to compare future contaminant transport experiments through frozen soil in the centrifuge. It was also demonstrated that the geotechnical centrifuge could be used to determine the wetting front velocity of contaminants into soil sampled from a contaminated site in the Arctic.

5.3 Potential Improvements

The current centrifuge procedures and apparatus allowed for the validation of the geotechnical centrifuge for contaminant transport research. For the frozen experiments, the soil had to be frozen in a cold room overnight prior to installing the cradle in the centrifuge and running it. Only one thaw cycle was achievable during a single experiment. The current climate box apparatus, which uses vortex tubes, can be improved to allow the soil within the cradle to go through multiple freeze-thaw cycles over the course of an experiment. The use of insulation was trialed in order to improve the freeze-thaw apparatus. Improvements were observed with the use of insulation; however, freezing temperatures were still not achievable. Using better or more insulation, or changing the location of the insulation could allow for freezing temperatures within the cradle.

The use of black light could also be investigated. Since pumpkin seed oil fluoresces under black light, it could be used instead of the regular LED lights in the centrifuge. If the black light produces less heat than the LED jeep lights currently in use, it could help to achieve frozen temperatures in the cradle with the freeze-thaw apparatus. The black light could also help observe the migration of the pumpkin seed oil through darker soil than was used in this research. As it was observed with the experiment using soil from Wrangle Bay, darker soil made it more difficult to see the oil as it was infiltrating through it. The use of a black light would help solve this issue.

5.4 Future Research

More experiments could be conducted in the acrylic column and in the centrifuge. With a better sealing method to prevent the loss of water, experiments with saturated soil could be conducted at acceleration ratios of 40 and 60g. The same experiments could also be conducted by using frozen soil.

The viscosity of the pumpkin seed oil could be determined using a viscometer or a rheometer. By knowing the viscosity of the pumpkin seed oil and also determine the viscosity of water, it would be possible to determine the hydraulic conductivity of the pumpkin seed oil through the soil being used.

Once an improved climate box is developed, the geotechnical centrifuge could be used to research the effects of multiple freeze-thaw cycles on the migration of oil through the soil. The improved climate box would allow for the control of the thermal conditions within the cradle during an experiment. Experiments could be conducted at constant temperatures. Changing the constant temperature for different experiments could allow for a better understanding of the relationship between temperature and the wetting front velocity of a contaminant.

Only the wetting front velocity of the oil was determined for all the experiments presented in this thesis. There is potential to develop the methods in order to measure the concentration of the contaminant during an experiment using image analysis. Images of oil within the sand at various concentration levels could be taken to create a baseline for a specific soil. Images of future experiments could then be compared to the baseline to determine the concentration of the contaminant in the sand throughout the experiment. This would be especially helpful when analyzing contaminated sites since the concentration could be determined and it would be possible to verify if the concentration exceed the legal threshold limits.

The thermal conditions of frozen experiments could be analyzed in more depth by increasing the number of thermistors used. The thermal properties of the soil used could also be determined in order to conduct numerical modelling of the thermal conditions during an experiment. The numerical modelling results could then be used to improve the freeze-thaw apparatus. The effect of the heat transfer on the contaminant transport could be investigated. Heat transfer does not scale in the centrifuge (Madabhushi 2015). However, the heat transfer by conduction is still occurring with the migration of the oil scaling in the centrifuge. The effects of heat transfer by conduction could be researched futher.

No monitoring of moisture content was conducted during the experiments. However, it was observed that the addition of moisture within the soil reduced the wetting front velocity of the oil. Additonal instrumentation could be added to the centrifuge cradle in order to record the moisture content of the soil at various locations throughout an experiment. This would allow for the quantifying of the direct relationship between the wetting front velocity and the moisture content in the soil.

By determining the wetting front velocities of the contaminants at contaminated sites with centrifuge experiments, the contaminant source zone and its potential plume could be estimated. This would help remediation efforts of these sites by having a better idea of where the contaminants are located beneath the surface. The improved efficiency of the site remediations would save time and financial resources. This means that more contaminated sites could be cleaned up during the summer season, which is typically when site remediations occur in the Arctic because of the lack of light during the winter months.

Climate change is having a significant on the Arctic climate and its landscape (Rudy 2016), with permafrost degradation being of serious concern. It is reasonable to question how the thawing of permafrost may affect the transport of contaminants that have been spilled at various sites in the Arctic. Some sites even use permafrost to contain contaminated soil. If permafrost degradation continues, it may lead to the release of contaminants that are currently immobile. The column experiment where freeze-thaw cycles were conducted demonstrated that thawing soil enabled the advective migration of oil, even into saturated soil. This shows that the released contaminants would then pose environmental risks to local communities and ecosystems. It is also important to consider that the release of contaminants due to permafrost degradation would further complicate the remediation of contaminated sites.

The study of contaminant transport through freezing and thawing soils is only one application of the temperature control apparatus that uses vortex tubes. Many other northern geotechnical, hydrological and geo-environmental engineering issues could be analyzed using this apparatus. The use of the centrifuge to research those issues would reduce costs compared to traditional research methods in the Arctic, which often requires complex and expensive field work. Such issues that could be researched include but are not limited to frost heave, thawing slope stability and active layer detachments.

REFERENCES

Andersland, O. B., and Ladanyi, B. (2004). *Frozen Ground Engineering*. Wiley, Hoboken.

ASTM International. (1993). *ASTM D2434-68: Standard Test Method for Permeability of Granular Soils (Constant Head)*. American Society for Testing and Materials, West Conshohocken.

ASTM International. (2003). *ASTM D422-63: Standar Test Method for Particle-Size Analysis of Soils*. American Society for Testing and Materials, West Conshohocken.

Azmatch, T. F., Sego, D. C., Arenson, L. U., and Biggar, K. W. (2012). “New ice lens initiation condition for frost heave in fine-grained soils.” *Cold Regions Science and Technology*, Elsevier B.V., 82, 8–13.

Beddoe, R. A., and Take, W. A. (2016). “Loss of slope support due to base liquefaction : comparison of 1g and centrifuge landslide flume experiments.” *Soils and Foundations*, 56(2), 251–264.

Bhatlu, N. (2014). “A Review on Contaminant Migration Studies in Geotechnical Centrifuge.” *Indian Geotechnical Society*, Kakinada, 9.

Biggar, K. (n.d.). *Contaminant Movement in Permafrost and Freezing Soils*. Edmonton.

Biggar, K. W., Haidar, S., Nahir, M., and Jarrett ’, P. M. (1998a). “Site Investigation of Fuel Spill Migration Into Permafrost.” *Journal of Cold Regions Engineering*, 12(2), 84–104.

Biggar, K. W., Haidar, S., Nahir, M., and Jarrett, P. M. (1998b). “Site Investigatoin of fuel spill migration into Permafrost.” *Journal of Cold Regions Engineering*, 12(2), 84–104.

Biggar, K. W., Nahir, M., and Haidar, S. (1998c). “Migration of petroleum contaminants into permafrost.” *Permafrost - Seventh International Conference*, Yellowknife, NWT, 43–49.

Broadbent, I. (2015). *Operating Manual - GT6/0.75 Geotechnical Beam Centrifuge*. Thomas Broadbent & Sons Ltd, Huddersfield, England.

Canadian Council of Ministers of the Environment. (2008). “Canada Wide Standard for Petroleum Hydrocarbons (PHC) in Soil.” *Petroleum Hydrocarbons in Soil – Technical Supplement*, 28.

Celorie, J. A., Vinson, T. S., Woods, S. L., and Istock, J. D. (1989). “Modeling Solute Transport by Centrifugation.” *Journal of Environmental Engineering*, 115(3), 513–526.

Chuvilin, E. M. (2009). “Migration of Petroleum in Permafrost-Affected Regions.” *Permafrost Soils: Soil Biology*, R. Margesin, ed., Springer, Berlin, 263–278.

Chuvilin, E. M., Naletova, N. S., Miklyaeva, E. C., Kozlova, E. V., and Instanes, A. (2001). “Factors affecting spreadability and transportation of oil in regions of frozen ground.” *Polar Record*, 37(202), 229–238.

Civan, F. (2000). “Unforzen Water in Freezing and Thawing Soils: Kinetics and Correlation.” *Journal of Cold Regions Engineering*, 14(3), 146–156.

Corté, J.-F. (1988). *Centrifuge 88*. A.A.Balkema, Rotterdam.

Fetter, C. W. (2001). *Applied Hydrogeology*. (P. Lynch, ed.), Prentice Hall, Upper Saddle River.

Fetter, C. W. (2008). *Contaminant Hydrogeology*. Waveland Press, Long Grove.

Filler, D. M., Van Stempvoort, D. R., and Leigh, M. B. (2009). “Remediation of Frozen Ground Contaminated with Petroleum Hydrocarbons: Feasibility and Limits.” *Permafrost Soils: Soil Biology*, R. Margesin, ed., Springer, Berlin, 279–301.

Fredlund, D. G., Rahardjo, H., and Fredlund, M. D. (2012). *Unsaturated Soil Mechanics in Engineering Practice*. Wiley, Hoboken.

Grant, S. A., and Bachmann, J. (2013). *Environmental Mechanics: Water, Mass and Energy Transfer in the Biosphere: The Philip Volume*. (P. A. C. Raats, D. E. Smiles, and A. W. Warrick, eds.), American Geophysical Union, Washington, DC.

Harris, C., Smith, J. S., Davies, M. C. R., and Rea, B. (2008). “An investigation of periglacial slope stability in relation to soil properties based on physical modelling in the geotechnical centrifuge.” *Geomorphology*, 93, 437–459.

Hyrd, M. J. (2016). “The DEW Line and Canada’s Arctic Waste: Legacy and Futurity.” *The Northern Review*, 42, 23–45.

Iwakun, O., and Biggar, K. (2007). “Behaviour of Spilled Petroleum Hydrocarbon at Colomac Mine Site, NWT.” *GeoOttawa*, Ottawa, 2106–2114.

Iwakun, O., Biggar, K., and Sego, D. (2010a). “Influence of cyclic freeze-thaw on the mobilization of LNAPL and soluble oil in a porous media.” *Cold Regions Science and Technology*, 64, 9–18.

Iwakun, O., Biggar, K., Sego, D., and Richardson, A. (2010b). “LNAPL Recovery in Permafrost Fractured Bedrock at the Colomac Mine Site, NWT.” *7th International Conference on Contaminants in Freezing Ground*, Kingston, 20.

Iwakun, O., Biggar, K., and Van Stempvoort, D. (2008). “Fuel contamination characterization in permafrost fractured bedrock at the Colomac mine site.” *Cold Regions Science and Technology*, 53(1), 56–74.

Kalinovich, I., Rutter, A., Poland, J. S., Cairns, G., and Rowe, R. K. (2008). “Remediation of PCB contaminated soils in the Canadian Arctic : Excavation and surface PRB technology.” *Science of the Total Environment*, Elsevier B.V., 407, 53–66.

Kern-Luetschg, M., and Harris, C. (2008). “Centrifuge modelling of solifluction processes: Displacement profiles associated with one-sided and two-sided active layer freezing.” *Permafrost and Periglacial Processes*, 19, 379–392.

Kingswood, J., Laporte, S., and Siemens, G. (2016). “Verification of physical modelling with a geotechnical centrifuge.” *GeoVancouver2016*.

Konrad, J. M., and Seto, J. T. C. (1991a). “Freezing of a clayey silt contaminated with an organic solvent.” *Journal of Contaminant Hydrology*, 8(3–4), 335–356.

Konrad, J. M., and Seto, J. T. C. (1991b). “Freezing of a clayey silt contaminated with an organic solvent.” *Journal of Contaminant Hydrogeology*, 8(3–4), 335–356.

Kumar, P. R. (2006). “An experimental methodology for monitoring contaminant transport through geotechnical centrifuge models.” *Environmental Monitoring and Assessment*, 117, 215–233.

Kumar, P. R. (2007). “Scaling laws and experimental modelling of contaminant transport mechanism through soils in a geotechnical centrifuge.” *Geotechnical and Geological Engineering*, 25, 581–590.

Laporte, S., and Siemens, G. (2017). “Physical Modelling of Undrained Slope Failure Using A Geotechnical Centrifuge.” *GeoOttawa*.

Larsen, T., Christensen, T. H., Pfeffer, F. M., and Enfield, C. G. (1992). “Landfill leachate effects on sorption of organic micorpollutants onto aquifer materials.” *Journal of Contaminant Hydrology*, 9, 307–324.

Madabhushi, G. (2015). *Centrifuge Modelling for Civil Engineers*. CRC Press, Boca Raton.

Nyer, E. K., and Skladany, G. J. (1989). “Relating the Physical and Chemical Properties of Petroleum Hydrocarbons to Soil and Aquifer Remediation.” *Ground Water Monitoring & Remediation*, 9(1), 54–60.

van der Perk, M. (2017). *Soil and Water Contamination*. CRC Press, Boca Raton.
Qin, H. (2019). “Centrifugal Modeling and Validation of Solute Transport within Unsaturated Zone.” *Water*, 11(610), 21.

Rudy, A. C. A. (2016). “Landscape Patterns of Permafrost Disturbance and Degradation in the Canadian High Arctic.” Queen’s University.

Smith, J. S. (2004). “Scaled Geotechnical Centrifuge Modelling of Gelifluction.” University of Wales, Cardiff.

Smith, S. (2011). *Trends in permafrost over northern Canada*. *Canadian Biodiversity: Ecosystem Status and Trends 2010*.

Stone, K. J. L., Smith, C. C., and Schofield, A. N. (1995). “A thermally controlled test chamber for centrifuge and laboratory experiments.” *Geotechnical Testing Journal*, 19(4), 441–445.

Tsaknis, J., Lalas, S., and Lazos, E. S. (1997). “Characterization of crude and purified pumplcin seed oil.” *Grasas y Aceites*, 48(5), 267–272.

Tumeo, M. A., and Davidson, B. (1993). “Hydrocarbon exclusion from ground water during freezing.” *Journal of Environmental Engineering-Asce*, 119(4), 715–724.

APPENDIX A #730 SILICA SAND CHARACTERIZATION

A.1 Introduction

This appendix covers the laboratory work that was done to determine the characteristics of the soil that are important for this research. The grain size distribution, the water entry pressure and the hydraulic conductivity of the #730 silica sand were determined by following their respective ASTM standards.

A.2 Grain Size Distribution

The grain size distribution for the #730 silica sand (Beddoe and Take 2016) was determined by following the procedures of ASTM D422–63. The mass of all the sieves, the bottom pan and the top lid was recorded. The sieves were then stacked with the larger diameter sieves being at the top. The pan was placed below the #230 sieve. 204.1 g of #730 silica sand was added to the sieve stack. The ASTM recommends approximately 200 g of soil. The lid was placed on top of the #10 sieve. The sieve stack was then placed in a sieve shaker for 15 minutes. The mass of each sieve with its retained sand was recorded. The mass of the retained sand was calculated and then the percentage of passing sand was calculated and plotted versus the sieve opening size (Figure A-1).

Table A-1: Sieve analysis results.

		Mass (g)			
Sieve #	Opening (mm)	Sieve	Sieve + Sand	Sand	% Passing
10	2	469.1	469.2	0.1	99.95
18	1	481.1	481.2	0.1	99.90
35	0.5	393.2	393.3	0.1	99.85
60	0.25	406.0	412.5	6.5	96.67
120	0.125	364.7	528.5	163.8	16.41
230	0.063	354.0	387.2	33.2	0.15
Pan	-	380.4	380.7	0.3	-
Lid	-	297.9	-	-	-
Total	-	3146.4	3052.6	204.1	-

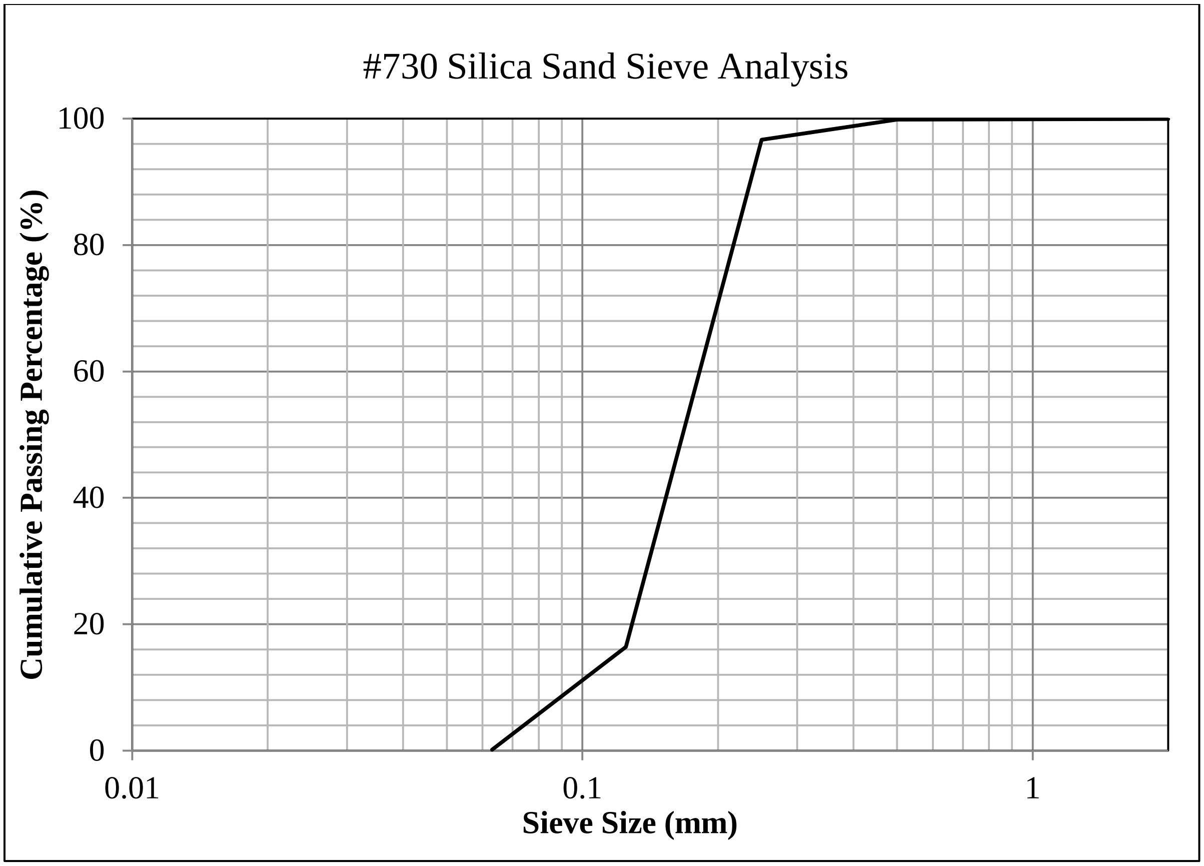

Figure A-1: #730 silica sand sieve analysis.

A.3 Water Entry Pressure

The water entry pressure for the #730 Silica sand is approximately 4.1 kPa while the air entry pressure is approximately 1.6 kPa (Figure A-2). This was determined by taking the soil water characteristic curve for the sand (Beddoe and Take 2016) and calculating the intersect of the tangents of the three inflection points of the curve. There are three inflection points for a soil water characteristic curve, the first for the boundary effect zone, the second for the transition zone and the third for the residual zone (Fredlund et al. 2012). The air entry value is at the intersect of the tangents of the inflection points for the boundary effect zone and the transition zone. The water entry value is at the intersect of the tangents of the inflection points for the transition zone and the residual zone.

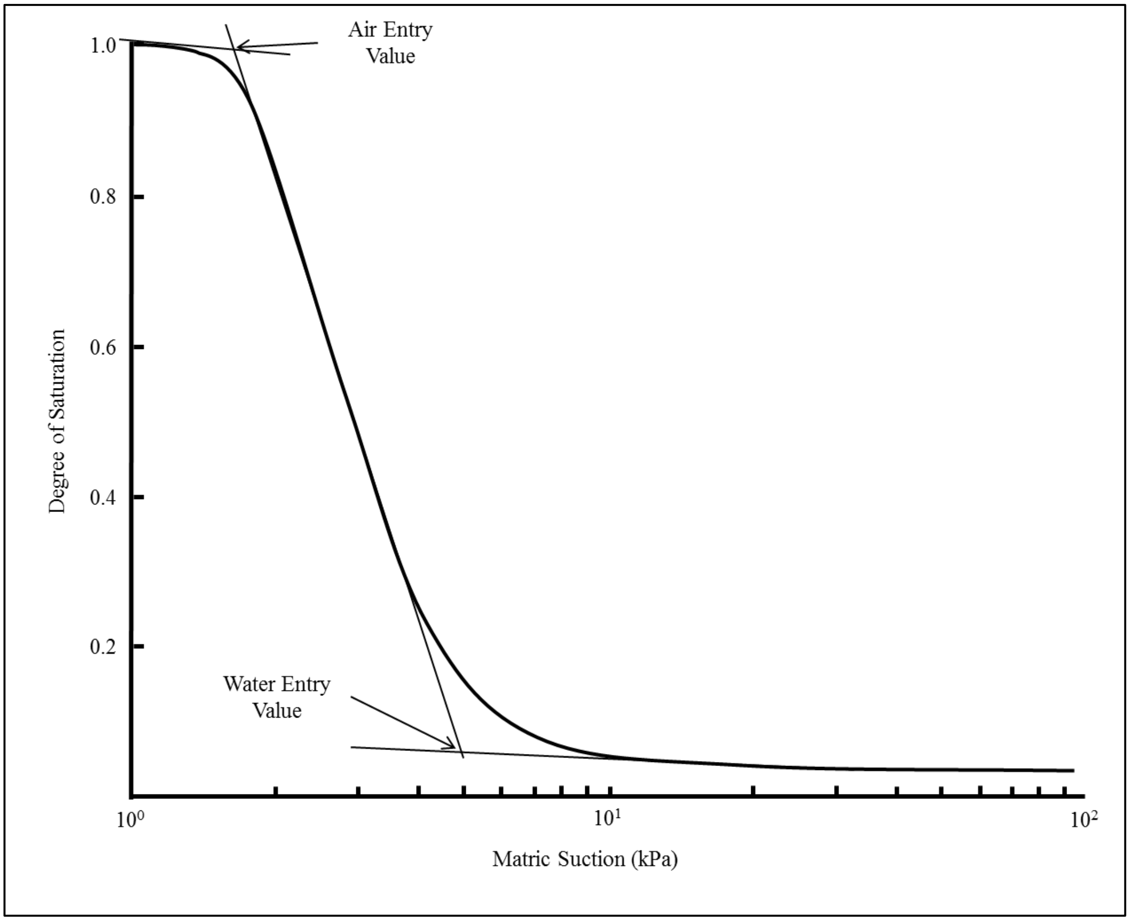

Figure A-2: Soil water characteristic curve for the #730 silica sand (recreated from Beddoe and Take 2016).

A.4 Hydraulic Conductivity

The hydraulic conductivity of the #730 silica sand was determined by conducting a constant head test in accordance with ASTM D2434-68. Figure A-3 represents a conceptual drawing of the permeameter that was used to conduct the constant head testing while Figure A-4 is a picture of the actual apparatus that was used for the constant head testing.

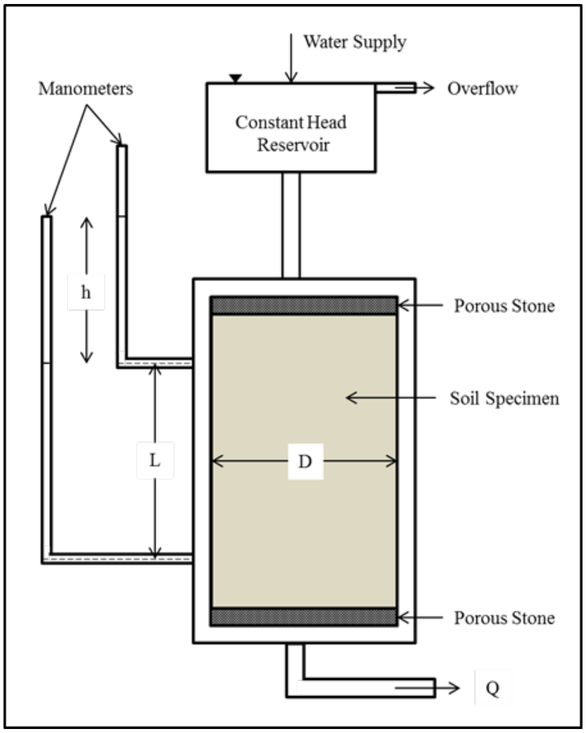

Figure A-3: Constant head permeameter conceptual diagram.

Figure A-4: Permeameter used for constant head testing.

Based on ASTM D2434-68, the following Equation 1 was used to calculate the hydraulic conductivity of the sand:

$$k = \frac{QL}{Ath} \ [1]$$

Where:

k = hydraulic conductivity (cm/s)
Q = quantity of water discharged (cm^3)
L = Distance between the manometers (cm)
A = surface area of the soil (cm^2)
t = total time of discharge (s)
h = difference in head on manometers (cm)

Two constant head tests were conducted to determine the hydraulic conductivity of the #730 silica sand. The head was changed between the two tests, but was not measured. The permeameter has two sets of manometers. The average head difference between each set of manometers was used in the calculations.

Table A-2: Results from constant head testing.

Variable	Test 1	Test 2
Q (cm^3)	77 ± 0.6%	103 ± 0.5%
L (cm)	12.8 ± 0.4%	12.8 ± 0.4%
A (cm^2)	78.54 ± 0.5%	78.54 ± 0.5%
t (s)	60 ± 0.8%	60 ± 0.8%
h (cm)	23.5 ± 0.2%	31.6 ± 0.2%
k (cm/s)	$8.90\text{x}10^{-3}$ ± 2.5%	$8.85\text{x}10^{-3}$ ± 2.4%

APPENDIX B ELLESMERE ISLAND SOIL CHARACTERIZATION

B.1 Introduction

As part of Operation NEVUS, soil samples were collected from several abandoned barrel caches on Ellesmere Island. The goal of this appendix is to present the results of the characterization of some of the soil samples that were received. The metadata for the samples is presented in addition to the moisture content calculations, the grain size distribution and the hydraulic conductivity of some of the soil samples.

B.2 Soil Samples

A total of 22 soil samples were collected at the various sites throughout Ellesmere Island (Table B-1). Two sample locations were selected for characterization: the samples from Eureka Site #5 and the samples from Wrangle Bay. The samples were selected because they are both sands.

Table B-1: Soil sample metadata.

Location	Date	Sample Point	Latitude	Longitude	Sub-Sample ID	Depth of Sample (cm)
Eureka	Jun-18	118	N79°59.698	W085°47.024	001	25
	Jun-18	119	N79°59.687	W085°47.017	002,003	25
D'Iberville	Jun-18	120	N80°36.346	W079°34.885	004,005	25
Eureka West	Jun-18	121	N79°59.973	W086°03.476	006,007, 008	25
Eureka West	Jun-18	121	N79°59.973	W086°03.476	009,010	50
Eureka Site #5	Jun-18	124	N79°53.861	W085°14.026	011,012	25
Scheryschew River	Jun-18	125	N80°23.443	W081°59.460	013,014	25
Lincoln Bay	Jul-18	141	N82°05.506	W062°00.274	015,016	25
Wrangle Bay	Jul-18	159	N82°00.821	W062°25.343	017,018	25
Site #4	Jul-18	166	N81°04.712	W070°00.280	019,020	25
Hazen Camp	Jul-18	173	N81°49.644	W071°19.592	021,022	25

B.3 Moisture Content

The samples were double bagged to ensure that they didn't dry out while in storage. The moisture content was measured for the two soil samples from Wrangle Bay, NU, which are sub-samples 017 and 018 (Table B-2).

Table B-2: Wrangle Bay moisture content results.

Soil Sample	017			018		
Tin Number	1	2	3	4	5	6
Tin Mass (g)	1.00	1.01	1.00	1.00	1.00	1.01
Mass Wet Sand + Tin (g)	13.31	9.07	13.76	11.65	10.81	18.34
Mass Wet Sand (g)	12.31	8.06	12.76	10.65	9.81	17.33
Mass Dry Sand + Tin (g)	12.28	8.42	12.72	10.78	9.98	16.80
Mass Dry Sand (g)	11.28	7.41	11.72	9.78	8.98	15.79
Moisture Content (%)	9.13	8.77	8.87	8.90	9.24	9.75
Average Moisture Content (%)	8.92			9.30		

B.4 Grain Size Distribution

The grain size distributions for the two soil samples from Wrangle Bay, NU were determined by following the procedures specified in ASTM D422–63. Although the samples were collected from the same location, separate grain size distribution curves were produced for each of the samples. The mass of all the sieves, the bottom pan and the top lid was recorded. The sieves were then stacked with the larger diameter sieves being at the top. The pan was placed below the #200 sieve. 392.10 g of soil from sample #017 from Wrangle Bay was added to the sieve stack (Table B-3), while 471.00 g was added from sample #018 (Table B-4). The ASTM recommends approximately 200 g of soil. The lid was placed on top of the #4 sieve. The sieve stack was then placed in a sieve shaker for 15 minutes. The mass of each sieve with its retained sand was recorded. The mass of the retained sand was calculated and then the percentage of passing sand was calculated and plotted versus the sieve opening size (Figure B-1).

Table B-3: Sieve analysis results for sample #017 from Wrangle Bay.

		Mass (g)			
Sieve #	Opening (mm)	Sieve	Sieve + Sand	Sand	% Passing
4	4.76	593.11	597.61	4.5	98.85
10	2	488.82	492.74	3.92	97.85
40	0.425	376.23	494.94	118.71	67.58
60	0.25	349.11	506.22	157.11	27.50
140	0.106	296.10	363.61	67.51	10.29
200	0.074	337.85	345.55	7.7	8.32
Pan	-	380.41	413.04	32.63	-
Lid	-	358.40	358.40	0	-
Total	-	3180.00	3572.10	392.10	-

Table B-4: Sieve analysis for sample #018 from Wrangle Bay.

		Mass (g)			
Sieve #	Opening (mm)	Sieve	Sieve + Sand	Sand	% Passing
4	4.76	593.07	606.98	13.91	97.05
10	2	488.86	496.03	7.17	95.52
40	0.425	376.67	525.95	149.28	63.83
60	0.25	349.46	523.19	173.73	26.95
140	0.106	296.20	372.01	75.81	10.85
200	0.074	337.90	347.77	9.87	8.76
Pan	-	373.30	414.54	41.24	-
Lid	-	358.40	358.40	0	-
Total	-	3173.9	3644.9	471.0	-

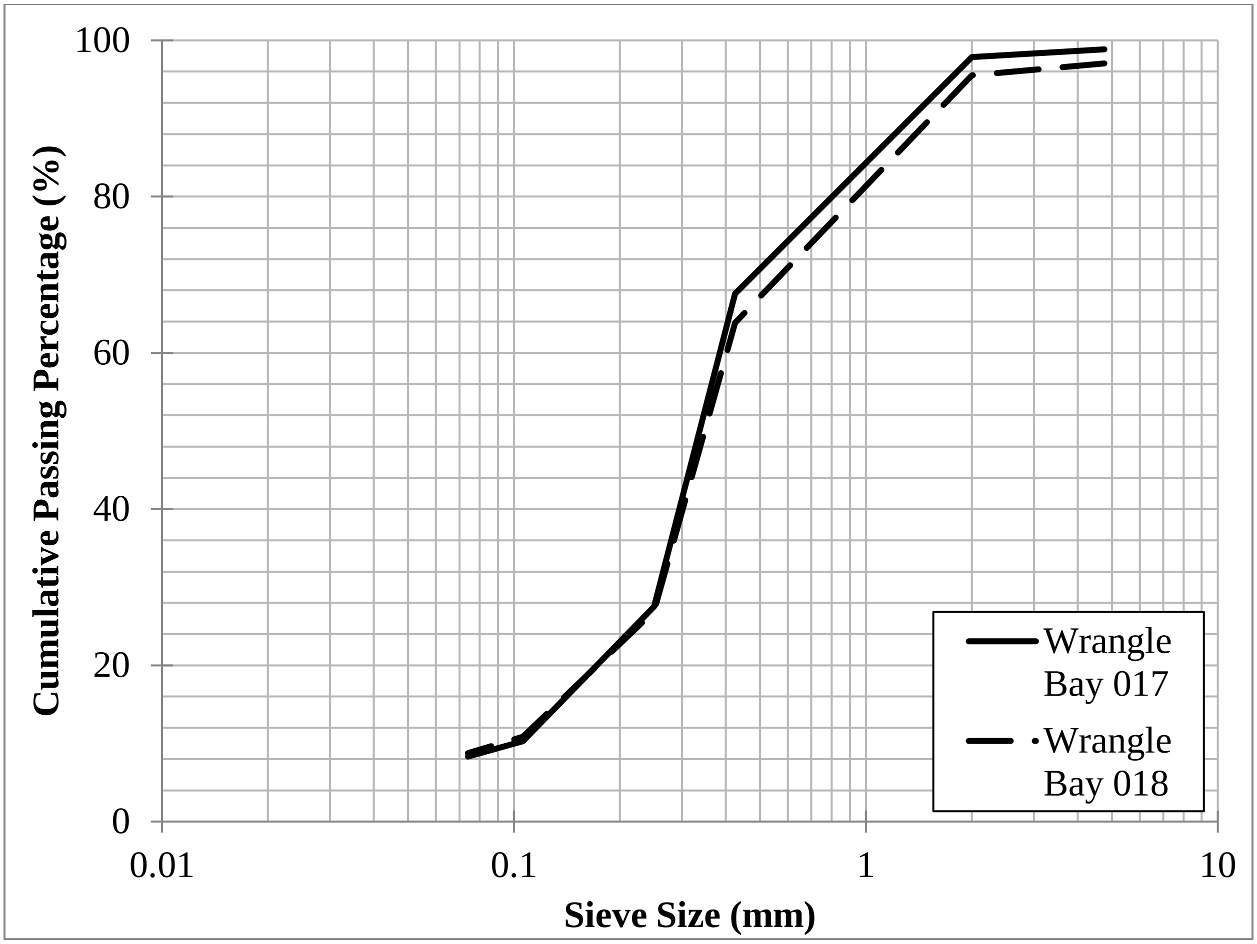

Figure B-1: Grain size distribution curves for the soil samples from Wrangle Bay, NU.

B.5 Hydraulic Conductivity

The hydraulic conductivity of the soil from Wrangle Bay, NU was determined by conducting a constant head test in accordance with ASTM D2434-68. Figure B-2 represents a conceptual drawing of the permeameter that was used to conduct the constant head testing while Figure B-3 is a picture of the actual apparatus that was used for the constant head testing.

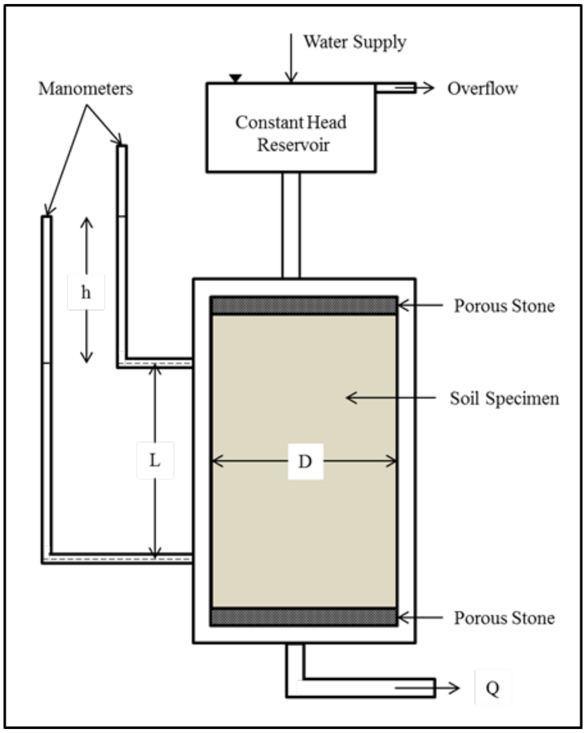

Figure B-2: Constant head permeameter conceptual diagram.

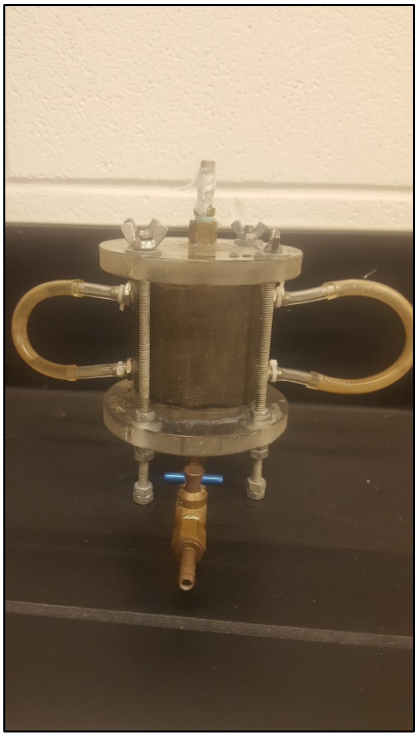

Figure B-3: Permeameter used for constant head testing.

Based on ASTM D2434-68, the following Equation 1 was used to calculate the hydraulic conductivity of the sand:

$$k = \frac{QL}{Ath} \ [1]$$

Where:

k = hydraulic conductivity (cm/s)
Q = quantity of water discharged (cm^3)
L = Distance between the manometers (cm)
A = surface area of the soil (cm^2)
t = total time of discharge (s)
h = difference in head on manometers (cm)

Three constant head tests were conducted to determine the hydraulic conductivity of the soil from Wrangle Bay. The elevation head was changed between the three tests, but was not measured. The permeameter has two sets of manometers. The average head difference between each set of manometers was used in the calculations. The average hydraulic conductivity of the soil was 2.60x10^{-3} cm/s.

Table B-5: Results from constant head testing.

Variable	Test 1	Test 2	Test 3
Q (cm^3)	43.0 ± 1.2%	43.0 ± 1.2%	34.50 ± 1.4%
L (cm)	5.0 ± 0.1%	5.0 ± 0.1%	5.0 ± 0.1%
A (cm^2)	44.18 ± 0.5%	44.18 ± 0.5%	44.18 ± 0.5%
t (s)	60 ± 0.8%	60 ± 0.8%	60 ± 0.8%
h (cm)	32.3 ± 0.2%	27.1 ± 0.2%	28.2 ± 0.2%
k (cm/s)	2.51x10^{-3} ± 2.8%	2.99x10^{-3} ± 2.8%	2.31x10^{-3} ± 3.0%

APPENDIX C PUMPKIN SEED OIL CHARACTERIZATION

C.1 Introduction

This Appendix covers the laboratory work that was done to determine the density, freezing point, interfacial tension and entry pressure of the pumpkin seed oil. These physical properties were determined in order to compare them to future PHC contaminants, including the oil samples acquired from Ellesmere Island. The physical properties listed above are known to affect the infiltration rate of fluids and how it will behave in frozen soil and soil that contains moisture.

C.2 Density

The density of the pumpkin seed oil was determined by gradually pouring pumpkin seed oil into a graduated cylinder and measuring the total mass of the graduated cylinder and the added oil. The oil was added in increments of 5 ml. The density would be calculated for each increment of oil added. The average density was found to be 0.910 g/ml (Table C- 1)

Table C-1: Density analysis results.

Volume Oil (ml)	Mass: Oil & Graduated Cylinder (g)	Mass Oil (g)	Calculated Density (g/ml)
0	68.52	0	-
6	73.80	5.44	0.907
10	77.59	9.07	0.907
14	81.31	12.80	0.914
20	86.73	18.21	0.911
25	91.28	22.76	0.910
		Average Density	0.910

C.3 Freezing Point

The freezing point of the pumpkin seed oil was determined by filling three plastic vials with pumpkin seed oil and placing them inside a cold room. The temperature of the oil in each vial was measured using a thermocouple. The consistency of the oil would be noted for each temperature recording. The temperature of the cold room was initially set at -11°C. The temperature of the cold room would be decreased in increments of 1°C until the pumpkin seed oil solidifies completely. The freezing point of the oil was found to be approximately -16°C (Table C-2).

Table C-2: Freezing point experiment results.

Temperature Recording	Vial #1 (°C)	Vial #2 (°C)	Vial #3 (°C)	State
1	20.8	20.5	20.1	Liquid
2	-10.5	-11.1	-10.7	Pasty
3	-11.7	-12.0	-11.8	More pasty than 2
4	-12.7	-13.5	-13.3	Near solid
5	-13.6	-14.1	-13.8	Near solid. Oil nearly doesn’t stick to thermocouple rod
6	-15.0	-15.0	-15.0	Near-solid
7	-16.8	-16.7	-16.7	Solid

C.4 Interfacial Tension

The interfacial tension of the pumpkin seed oil was determined by conducting a capillary rise experiment with both water and the pumpkin seed oil (Figure C-1). The capillary rise experiments were conducted at room temperature for the water (Figure C-2) and pumpkin seed oil (Figure C-3) as well as at 5°C and -10°C solely for the oil. One glass capillary tube with an inner diameter of 1.8 mm was used for the water and a different one with the same inner diameter was used for the pumpkin seed oil. The height of the oil was measured using calipers while the interface angle was calculated by taking a picture of the capillary tubes and drawing a line tangent to the curve and using the equation for capillary rise (Equation 1) is as follows:

$$h_c = \frac{2\sigma \cos\theta}{\rho g r} \, [1]$$

Where:

h_c = Height of fluid (mm)
σ = Interfacial tension (N/m)
θ = Contact angle
ρ = Density (g/ml)
g = Gravitational acceleration (N/m^2)
r = Inner radius of the capillary tube (mm)

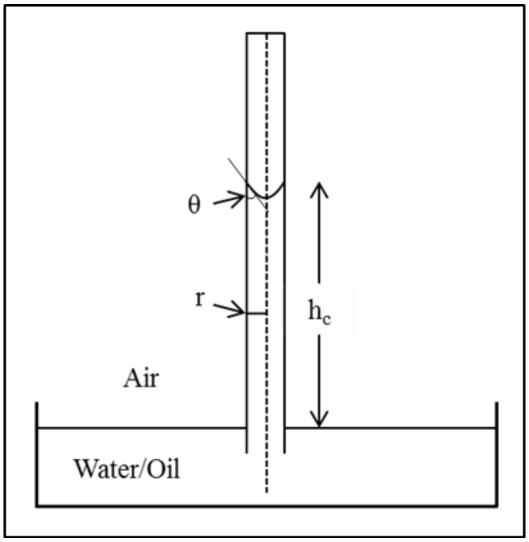

Figure C-1: Capillary rise experiment.

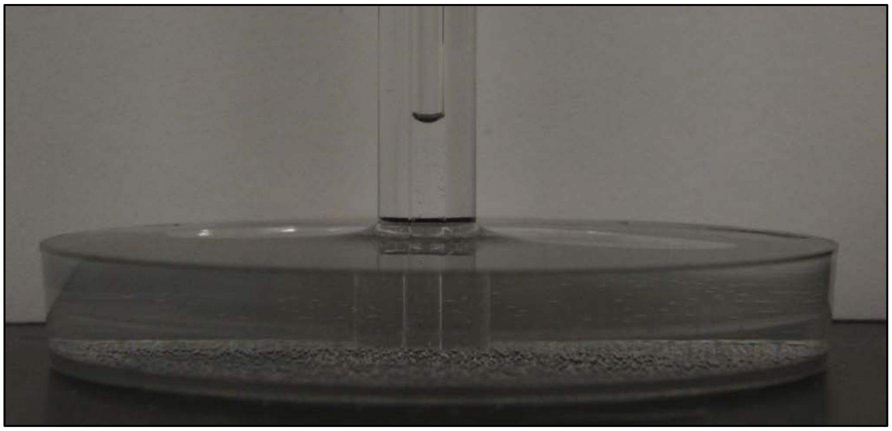

Figure C-2: Water capillary rise experiment.

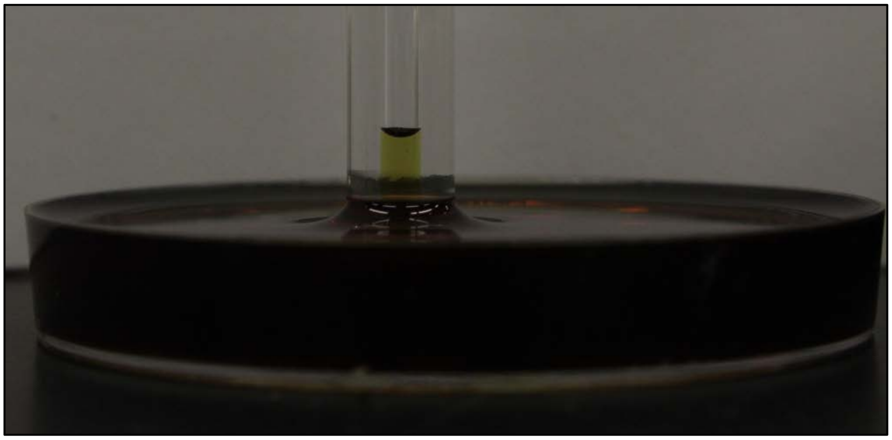

Figure C-3: Pumpkin seed oil capillary rise experiment.

Table C-3: Capillary rise experiment results (22°C).

Parameter	Water	Oil
h_c (mm)	10.35	3.58
θ (degrees)	49.11	42.07
ρ (g/ml)	1.00	0.91
g (m/s^2)	9.81	9.81
r (mm)	0.9	0.9
σ (N/m)	0.070	0.019

Table C-4: Capillary rise experiment results (5°C).

Parameter	Oil
$\boldsymbol{h_c}$ (mm)	6.98
$\boldsymbol{\theta}$ (degrees)	47.8
$\boldsymbol{\rho}$ (g/ml)	0.91
$\boldsymbol{g}$ (m/s^2)	9.81
$\boldsymbol{r}$ (mm)	0.9
$\boldsymbol{\sigma}$ (N/m)	0.042

C.5 Entry Pressure

The entry pressure was determined using the Equation 2 listed below. The water entry pressure ($P_c^{air-water}$) was calculated in Appendix A using the soil water characteristic curve of the #730 silica sand (Beddoe and Take 2016). The air-water and air-oil interfacial tension ($\sigma^{air-water}$ & $\sigma^{air-oil}$) were determined by conducting capillary rise experiments. By inputting the three parameters into Equation 2 we are able to isolate the oil entry pressure ($P_c^{air-oil}$) and calculate its value of 1,112.9 Pa, or 1.1 kPa at room temperature (Equation 3).

$$\frac{P_c^{air-water}}{\sigma^{air-water}} = \frac{P_c^{air-oil}}{\sigma^{air-oil}} \text{ [2]}$$

$$\frac{4{,}100\ Pa}{0.07\ N/m} * 0.019 N/m = 1{,}112.9\ Pa \text{ [3]}$$

Table C-5: Pumpkin seed oil entry pressure at various temperatures.

Temperature (°C)	Entry Pressure (kPa)
22	1.11
5	2.46

APPENDIX D CENTRIFUGE EXPERIMENTAL SETUP

D.1 Centrifuge Experimental Setup Overview

This appendix covers the general instructions to setup a contaminant transport experiment in RMC’s geotechnical centrifuge. Note that the instructions will vary based on experiment layout, such as using vortex tubes, having an air channel plate at the bottom of the cradle or the insulation layout. The instructions were created in order to have repeatable experiment in order to confidently analyze the data acquired based on known conditions.

D.2 Centrifuge Experimental Setup

1. Clean the centrifuge cradle with water and remove any excess grease with Grease Buster or any other grease removal product. Follow instructions on the can for application and removal of the product. Clean any hardware used for the cradle assembly. Wear protective eyewear, a respirator mask, a lab coat and nitrile gloves while handling Grease Buster. Ensure that the acrylic windows are cleaned with excess grease removed as well. It is recommended that the cradle and its parts be left to dry overnight after using the grease removal product.

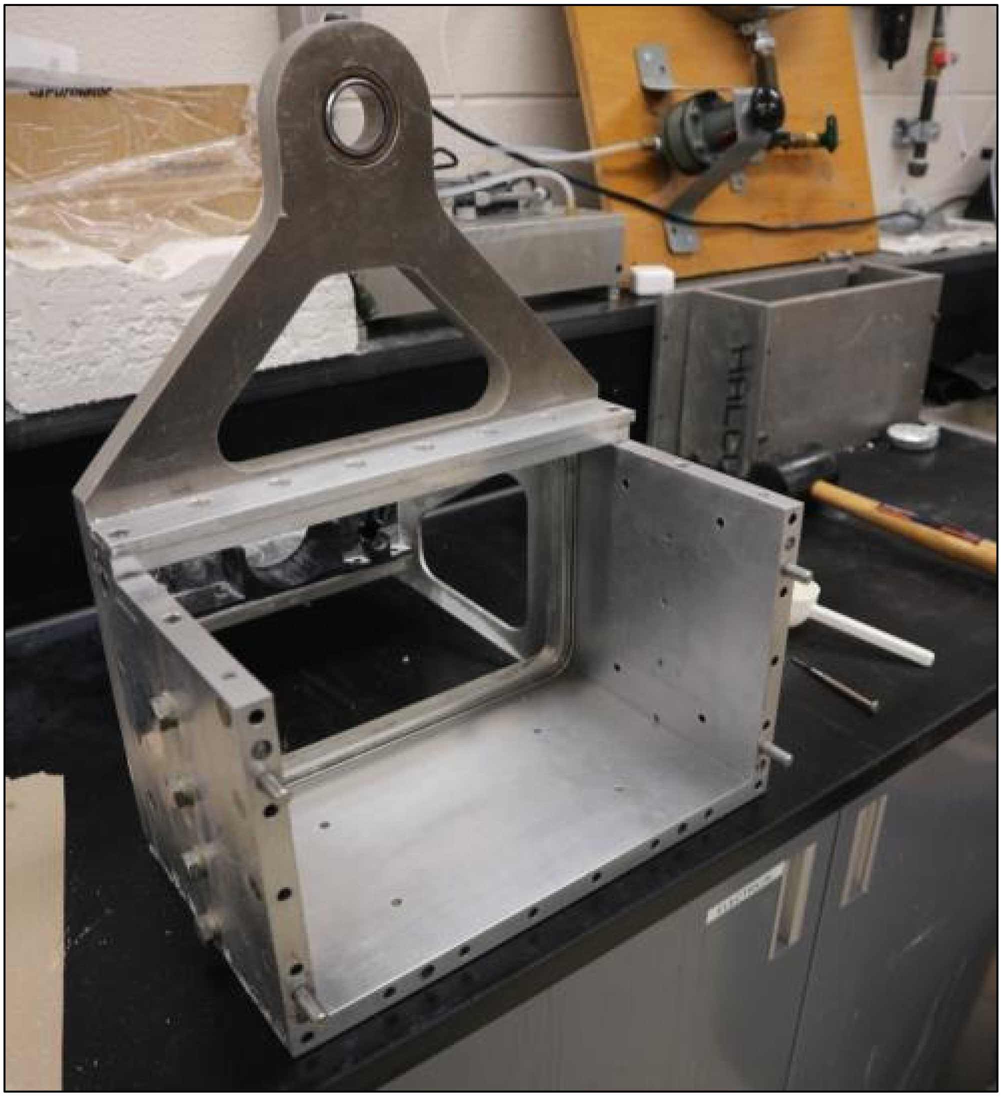

Figure D-1: Disassembled centrifuge cradle.

2. Fill the desired amount of 6 ml vials with pumpkin seed oil and insert them in the freezer. The freezer temperature must be lower than -10°C for the oil to freeze. It will take several hours for the oil to freeze in a conventional freezer.

3. Apply high vacuum grease in the track on the inside cradle side plate on the camera side of the cradle. Insert the rubber seal inside the track. Apply high vacuum grease around the rubber seal until the track is filled with grease. Grease is only required in the bottom and the side portions of the tracks. It is recommended to wear nitrile gloves while applying the grease.

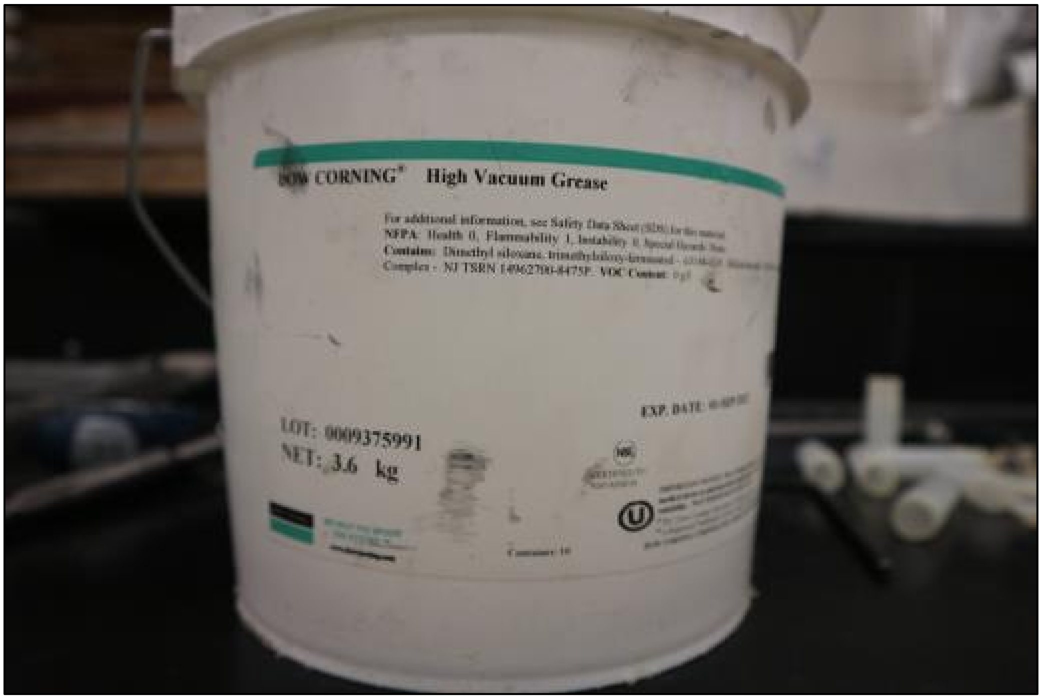

Figure D-2: Dow Corning High Vacuum Grease.

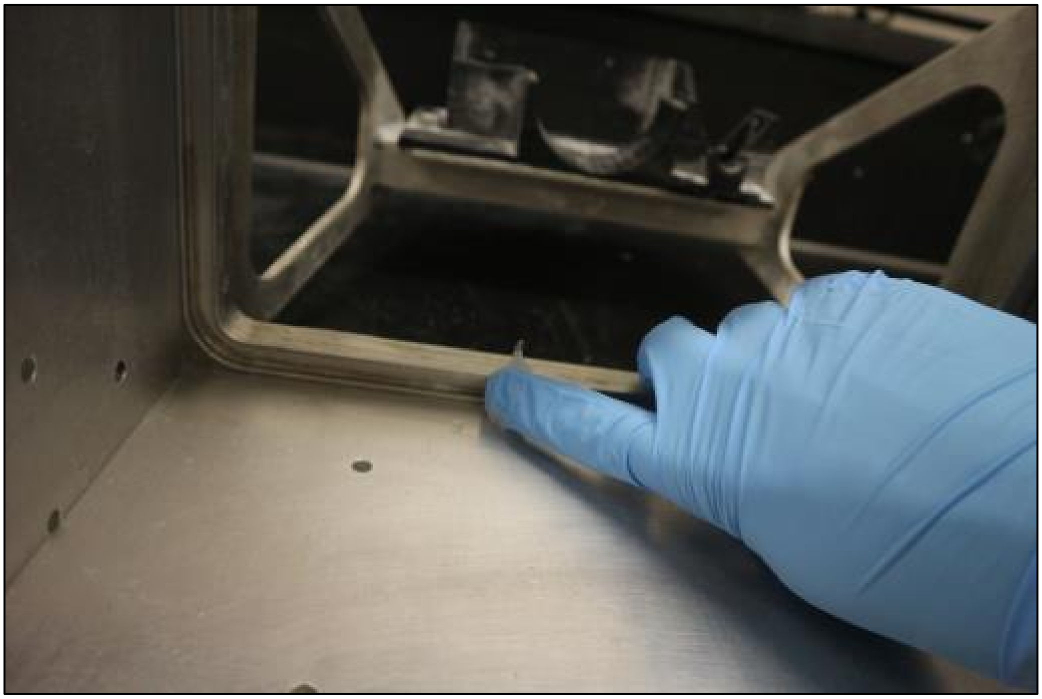

Figure D-3: Applying grease in bottom track for rubber seal.

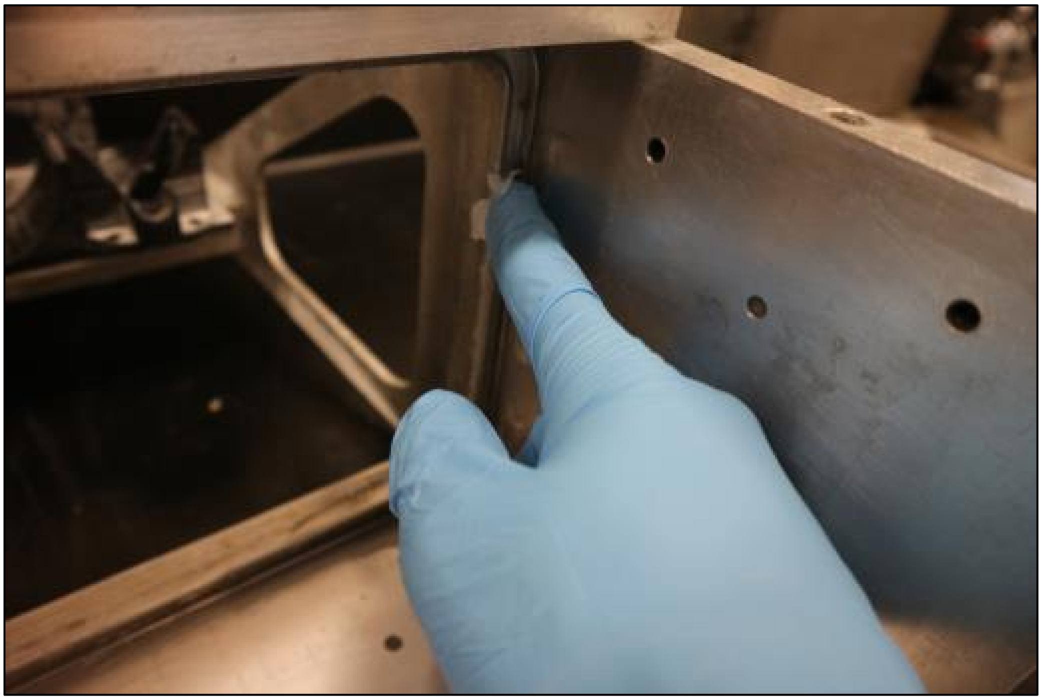

Figure D-4: Applying grease in side tracks for rubber seal.

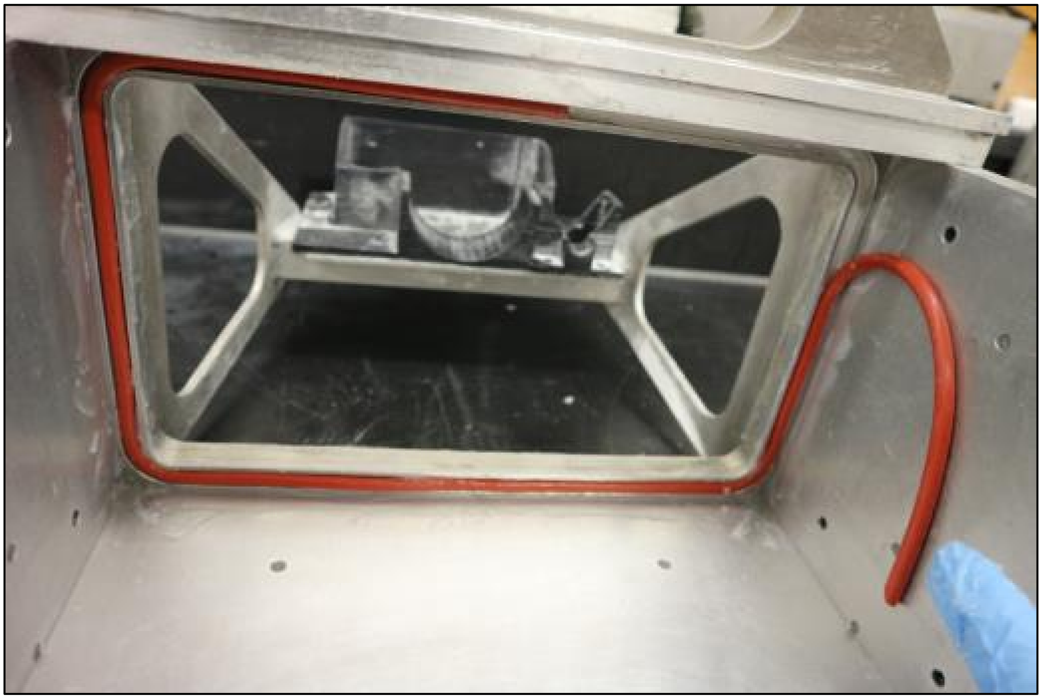

Figure D-5: Installing rubber seal.

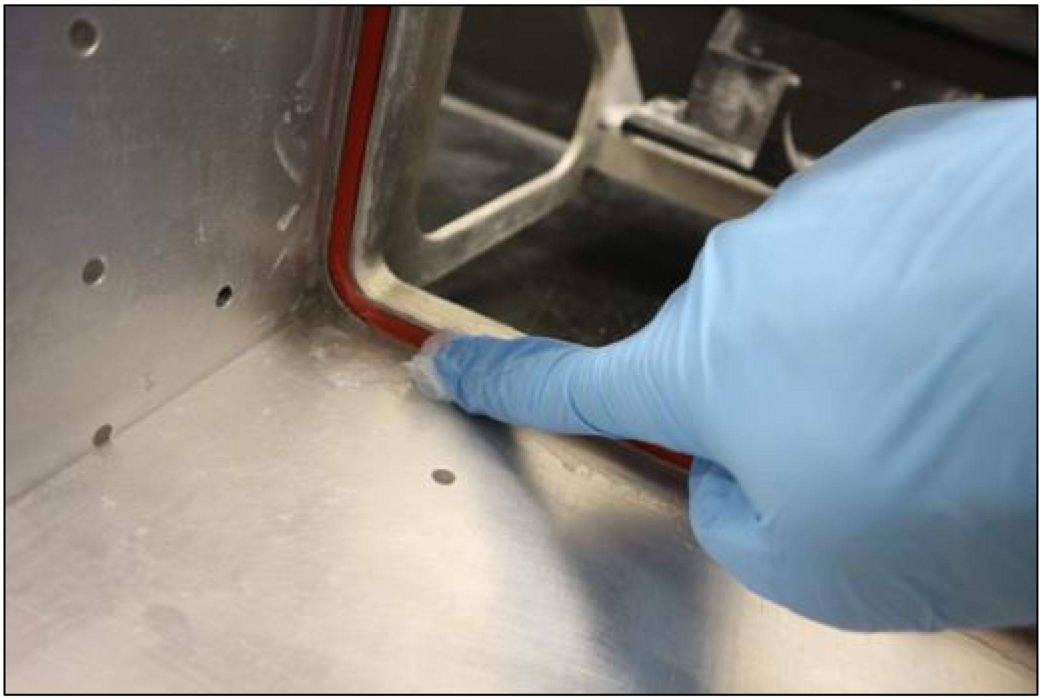

Figure D-6: Filling gaps around rubber seal with grease in bottom track.

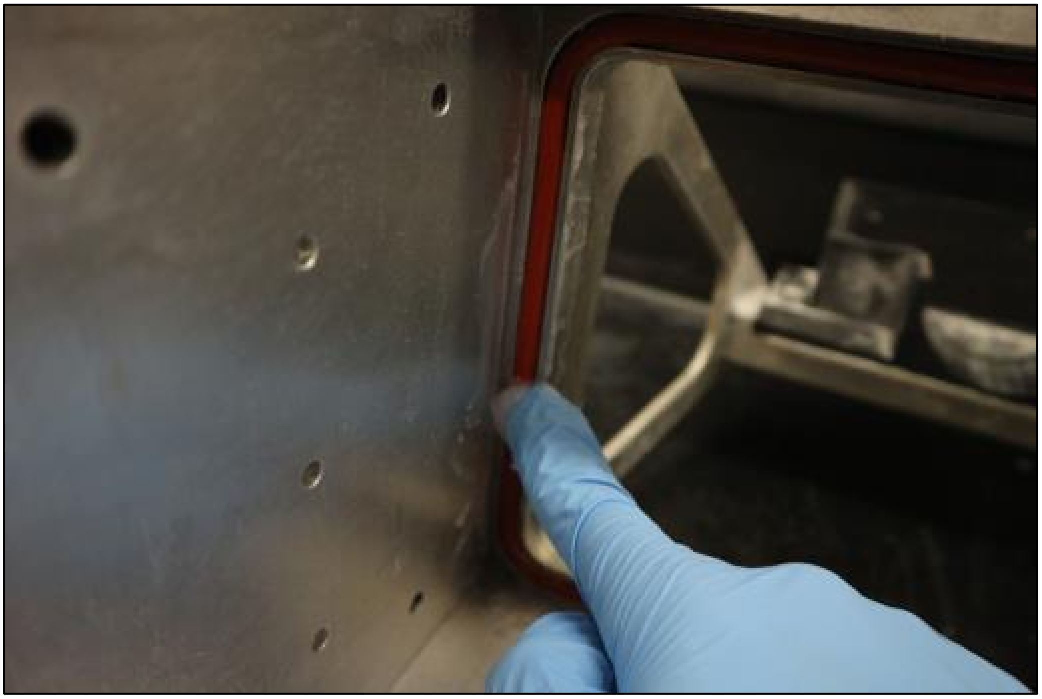

Figure D-7: Filling gaps around rubber seal in side tracks.

4. Slide in the acrylic window with the markers. Ensure that the markers are on the inside of the cradle so that they are visible from the camera's viewpoint. Ensure that there is no sand, grease or other materials at the bottom or the sides of the acrylic window. The presence of such materials may cause a leak of the water within the cradle.

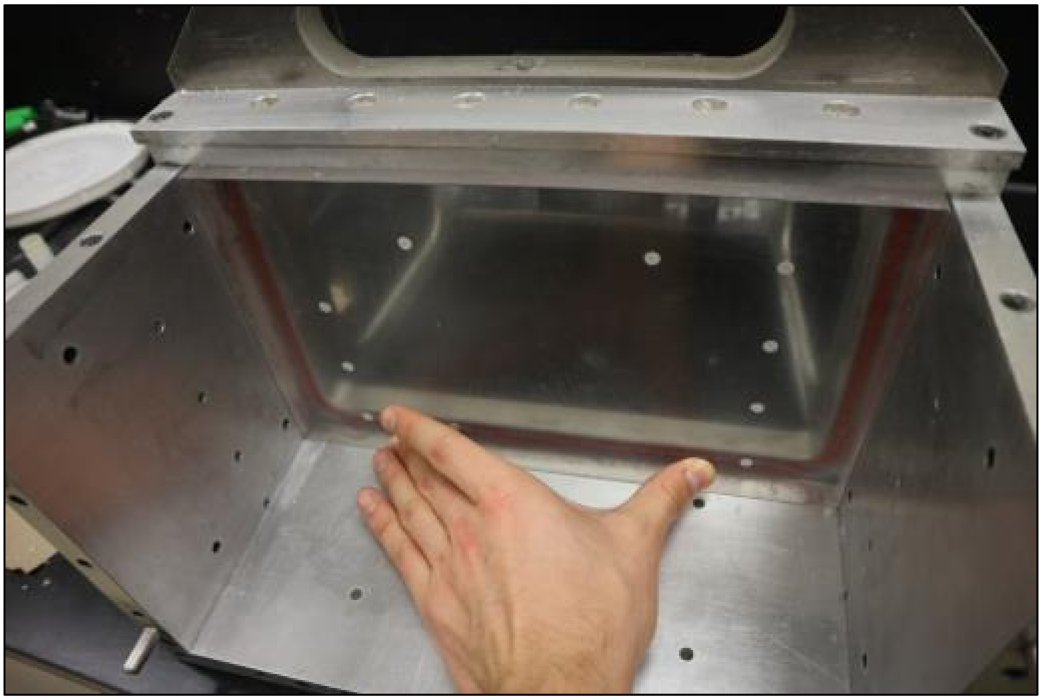

Figure D-8: Installing camera side acrylic window.

5. Apply high vacuum grease at the intersection of the acrylic window and the cradle to prevent any leaks.

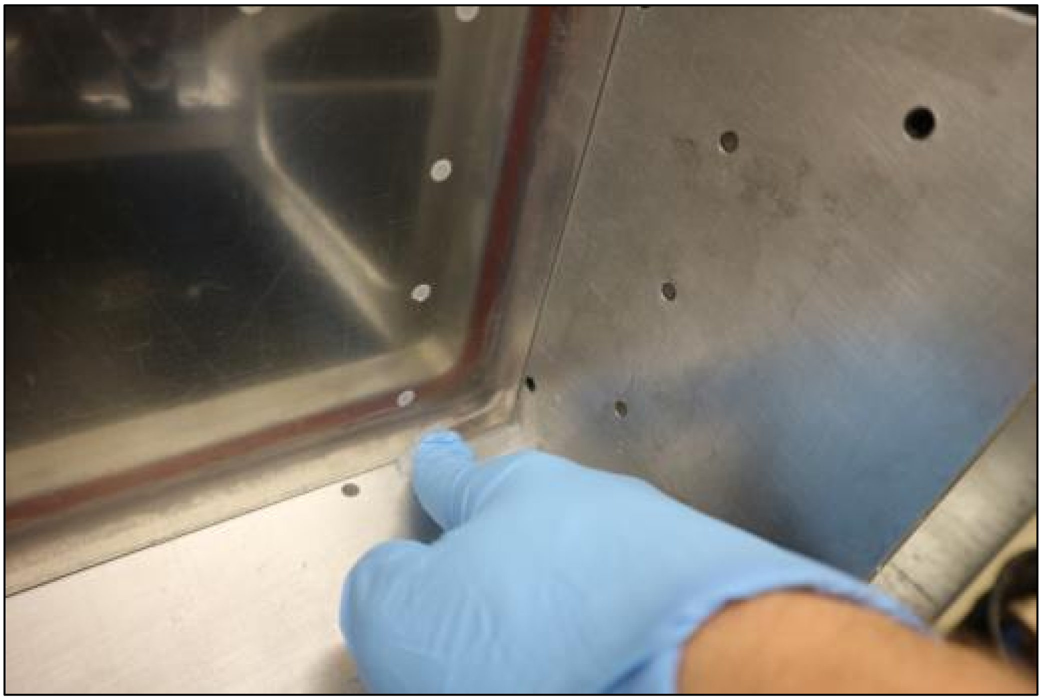

Figure D-9: Applying grease at intersection of the cradle bottom plate and the acrylic window.

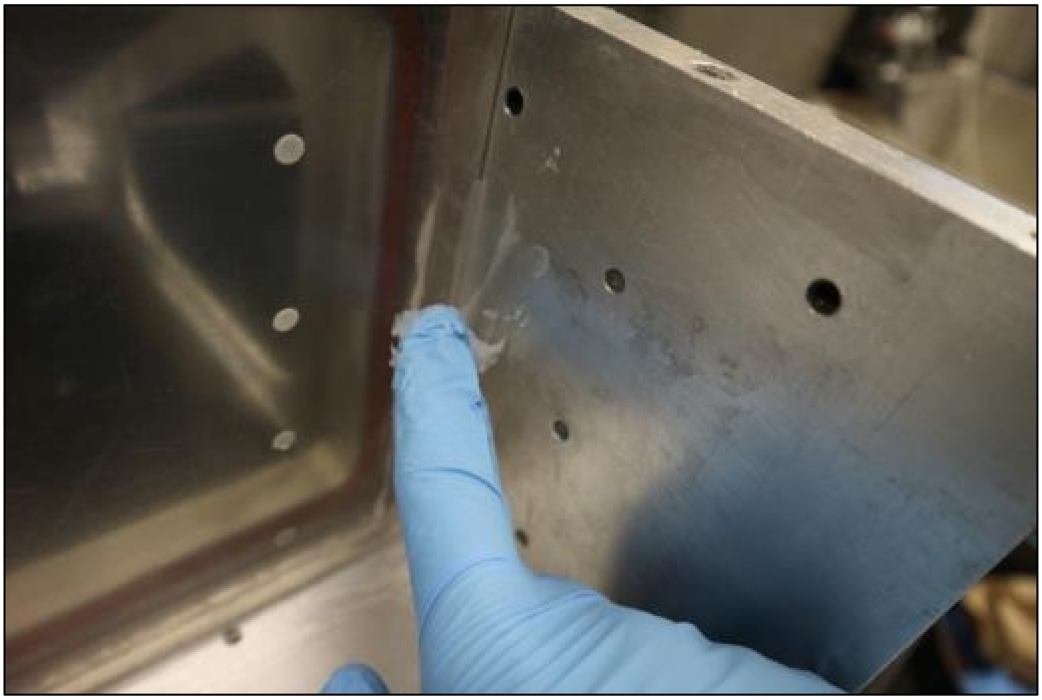

Figure D-10: Applying grease at intersection of the cradle end plates and the acrylic window.

6. Install all four plastic spacer strips with the M6x12 stainless steel capscrews.

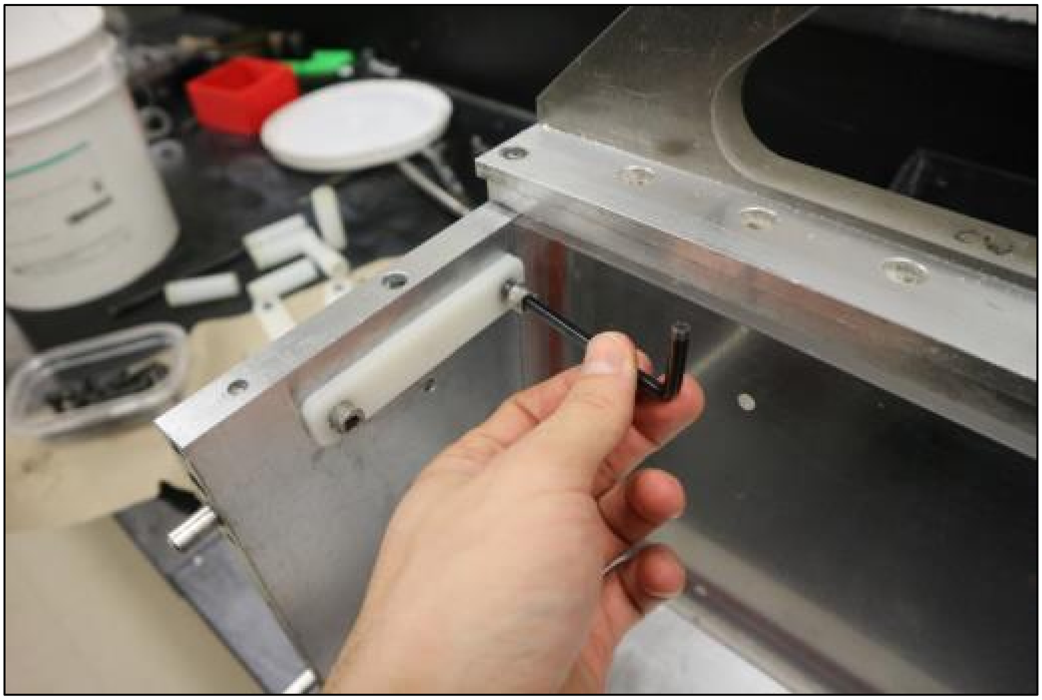

Figure D-11: Installation of plastic spacer strips.

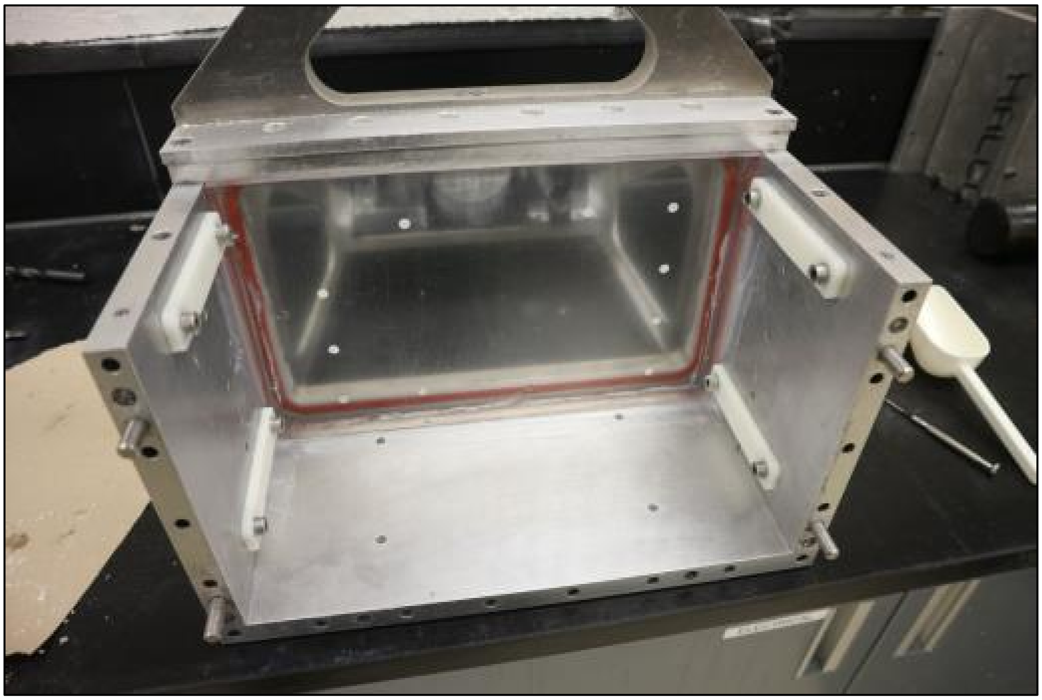

Figure D-12: Four plastic spacer strips installed on cradle.

7. After the spacer strips are installed, apply more high vacuum grease at the intersection of the acrylic window and the base and end plates to ensure an opening was not created during the spacer strip installation.

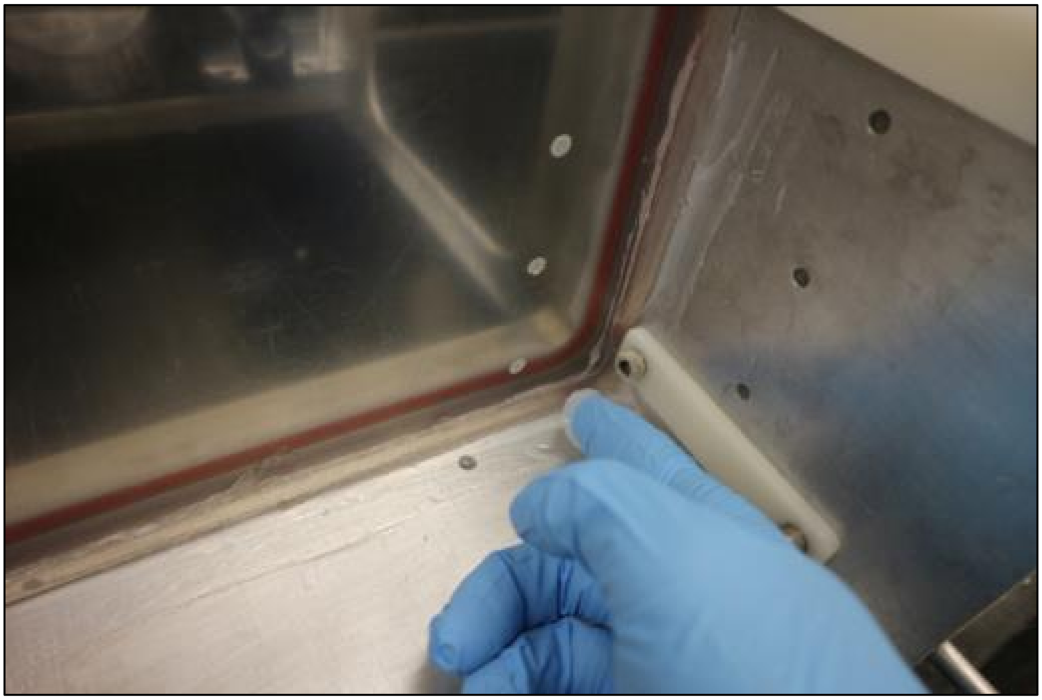

Figure D-13: Applying more grease after installation of plastic spacer strips.

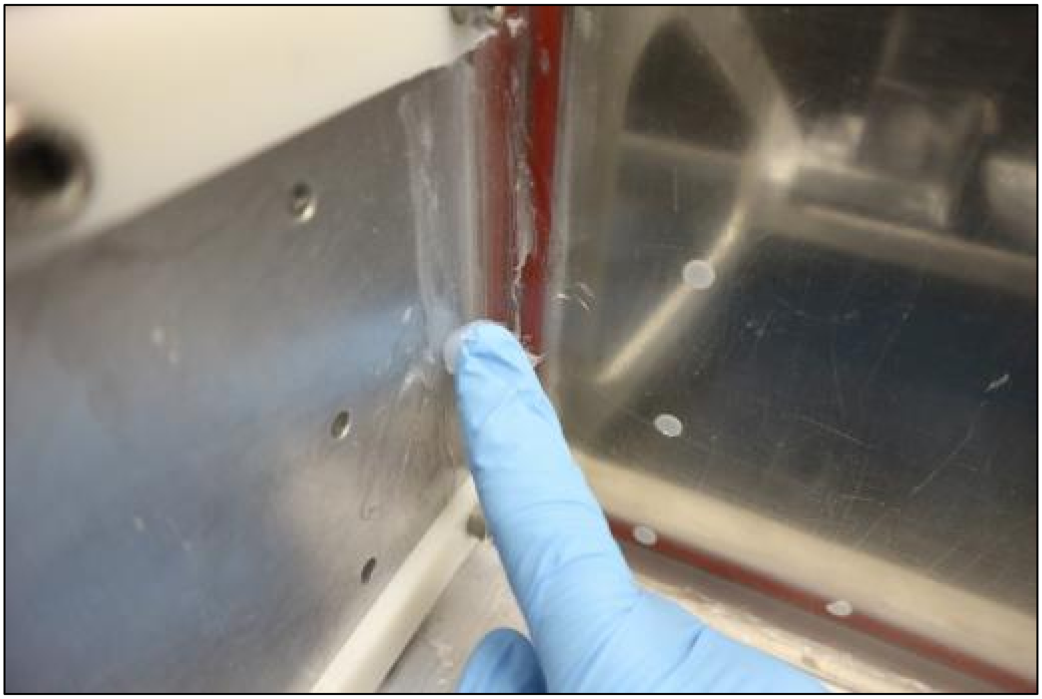

Figure D-14: Applying more grease after installation of plastic spacer strips.

8. Apply high vacuum grease inside the track of the other side plate then insert the rubber seal. Apply high vacuum grease inside the track, around the seal. Apply high vacuum grease around the rubber seal until the track is filled with grease. Grease is only required in the bottom and the side tracks. It is recommended to wear nitrile gloves while applying the grease

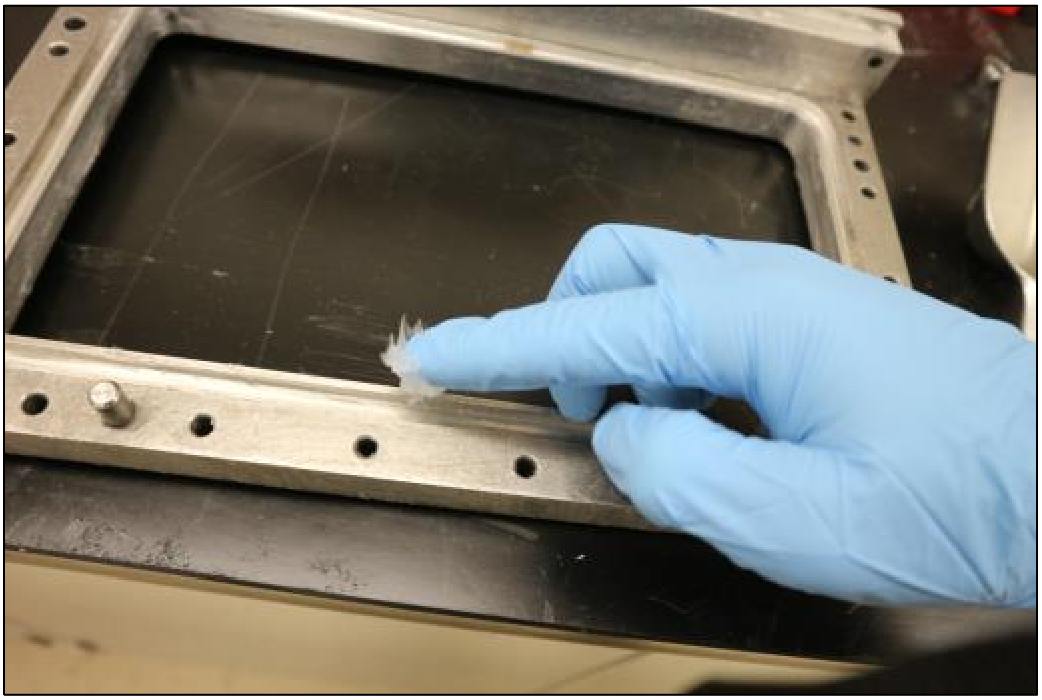

Figure D-15: Applying grease in bottom track of the other cradle side plate.

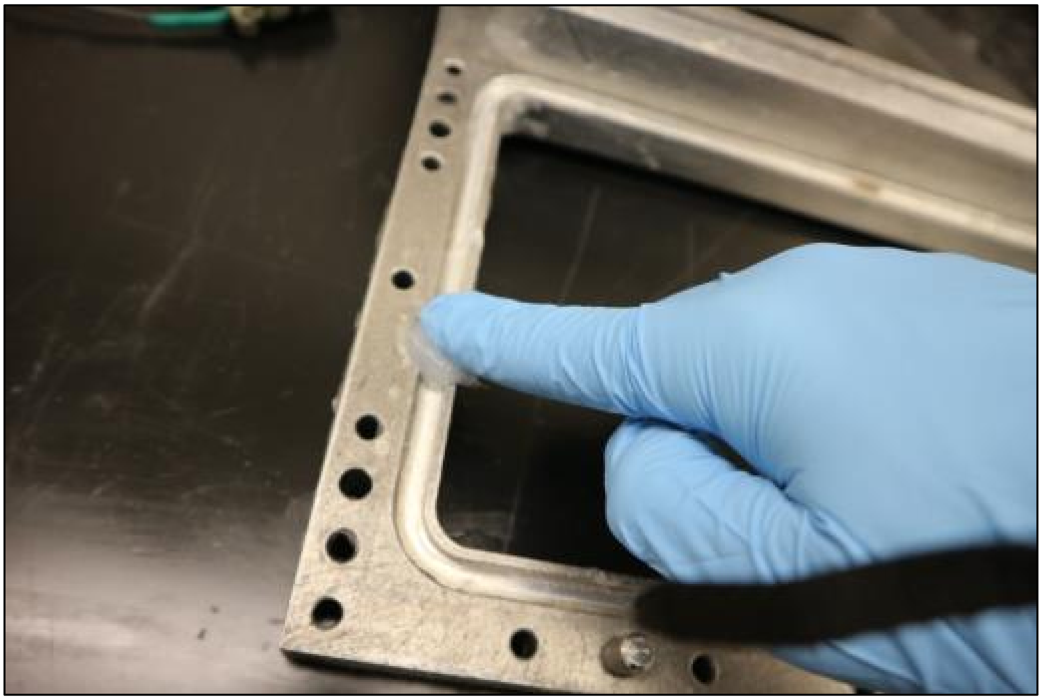

Figure D-16: Applying grease in side tracks of the other cradle side plate.

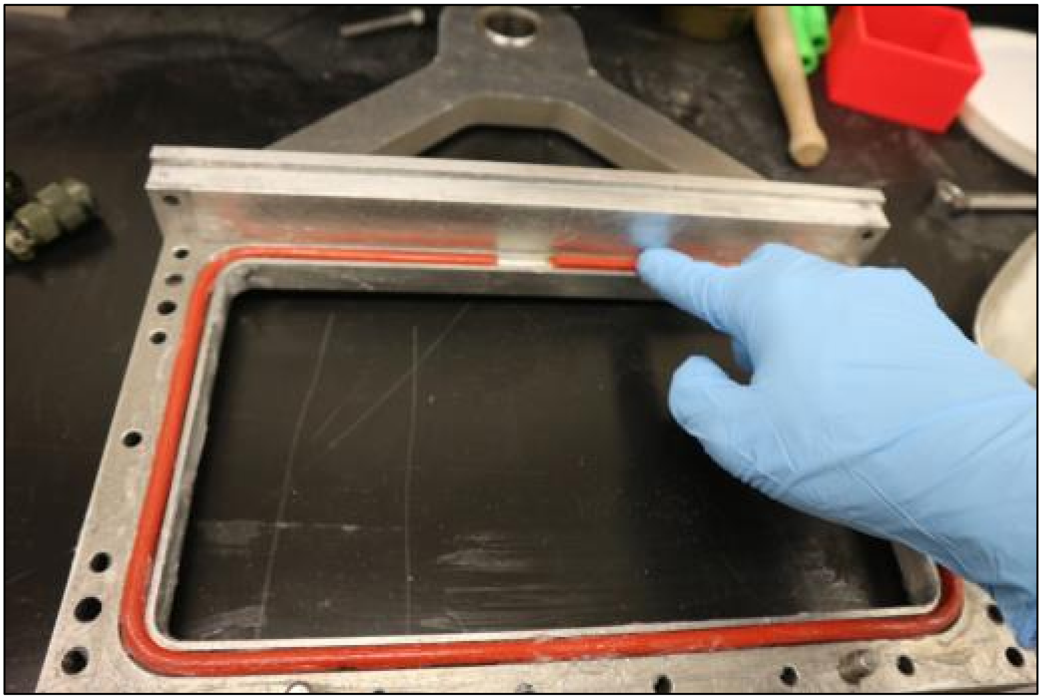
Figure D-17: Installing rubber seal in the other side plate.

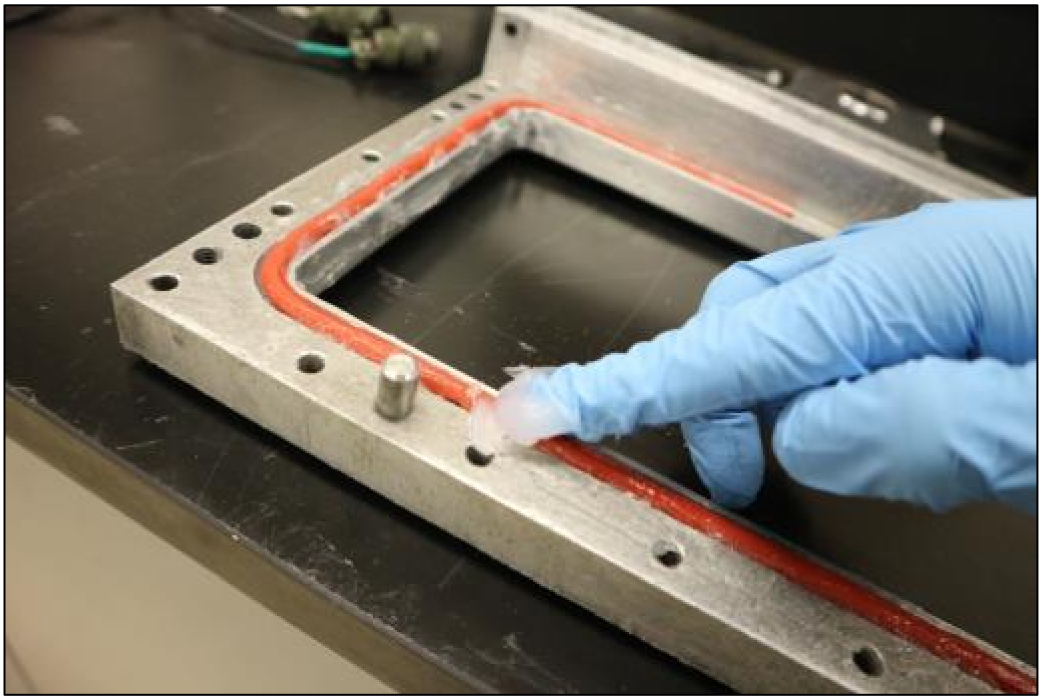
Figure D-18: Filling gaps around rubber seal with grease.

9. Slide in the second acrylic window. Ensure that there is no sand, grease or other materials at the bottom of the acrylic window. The presence of such materials may cause a leak of the water within the cradle.

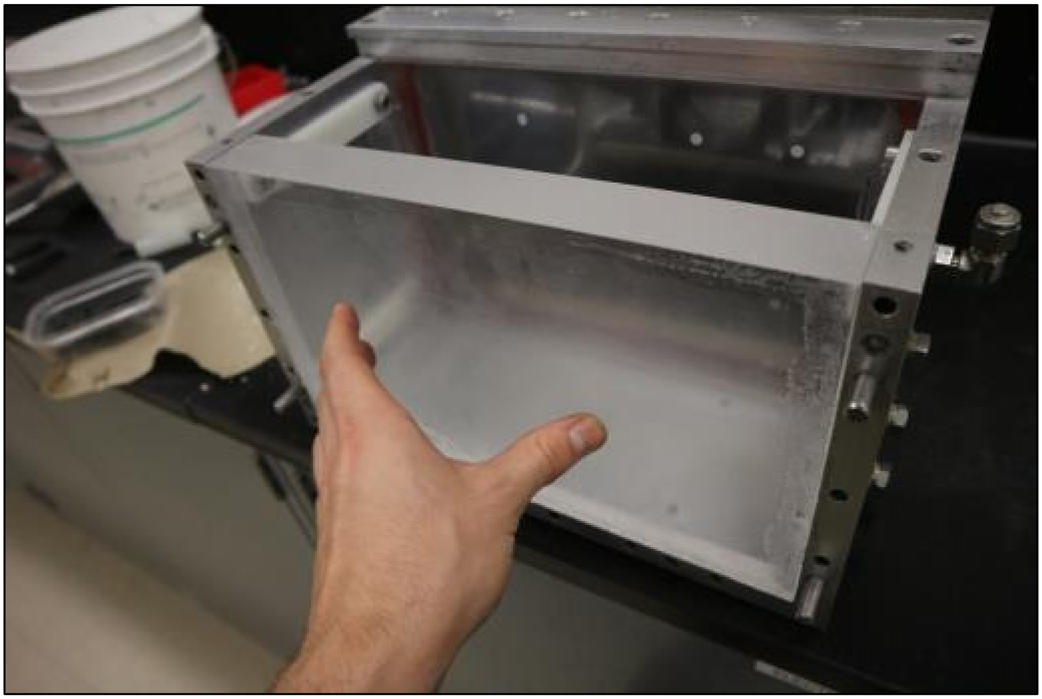

Figure D-19: Installation of the second acrylic window.

10. Ensure that all dowels are inserted in the cradle side plate. Slide the side plate onto the base and end plates with the help of a rubber mallet.

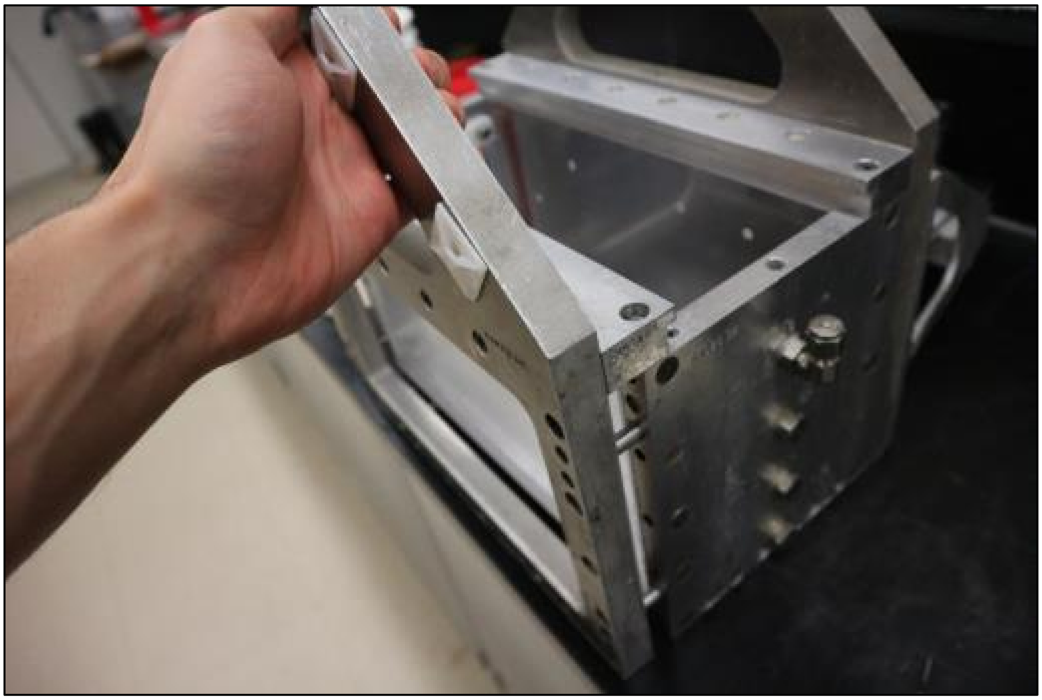

Figure D-20: Installation of second cradle side plate.

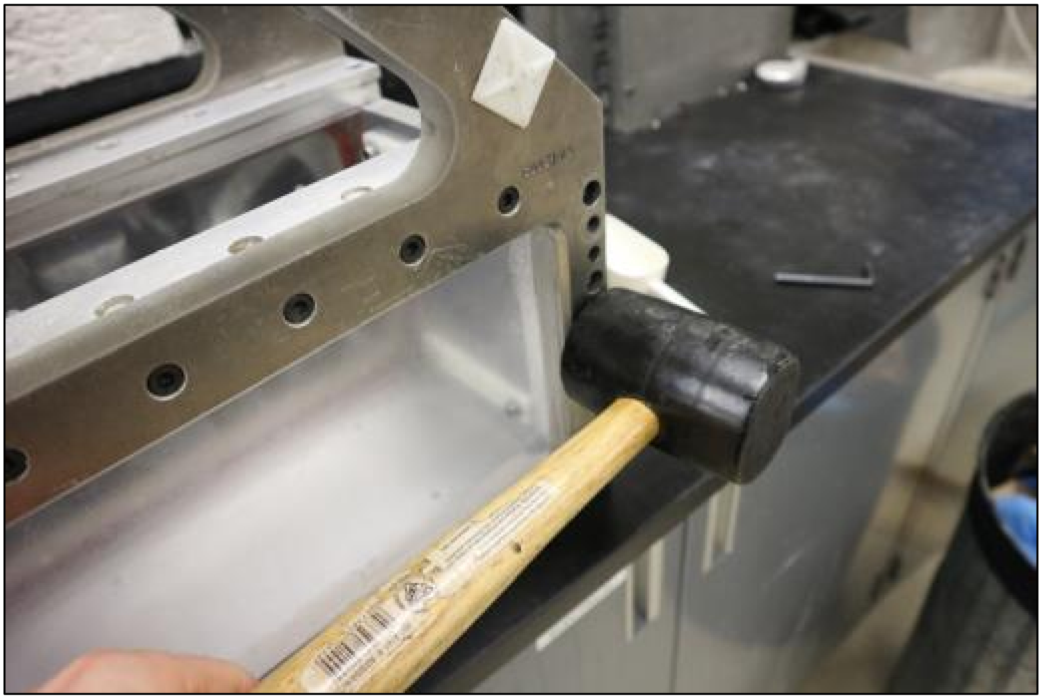

Figure D-21: Using mallet to help install second cradle side plate.

11. Insert the sixteen (16) M6x30 socket head capscrews and tighten the ones at the bottom of the side plate.

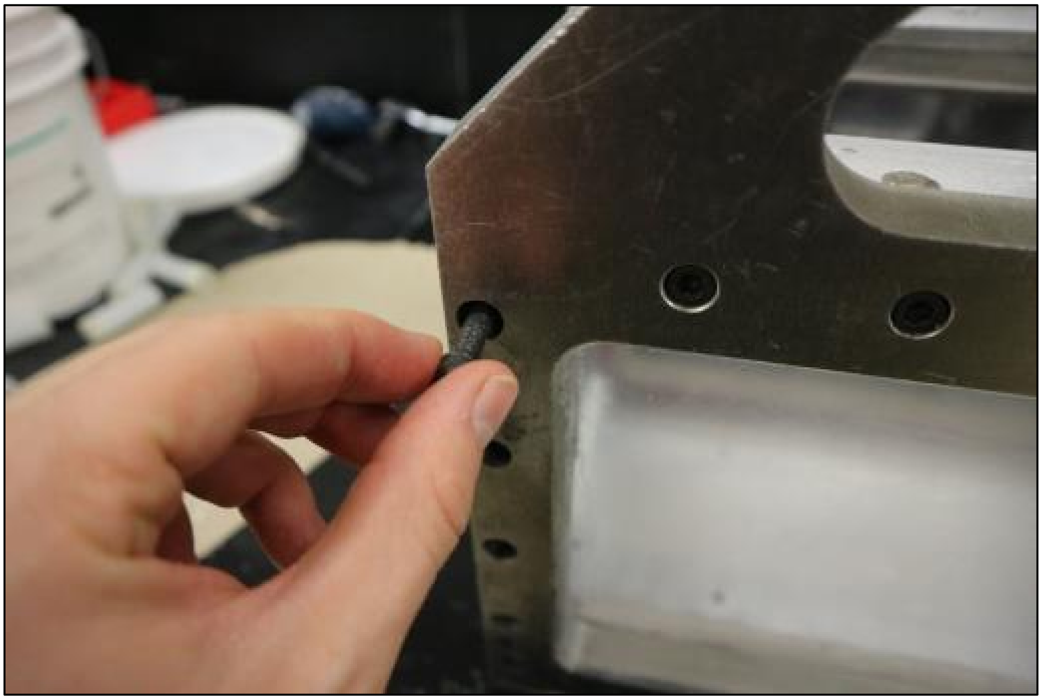

Figure D-22: Installing capscrews in side plate.

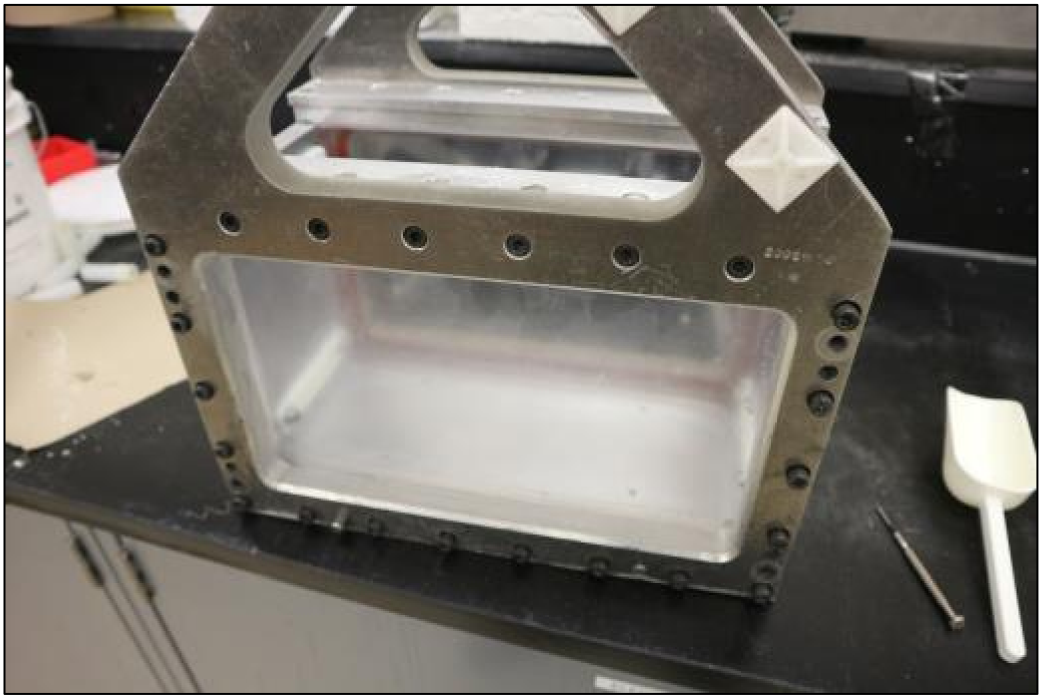

Figure D-23: Capscrews ready for tightening.

Figure D-24: Tightening capscrews.

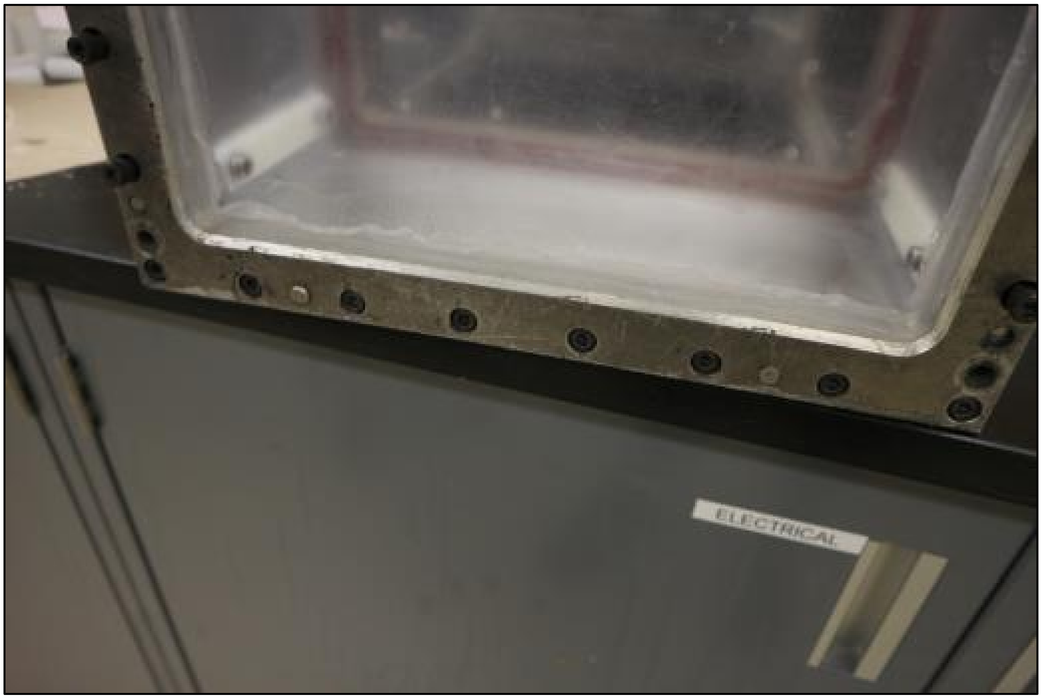

Figure D-25: Bottom row of capscrews tightened.

12. Apply high vacuum grease at the intersection of the second acrylic window and the cradle to prevent leaks.

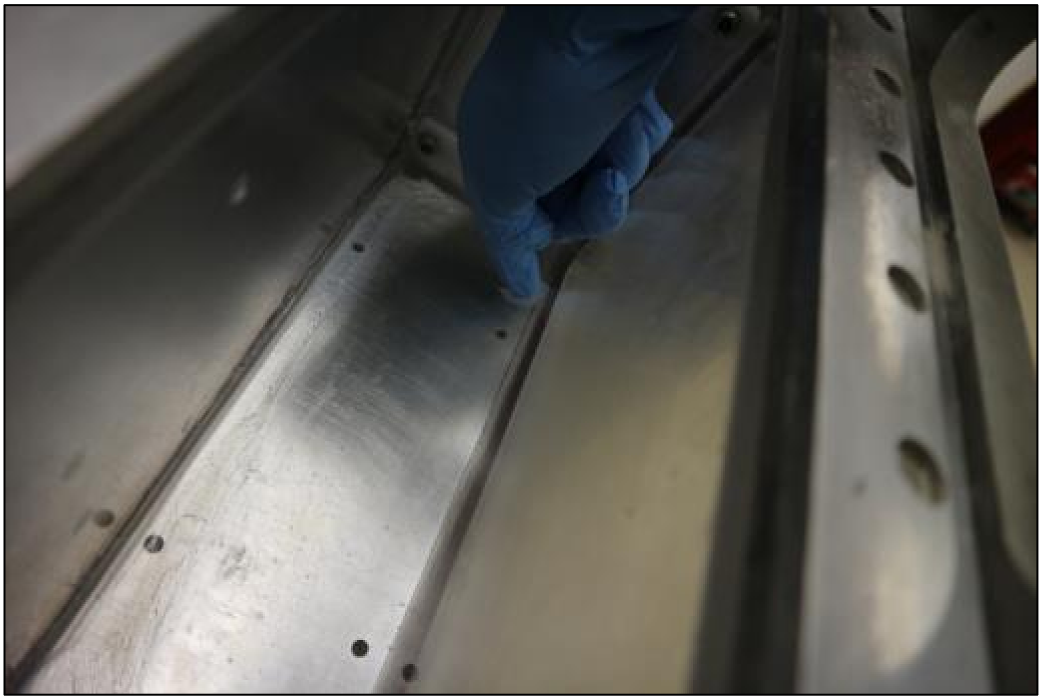

Figure D-26: Applying grease at intersection of the second acrylic window and the cradle.

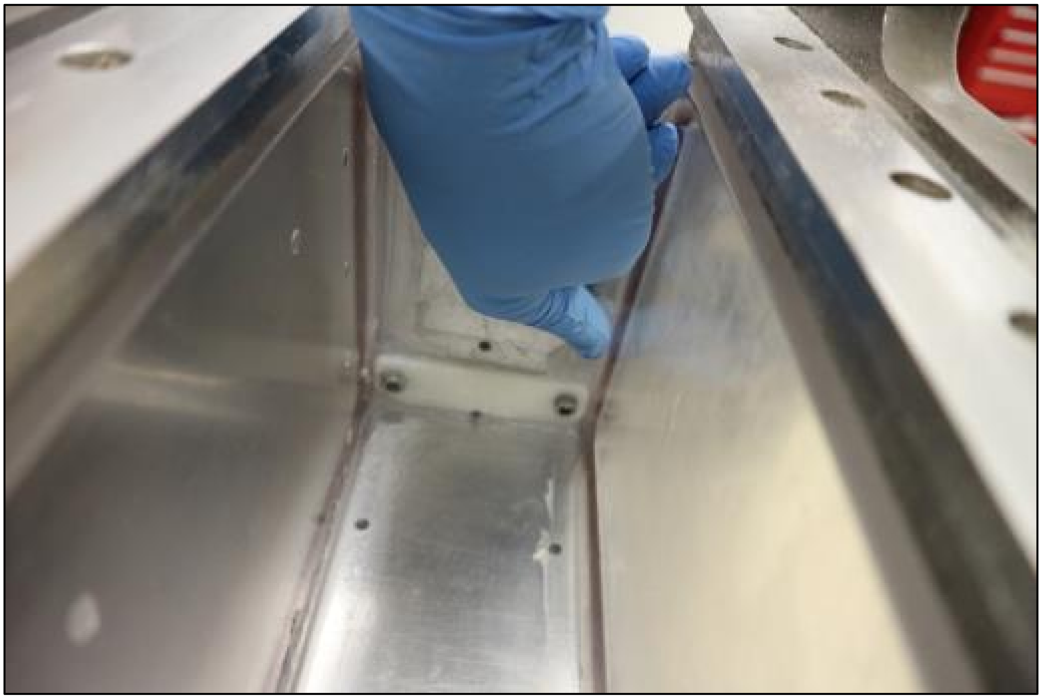

Figure D-27: Applying grease at the intersection of the acrylic window and the cradle.

13. Record the mass of a large stainless steel pan and then fill it with approximately 8 kg of #730 silica sand (Beddoe & Take, 2015). Record the mass of sand added to the pan.

Figure D-28: Recording mass of steel pan.

14. Add water to the sand to reach the desired initial moisture content. Record the mass of water added to the sand. Ensure that the sand and water are mixed properly so that the moisture content is consistent. #730 silica sand reaches saturation at a water content of approximately 18.

Figure D-29: Recording mass of sand.

Figure D-30: Recording mass of water added to sand.

Figure D-31: Mixing of sand and water.

15. Slide the climate box approximately 3-5 cm into the cradle rails. The space between the inserted end of the box and the closest end plate should be large enough for the thermistors to pass through. Ensure that the areas where the box will slide are free from any sand, grease or other materials.

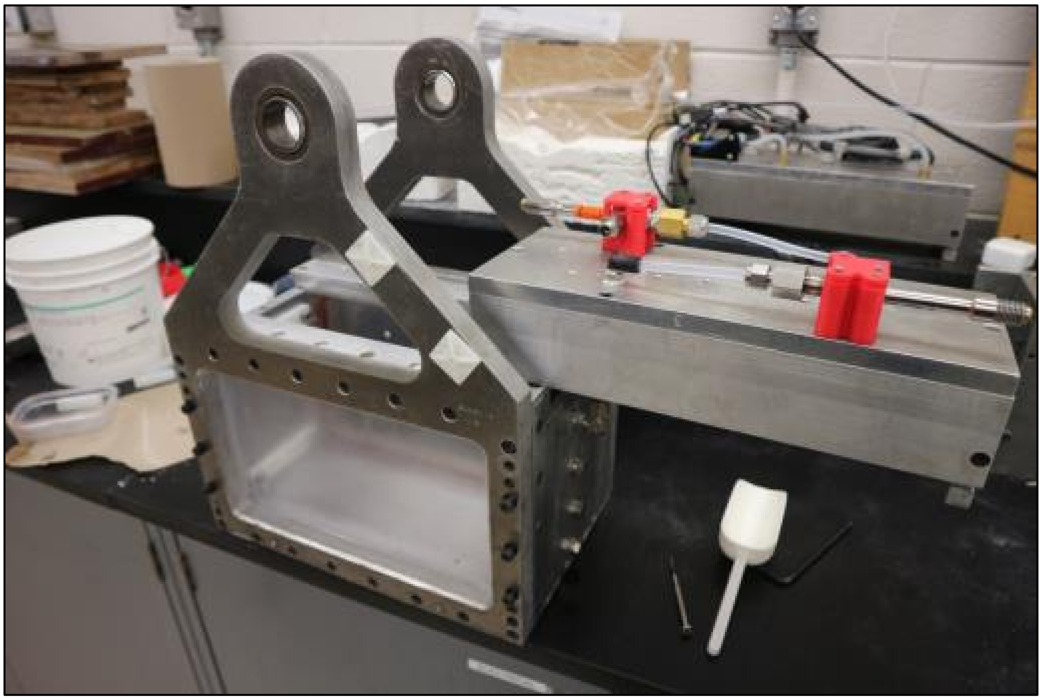

Figure D-32: Sliding the climate box onto the cradle rails.

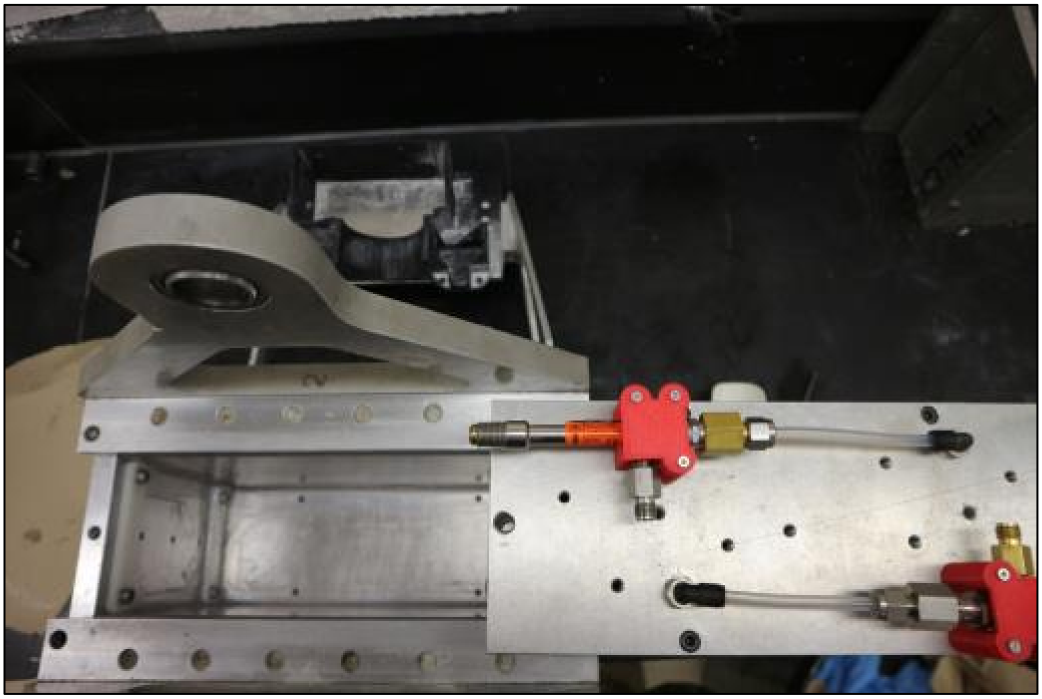

Figure D-33: Top view of climate box on the cradle.

16. Before adding the sand and water to the cradle, ensure that all gaps are well sealed with high vacuum grease.

17. If insulation is required inside the cradle for the experiment, it can be added at this stage, prior to adding the soil in the cradle. Measure the height of the insulation.

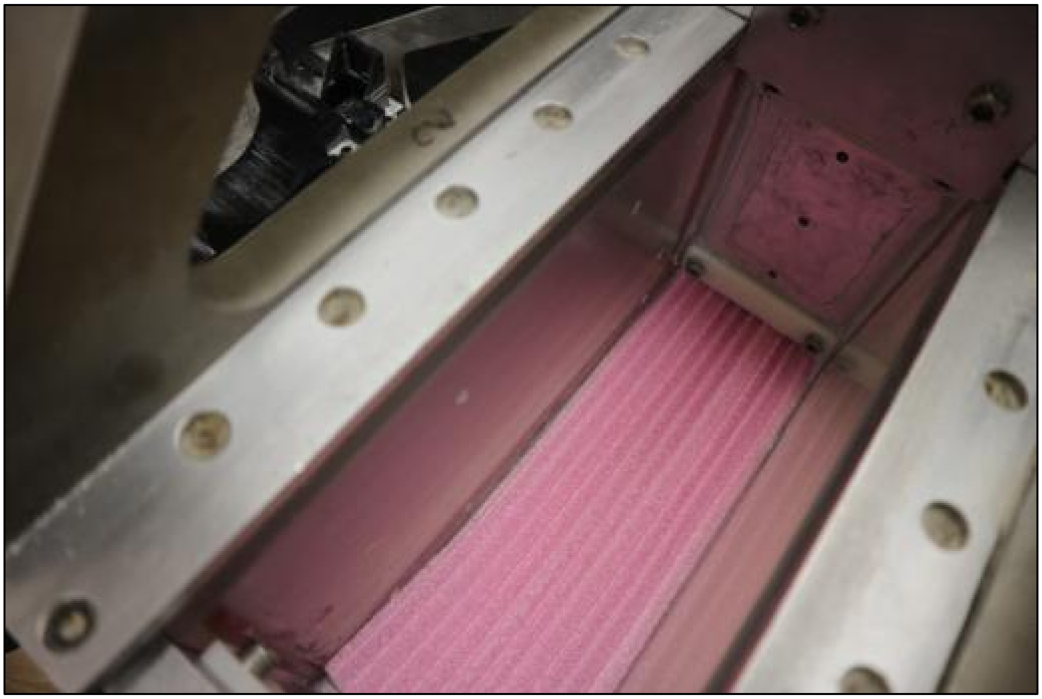

Figure D-34: Placing insulation at the bottom of the cradle.

18. Add the sand/water mixture to the cradle in layers of approximately 1 cm. Compact each layer with a rubber tamper. Ensure that the sand is compacted evenly throughout the whole area.

Figure D-35: Adding sand and water mixture to the cradle.

Figure D-36: Compaction of sand in the cradle.

19. Place the thermistors based on the desired layout within the soil. They shall first be inserted in a hole in the top of the climate box, then inserted through the gap between the climate box and the cradle end plate and lastly, in the soil. The thermistors should be installed as the sand layers are added to prevent any added stress on the thermistors by punching them through the soil.

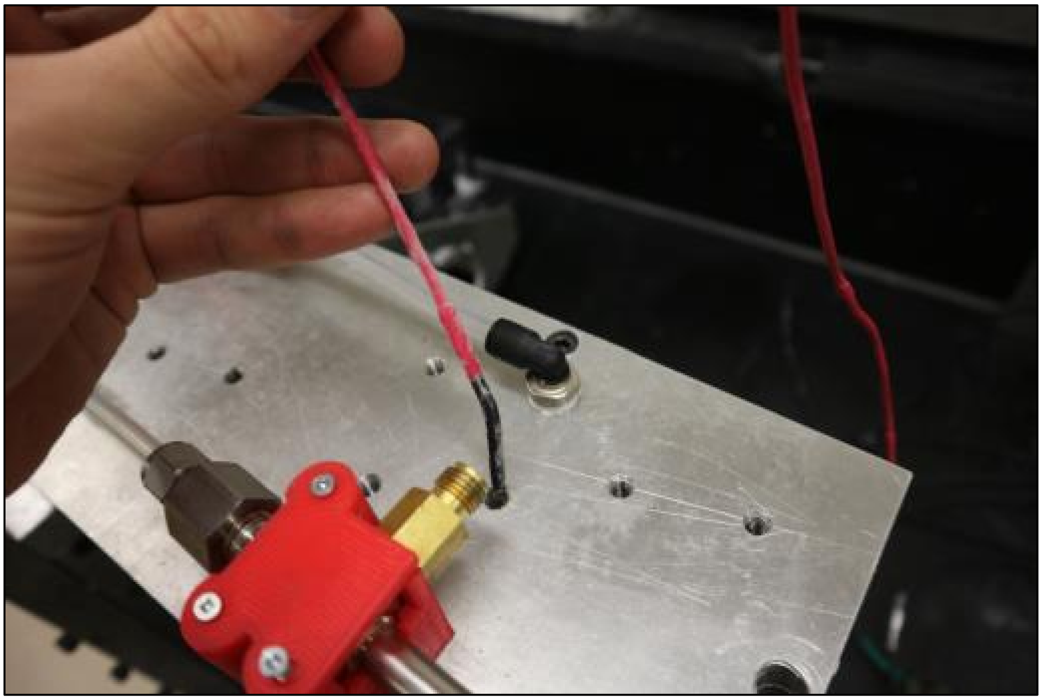

Figure D-37: Inserting thermistor through climate box.

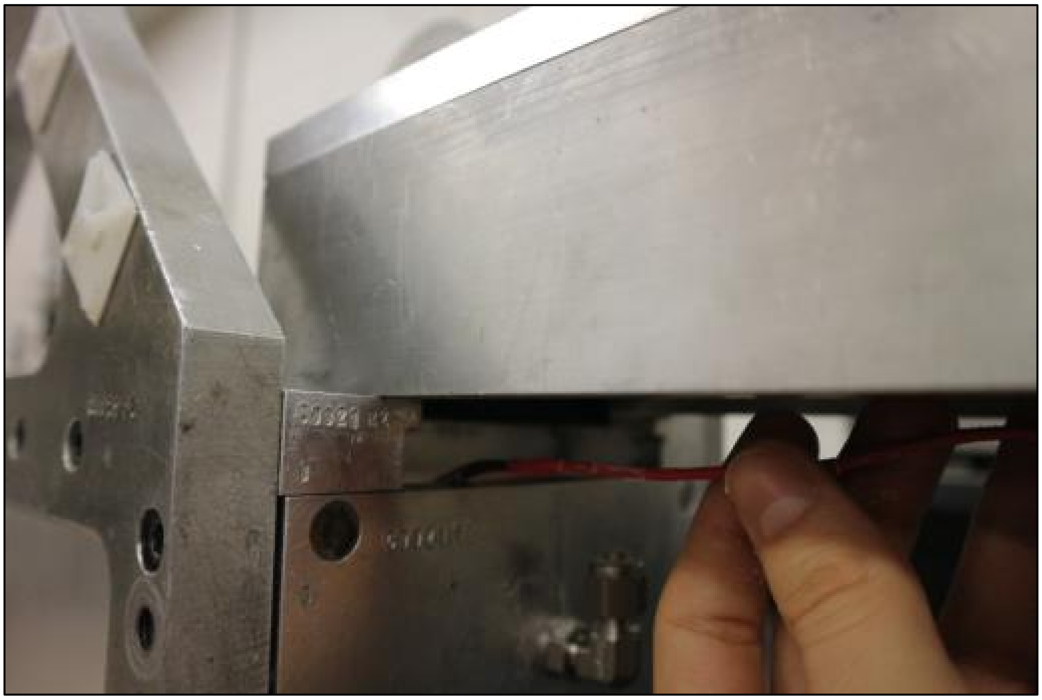

Figure D-38: Passing thermistor between the climate box and the cradle.

Figure D-39: Inserting the thermistor in the sand prior to compaction.

20. If the cradle is being frozen prior to the experiment, insert vial spacers where the oil vials will be added in the soil. This will make it easier to insert the vials in the frozen soil prior to the start of the experiment. Ensure that the top of the vial spacers are below the top of the acrylic windows. Ensure that the vial spacers are as close to the acrylic window as possible.

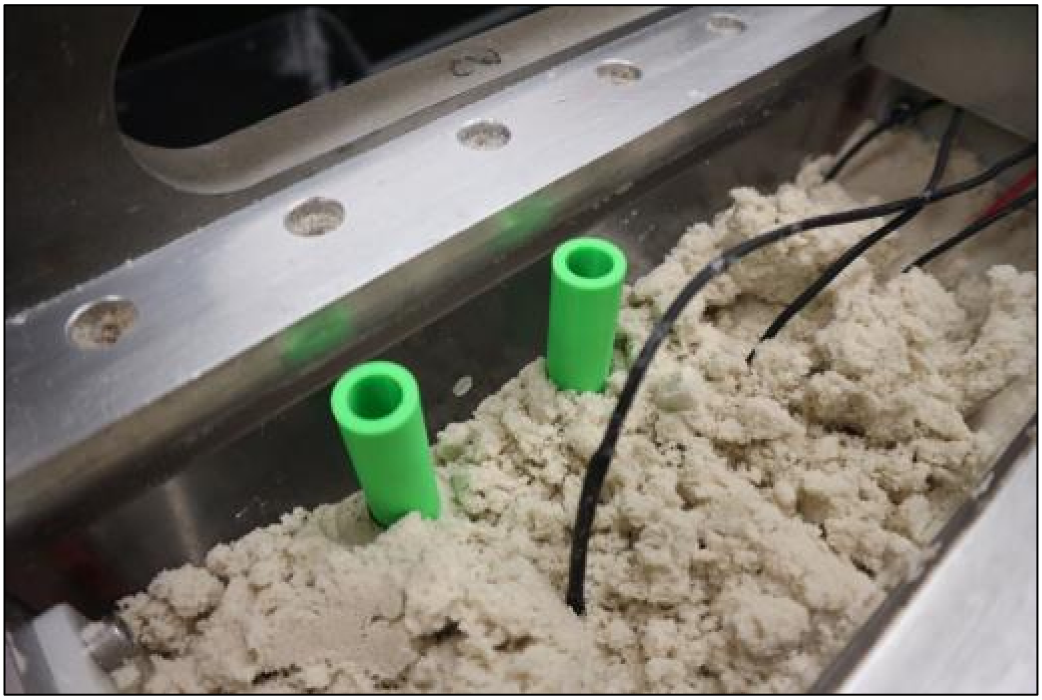

Figure D-40: Inserting vial spacers in the sand.

21. Once the desired amount of soil is added inside the cradle, ensure that it is level and compacted evenly then measure and record the height difference between the top of the cradle and the soil. Determine the volume occupied by the soil and water mixture. Remember to remove the volume occupied by the plastic spacer strips, the M6x12 stainless steel capscrews and the insulation.

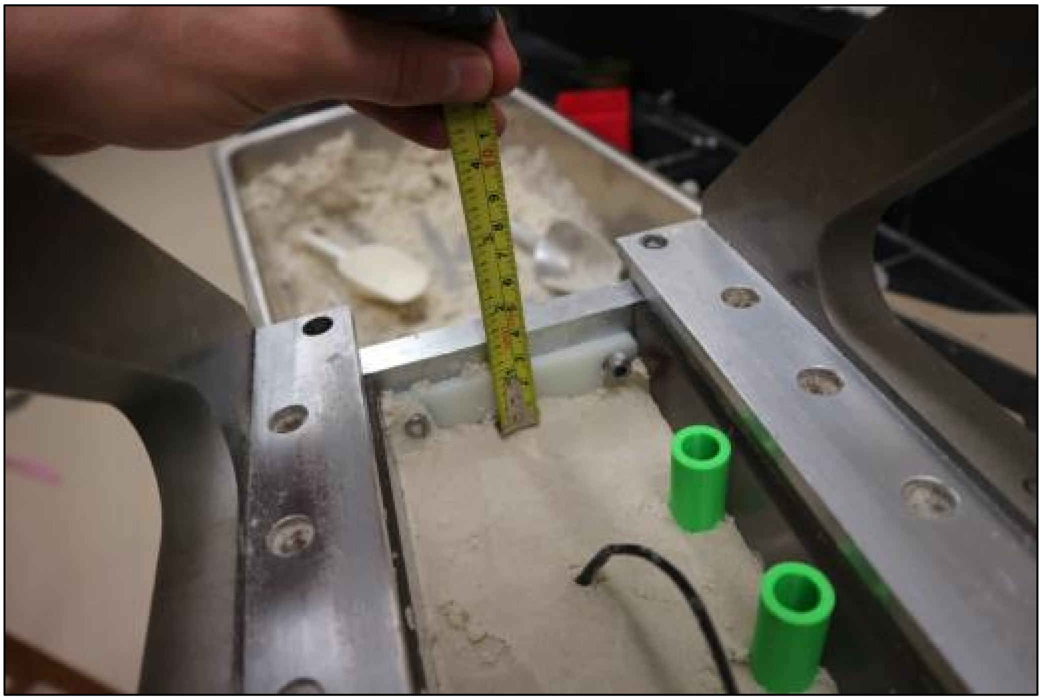

Figure D-41: Determining height of soil in the cradle.

22. Collect at least three samples of the remaining soil & water mixture and record their moisture content. This will determine the initial moisture content of the soil in the cradle. Calculate the void ratio and porosity of the sample after the moisture content is determined.

23. Record the mass of the primary cradle with the camera in the camera mount and record the mass of the secondary cradle, which balances the weight of the primary cradle. Both cradles should be within 0.5 kg. The secondary cradle's weight can be changed with small weight bags.

Figure D-42: Recording mass of cradle after adding sand.

24. If the cradle is being frozen prior to the experiment, it can now be put in a freezer or cold room at the desired temperature. It is recommended to freeze the cradle overnight to ensure a uniform temperature throughout the soil.

25. When ready to start the experiment, remove the vial spacers from the soil. Remove the caps from the oil vials and insert them upside down in the soil where the vial spacers were placed. It is recommended to add some wet soil to fill the empty space at the mouth of the vials. This will prevent the oil from seeping along the acrylic window. The vial should be inserted as close to the acrylic window as possible. Record the time at which the oil vials are added into the soil.

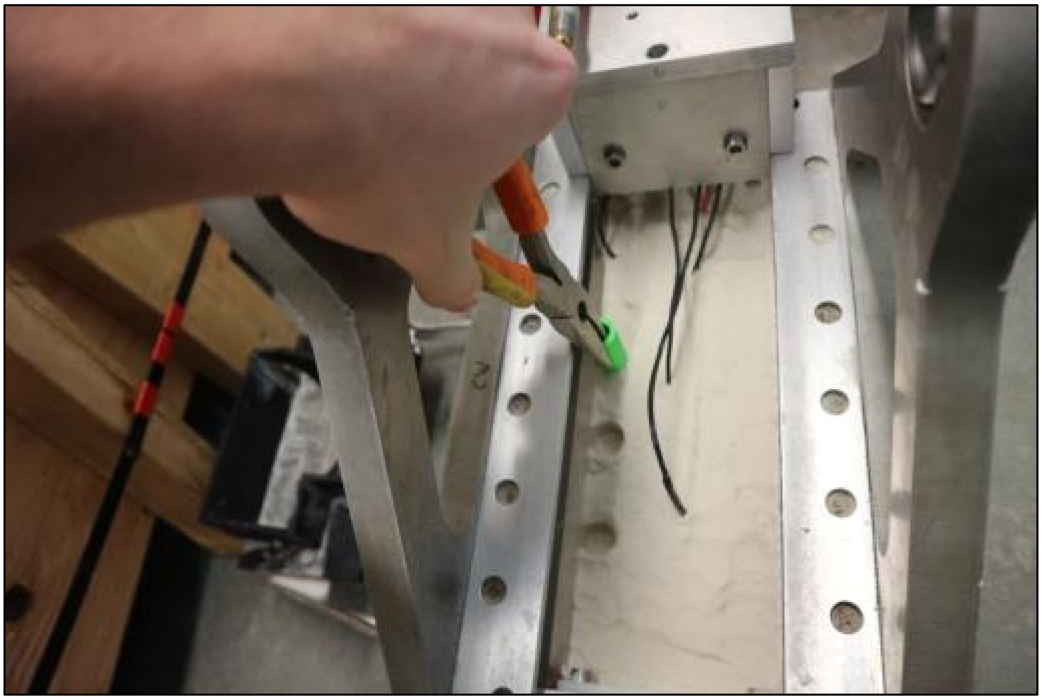

Figure D-43: Removal of vial spacers from the sand.

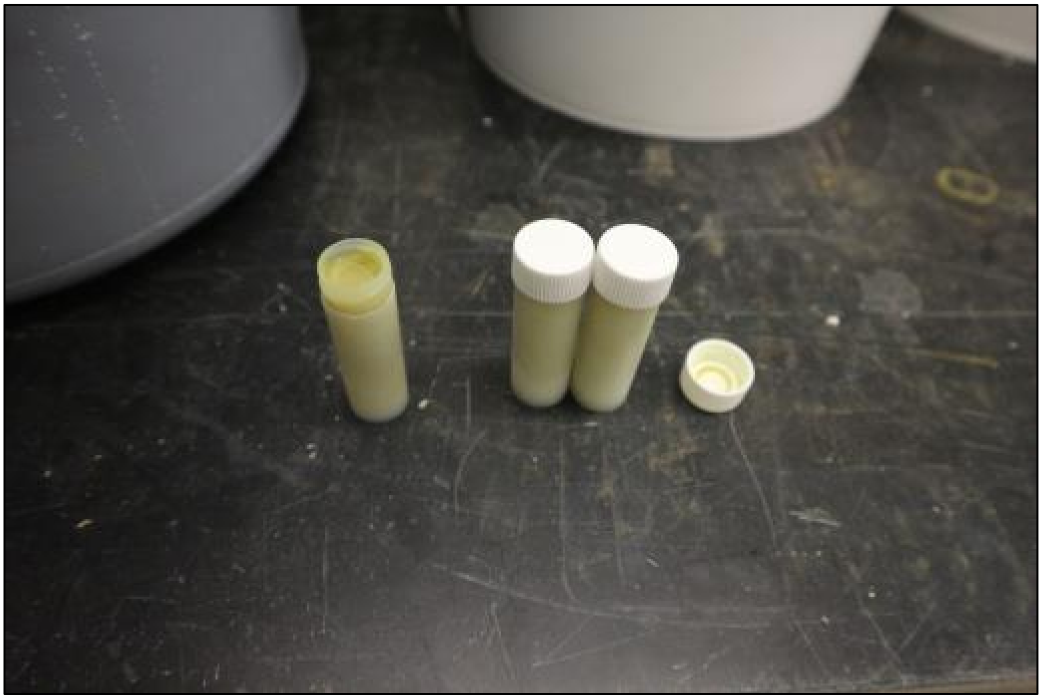

Figure D-44: Removal of caps from the oil vials.

Figure D-45: Adding sand to fill the gap in the oil vial.

Figure D-46: Inserting oil vials in the sand.

26. Slide the climate box over the soil. Insert and tighten the two screw rods; one at each end of the climate box. When sliding the climate over the soil, ensure that thermistor wires are not hanging below the climate box. They can be sheared when sliding the climate box into position.

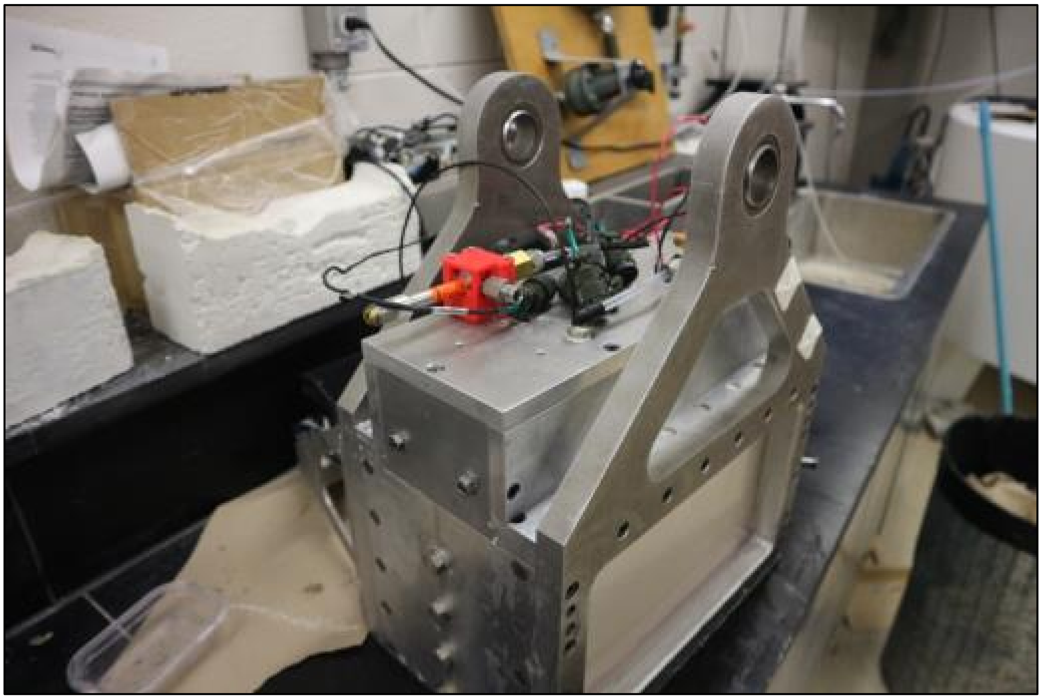

Figure D-47: Placing climate box into position for centrifuge flight.

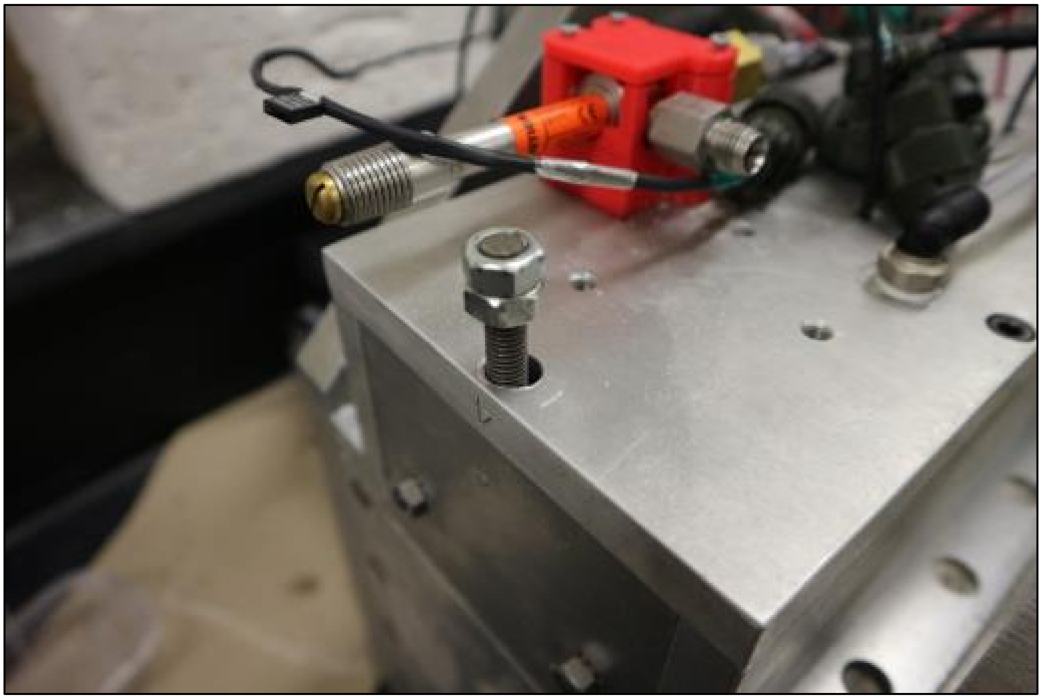

Figure D-48: Installing screw rods to secure the climate box.

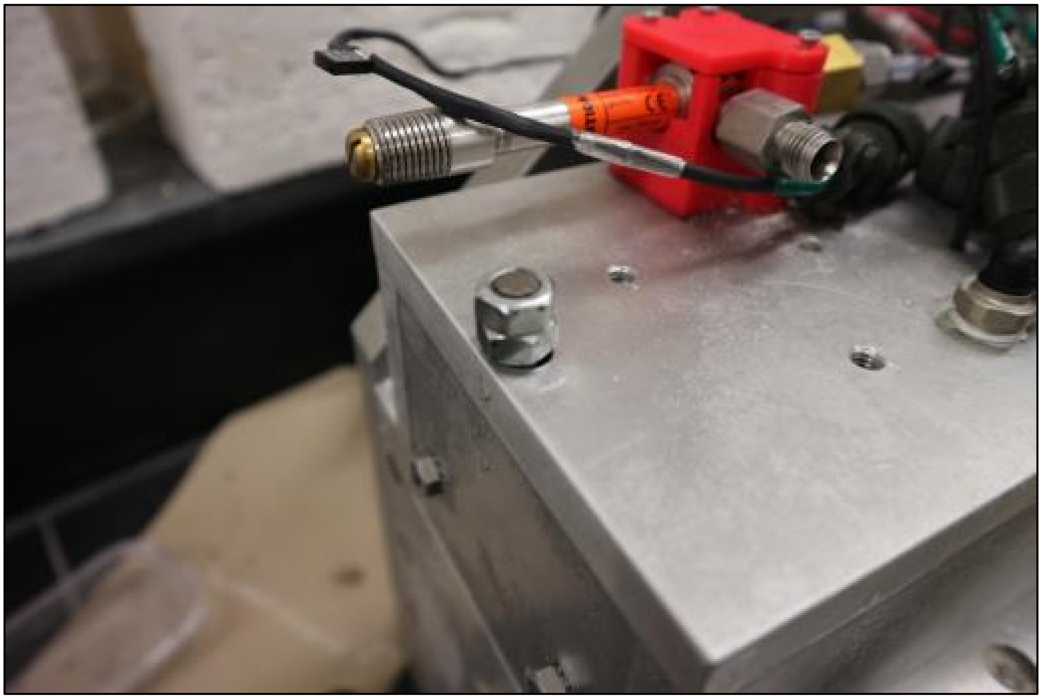

Figure D-49: Tightened screw rod.

27. Tighten the remaining M6x30 screws to secure the side plate. Ensure that there are no leaks. If water is leaking from the cradle, the experiment must be aborted and restarted from Step 1.

28. Place the wooden stand at the bottom of the centrifuge casing.

Figure D-50: Wooden stand placed at the bottom of the centrifuge casing.

29. Rotate the centrifuge’s beam to the angle shown in the image below. This is the position that makes it the easiest to insert the cradle in the centrifuge.

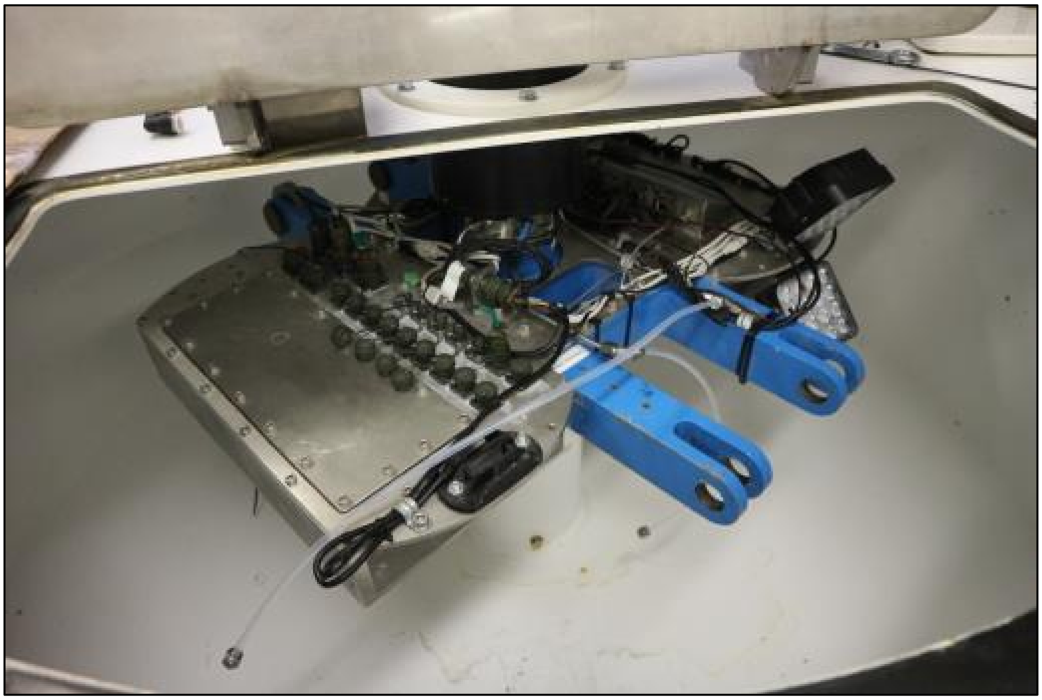

Figure D-51: Position of centrifuge beam for insertion of cradle.

30. Insert the primary cradle into the casing and on the wooden support. Remove the camera from the camera mount before inserting the cradle to prevent damage to the camera.

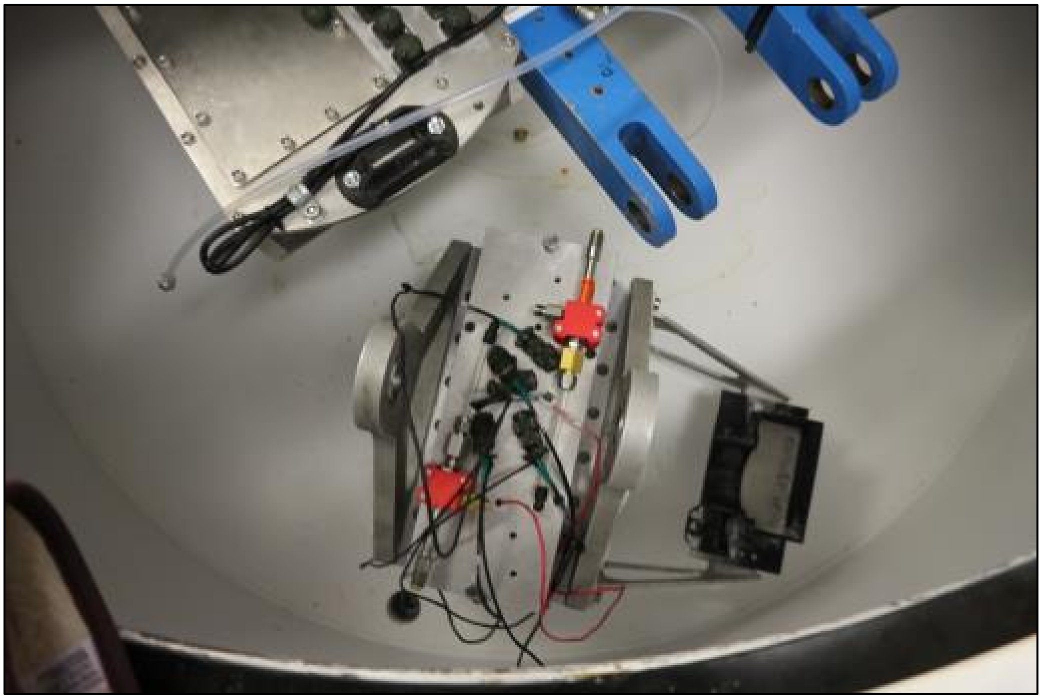

Figure D-52: Cradle placed on wooden stand inside the centrifuge casing.

31. Line up the cradle bearings with the pivot points on the centrifuge beam and then insert the pivot pins. A rubber mallet can be used to help insert the pivot pins. Screw the two parts of the pivots pins together.

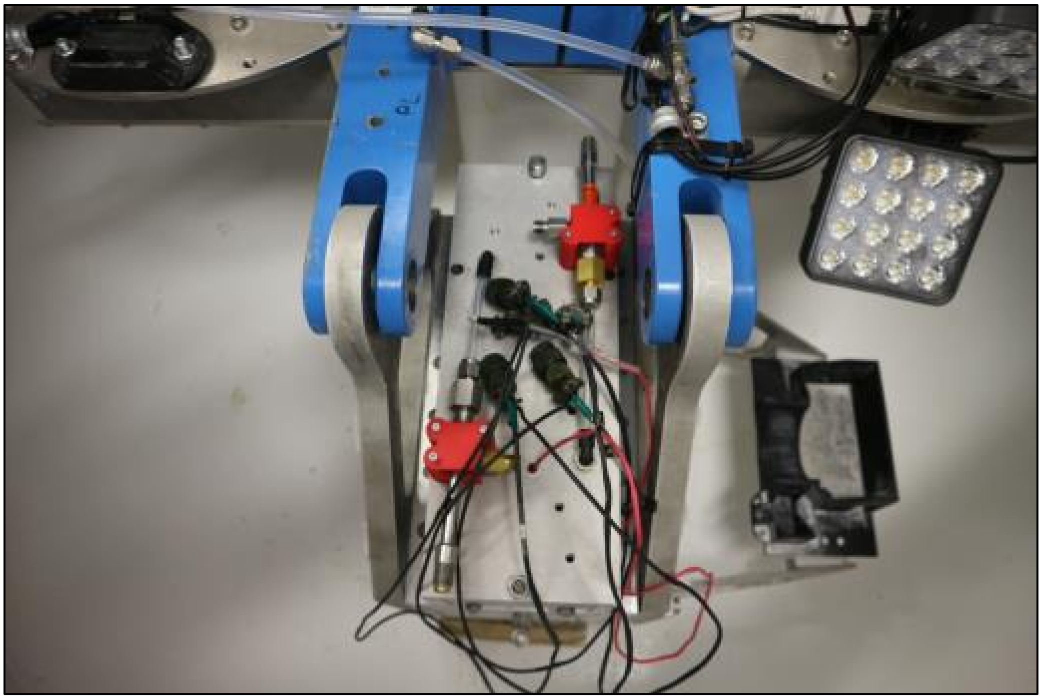

Figure D-53: Cradle and centrifuge beam pivot points lined up.

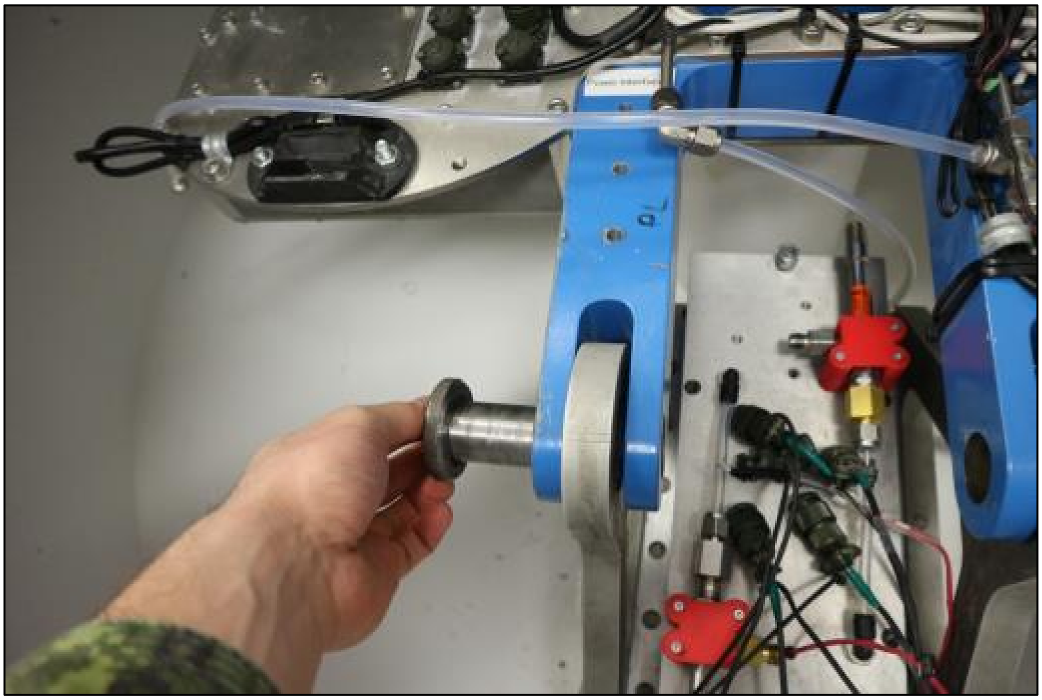

Figure D-54: Insertion of pivot pins.

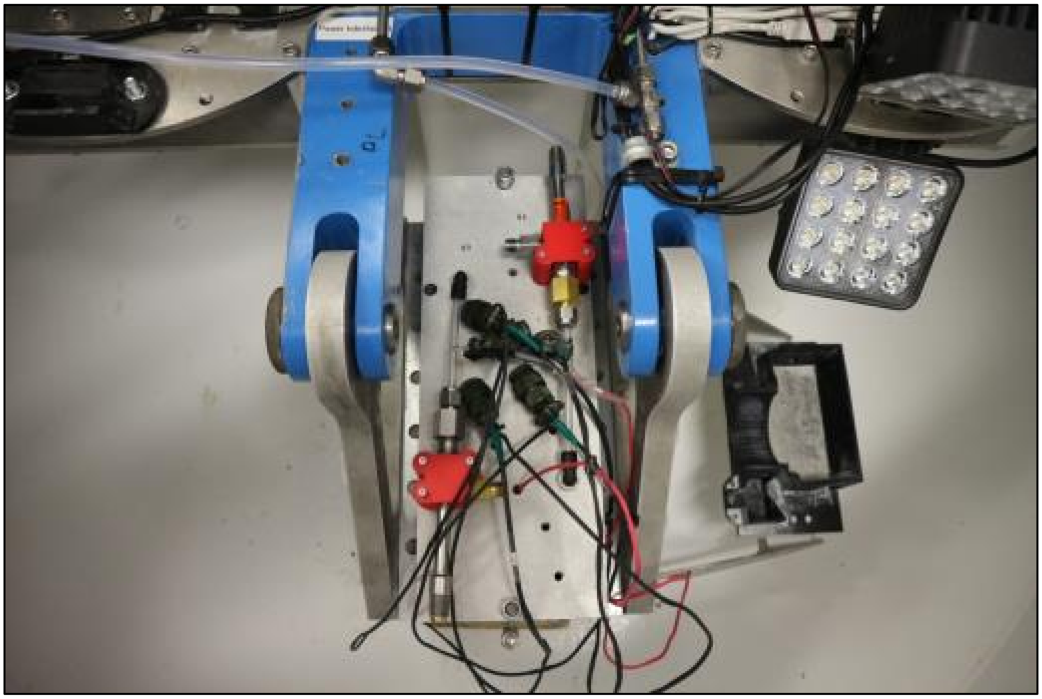

Figure D-55: Both pivot pins inserted.

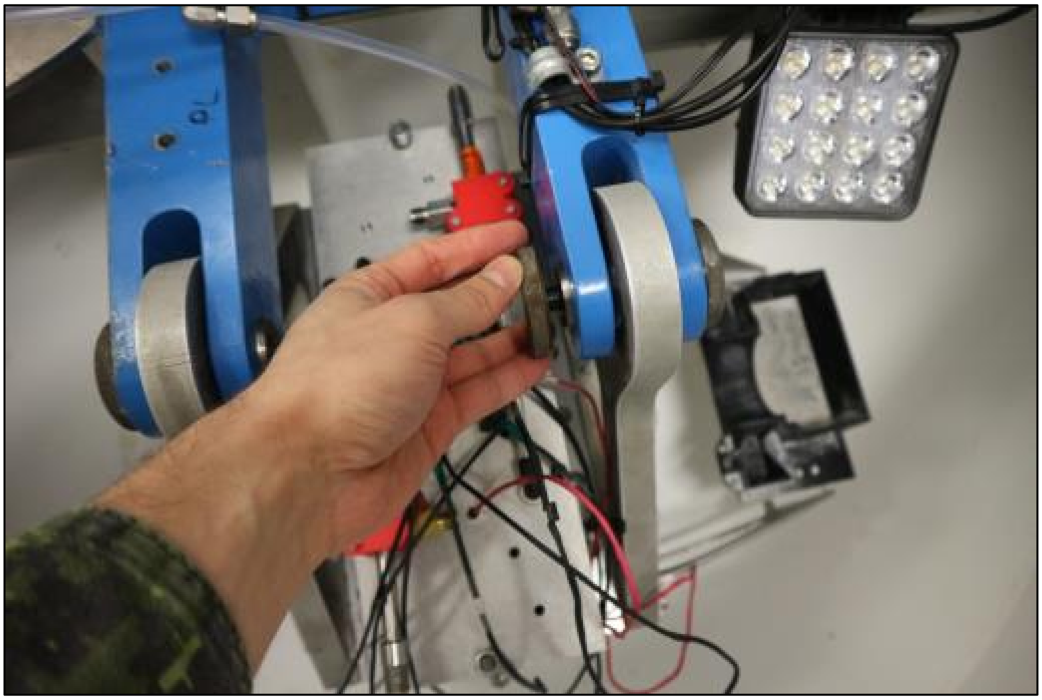

Figure D-56: Screwing on pivot pin caps.

32. Repeat Steps 28 to 31 for the secondary cradle.

33. Remove the wooden stand from under the cradle and take it out of the centrifuge casing.

Figure D-57: Removal of wooden stand from the centrifuge casing.

34. Install the camera and the webcam into their respective mounts on the camera support bracket. Plug the USB cable into the camera.

Figure D-58: Positioning webcam in the camera mount.

Figure D-59: Connecting the power supply for the camera.

Figure D-60: Inserting the power supply into the camera.

Figure D-61: Placing the camera in the camera mount.

35. Connect the thermistors to their respective analog ports i.e. Thermistor 1 goes into Port 1, Thermistor 2 into Port 2, etc.

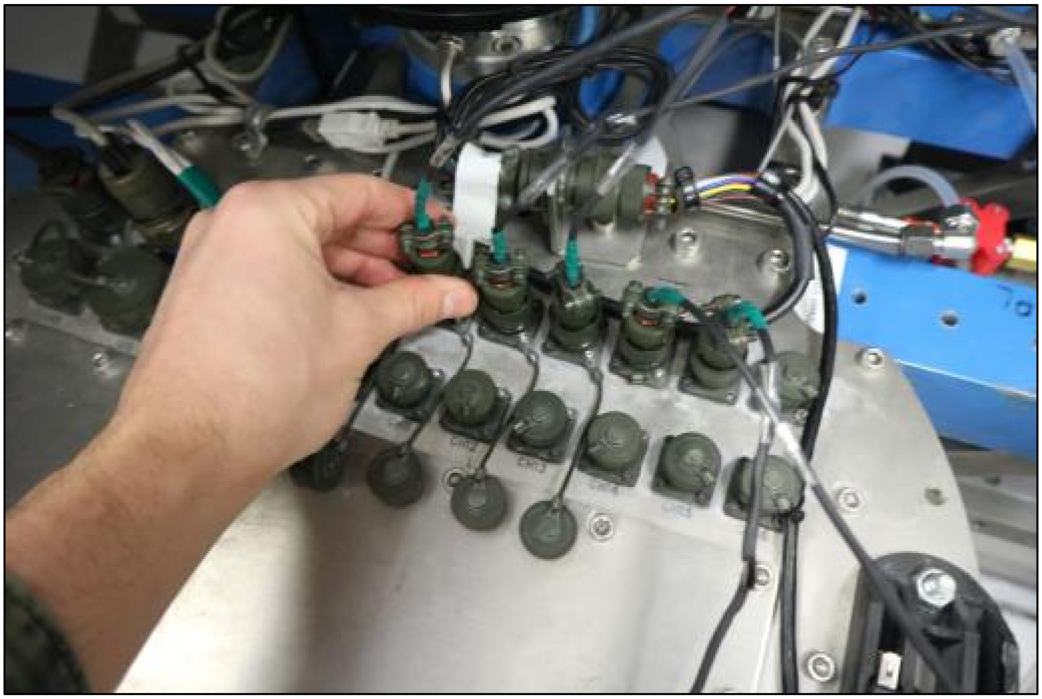

Figure D-62: Connecting the thermistors to the analog ports.

36. If it is required for the experiment, connect the solenoid valve’s USB male connector in the USB female connection for the power supply.

37. Tie down all loose wires (cameras, thermistors, and solenoid) with zip ties and cut off the excess ends. Ensure that there is a bit of extra length in the wires going into or onto the cradle. This will prevent the cradle from "pulling" on the wires once the centrifuge is running and the cradle is in the upright position. The amount of extra length required can be verified by pulling the cradle to the upright position once the wires have been tied down.

Figure D-63: Securing wires to the cradle with zip ties.

Figure D-64: Securing the wires to the cradle with zip ties.

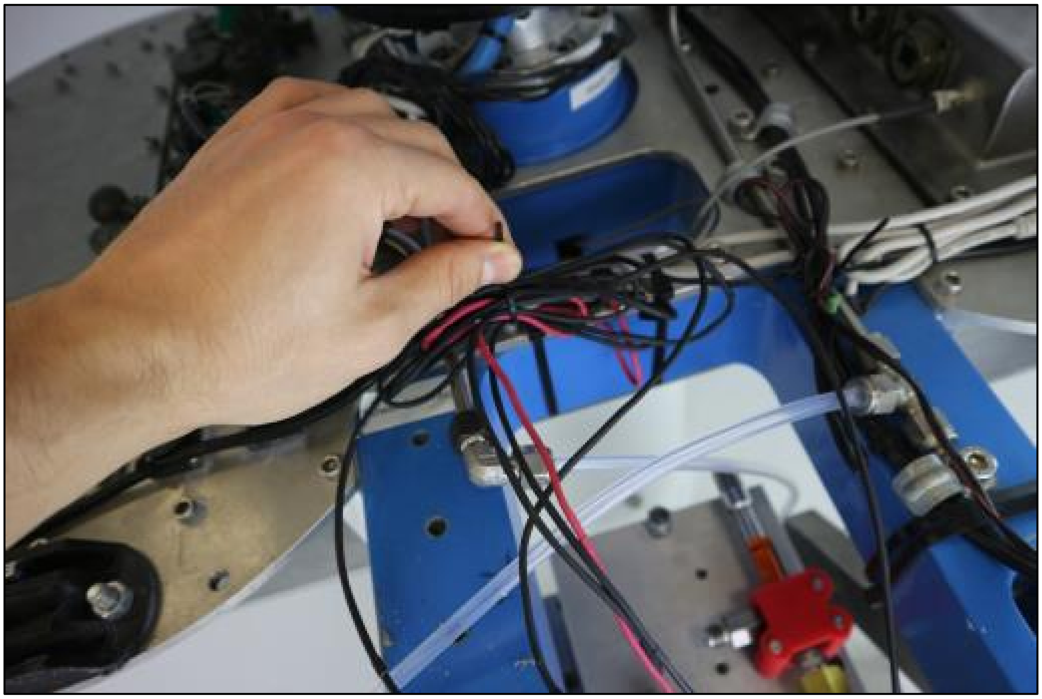

Figure D-65: Securing the thermistor wires to the centrifuge beam with zip ties.

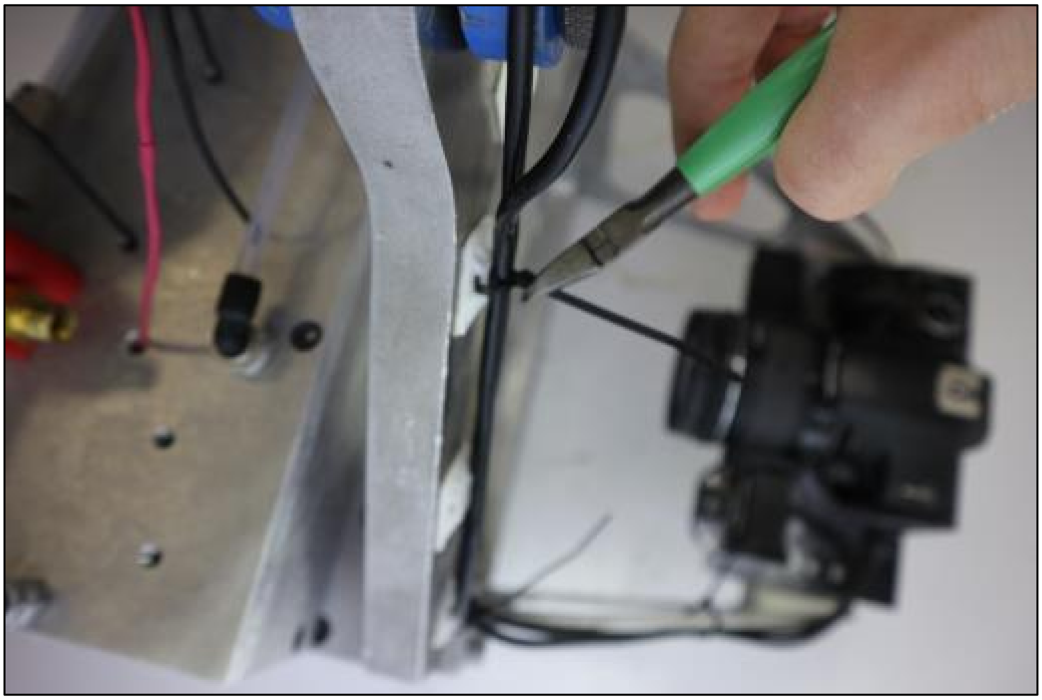

Figure D-66: Cutting off the excess from the zip ties.

38. If required for the experiment, connect the compressed air supply to the vortex tubes using PLA tubing.

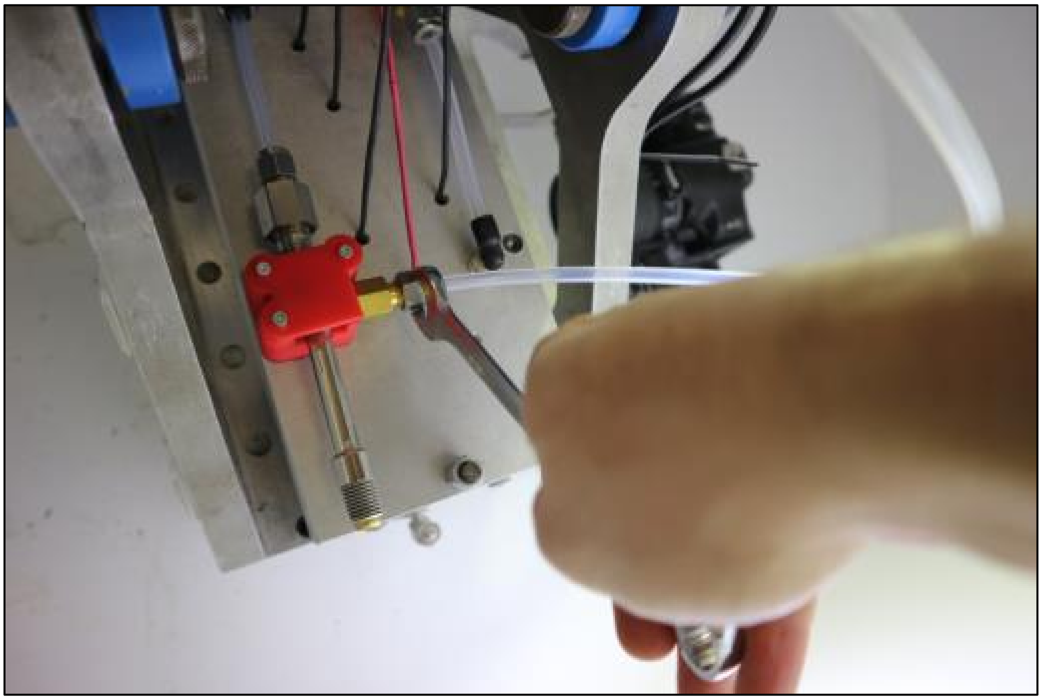

Figure D-67: Connecting vortex tubes to the compressed air supply.

39. Turn on the camera. The EOS Utility software should automatically start up on the centrifuge in-flight computer screen. Click on the “Camera settings/Remote shooting” button. The destination folder for the pictures can be changed by clicking on the “Folder” icon. Click on “Timer Shooting Settings”. Input the desired picture interval to begin taking pictures. Record the time at which the first picture is taken. Ensure that there is enough space on the computer for the amount of pictures that will be taken during the experiment.

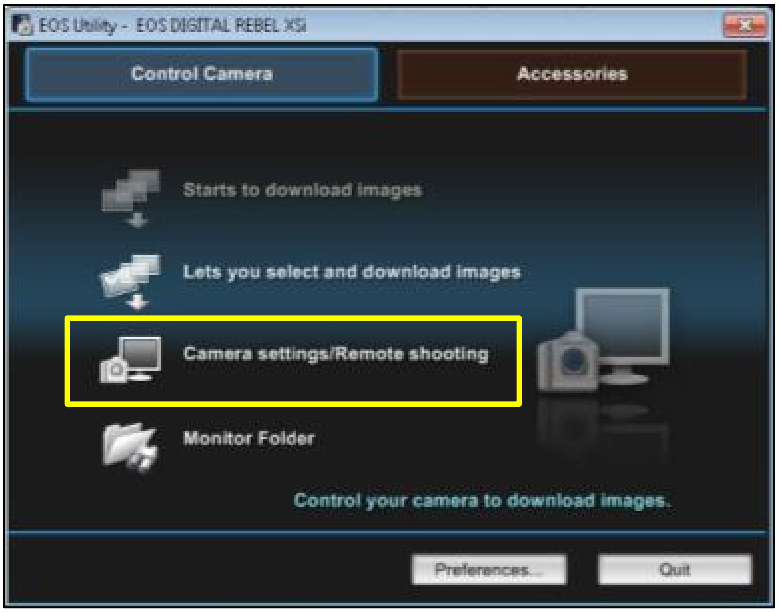

Control your camera to download images.

Figure D-68: EOS Utility interface when the camera is turned on.

Canon Data

Picture Style	Standard
Detail set.	3 , 0 , 0 , 0
Register User Defined style	
WB SHIFT	0,0

Figure D-69: EOS Utility remote shooting interface.

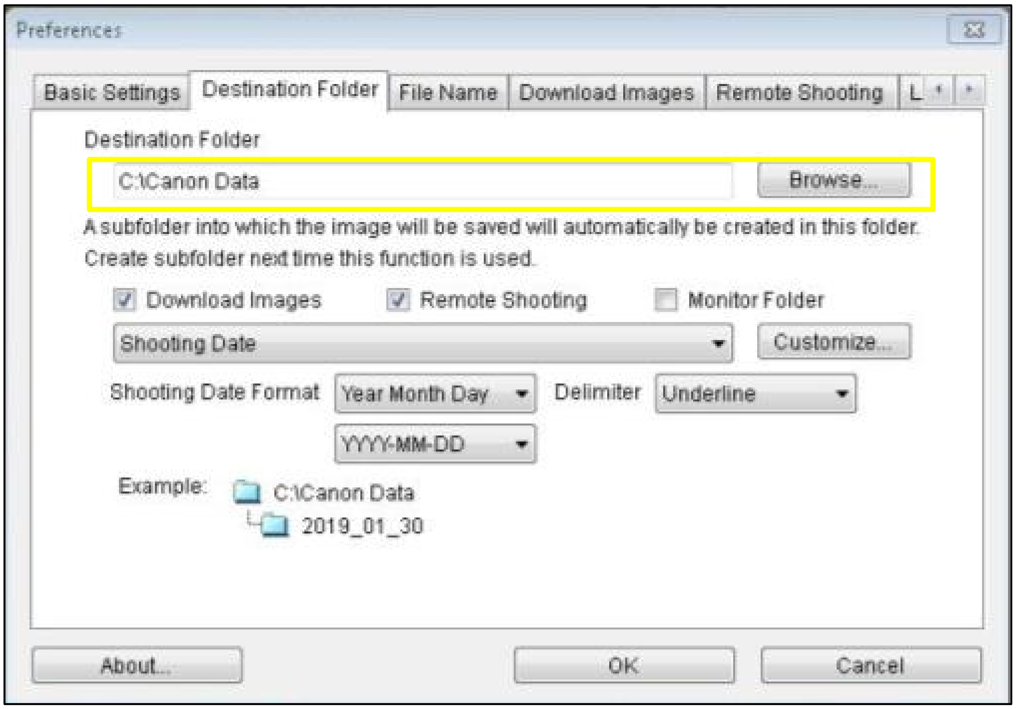

Destination Folder

C:\Canon Data

A subfolder into which the image will be saved will automatically be created in this folder.

Create subfolder next time this function is used.

☑ Download Images ☑ Remote Shooting ☐ Monitor Folder

Shooting Date

Shooting Date Format: Year Month Day, YYYY-MM-DD

Delimiter: Underline

Example: C:\Canon Data
└ 2019_01_30

Figure D-70: EOS Utility interface to change the destination folder.

Shooting menu

Picture Style Standard

Detail set. 3 , 0 , 0 , 0

Register User Defined style

WB SHIFT 0,0

Figure D-71: EOS Utility remote shooting interface.

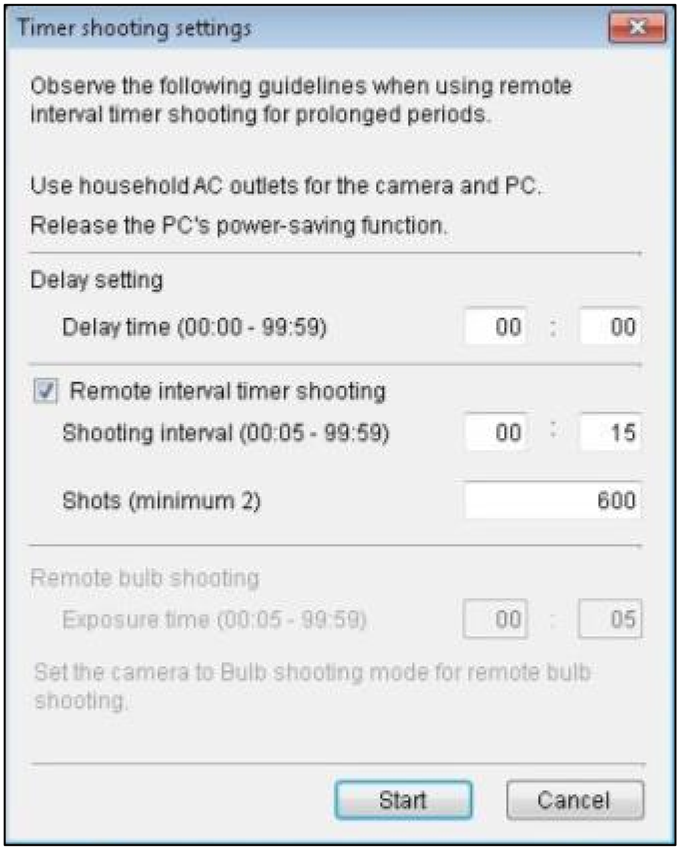
Timer shooting settings

Observe the following guidelines when using remote interval timer shooting for prolonged periods.

Use household AC outlets for the camera and PC.

Release the PC's power-saving function.

Delay setting

Delay time (00:00 - 99:59) 00 : 00

☑ Remote interval timer shooting

Shooting interval (00:05 - 99:59) 00 : 15

Shots (minimum 2) 600

Remote bulb shooting

Exposure time (00:05 - 99:59) 00 : 05

Set the camera to Bulb shooting mode for remote bulb shooting.

Figure D-72: EOS Utility interface for timer shooting settings.

40. Turn on the Acqlipse software on the in-flight computer. Open the setup file that was created during the calibration of the thermistors. Disable the ports of the thermistors that will not be used during the experiment. Run the software and begin data acquisition. Record the time at which data acquisition begins.

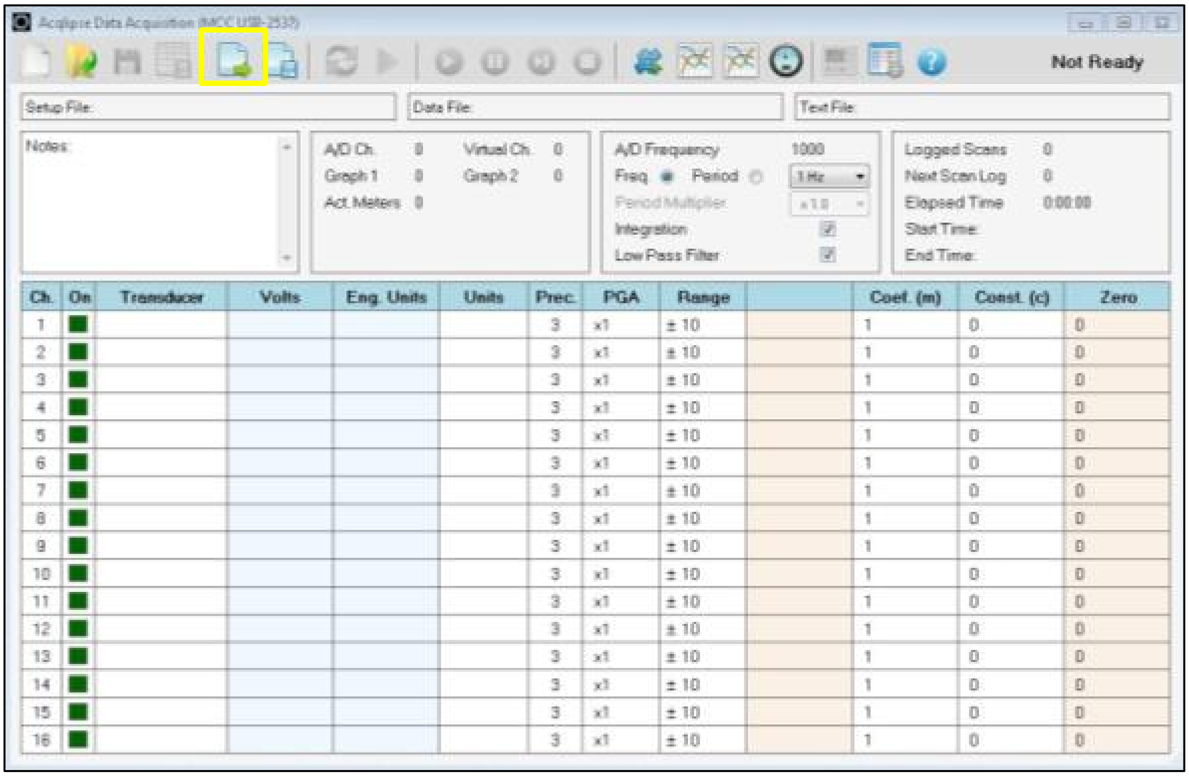

Setup File:
Data File:
Text File:
Notes:

A/D Ch. 0
Virtual Ch. 0
Graph 1 0
Graph 2 0
Act. Meters 0

A/D Frequency 1000
Freq ● Period ○ 1 Hz
Period Multiplier x1.0
Integration ☑
Low Pass Filter ☑

Logged Scans 0
Next Scan Log 0
Elapsed Time 0:00:00
Start Time:
End Time:

Ch.	On	Transducer	Volts	Eng. Units	Units	Prec.	PGA	Range		Coef. (m)	Const. (c)	Zero
1	🟩					3	x1	± 10		1	0	0
2	🟩					3	x1	± 10		1	0	0
3	🟩					3	x1	± 10		1	0	0
4	🟩					3	x1	± 10		1	0	0
5	🟩					3	x1	± 10		1	0	0
6	🟩					3	x1	± 10		1	0	0
7	🟩					3	x1	± 10		1	0	0
8	🟩					3	x1	± 10		1	0	0
9	🟩					3	x1	± 10		1	0	0
10	🟩					3	x1	± 10		1	0	0
11	🟩					3	x1	± 10		1	0	0
12	🟩					3	x1	± 10		1	0	0
13	🟩					3	x1	± 10		1	0	0
14	🟩					3	x1	± 10		1	0	0
15	🟩					3	x1	± 10		1	0	0
16	🟩					3	x1	± 10		1	0	0

Figure D-73: Acqlipse software interface.

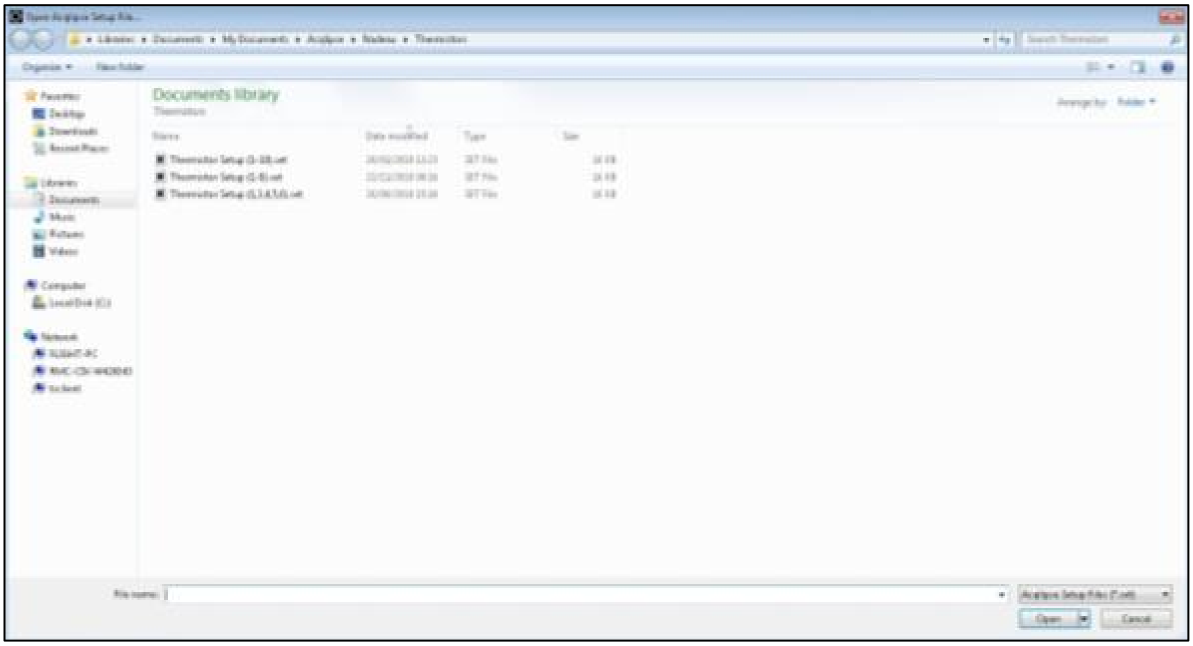

Figure D-74: Opening setup file for Acqlipse.

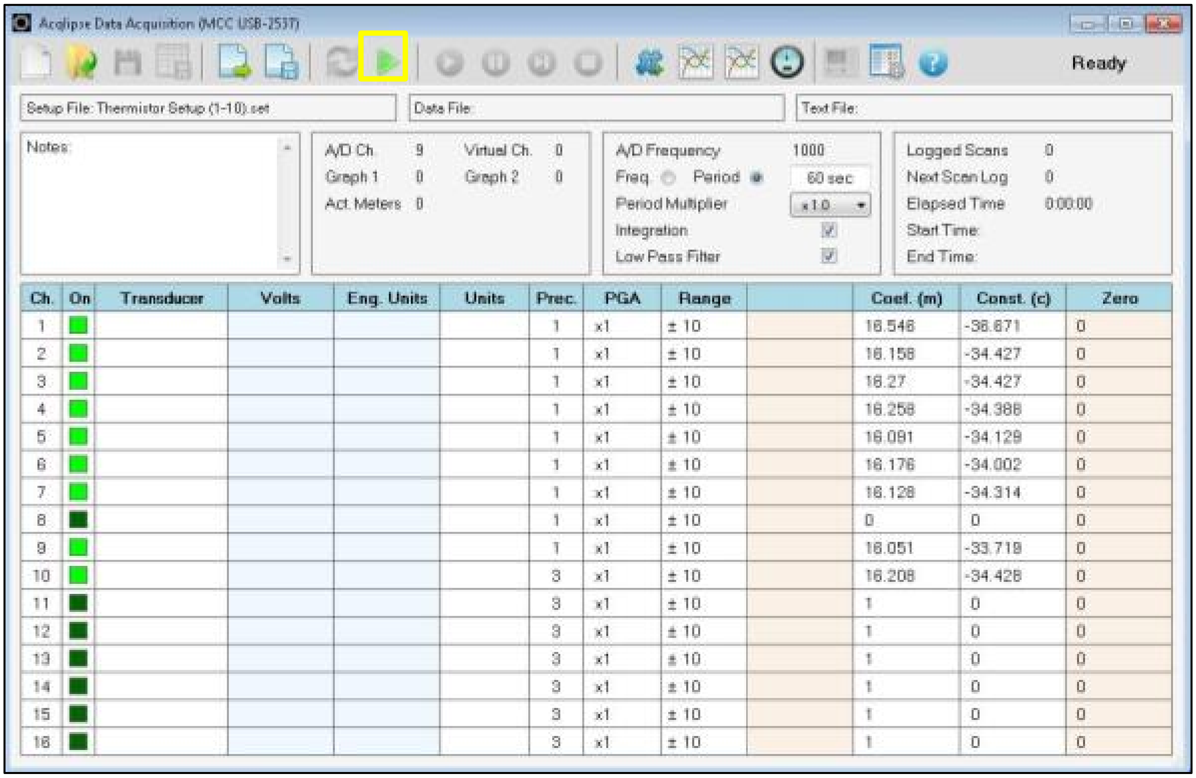

Setup File: Thermistor Setup (1-10).set

Data File:

Text File:

Notes:

A/D Ch. 9
Virtual Ch. 0
Graph 1 0
Graph 2 0
Act. Meters 0

A/D Frequency 1000
Freq. ○ Period ● 60 sec
Period Multiplier x1.0
Integration ☑
Low Pass Filter ☑

Logged Scans 0
Next Scan Log 0
Elapsed Time 0:00:00
Start Time:
End Time:

Ch.	On	Transducer	Volts	Eng. Units	Units	Prec.	PGA	Range		Coef. (m)	Const. (c)	Zero
1	🟩					1	x1	± 10		16.546	-36.671	0
2	🟩					1	x1	± 10		16.158	-34.427	0
3	🟩					1	x1	± 10		16.27	-34.427	0
4	🟩					1	x1	± 10		16.258	-34.388	0
5	🟩					1	x1	± 10		16.091	-34.129	0
6	🟩					1	x1	± 10		16.176	-34.002	0
7	🟩					1	x1	± 10		16.128	-34.314	0
8	■					1	x1	± 10		0	0	0
9	🟩					1	x1	± 10		16.051	-33.719	0
10	🟩					3	x1	± 10		16.208	-34.428	0
11	■					3	x1	± 10		1	0	0
12	■					3	x1	± 10		1	0	0
13	■					3	x1	± 10		1	0	0
14	■					3	x1	± 10		1	0	0
15	■					3	x1	± 10		1	0	0
16	■					3	x1	± 10		1	0	0

Figure D-75: Setting up Acqlipse for data acquisition.

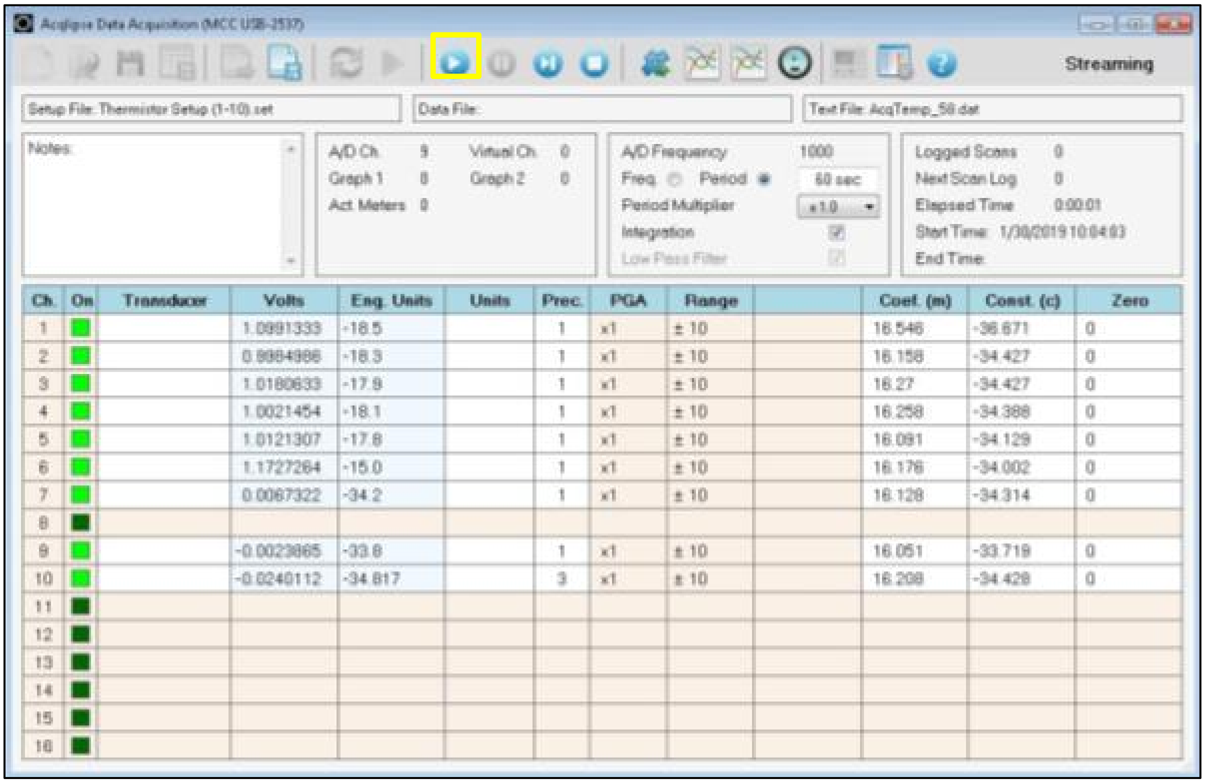

Setup File: Thermistor Setup (1-10).set

Data File:

Text File: AcqTemp_58.dat

Notes:

A/D Ch. 9
Virtual Ch. 0
Graph 1 0
Graph 2 0
Act. Meters 0

A/D Frequency 1000
Freq. ○ Period ● 60 sec
Period Multiplier x1.0
Integration ☑
Low Pass Filter ☑

Logged Scans 0
Next Scan Log 0
Elapsed Time 0:00:01
Start Time: 1/30/2019 10:04:03
End Time:

Ch.	On	Transducer	Volts	Eng. Units	Units	Prec.	PGA	Range		Coef. (m)	Const. (c)	Zero
1	🟩		1.0991333	-18.5		1	x1	± 10		16.546	-36.671	0
2	🟩		0.9984986	-18.3		1	x1	± 10		16.158	-34.427	0
3	🟩		1.0180633	-17.9		1	x1	± 10		16.27	-34.427	0
4	🟩		1.0021454	-18.1		1	x1	± 10		16.258	-34.388	0
5	🟩		1.0121307	-17.8		1	x1	± 10		16.091	-34.129	0
6	🟩		1.1727264	-15.0		1	x1	± 10		16.176	-34.002	0
7	🟩		0.0067322	-34.2		1	x1	± 10		16.128	-34.314	0
8	■											
9	🟩		-0.0023865	-33.8		1	x1	± 10		16.051	-33.719	0
10	🟩		-0.0240112	-34.817		3	x1	± 10		16.208	-34.428	0
11	■											
12	■											
13	■											
14	■											
15	■											
16	■											

Figure D-76: Acqlipse ready for data acquisition.

41. Turn on the Webcam Viewer software. Click the “Connect” button. This will give a live feed of the experiment. This software does not record video. A snap picture can be taken by double-clicking on the display.

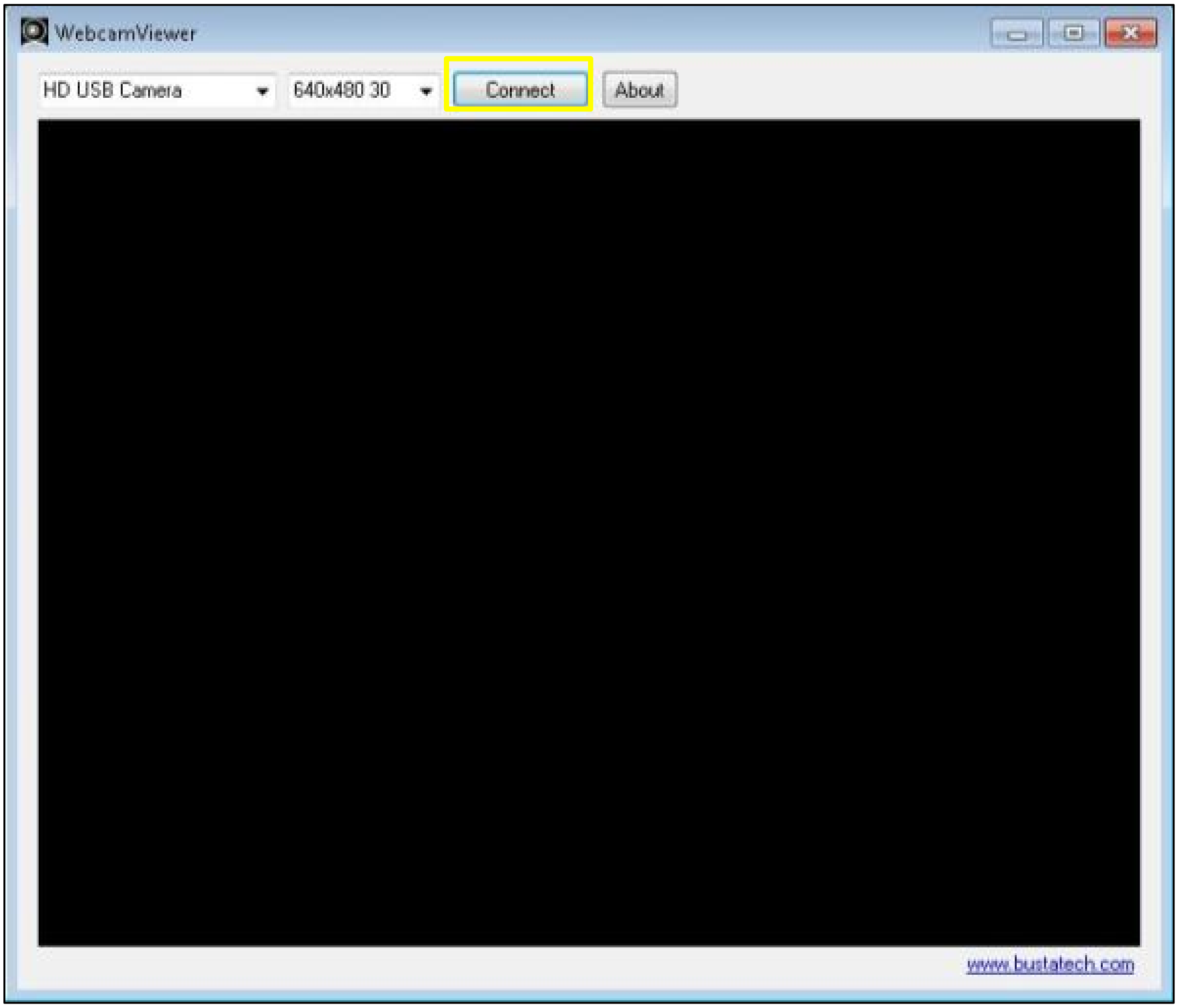

Figure D-77: Webcam Viewer interface.

42. Ensure that there is no loose debris, tools, or materials in the centrifuge casing or on the centrifuge beam. Do so by looking inside the casing, rotating the beam and inspecting for loose items.

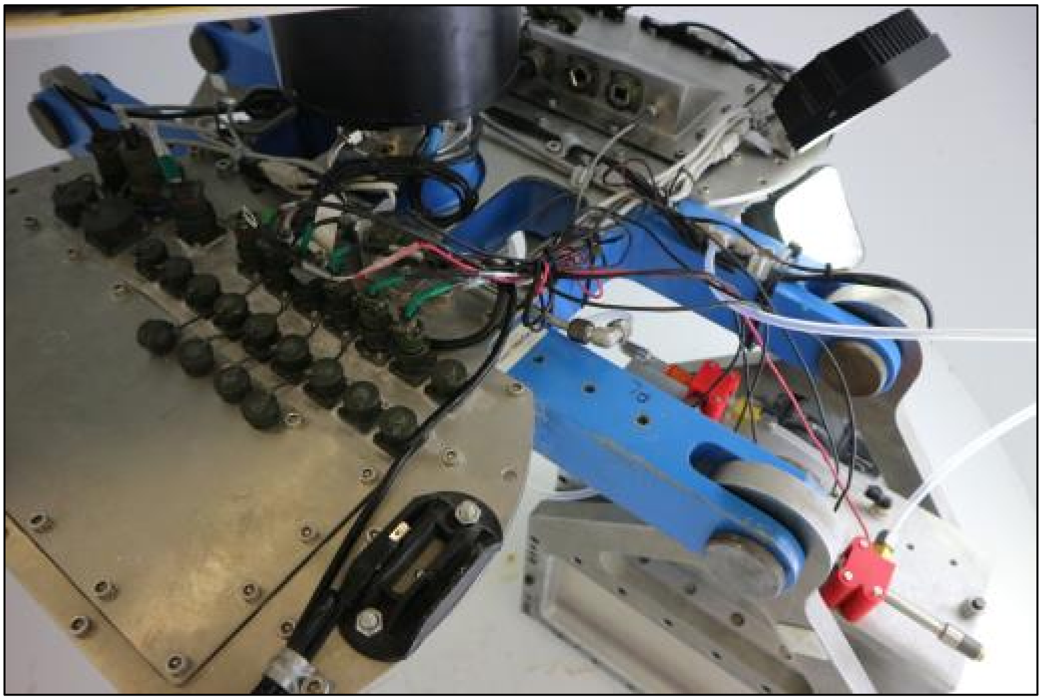

Figure D-78: Centrifuge ready to start of experiment.

43. Once everything is secured, close the casing lid and turn the handles into the locked position.

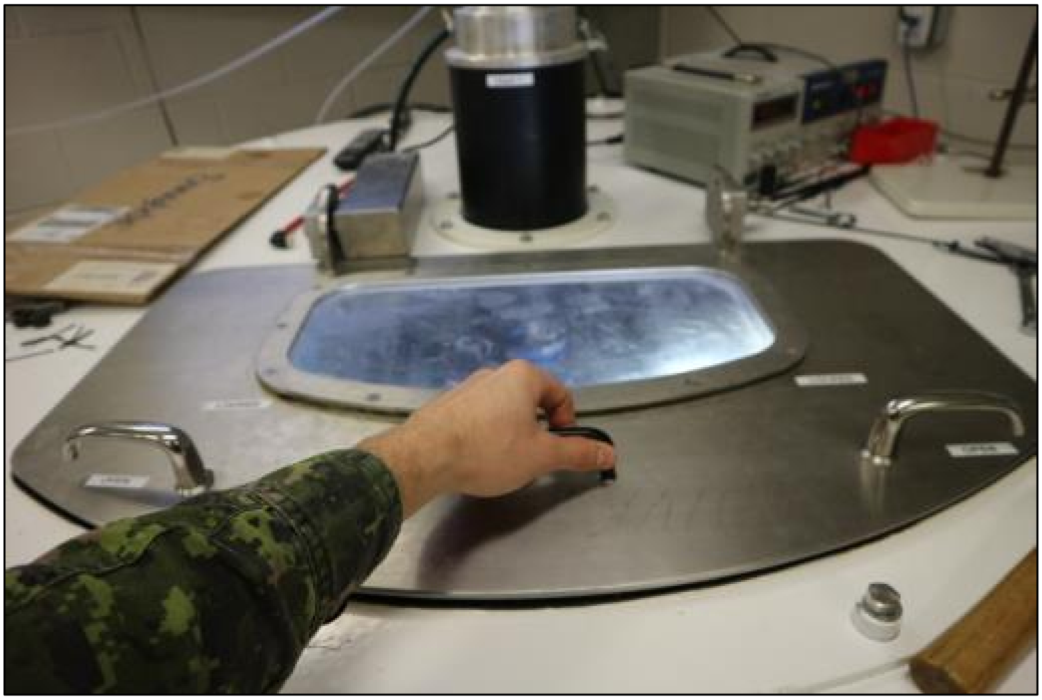

Figure D-79: Closing centrifuge casing lid.

Figure D-80: Placing centrifuge casing lid handles into the locked position.

44. Turn on the lights from the power supply outside the centrifuge casing.

Figure D-81: Turning on lights.

45. On the centrifuge's display panel, input a maximum rotating speed of 638 rpm then input the desired acceleration ratio. If using the Canon Rebel T6, it is recommended that the acceleration ratio does not exceed 60g since the camera has not been tested above that speed and may be damaged by a higher acceleration ratio.

CENTRIFUGE STOPPING LID NOT LOCKED

MASTER PASSWORD	****
OPERATOR PASSWORD	****
MAXIMUM ALLOWABLE SPEED	638
MACHINE SPEED PRESET	165
MACHINE g PRESET	20
VIBRATION ALARM LEVEL	[illegible]
VIBRATION TRIP LEVEL	35
ACCELERATION RATE (RPM/SEC)	3
DECELERATION RATE (RPM/SEC)	3
PAYLOAD RADIUS (m)	0.66

VIBRATION 0.2

MAX g 300.0

TARGET SPEED 165.0

CENTRIFUGE SPEED 13.4

TARGET g 20.1

CALCULATED g 0.1

Figure D-82: Inputting maximum centrifuge speed and acceleration ratio.

46. If the display shows an error message, such as "Lid Not Locked" or "Inverter Fault", press the "Reset Fault" button until it displays "Ready to Start".

READY TO START

MASTER PASSWORD	****
OPERATOR PASSWORD	****
MAXIMUM ALLOWABLE SPEED	638
MACHINE SPEED PRESET	165
MACHINE g PRESET	20
VIBRATION ALARM LEVEL	18
VIBRATION TRIP LEVEL	35
ACCELERATION RATE (RPM/SEC)	3
DECELERATION RATE (RPM/SEC)	3
PAYLOAD RADIUS (m)	0.66

VIBRATION 0.3

MAX g 300.0

TARGET SPEED 165.0

CENTRIFUGE SPEED 0.0

TARGET g 20.1

CALCULATED g 0.0

Figure D-83: Preparing centrifuge for flight.

47. Press the “Start” button on the display panel to start the centrifuge. Record the time at which the centrifuge is started. It can take up to a few minutes for the centrifuge to reach the desired speed.

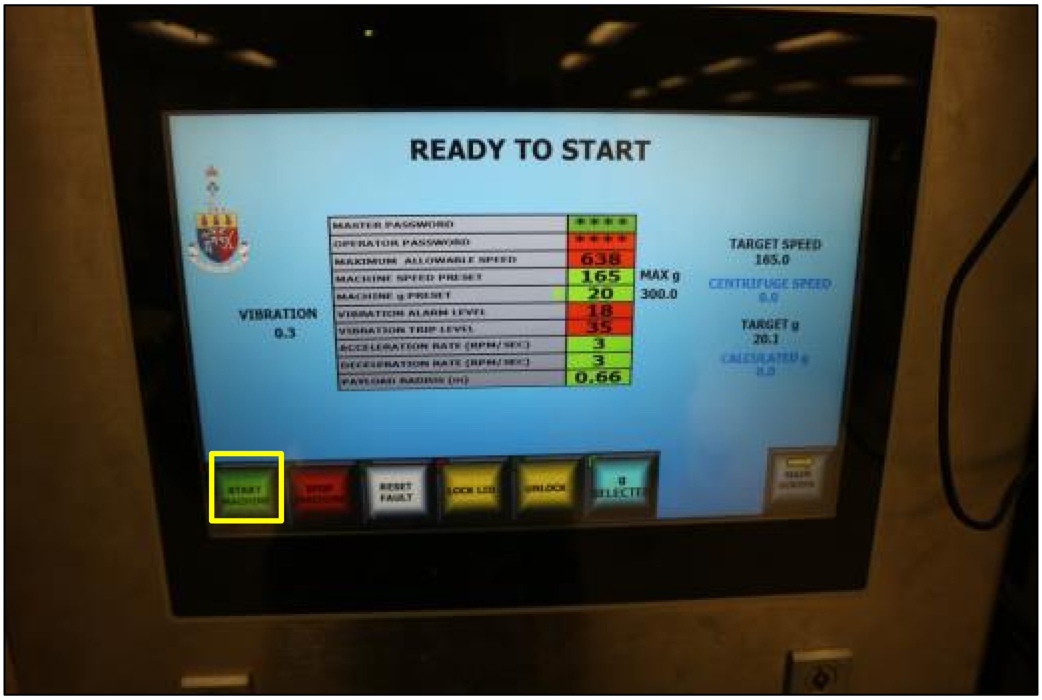

READY TO START

MASTER PASSWORD	****
OPERATOR PASSWORD	****
MAXIMUM ALLOWABLE SPEED	638
MACHINE SPEED PRESET	165
MACHINE g PRESET	20
VIBRATION ALARM LEVEL	18
VIBRATION TRIP LEVEL	35
ACCELERATION RATE (RPM/SEC)	3
DECELERATION RATE (RPM/SEC)	3
PAYLOAD RADIUS (m)	0.66

VIBRATION 0.3

MAX g 300.0

TARGET SPEED 165.0

CENTRIFUGE SPEED 0.0

TARGET g 20.1

CALCULATED g 0.0

Figure D-84: Centrifuge ready to start.

CENTRIFUGE ACCELERATING

MASTER PASSWORD	****
OPERATOR PASSWORD	****
MAXIMUM ALLOWABLE SPEED	638
MACHINE SPEED PRESET	165
MACHINE g PRESET	20
VIBRATION ALARM LEVEL	18
VIBRATION TRIP LEVEL	35
ACCELERATION RATE (RPM/SEC)	3
DECELERATION RATE (RPM/SEC)	3
PAYLOAD RADIUS (m)	0.66

VIBRATION 0.1

MAX g 300.0

TARGET SPEED 165.0

CENTRIFUGE SPEED 45.6

TARGET g 20.1

CALCULATED g 1.5

Figure D-85: Centrifuge accelerating.

CENTRIFUGE AT SPEED

MASTER PASSWORD	****
OPERATOR PASSWORD	****
MAXIMUM ALLOWABLE SPEED	638
MACHINE SPEED PRESET	165
MACHINE g PRESET	20
VIBRATION ALARM LEVEL	18
VIBRATION TRIP LEVEL	35
ACCELERATION RATE (RPM/SEC)	3
DECELERATION RATE (RPM/SEC)	3
PAYLOAD RADIUS (m)	0.66

VIBRATION 0.4

MAX g 300.0

TARGET SPEED 165.0

CENTRIFUGE SPEED [illegible]

TARGET g 20.1

CALCULATED g [illegible]

Figure D-86: Centrifuge at speed.

48. Place a piece of cardboard over the lid window to prevent flashing from the lights inside the centrifuge.

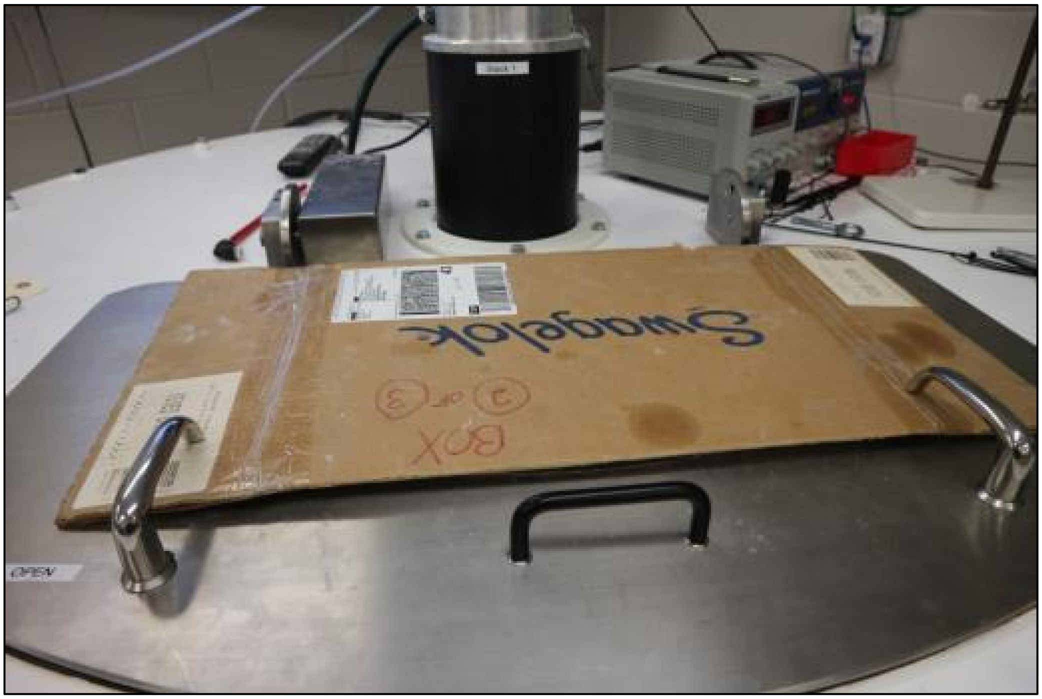

Figure D-87: Blocking the casing lid window.

49. If required for the experiment, turn on the compressed air supply for the vortex tubes.

Figure D-88: Turning on compressed air supply.

50. While the experiment is running, it is highly recommended to have a vibration rating that is below three (3). The vibration rating is situated on the centrifuge display panel. If it is higher than three (3), it is likely because the cradles were not balanced properly.

CENTRIFUGE AT SPEED

MASTER PASSWORD	****
OPERATOR PASSWORD	****
MAXIMUM ALLOWABLE SPEED	638
MACHINE SPEED PRESET	165
MACHINE g PRESET	20
VIBRATION ALARM LEVEL	18
VIBRATION TRIP LEVEL	35
ACCELERATION RATE (RPM/SEC)	3
DECELERATION RATE (RPM/SEC)	3
PAYLOAD RADIUS (m)	0.66

VIBRATION 0.4

MAX g 300.0

TARGET SPEED 165.0

CENTRIFUGE SPEED 165.8

TARGET g 20.1

CALCULATED g 20.3

Figure D-89: Verification of centrifuge vibration rating.

51. Once the experiment is finished, the centrifuge can be stopped by pressing the “Stop Machine” button on the centrifuge control panel.

MASTER PASSWORD	****
OPERATOR PASSWORD	****
MAXIMUM ALLOWABLE SPEED	638
MACHINE SPEED PRESET	165
MACHINE g PRESET	20
VIBRATION ALARM LEVEL	18
VIBRATION TRIP LEVEL	35
ACCELERATION RATE (RPM/SEC)	3
DECELERATION RATE (RPM/SEC)	3
PAYLOAD RADIUS (m)	0.66

Figure D-90: Stopping the centrifuge.

MASTER PASSWORD	****
OPERATOR PASSWORD	****
MAXIMUM ALLOWABLE SPEED	638
MACHINE SPEED PRESET	165
MACHINE g PRESET	20
VIBRATION ALARM LEVEL	18
VIBRATION TRIP LEVEL	35
ACCELERATION RATE (RPM/SEC)	3
DECELERATION RATE (RPM/SEC)	3
PAYLOAD RADIUS (m)	0.66

Figure D-91: Centrifuge decelerating.

52. Stop the camera remote shooting.

Timer shooting status

Time until next shot 00:16
No. of shots already taken 112
No. of failed shots 0
No. of shots to be taken 888

Stop

Figure D-92: Stopping the remote camera shooting.

53. Stop the thermistor data acquisition.

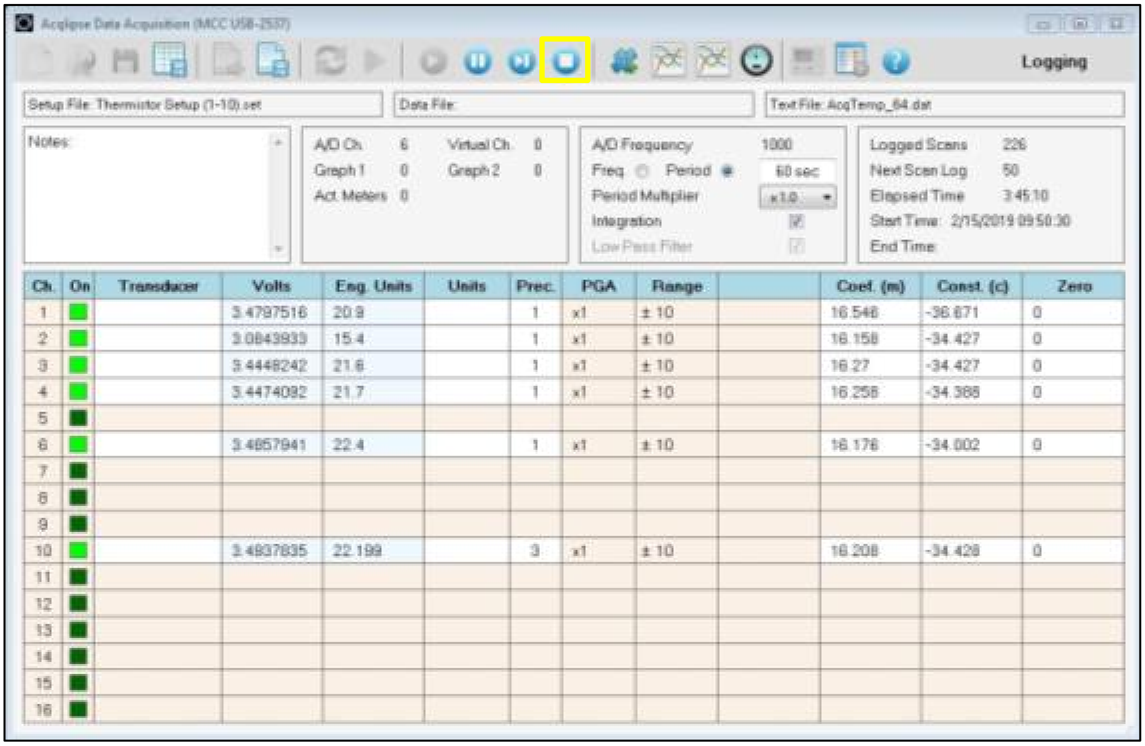
Acqlipse Data Acquisition (MCC USB-2537)

Logging

Setup File: Thermistor Setup (1-10).set

Data File:

Text File: AcqTemp_64.dat

Notes:

A/D Ch. 6
Virtual Ch. 0
Graph 1 0
Graph 2 0
Act. Meters 0

A/D Frequency 1000
Freq ○ Period ● 60 sec
Period Multiplier x1.0
Integration ☑
Low Pass Filter ☑

Logged Scans 226
Next Scan Log 50
Elapsed Time 3:45:10
Start Time: 2/15/2019 09:50:30
End Time:

Ch.	On	Transducer	Volts	Eng. Units	Units	Prec.	PGA	Range		Coef. (m)	Const. (c)	Zero
1	🟩		3.4797516	20.9		1	x1	± 10		16.546	-36.871	0
2	🟩		3.0843933	15.4		1	x1	± 10		16.158	-34.427	0
3	🟩		3.4448242	21.6		1	x1	± 10		16.27	-34.427	0
4	🟩		3.4474082	21.7		1	x1	± 10		16.258	-34.388	0
5	■											
6	🟩		3.4857941	22.4		1	x1	± 10		16.176	-34.002	0
7	■											
8	■											
9	■											
10	🟩		3.4837835	22.199		3	x1	± 10		16.208	-34.428	0
11	■											
12	■											
13	■											
14	■											
15	■											
16	■											

Figure D-93: Stopping the thermistor data acquisition.

54. Save the temperature data in a .txt file.

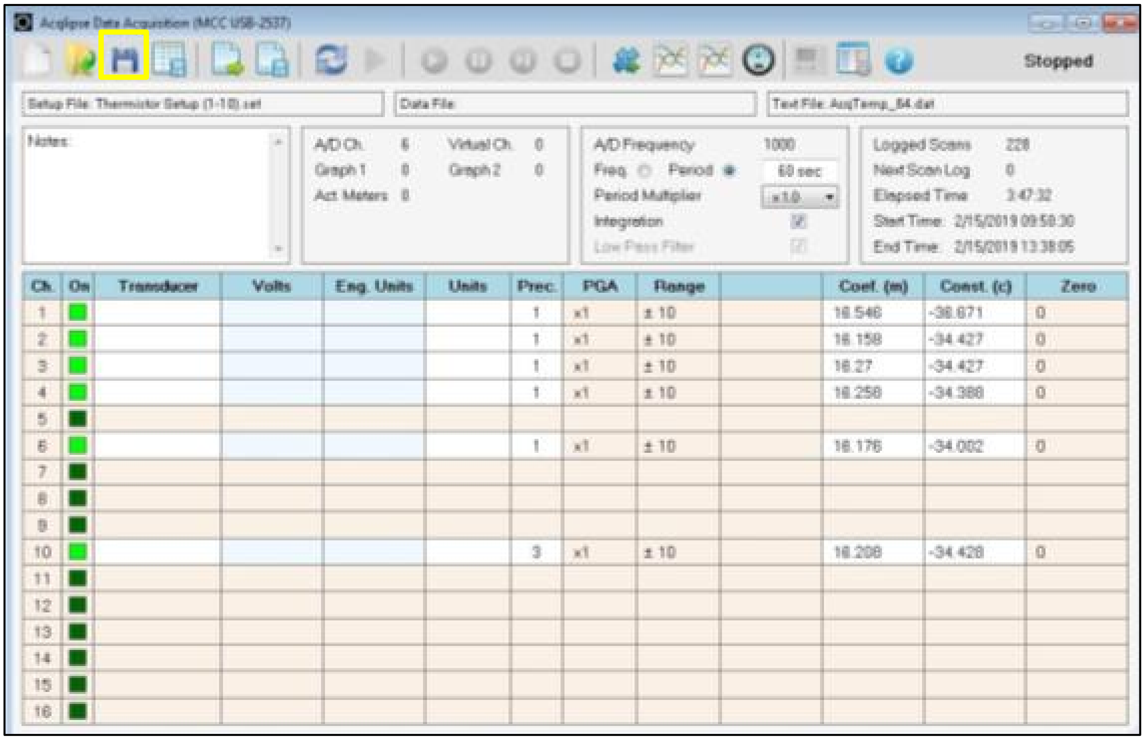
Acqlipse Data Acquisition (MCC USB-2537)

Stopped

Setup File: Thermistor Setup (1-10).set

Data File:

Text File: AcqTemp_64.dat

Notes:

A/D Ch. 6
Virtual Ch. 0
Graph 1 0
Graph 2 0
Act. Meters 0

A/D Frequency 1000
Freq ○ Period ● 60 sec
Period Multiplier x1.0
Integration ☑
Low Pass Filter ☑

Logged Scans 228
Next Scan Log 0
Elapsed Time 3:47:32
Start Time: 2/15/2019 09:50:30
End Time: 2/15/2019 13:38:05

Ch.	On	Transducer	Volts	Eng. Units	Units	Prec.	PGA	Range		Coef. (m)	Const. (c)	Zero
1	🟩					1	x1	± 10		16.546	-36.871	0
2	🟩					1	x1	± 10		16.158	-34.427	0
3	🟩					1	x1	± 10		16.27	-34.427	0
4	🟩					1	x1	± 10		16.258	-34.388	0
5	■											
6	🟩					1	x1	± 10		16.176	-34.002	0
7	■											
8	■											
9	■											
10	🟩					3	x1	± 10		16.208	-34.428	0
11	■											
12	■											
13	■											
14	■											
15	■											
16	■											

Figure D-94: Saving the thermistor data.

55. Once the centrifuge has completely stopped spinning, press the “Unlock Lid” button on the centrifuge control panel.

READY TO START

MASTER PASSWORD	****
OPERATOR PASSWORD	****
MAXIMUM ALLOWABLE SPEED	638
MACHINE SPEED PRESET	165
MACHINE g PRESET	20
VIBRATION ALARM LEVEL	18
VIBRATION TRIP LEVEL	35
ACCELERATION RATE (RPM/SEC)	3
DECELERATION RATE (RPM/SEC)	3
PAYLOAD RADIUS (m)	0.66

VIBRATION 0.2

MAX g 300.0

TARGET SPEED 165.0

CENTRIFUGE SPEED 0.0

TARGET g 20.1

CALCULATED g 0.0

Figure D-95: Unlocking the centrifuge casing lid.

56. Turn the centrifuge lid handles to the “Open” position and open the lid.

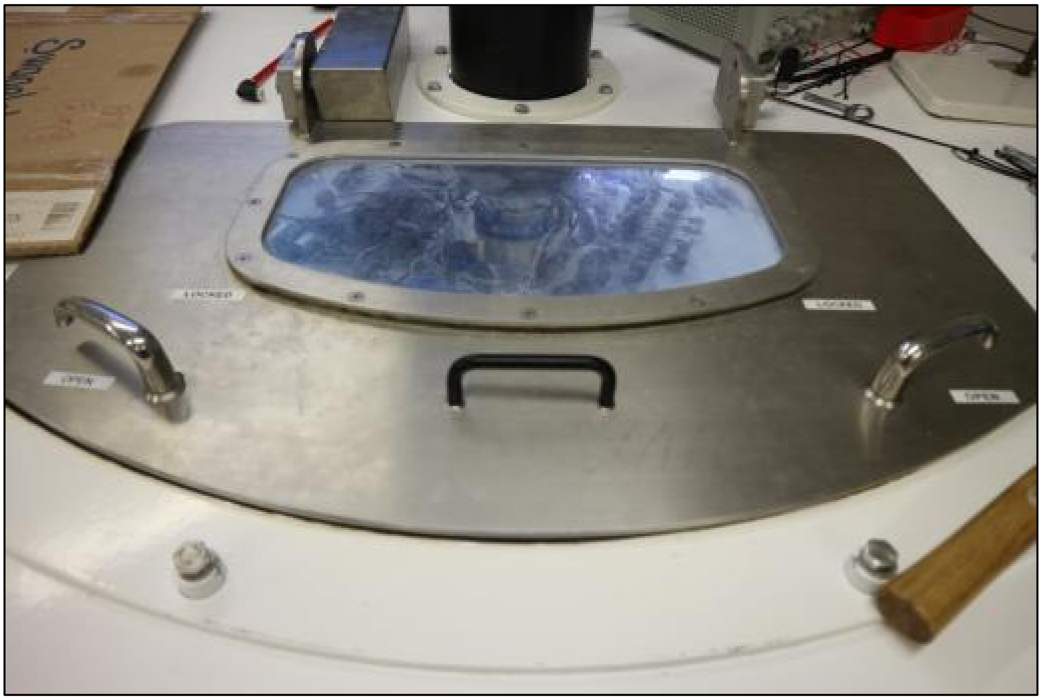

Figure D-96: Unlocking the lid handles and opening the lid.

57. Cut all the zip ties that were attached to tie down the wires.

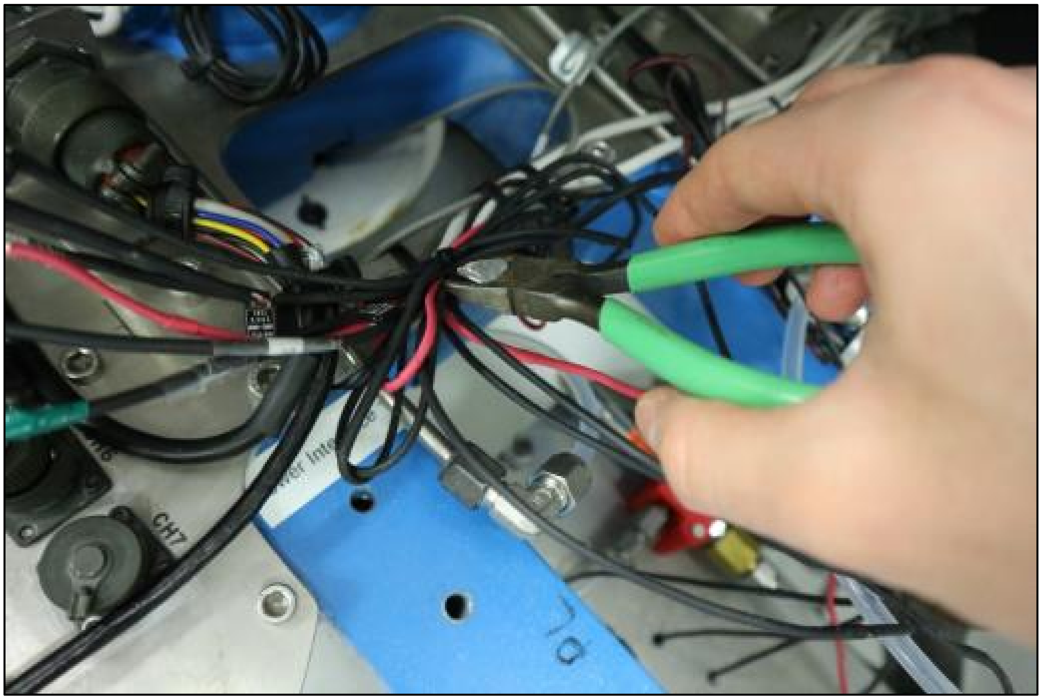

Figure D-97: Cutting the zip ties securing the thermistors.

Figure D-98: Cutting the zip ties securing the camera wires.

58. Disconnect the thermistors from their analog ports.

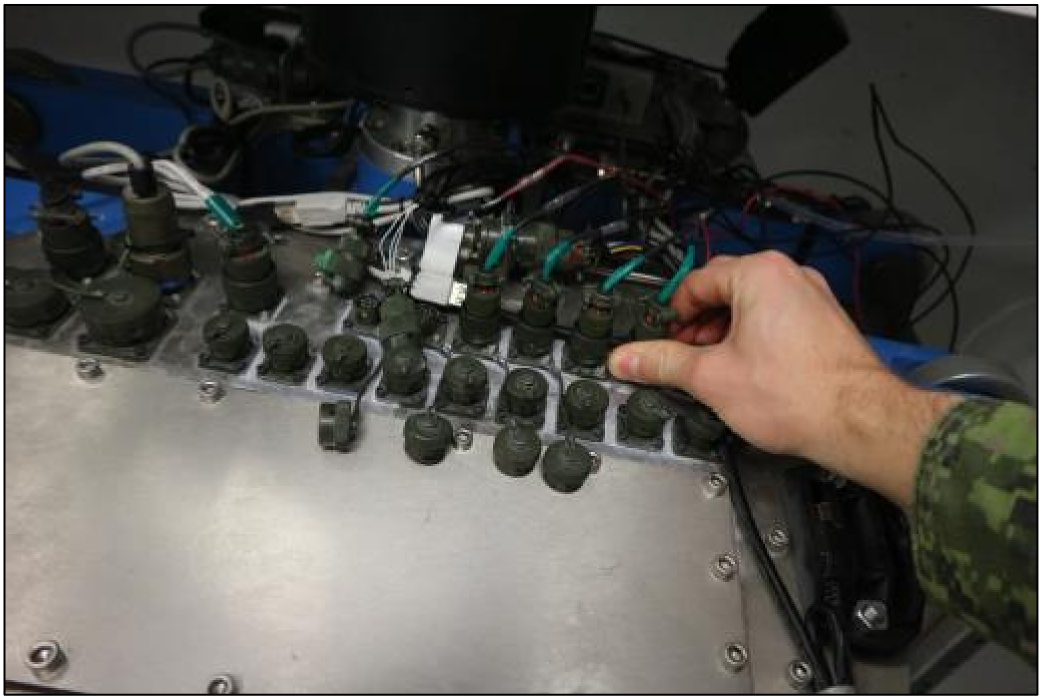

Figure D-99: Disconnecting the thermistors from the analog ports.

59. Disconnect the camera's USB connection and its power supply. Remove the camera and the webcam from the mount.

60. Disconnect the power supply to the solenoid valve if it was used during the experiment.

61. Remove the cradle from the centrifuge and place it on a workbench.

62. Pull the thermistors out from the soil.

63. Loosen the capscrews on the side plate and slightly nudge it out to leave enough space for the climate box to slide out.

64. Remove the two screw rods then slide the climate box off the cradle.

65. Collect soil to measure the water content distribution throughout the sample. It is recommended to use the same soil collection pattern to be able to compare the results with other experiments.

Figure D-100: Collecting soil to measure the water content throughout the sample.

Figure D-101: Collected soil to measure water content throughout the sample.

66. Download the experiment pictures and the temperature data from the in-flight computer.

Figure D-102: Collecting pictures and temperature data from the centrifuge in-flight computer.

APPENDIX E THERMISTOR ASSEMBLY AND CALIBRATION

E.1 Overview of Thermistor Assembly and Calibration

Temperature is an important factor when conducting research of contaminant transport in frozen soils. As such, it is crucial to be able to track and record the temperature of the soil throughout the sample during an experiment in the geotechnical centrifuge. This appendix covers the materials and equipment required to build the thermistors as well as the assembly and calibration instructions.

E.2 Thermistor Bill of Material

Table E-1 lists the materials that are required to assemble one thermistor. The prices for wires and heat shrink tubing are for the lengths specified in Table 1 and not for the whole rolls ordered from Digi-Key. The thermistors are fragile and susceptible to breaking after repeated use. When a thermistor breaks, it is possible to re-use the resistors and the 7-pin analog connectors to build another thermistor. Those two parts comprise the recyclable portion of the price while the thermistor bead, the wiring and the heat shrink tubing are consumable items. The length of the wiring and heat shrink tubing is adequate for use of the thermistors in the primary cradle of RMC’s geotechnical centrifuge.

Table E-1: Thermistor bill of materials.

Item	Quantity	Serial Number	Price
NTC Thermistor 10K OHM 0.1C BEAD U.S. SENSOR/LITTLEFUSE INC	1	615-1003-ND Digi-Key	$2.52
RESISTOR 25K OHM 0.6W 0.01% RADIAL RIEDON	1	USR2G-25KX1-ND Digi-Key	$29.46
7-PIN ANALOG CONNECTOR	1	APH 62GB-16F10-07PN PEI Genesis	$32.16
HOOK-UP STRND 30AWG WHITE 50' ADAFRUIT INDUSTRIES LLC	1 x 36 in	1528-1737-ND Digi-Key	$0.42
HOOK-UP STRND 30AWG BLACK 50' ADAFRUIT INDUSTRIES LLC	1 x 30 in 1 x 4 in	1528-1732-ND Digi-Key	$0.39
HOOK-UP STRND 30AWG RED 50' ADAFRUIT INDUSTRIES LLC	1 x 6 in	1528-1733-ND Digi-Key	$0.07
F221B1/16 BK100 HEATSHRINK 1/16 IN X 4FT BLACK	4 x 2 in	A116B-4-ND Digi-Key	$0.28
F221B1/8 BK100 HEATSHRINK 1/8 IN X 4FT BLACK	4 x 9 in	A018B-4-ND Digi-Key	$1.51

Item	Quantity	Serial Number	Price
F221B3/16 BK100 HEATSHRINK 3/16 IN X 4FT BLACK	1 x 4 in	A316B-4-ND Digi-Key	$0.20
		Total	$67.01
		Recyclable Total	$61.62
		Consumable Total	$5.39

E.3 Thermistor Assembly Supplies and Equipment

Table E-2 list the consumable supplies required to assemble the thermistors. The supplies listed are adequate for the assembly of multiple thermistors.

Table E-2: Thermistor assembly supplies.

Item	Quantity	Serial Number	Price
Silicone Conformal Coating	55 ml	422B-55ML QKits – Kingston, ON	$18.00
Soldering Flux Paste	10 ml	8341-10ML QKits – Kingston, ON	$16.71
Lead Free Solder – 0.8mm	200 g	SRW-LF-080-200 QKits – Kingston, ON	$24.45
Electrical Tape	1 roll		~ $6.00
Labels			
Clear Packing Tape			~ $3.00
Nitrile Gloves	Pair		~$0.30
Absorbent Pads	1 (15x19in)		~$1.00

Below is a list of the equipment required for the assembly of the thermistors. Prices are not provided since they can vary highly based on the brand, type and supplier of the equipment and since this equipment is normally available in academic laboratories.

Equipment Required – Thermistors

1. Soldering iron
2. Soldering tips
3. Wire strippers
4. Utility knife
5. Small vice
6. Measuring tape
7. 3rd hand
8. Heat gun
9. Lab coat
10. Eye protection
11. Fume Hood

E.4 Thermistor Electrical Drawing

Below is the drawing for the thermistors. The connections for the data channel and the power supply are all found within the 7-pin analog connectors.

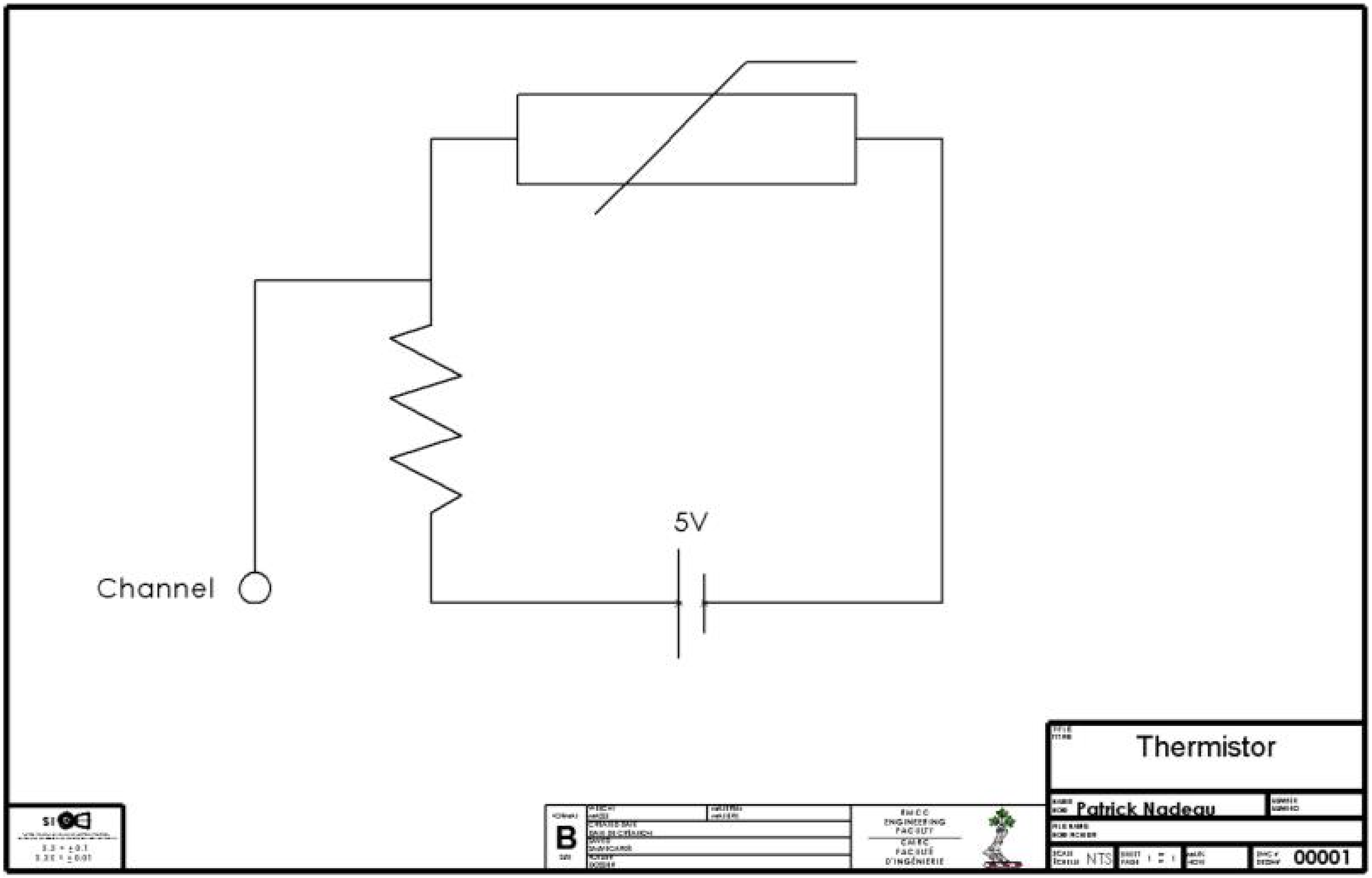

Figure E-1: Thermistor electrical drawing.

E.5 Thermistor Assembly Instructions

Below are the step-by-step instructions for the assembly of the thermistors.

1. Cut wiring and heat shrink tubing to lengths specified in bill of materials (BOM).

Figure E-2: Thermistor materials.

2. Strip 5 mm from each end of the wires and spin the exposed wire strands. It is recommended to use a utility knife since wire stripper may damage and/or cut the thin wire strands.

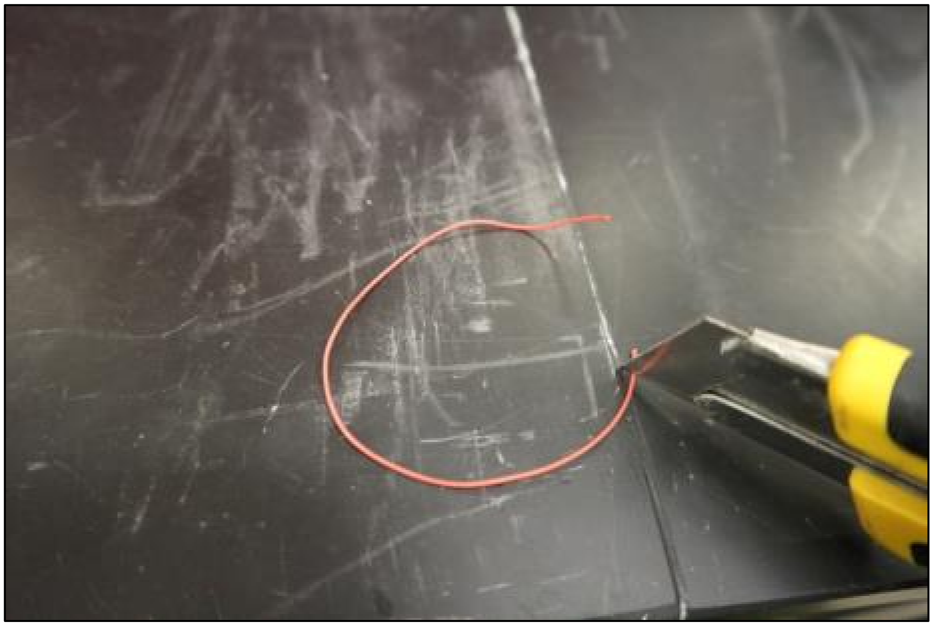

Figure E-3: Wire stripping.

3. Apply solder to exposed wiring for all the wires. Eye protection is highly recommended while soldering.

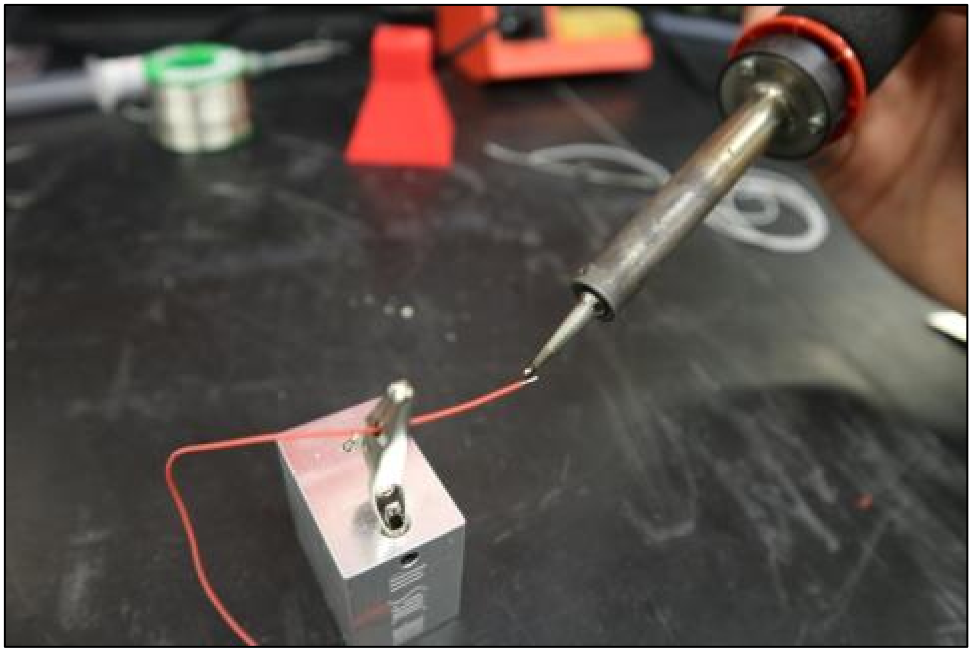

Figure E-4: Wire soldering.

4. Apply solder to the ends of the thermistor strands, where the connections with the wires will be made.

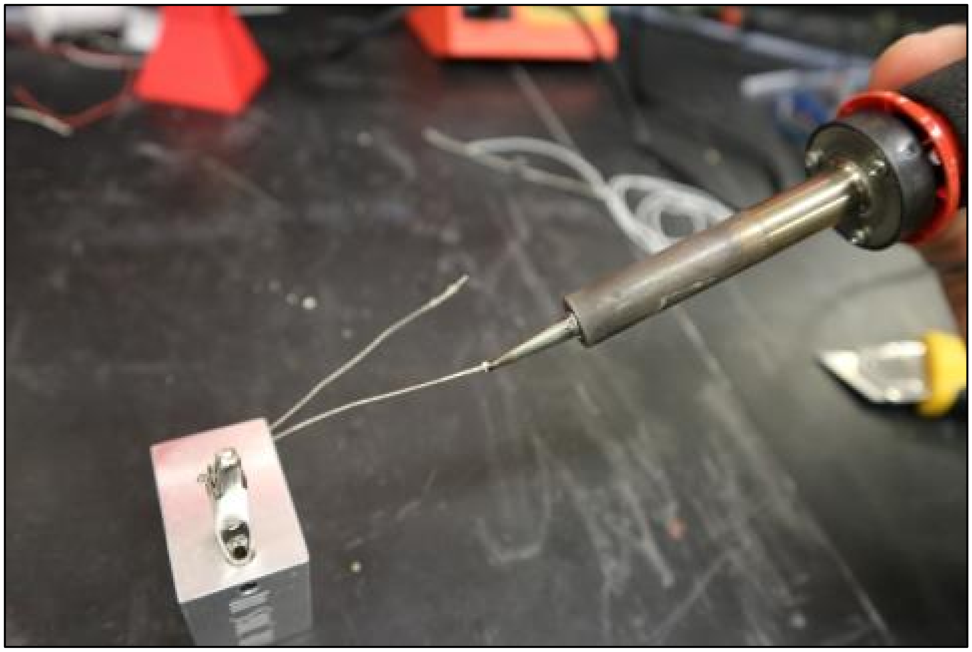

Figure E-5: Thermistor soldering.

5. Insert the 36″ white wire and the 30″ black wire through different 1/16″ heat shrink tubes.

Figure E-6: Passing wires through heat shrink tubing.

6. Solder the 36″ white wire and the 30″ black wire to their own thermistor strand.

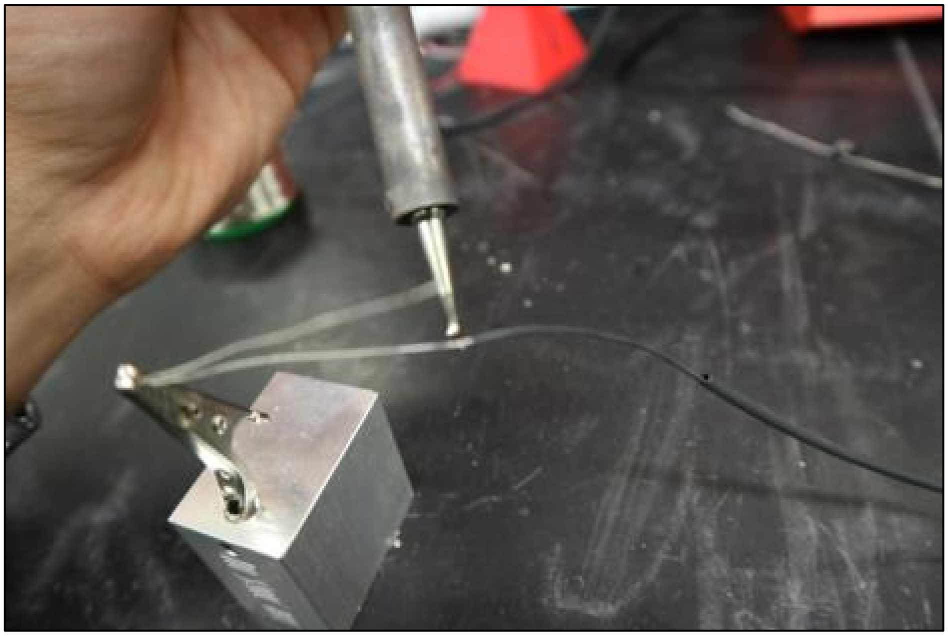

Figure E-7: Thermistor and wire soldering.

7. Bring the heat shrink tubes as close as possible to the thermistor bead and heat up the tubing with a heat gun.

Figure E-8: Heat shrink tubing installation.

8. Insert both the black and white wires through the same 1/8″ shrink tubing. The shrink tubing should be cut into lengths of 8-10″ so it is easier to pass the wiring through.

Figure E-9: Heat shrink tubing installation.

9. Heat up the shrink tubing one length at a time. Wait to heat up the last length of tubing.

10. Insert the black wire through 1/16″ shrink tubing.

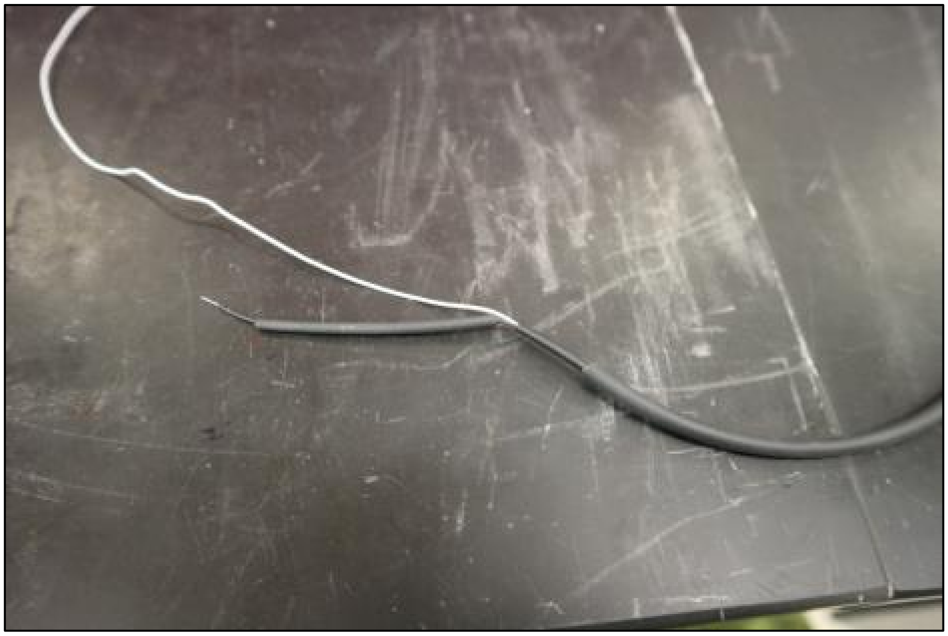

Figure E-10: Passing wire through heat shrink tubing.

11. Apply solder to the ends of the resistor strands. Apply solder between the resistor and the end of the strand that will be connected to the wire that connects the thermistor with the resistor.

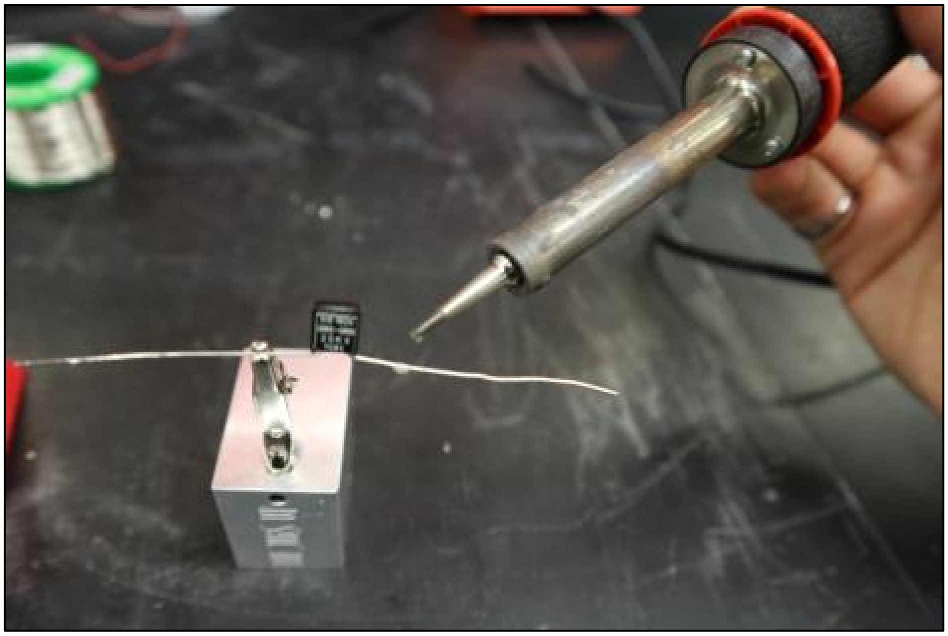

Figure E-11: Applying solder to resistor.

12. Solder the black wire to the resistor strand.

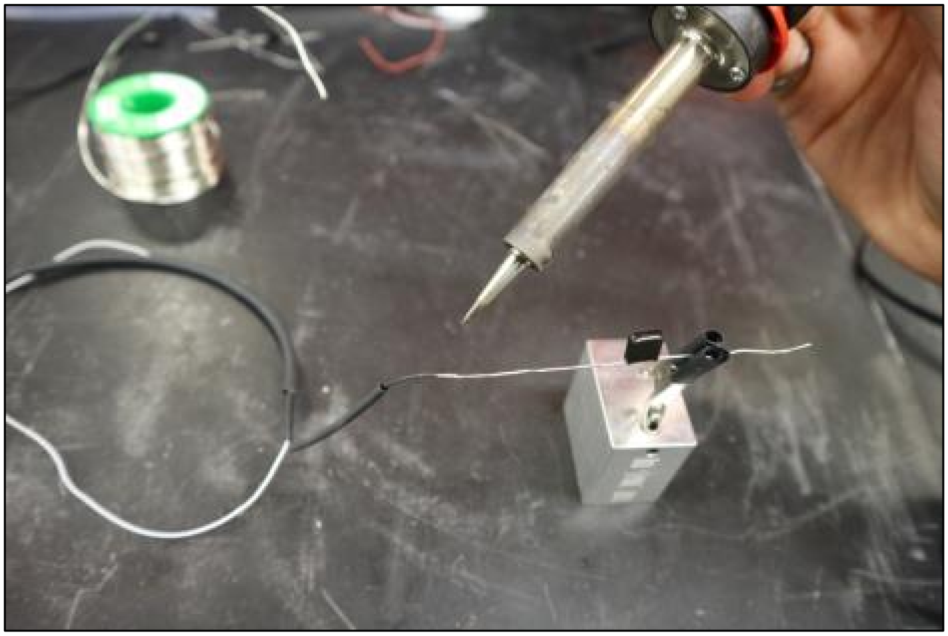

Figure E-12: Soldering wire to resistor.

13. Solder the red wire to the resistor strand connected to the black wire.

14. Bring the 1/16″ shrink tubing as close as possible to the resistor and heat it up with the heat gun, then do the same with the 1/8″ shrink tubing afterwards.

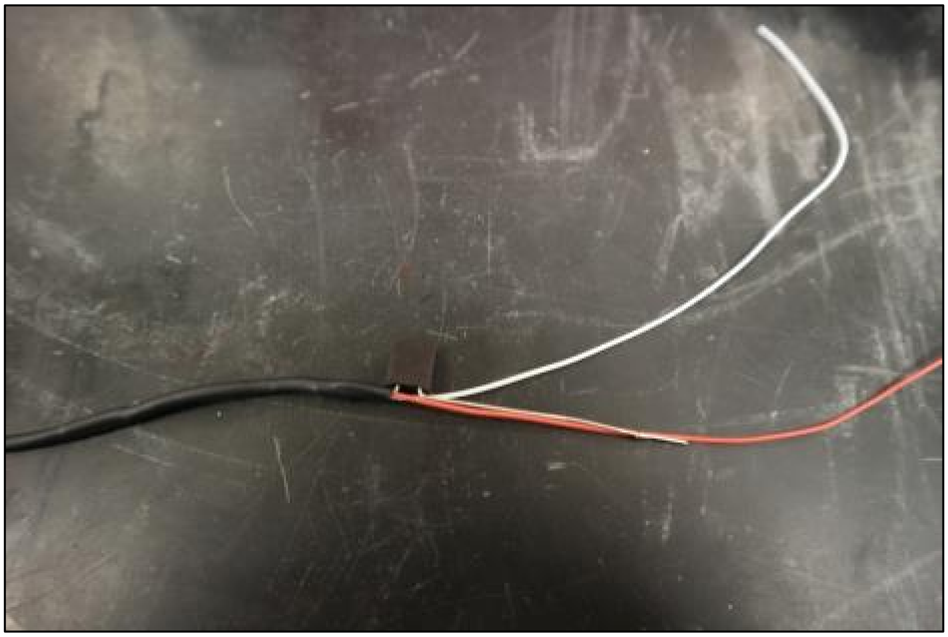

Figure E-13: Heat shrink tubing installation.

15. Solder the 4″ black wire to the other resistor strand.

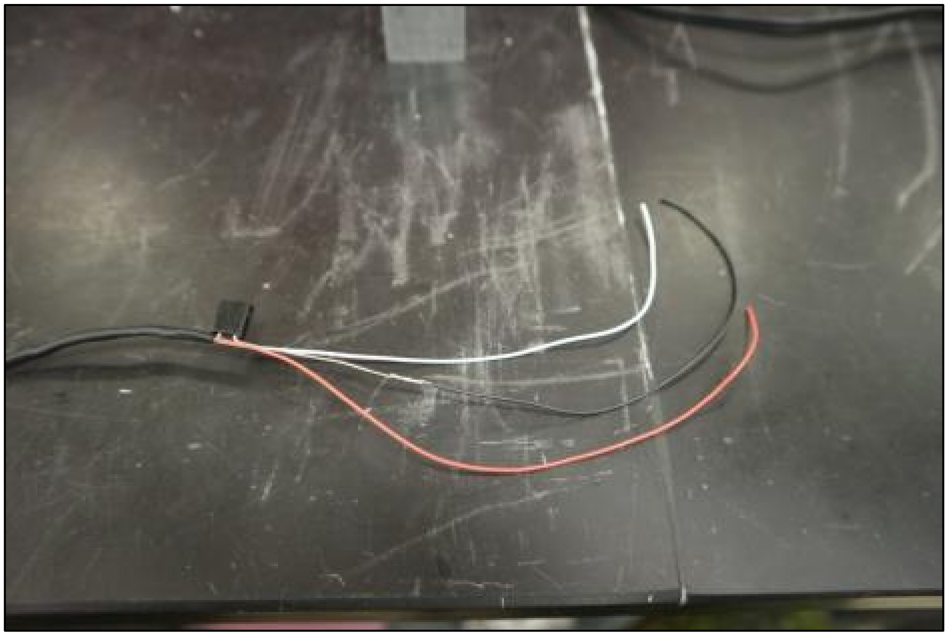

Figure E-14: Soldering wire to resistor.

16. Insert the black wire through 1/16″ shrink tubing while bringing the shrink tubing as close to the resistor as possible. Heat up the shrink tubing.

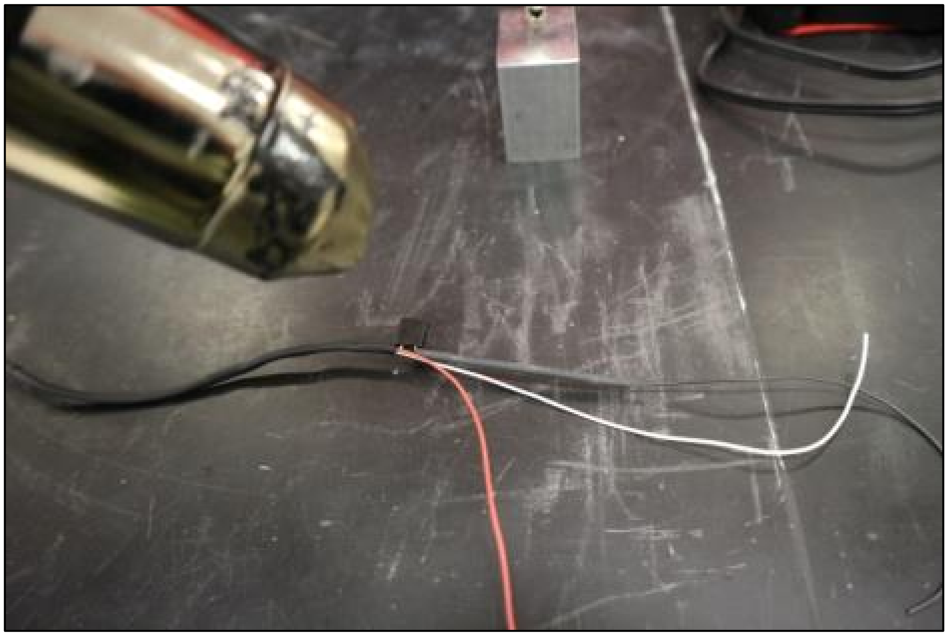

Figure E-15: Heat shrink tubing installation.

17. Insert the black, white and red wire through 3/16″ tubing. Ensure that there is between 1.5-2″ of wire past the shrink tubing.

18. Bring the shrink tubing as close to the resistor as possible then heat it up.

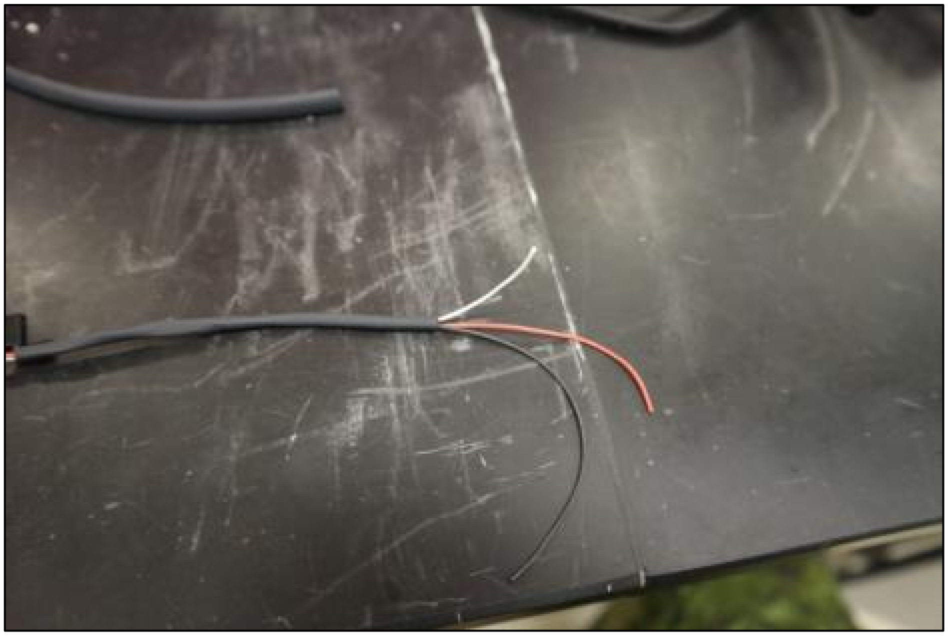

Figure E-16: Heat shrink tubing installation.

19. Ensure that the three wires are the same length past the shrink tubing. If not, cut them to the same length, re-strip the ends and apply solder to the exposed wire.

Figure E-17: Wire verification.

20. Insert the wires through the endbell and cable clamp of the analog connector and then through the ferrule/compression ring.

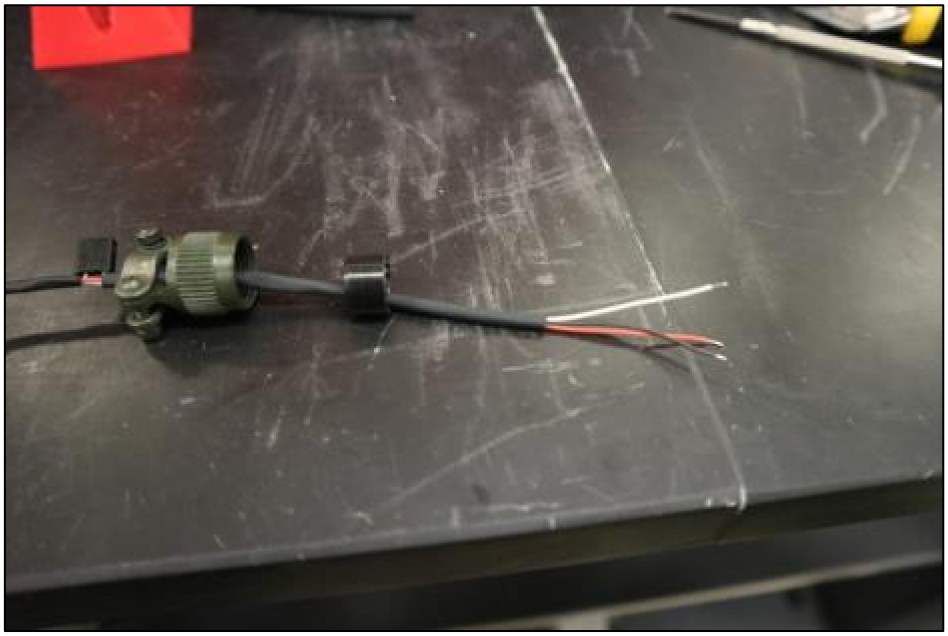

Figure E-18: Passing wires through the endbell clamp, cable clamp and compression ring.

21. Insert the wires through the wire sealing grommet. The white wire goes through the “C” opening, the black wire goes through the “G” opening and the red wire goes through the “F” opening.

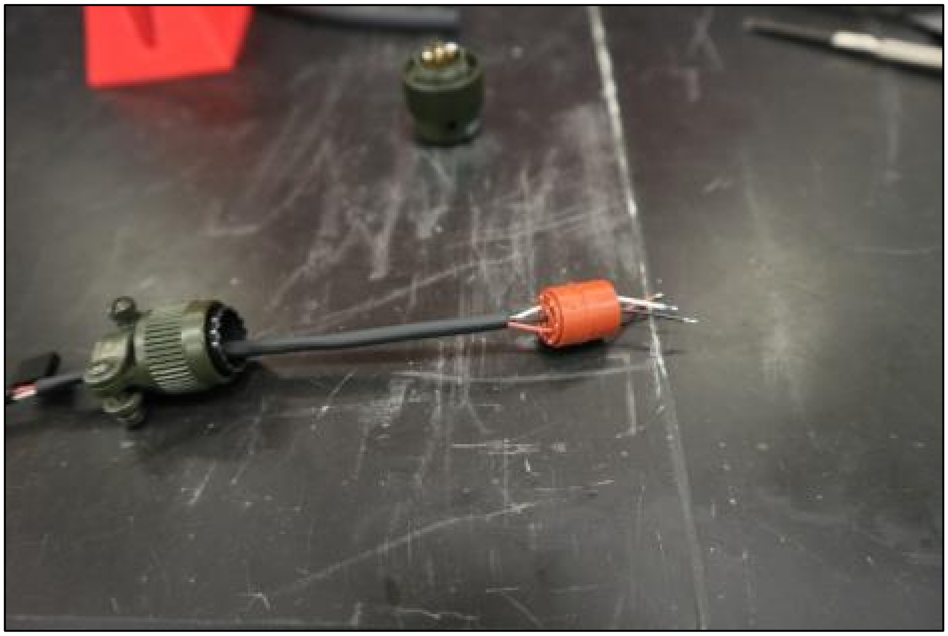

Figure E-19: Inserting wires through wire sealing grommet.

22. Solder the wires to the contacts of the analog connector. Connect the white wire to the C contact, the black wire to the G contact and the red wire to the F contact.

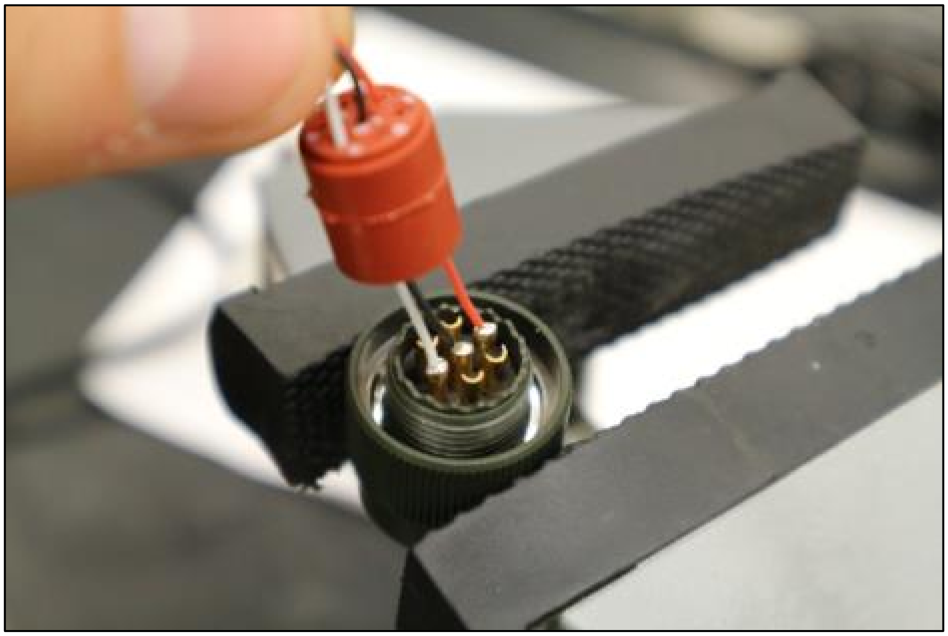

Figure E-20: Soldering wires to analog connector.

23. Bring down the grommet and the compression ring to cover the connections.

Figure E-21: Placing wire sealing grommet and compression ring.

24. Wrap electrical tape around the three wires from just above the shrink tubing to just above the wire sealing grommet. Ensure that there is enough tape that the wires will be held in place by the cable clamp but not too much that it will not be able to pass through the cable clamp.

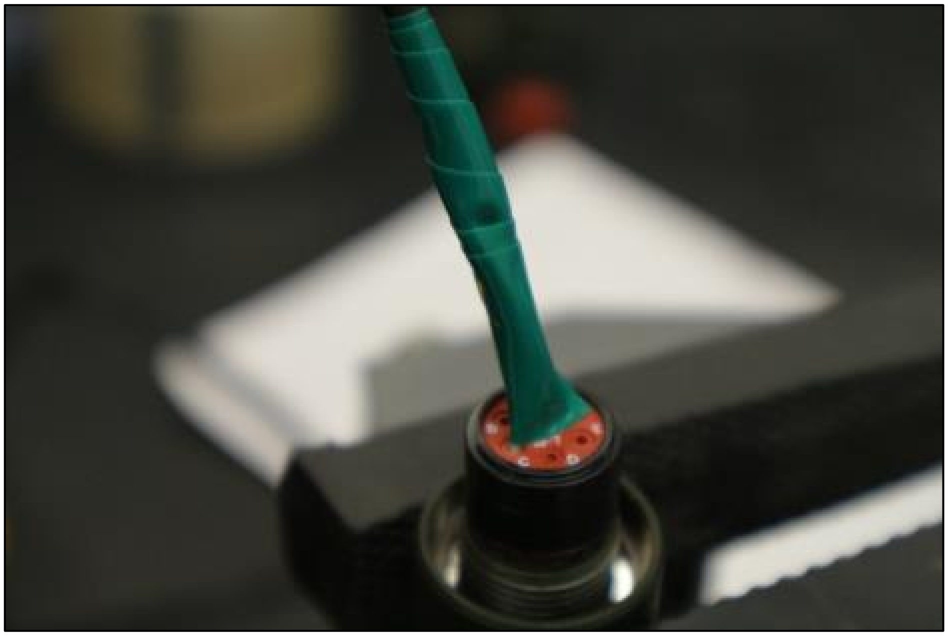

Figure E-22: Wrapping electrical tape around wires.

25. Screw on the endbell to the analog connector and tighten the cable clamp.

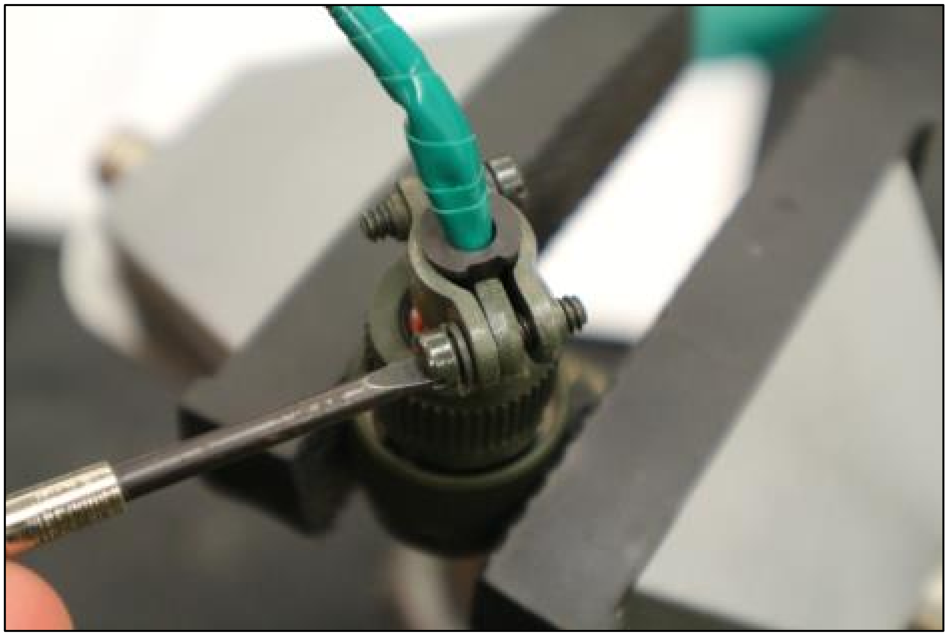

Figure E-23: Installing endbell and cable clamp.

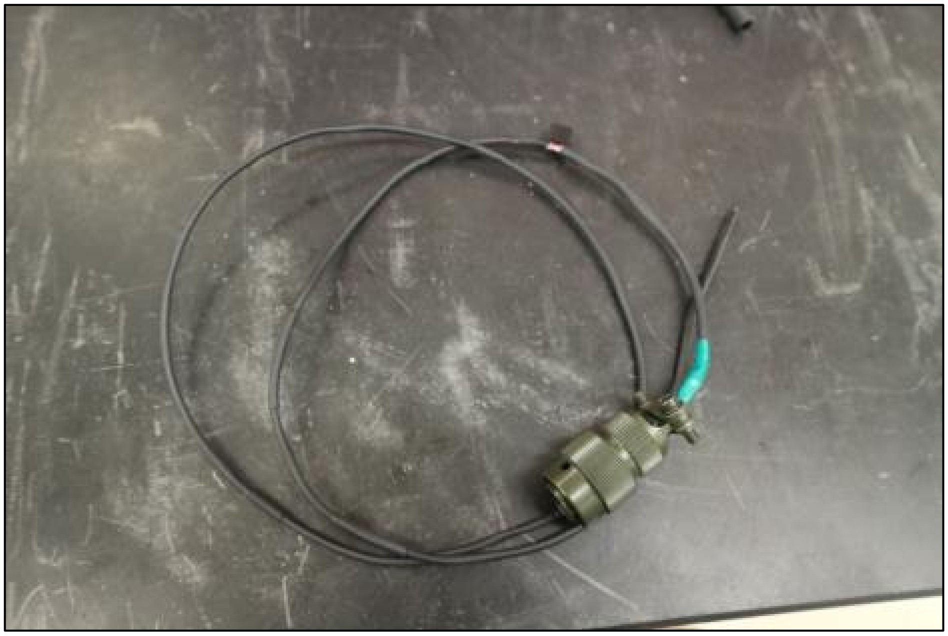

Figure E-24: Assembled thermistor.

26. Connect the thermistor to the in-flight centrifuge computer and perform a quick functionality test with the Acqlipse software. Do so by pinching the thermistor bead. This will cause the voltage to increase. The voltage should decrease after you release the bead. If the thermistor bead does not respond, the thermistor was not assembled properly or some defective materials and/or parts were used.

27. Apply two coat of silicone conformal coating to the first 4-6″ of the thermistor. Apply the coating inside a fume hood. The use of eye protection, a lab coat and nitrile gloves is highly recommended while applying the coating. Ensure that the exposed thermistor strands are covered and the heat shrink tubing openings are sealed. Let each coat dry for 48 hours in the fume hood.

E.6 Thermistor Calibration

Below are step-by-step instructions for the calibration of the thermistors for use within the geotechnical centrifuge. Once the thermistors are calibrated, the temperature can be tracked and recorded during an experiment. This will help understand the effects of temperature on contaminant transport in the geotechnical centrifuge.

1. Prepare a solution of 100 ml of water and 20 g of table salt in a beaker. This will lower the water's freezing point to approximately -20°C.

Figure E-25: Water and table salt solution.

2. Place the solution in a freezer until it reaches approximately -15 °C.

3. Connect the thermistors to be calibrated to the centrifuge’s in-flight computer.

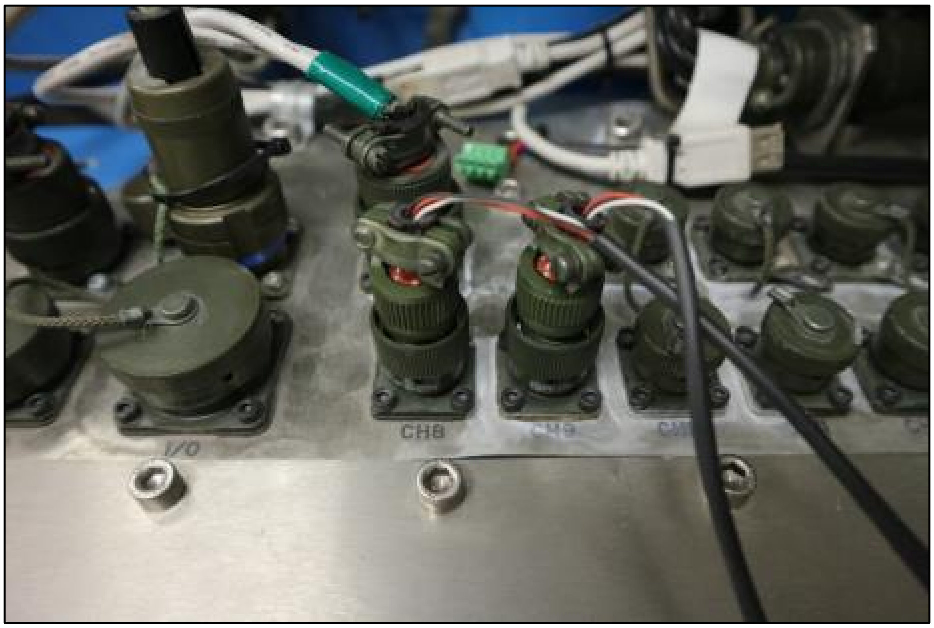

Figure E-26: Thermistors connected to the centrifuge’s analog ports.

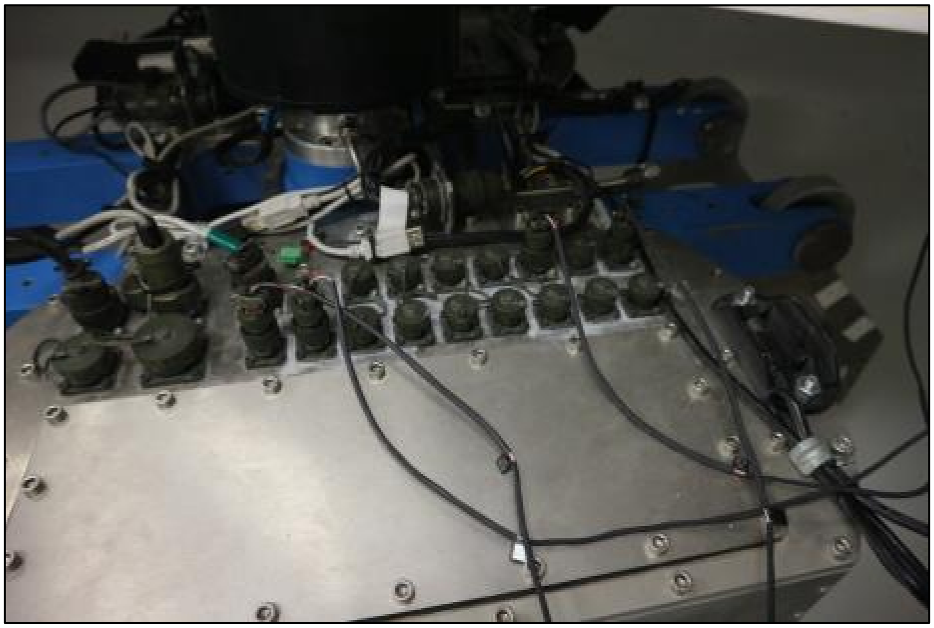

Figure E-27: Centrifuge’s analog ports.

4. Secure the thermistors to a thermocouple with the beads of the thermistors being as close as possible to the tip of the thermocouple.

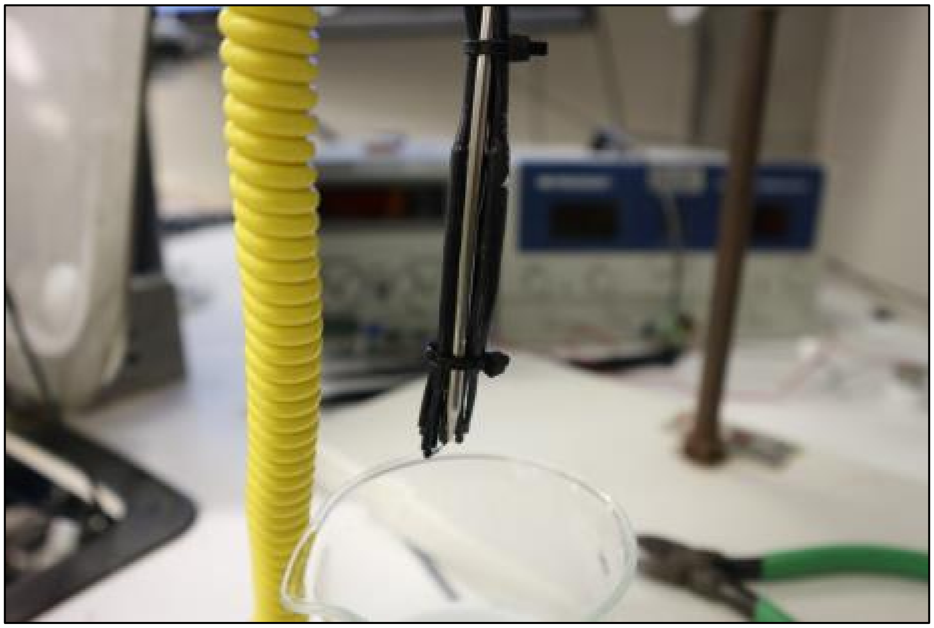

Figure E-28: Thermistors attached to thermocouple.

5. Lower the thermocouple and the thermistor beads into the solution at mid-height.

Figure E-29: Thermocouple and thermistors in saline solution.

6. Open the Acqlipse software.

7. Activate the ports that have thermistors connected.

8. Set the voltage recording period to 10 seconds.

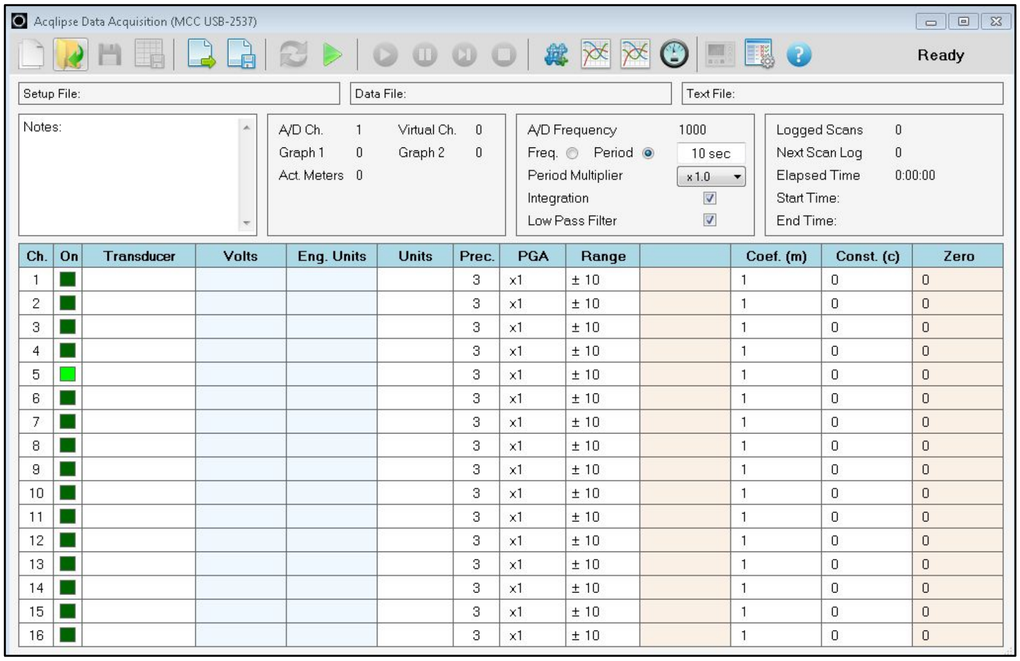

Setup File:
Data File:
Text File:
Notes:

A/D Ch. 1
Virtual Ch. 0
Graph 1 0
Graph 2 0
Act. Meters 0

A/D Frequency 1000
Freq. ○ Period ● 10 sec
Period Multiplier x 1.0
Integration ☑
Low Pass Filter ☑

Logged Scans 0
Next Scan Log 0
Elapsed Time 0:00:00
Start Time:
End Time:

Ch.	On	Transducer	Volts	Eng. Units	Units	Prec.	PGA	Range		Coef. (m)	Const. (c)	Zero
1	■					3	x1	± 10		1	0	0
2	■					3	x1	± 10		1	0	0
3	■					3	x1	± 10		1	0	0
4	■					3	x1	± 10		1	0	0
5	🟩					3	x1	± 10		1	0	0
6	■					3	x1	± 10		1	0	0
7	■					3	x1	± 10		1	0	0
8	■					3	x1	± 10		1	0	0
9	■					3	x1	± 10		1	0	0
10	■					3	x1	± 10		1	0	0
11	■					3	x1	± 10		1	0	0
12	■					3	x1	± 10		1	0	0
13	■					3	x1	± 10		1	0	0
14	■					3	x1	± 10		1	0	0
15	■					3	x1	± 10		1	0	0
16	■					3	x1	± 10		1	0	0

Figure E-30: Acqlipse software main interface.

9. Start the data acquisition.

10. Every 10 seconds record the temperature indicated by the thermocouple reader.

11. Keep recording until the water reaches room temperature.

12. Stop the data acquisition by the Acqlipse software and save the data to a .txt file.

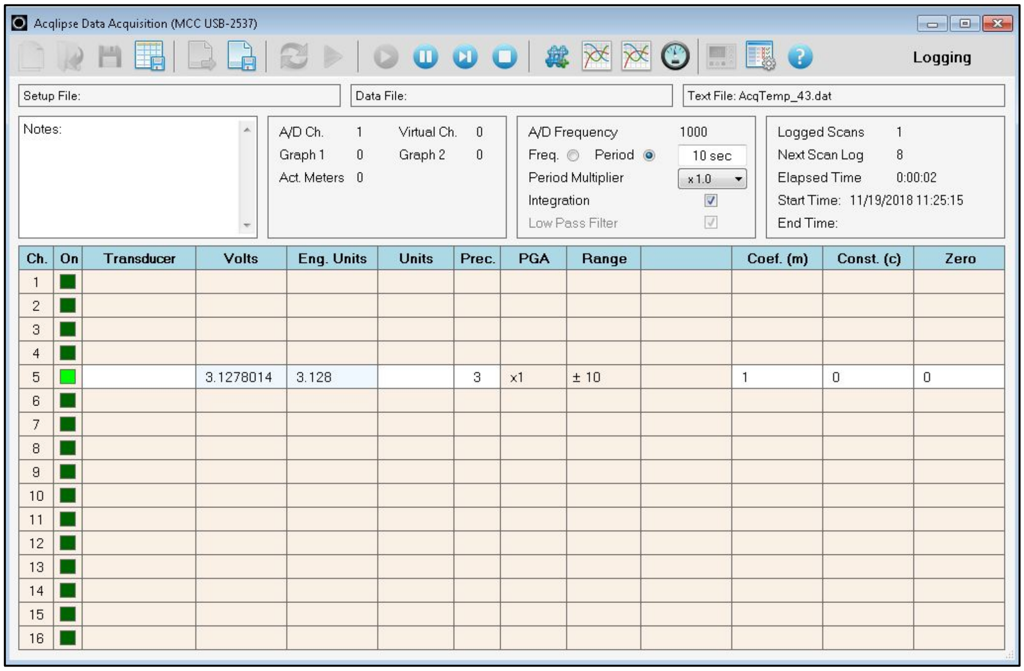

Setup File:

Data File:

Text File: AcqTemp_43.dat

Notes:

A/D Ch. 1
Virtual Ch. 0
Graph 1 0
Graph 2 0
Act. Meters 0

A/D Frequency 1000
Freq. ○ Period ● 10 sec
Period Multiplier x 1.0
Integration ☑
Low Pass Filter ☑

Logged Scans 1
Next Scan Log 8
Elapsed Time 0:00:02
Start Time: 11/19/2018 11:25:15
End Time:

Ch.	On	Transducer	Volts	Eng. Units	Units	Prec.	PGA	Range		Coef. (m)	Const. (c)	Zero
1	🟩											
2	🟩											
3	🟩											
4	🟩											
5	🟩		3.1278014	3.128		3	x1	± 10		1	0	0
6	🟩											
7	🟩											
8	🟩											
9	🟩											
10	🟩											
11	🟩											
12	🟩											
13	🟩											
14	🟩											
15	🟩											
16	🟩											

Figure E-31: Acqlipse software interface during data recording.

13. Insert the recorded voltage data from the .txt file into Excel.

14. Insert the recorded temperature into the same Excel file.

15. Ensure that the recorded temperature and voltage data are matched up according the proper time that each was recorded.

16. Plot a graph of the voltage (x axis) versus temperature (y axis).

17. Determine the slope and the y axis intersect of the plotted data.

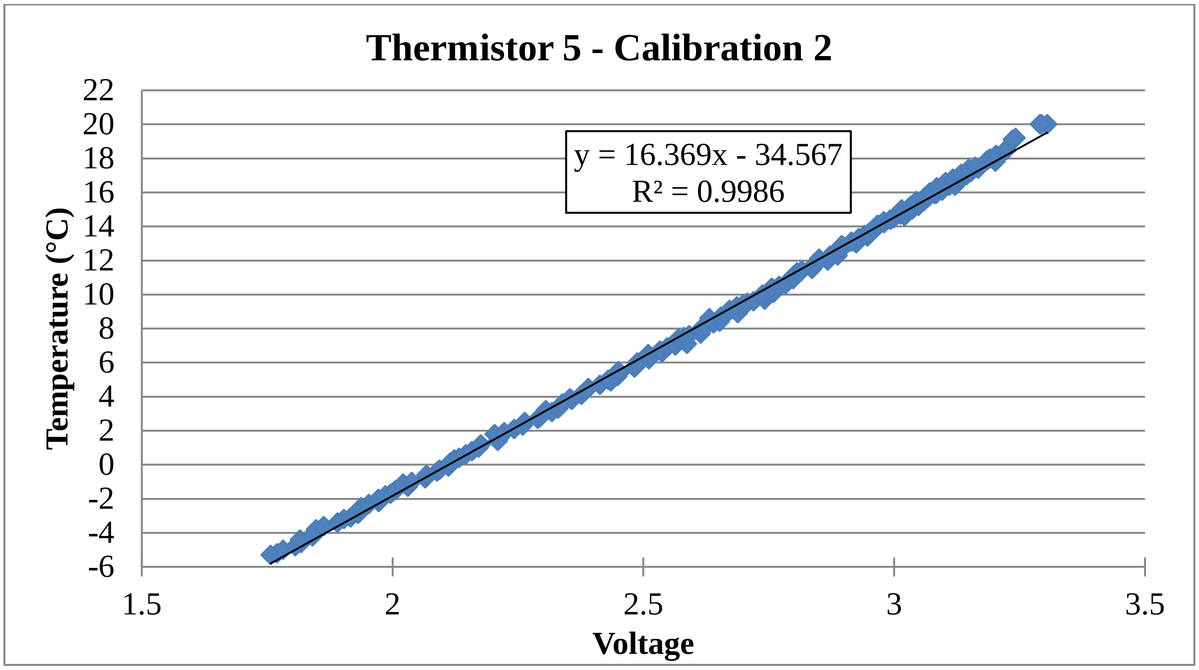

Figure E-32: Example of temperature versus voltage slope for a thermistor calibration.

18. The slope and the intersect can then be inputted into the Acqlipse software, which will then provide temperature data in real-time as voltage is being recorded. To ensure reliable temperature data during experiments, it is recommended to connect the thermistors to the same analog port that was used for calibration.

19. Label the thermistors based on the number of the analog port that was used for calibration. Use paper and clear packing tape to label the thermistors.

APPENDIX F COLUMN EXPERIMENTAL SETUP

F.1 Introduction

This appendix will present the instrumentation for the column experiments. It will also list the instructions that enable experiments to be repeatable and consistent. The column was built using ¾” plexiglas (Figure F-1). The interior dimensions of the column are 533.4 x 342.9 x 177.8 mm (H x W x D) (Figure F-2).

Figure F-1: Plexiglas column used for contaminant transport experiments

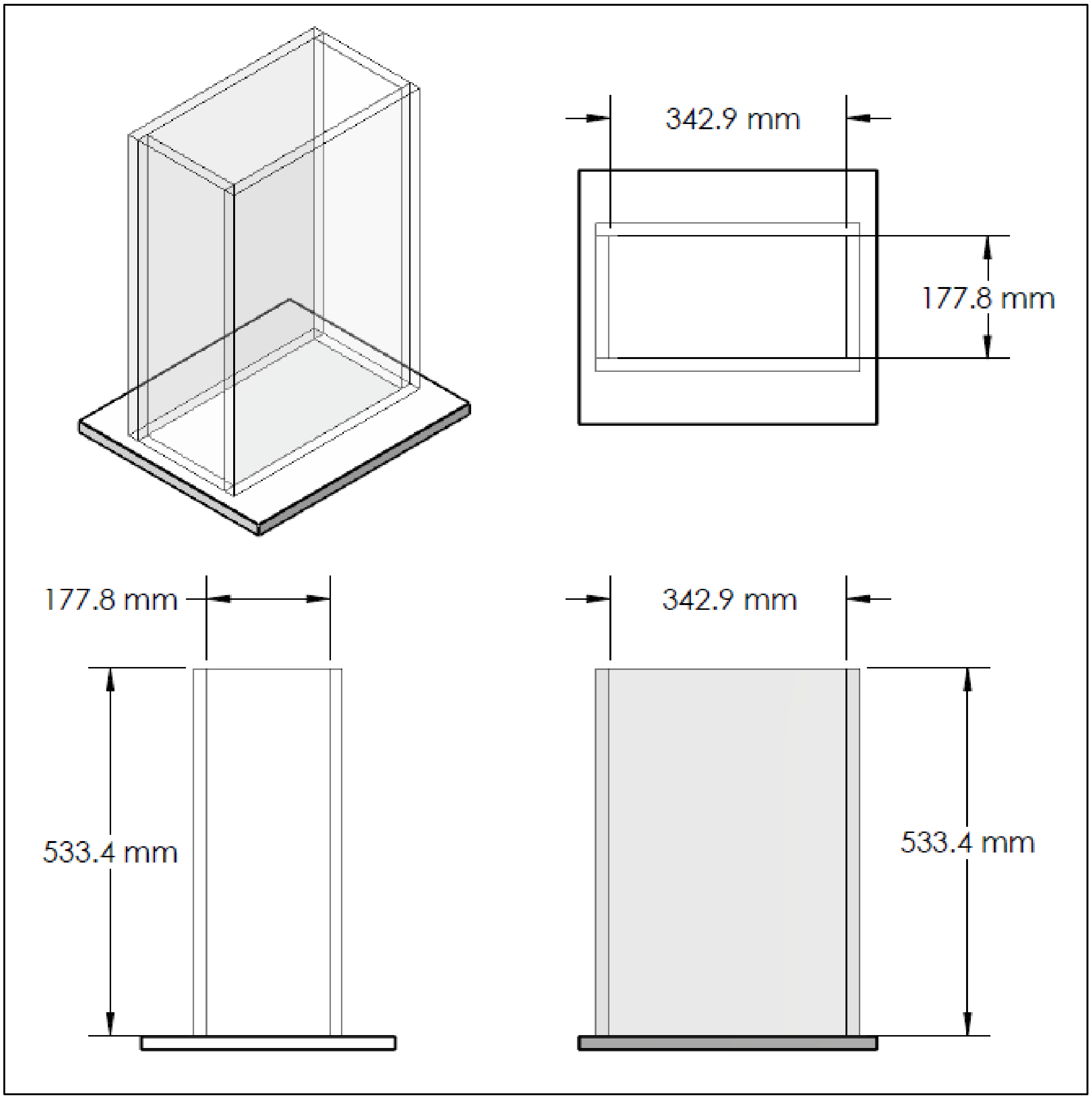

Figure F-2: Interior dimensions of the acrylic column.

F.2 Instrumentation

A Canon Rebel T6 camera was used to take pictures of the oil infiltrating the sand in the column. The pictures could then be analyzed using the MATLAB code detailed in Appendix D. The camera was placed in front of the column face.

Thermocouples were inserted into the sand through ports in the side of the column (Figure F-3 & Figure F-8). The thermocouples allow for the monitoring and recording of temperature throughout the sand during an experiment. The thermocouple data is recorded using the LABVIEW program. The block diagram for the thermocouple temperature recording is shown in Figure F-4. The thermocouples were calibrated using LABVIEW's Calibration Wizard. Silicone conformal coating was applied to the thermocouples in order to waterproof them, which prevents them from rusting when they are exposed to water. The calibration was executed while the thermocouples were placed in a saline solution with an initial temperature of -20°C, which was then left to increase to room temperature. Calibration points were recorded approximately every 5°C while the water's temperature increased.

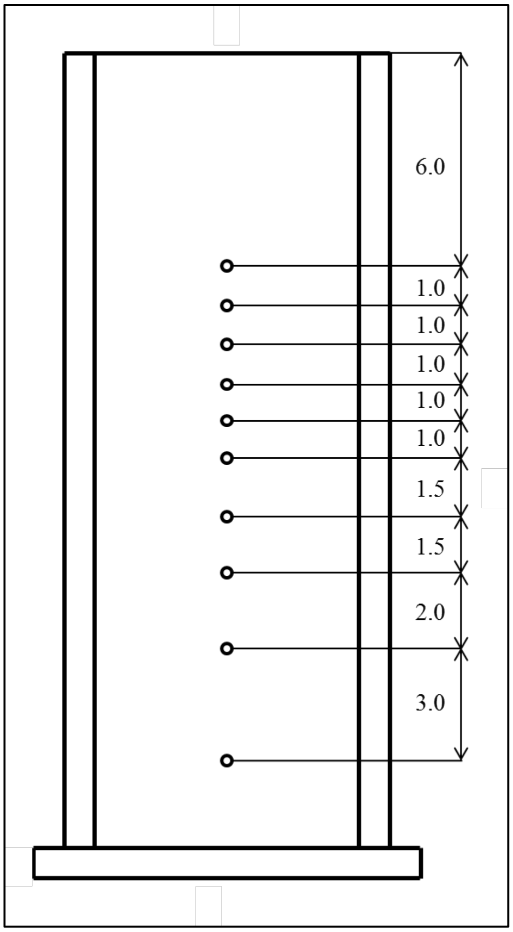

Figure F-3: Column thermocouple ports (distance in inches).

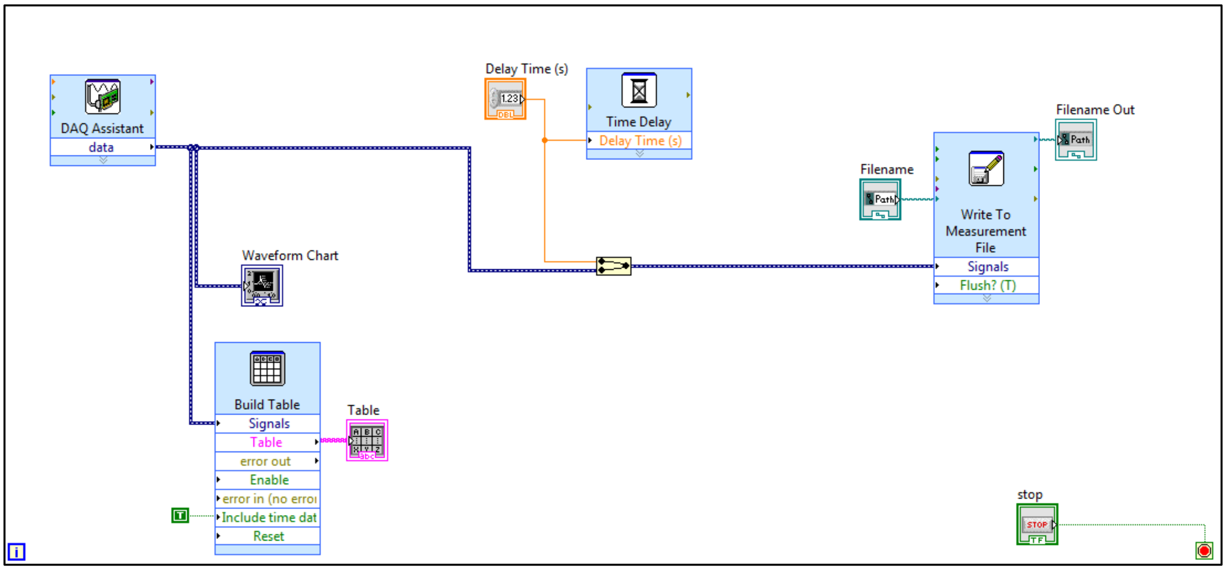

Figure F-4: LABVIEW thermocouple block diagram.

Table F-1 lists some issues that can be encountered with the thermocouples and the solution to the issues.

Table F-1: Thermocouple troubleshooting.

Problem	Likely Cause	Solution
Temperature reads around 22-25°C even though it shouldn't	The stripped wires at the DAQ are probably touching, so the output is room temperature.	Try adjusting the wires so they're not touching
Temperature reads 100°C	The wires aren't connected to the DAQ.	Adjust them and make sure that the screws are tight
The temperature increases when it should decrease and vice versa	The wires are backwards somewhere.	Check that white is positive and red is negative at the DAQ, and inside the connectors (both male and female)
It seems like the thermocouples aren't calibrated properly, even though they were calibrated recently.	The readings will be off by a few degrees if the thermocouple is connected to the wrong extension wire.	Make sure that the thermocouple is connected to the same extension wire that was used for the calibration.

F.3 Experimental Setup Instructions

1. The #730 silica sand that will be used for the experiment must be dry and be sieved with the #20 sieve. This will remove any debris and the ceramic spheres that are found in the sand.

2. Mix the sand with water to the desired moisture content for the experiment. Mix the sand and water in batches of 3kg of soil plus the desired water. Ensure that at least three samples of the soil and water mix are taken to measure the moisture content of the soil in the column.

3. Place the column on a shaker table.

4. Add the sand and water mix to the column in layers of approximately 1 cm. Tamp down the sand as much as possible. A Plexiglas plate on a wooden dowel was used to tamp the sand (Figure F-5).

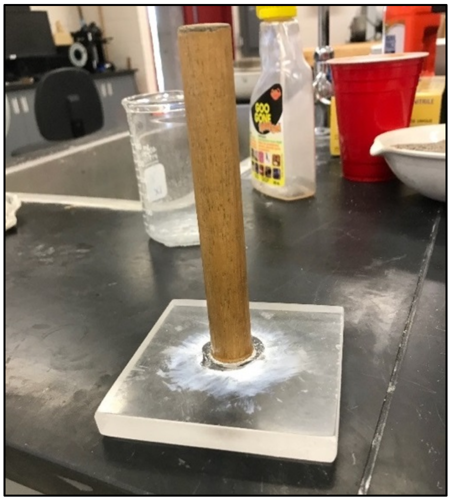

Figure F-5: Plexiglas tamper.

5. Once the 3 kg of sand has been added to the column and tamped down, ensure that the soil is as level as possible. Then add an acrylic plate which has been cut to the inner dimensions of the column. Weights are to be placed on the plate according to Figure F-6. Ensure that the weights are wrapped in felt to prevent them from scratching the column walls. Turn on the shaker table to help compact the sand. Run the shaker table for three minutes (Figure F-7).

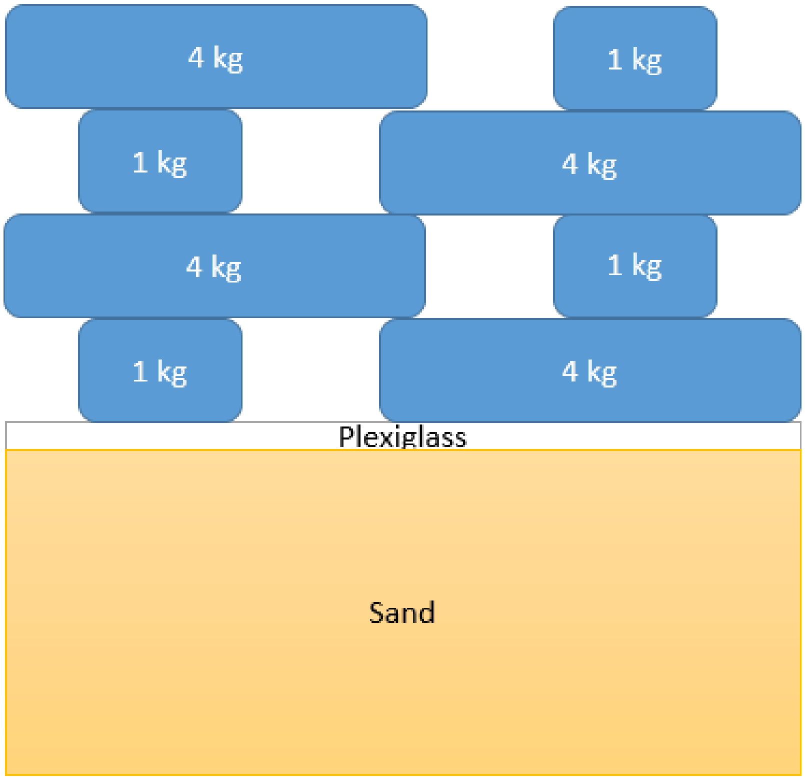

Figure F-6: Arrangement of weights on the Plexiglas plate.

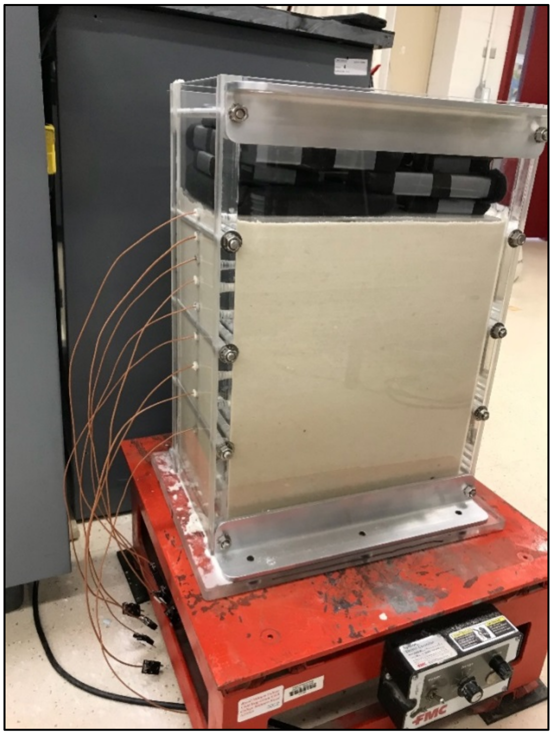

Figure F-7: Vibratory compaction of the sand in the column.

6. Insert the thermocouples through the side ports in the column as the height of the soil reaches the ports. Once a thermocouple is inserted in the port, insert it through a rubber plug in which a slit has been cut lengthwise to reach the inner channel of the plug. The plug can now be pushed back into the port (Figure F-8). Measure the length to which the thermocouple is inserted in the sand. If a high water content is used for an experiment, it is recommended to used high vacuum grease to seal the thermocouples ports on the outside of the column to prevent water from escaping the column.

Figure F-8: Thermocouples arrangement in the column.

7. Repeat steps 4, 5 & 6 until the desired sand height for the experiment has been achieved.

8. Use the steel cables to hoist the column into the freezer. Lower the column onto the scissor jack located at the bottom of the freezer. Ensure that the column face is perpendicular to the camera. Place the camera in the freezer. The camera should be raised 39 cm when the column is in the freezing position and 54 cm when the column is in the thawing position. Foam insulation was used to raise the camera for these experiments. Place the jeep lights in the position shown in Figure F-9 and connect them to a DC power source.

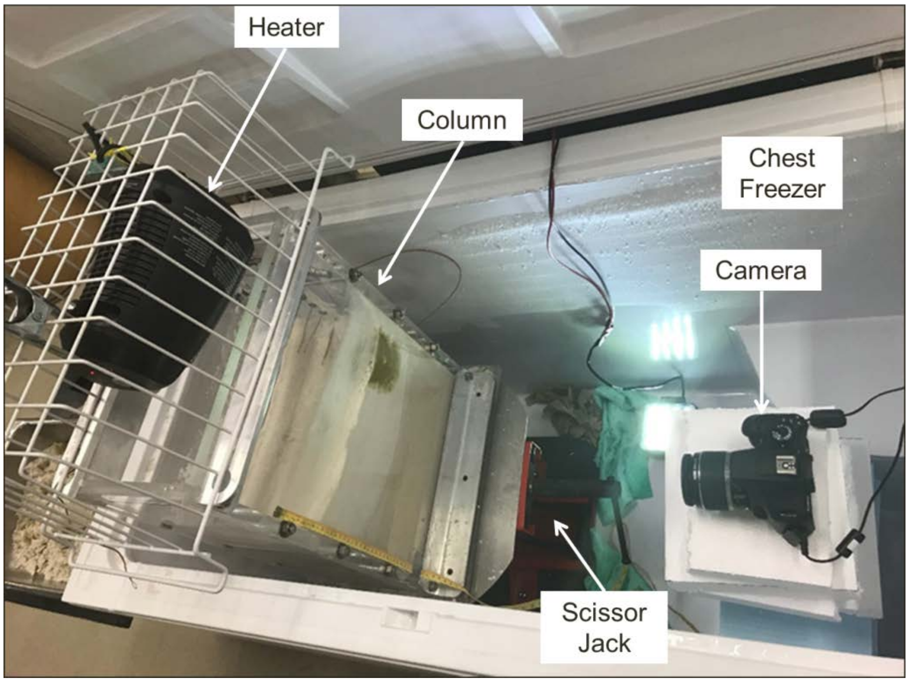

Figure F-9: Column experiment setup.

9. Connect the camera to its power source and to a laptop using a USB cable.

10. Set the freezer to the desired temperature (Figure F-10). The black mark shows where the freezer will maintain freezing temperatures (level 0.5). Temperatures of approximately -20°C are achievable when the dial is set to level 7.

Figure F-10: Freezer control dial.

11. Connect the thermocouples to the DAQ, which is connected to the same laptop as the camera.

12. The camera focus must be adjusted before starting the remote shooting. This is done by placing the camera on the foam insulation to the desired height (freezing or thawing height). The camera should then be set to “Auto Focus” (Figure F-11). Hold the shutter button until the focus is adjusted then take a picture. The camera will adjust the focus based on the focal length of the lens and the distance from the column. Verify on the laptop that the focus has been adjusted to get a clear picture. Set the camera to the manual focus setting.

13. The EOS Utility program is used for remote shooting with the camera (Figure F-12). The picture time interval and the total amount of pictures to be taken can be changed in the remote shooting settings (Figure F-13).

Figure F-11: Camera focus settings.

Figure F-12: EOS Utility remote shooting interface.

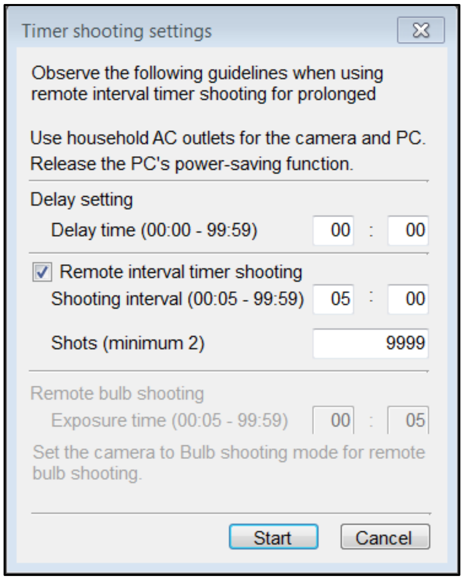

Observe the following guidelines when using remote interval timer shooting for prolonged

Use household AC outlets for the camera and PC.
Release the PC's power-saving function.

Delay setting
Delay time (00:00 - 99:59) 00 : 00

☑ Remote interval timer shooting
Shooting interval (00:05 - 99:59) 05 : 00
Shots (minimum 2) 9999

Remote bulb shooting
Exposure time (00:05 - 99:59) 00 : 05
Set the camera to Bulb shooting mode for remote bulb shooting.

Figure F-13: Timer settings for remote shooting.

14. Start the LABVIEW program (Figure F-14), which will be used to record the thermocouple temperatures throughout the column. Input the interval time between recordings in the “Delay Time” box. To start recording temperatures, click on the white arrow in the top left portion of the interface. It will prompt you to select the file name and location. When the program is running the arrow will turn black. The program can be stopped immediately by clicking on the red octagon. Pressing the “Stop” button will stop the program after the next recording is taken. The data is saved in an Excel file, where it can be plotted.

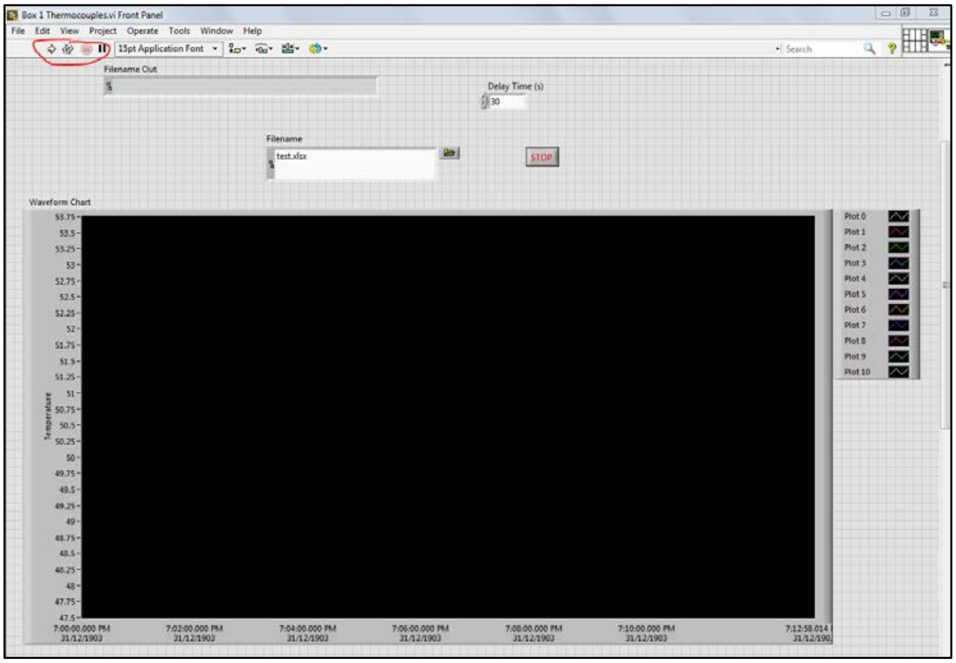

Filename Out

Delay Time (s) 30

Filename test.xlsx

Figure F-14: LABVIEW main interface.

15. If frozen soil is desired at the beginning of the experiment, the column can be lowered into the freezer with the scissor jack. The column is typically left to freeze overnight prior to starting an experiment.

16. Once the oil is ready to be added, open the freezer and add the oil to the column. This can be done by drilling holes near the acrylic window with a drill bit and adding the oil with a plastic syringe. The oil can also be added by cooling the pumpkin seed oil until it freezes in a plastic vial. The vial can then be placed upside down in the column. The oil will melt over time and infiltrate through the sand.

17. If a thaw cycle is desired for an experiment, the freezer must be opened and the column raised with the scissor jack. The column is to be raised approximately 10 cm above the edge of the freezer.

18. Foam insulation that has been cut to fit around the column is to be placed on the freezer (Figure C-14). The insulation ensure that only the open end of the column is subject to room-temperature air.

Figure F-15: Column raised in the thaw position.

19. Stop the remote shooting and raise the camera by adding more foam insulation under it. Repeat Step 12 to re-adjust the focus of the camera. Restart the remote shooting of the camera.

20. Suspend the heater from one of the freezer’s basket and plate it over the column. Ensure that one end of the basket is raised since the heater’s face is angled.

21. Repeat as many freeze thaw cycles as required or desired for the experiment.

22. Collect the images and the temperature data from the laptop for analysis.

APPENDIX G IMAGE ANALYSIS

G.1 Introduction

Once an experiment is completed, the data can be analyzed with the help of a MATLAB code. This code allows taking the pictures from an experiment and quantifying the depth of the oil by tagging the location of the oil front for all the pictures. The depth of oil front is then plotted versus time based on the time interval between each picture. With this code it is possible to quantity the depth of oil front over time for each experiment. The experiments can then be objectively compared based on the different conditions for each experiment.

G.2 Running the MATLAB Code

1. To use the MATLAB code to quantify the oil infiltration results, the MATLAB software must be opened. Afterwards the code, must be opened from MATLAB.

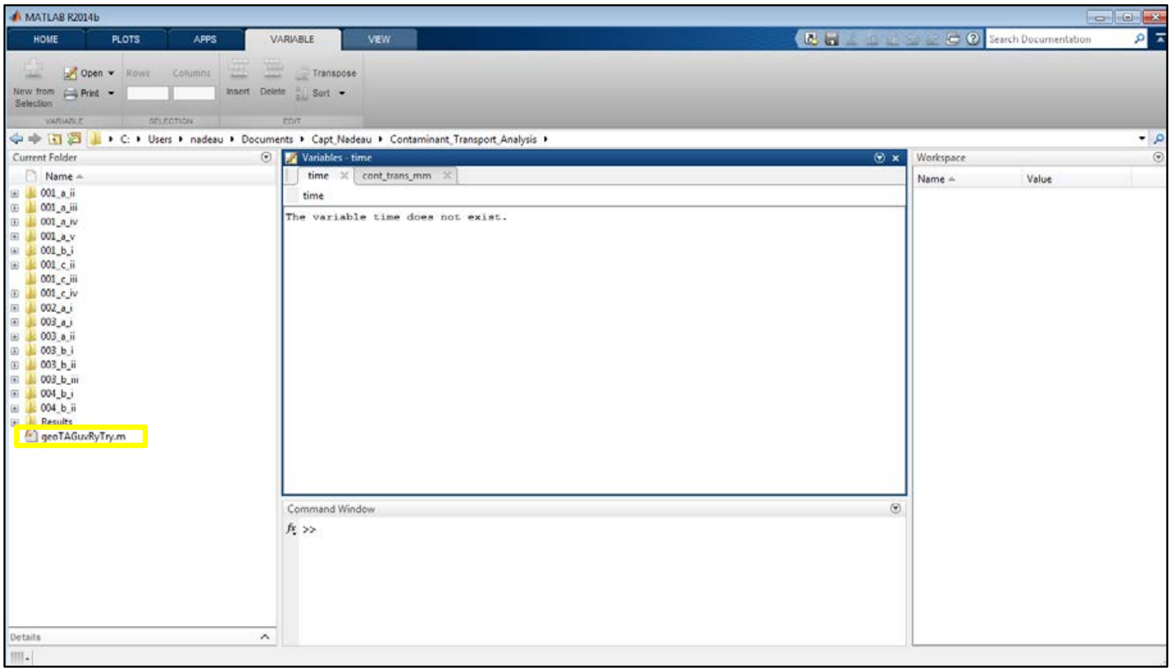

```
The variable time does not exist.
```

```
fx >>
```

Figure G-1: MATLAB R2014b interface.

2. The current directory must now be changed to the folder where the pictures to be analyzed are located. Ensure that the PIV codes are added to the path since some of its functions are used in this code.

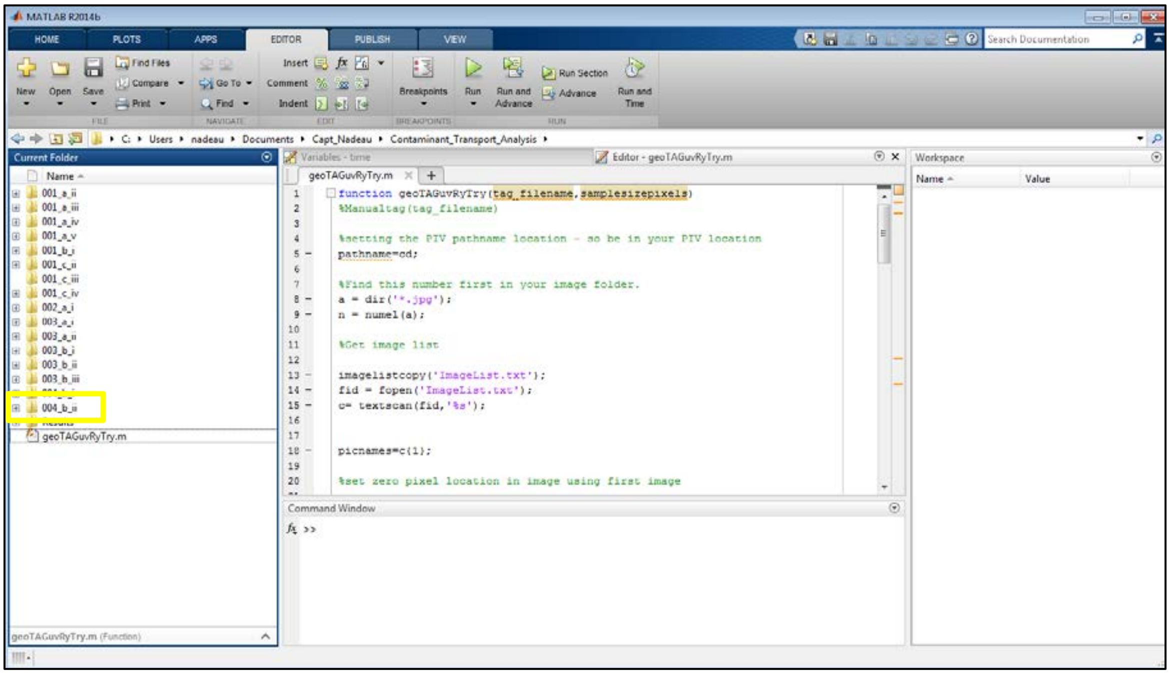

```
function geoTAGuvRyTry(tag_filename,samplesizepixels)
%Manualtag(tag_filename)

%setting the PIV pathname location - so be in your PIV location
pathname=cd;

%Find this number first in your image folder.
a = dir('*.jpg');
n = numel(a);

%Get image list

imagelistcopy('ImageList.txt');
fid = fopen('ImageList.txt');
c= textscan(fid,'%s');


picnames=c(1);

%set zero pixel location in image using first image
```

Figure G-2: Changing the current directory to the picture location.

3. The code can now be started.

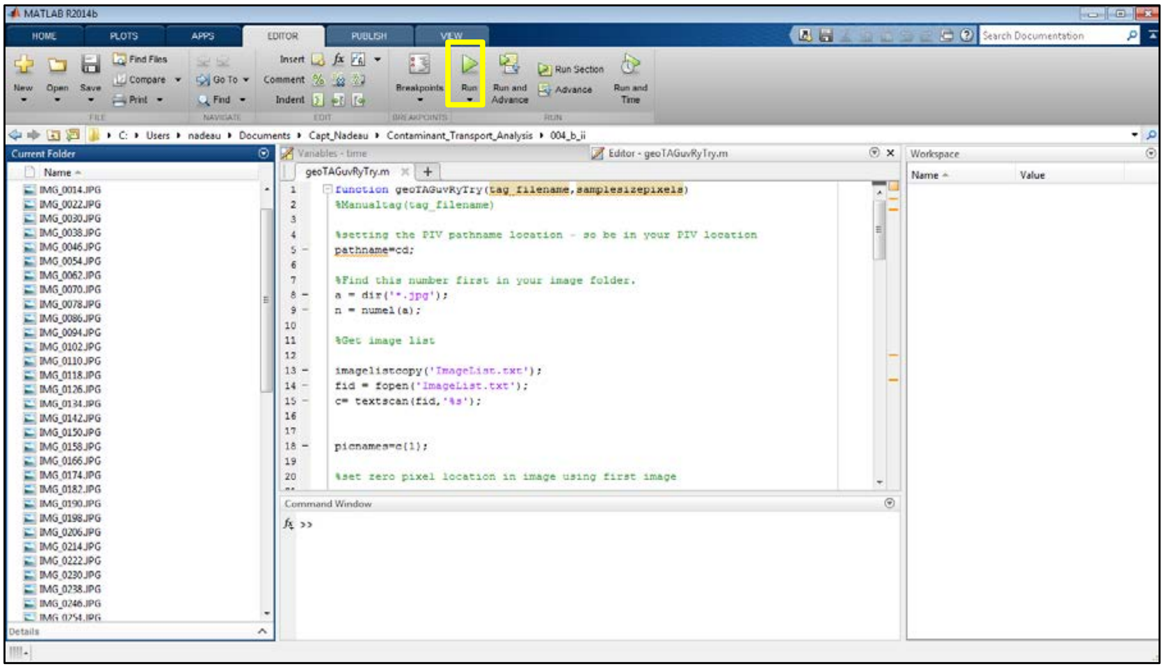

```
function geoTAGuvRyTry(tag_filename,samplesizepixels)
%Manualtag(tag_filename)

%setting the PIV pathname location - so be in your PIV location
pathname=cd;

%Find this number first in your image folder.
a = dir('*.jpg');
n = numel(a);

%Get image list

imagelistcopy('ImageList.txt');
fid = fopen('ImageList.txt');
c= textscan(fid,'%s');


picnames=c(1);

%set zero pixel location in image using first image
```

Figure G-3: Running the code.

4. The first step of the code is to tag the “zero” location for each of the three oil vial location. To zero the three oil vials, simply click the bottom part of the vial. This code is set up to be able to analyze the results of three oil vials. If more than three oil vials are used for an experiment, the code will have to be run more than once. After the three vials have been zeroed, hit “enter” on your keyboard. The same interface as the zeroing will be visible after pressing “enter”. The depth of the oil front can now be tagged for each picture. Simply click on the deepest part of the oil front for each picture then press “enter”. After pressing “enter” it will transition to the next picture. Tag the depth of oil front for all three vials for each picture in the folder.

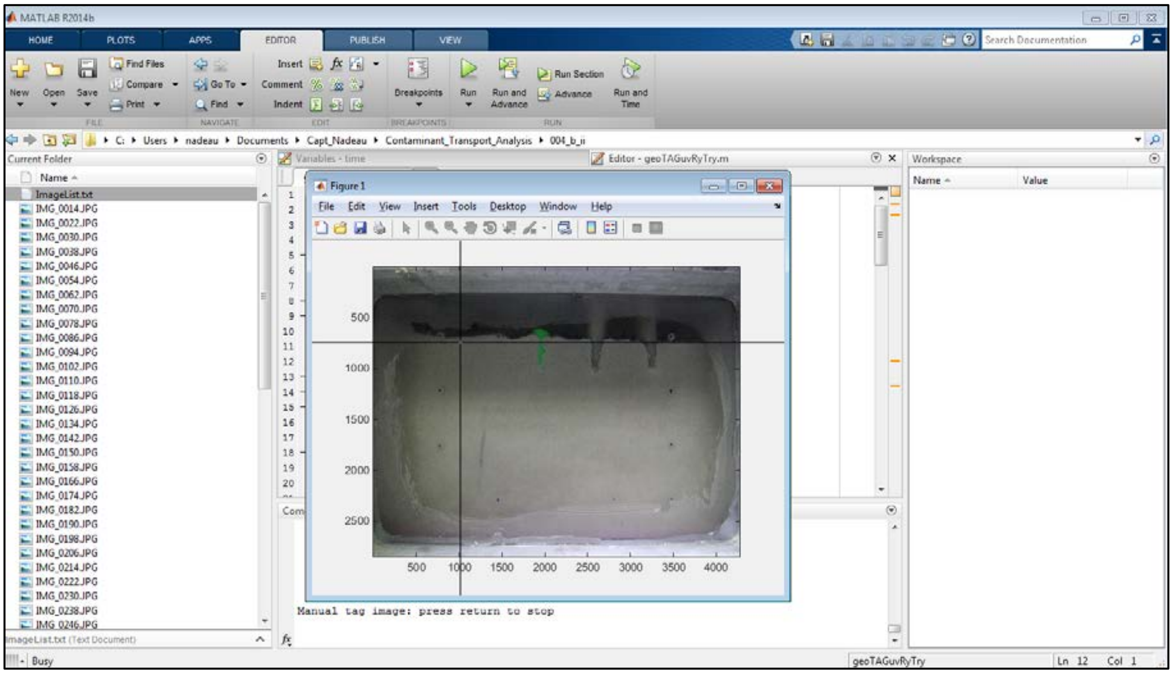

```
Manual tag image: press return to stop
```

Figure G-4: Image zeroing and tagging of the oil front.

5. Once all of the pictures have been tagged, it will go back to the initial MATLAB interface. Input the time interval between pictures, in minutes.

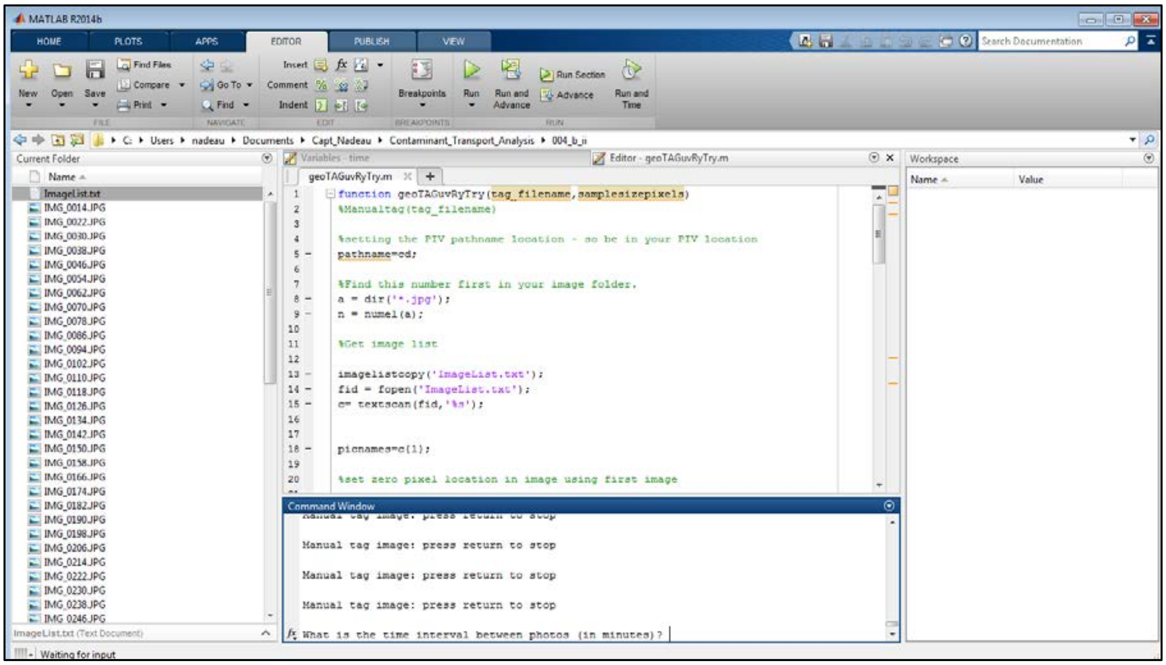

```
function geoTAGuvRyTry(tag_filename,samplesizepixels)
%Manualtag(tag_filename)

%setting the PIV pathname location - so be in your PIV location
pathname=cd;

%Find this number first in your image folder.
a = dir('*.jpg');
n = numel(a);

%Get image list

imagelistcopy('ImageList.txt');
fid = fopen('ImageList.txt');
c= textscan(fid,'%s');


picnames=c{1};

%set zero pixel location in image using first image
```

```
Manual tag image: press return to stop

Manual tag image: press return to stop

Manual tag image: press return to stop

What is the time interval between photos (in minutes)?
```

Figure G-5: Inputting picture time interval.

6. The code will then ask for the pixel to mm ratio. The ratio was determined by uploading a picture to GetData of an experiment from the camera's regular shooting position. The axes of the picture were set as the pixel size of the pictures (4272x2848). Data points were then added at two points along the ends of the acrylic window, which is a known distance of 300 mm. The GetData software gives coordinates of points based on the axes. The pixel distance between the two points was divided by 300 mm to get a pixel ratio of 12.8. For the pixel to mm ratio for the column, the same method was used. A measuring tape on the column was used as the known distance. The pixel to mm ratio was determined to be 11.3 for the column experiments.

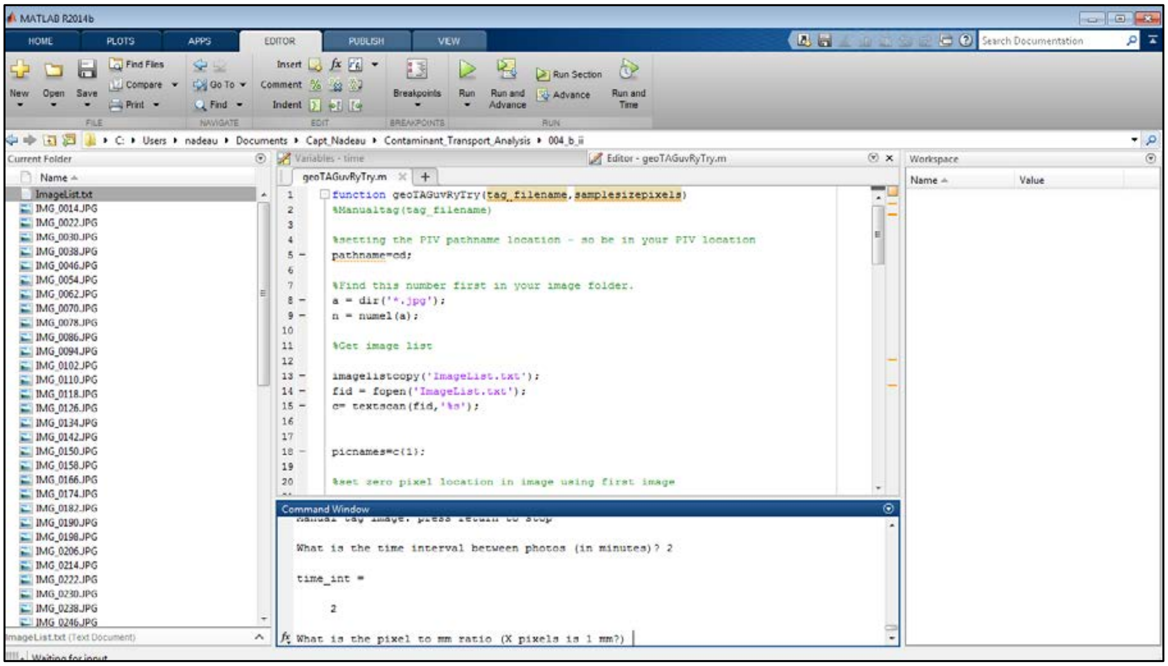

```
function geoTAGuvRyTry(tag_filename,samplesizepixels)
%Manualtag(tag_filename)

%setting the PIV pathname location - so be in your PIV location
pathname=cd;

%Find this number first in your image folder.
a = dir('*.jpg');
n = numel(a);

%Get image list

imagelistcopy('ImageList.txt');
fid = fopen('ImageList.txt');
c= textscan(fid,'%s');


picnames=c{1};

%set zero pixel location in image using first image
```

```
What is the time interval between photos (in minutes)? 2

time_int =

     2

What is the pixel to mm ratio (X pixels is 1 mm?)
```

Figure G-6: Inputting the pixel to mm ratio.

7. The code produces a plot of the depth of the oil (in mm) front for the three vials versus time (in minutes).

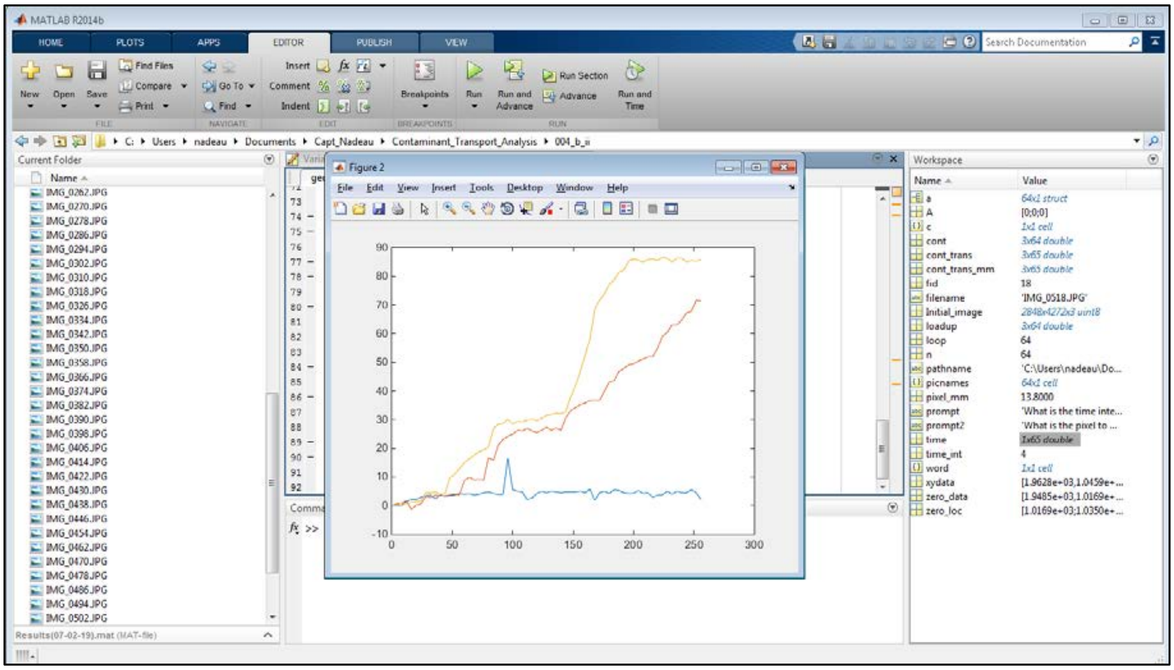

Name	Value
a	64x1 struct
A	[0;0;0]
c	1x1 cell
cont	3x64 double
cont_trans	3x65 double
cont_trans_mm	3x65 double
fid	18
filename	'IMG_0518.JPG'
Initial_image	2848x4272x3 uint8
loadup	3x64 double
loop	64
n	64
pathname	'C:\Users\nadeau\Do...
picnames	64x1 cell
pixel_mm	13.8000
prompt	'What is the time inte...
prompt2	'What is the pixel to ...
time	1x65 double
time_int	4
word	1x1 cell
xydata	[1.9628e+03,1.0459e+...
zero_data	[1.9485e+03,1.0169e+...
zero_loc	[1.0169e+03;1.0350e+...

Figure G-7: Graph of depth of oil front versus time.

8. The axes can be labelled and modified as desired by clicking on “Edit” then “Axes Properties”. The x axis is labelled as “Time (min)” and the y axis is labelled as “Depth of Oil Front (mm)”. The y axis is reversed to give a better visual representation of the results.

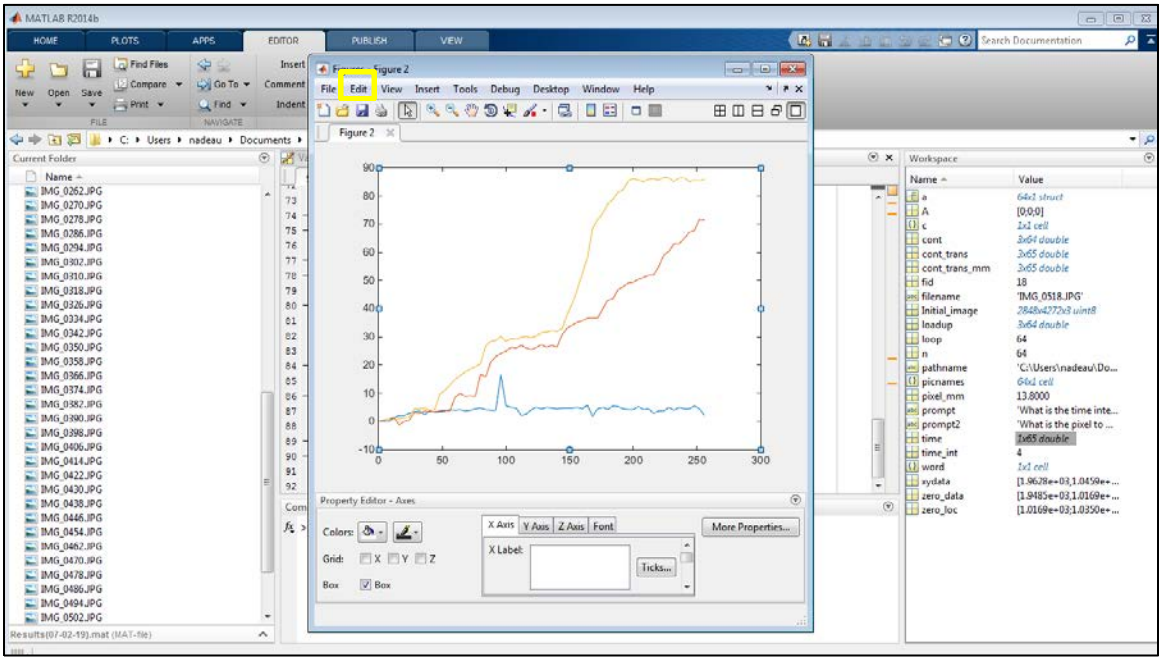

Property Editor - Axes

Colors:

Grid: ☐ X ☐ Y ☐ Z

Box ☑ Box

X Label:

Name	Value
a	64x1 struct
A	[0;0;0]
c	1x1 cell
cont	3x64 double
cont_trans	3x65 double
cont_trans_mm	3x65 double
fid	18
filename	'IMG_0518.JPG'
Initial_image	2848x4272x3 uint8
loadup	3x64 double
loop	64
n	64
pathname	'C:\Users\nadeau\Do...
picnames	64x1 cell
pixel_mm	13.8000
prompt	'What is the time inte...
prompt2	'What is the pixel to ...
time	1x65 double
time_int	4
word	1x1 cell
xydata	[1.9628e+03,1.0459e+...
zero_data	[1.9485e+03,1.0169e+...
zero_loc	[1.0169e+03;1.0350e+...

Figure G-8: Modifying the axes properties.

9. The graph can then be saved as a JPEG image.

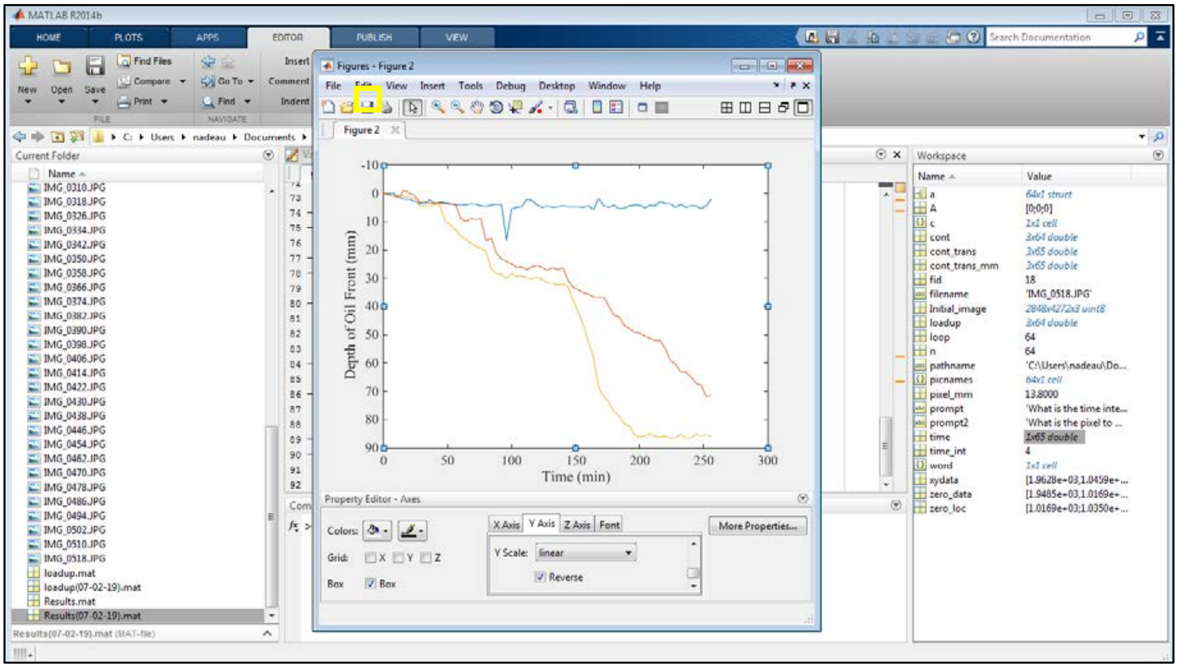

Colors:

Grid: ☐ X ☐ Y ☐ Z

Box ☑ Box

Y Scale: linear

☑ Reverse

Name	Value
a	64x1 struct
A	[0;0;0]
c	1x1 cell
cont	3x64 double
cont_trans	3x65 double
cont_trans_mm	3x65 double
fid	18
filename	'IMG_0518.JPG'
Initial_image	2848x4272x3 uint8
loadup	3x64 double
loop	64
n	64
pathname	'C:\Users\nadeau\Do...
picnames	64x1 cell
pixel_mm	13.8000
prompt	'What is the time inte...
prompt2	'What is the pixel to ...
time	1x65 double
time_int	4
word	1x1 cell
xydata	[1.9628e+03,1.0459e+...
zero_data	[1.9485e+03,1.0169e+...
zero_loc	[1.0169e+03;1.0350e+...

Figure G-9: Saving the graph as an image.

10. The data produced from the code can be found in the MATLAB workspace. The data for the depth of oil front can be found in "cont_trans_mm" and the time data can be found in "time".

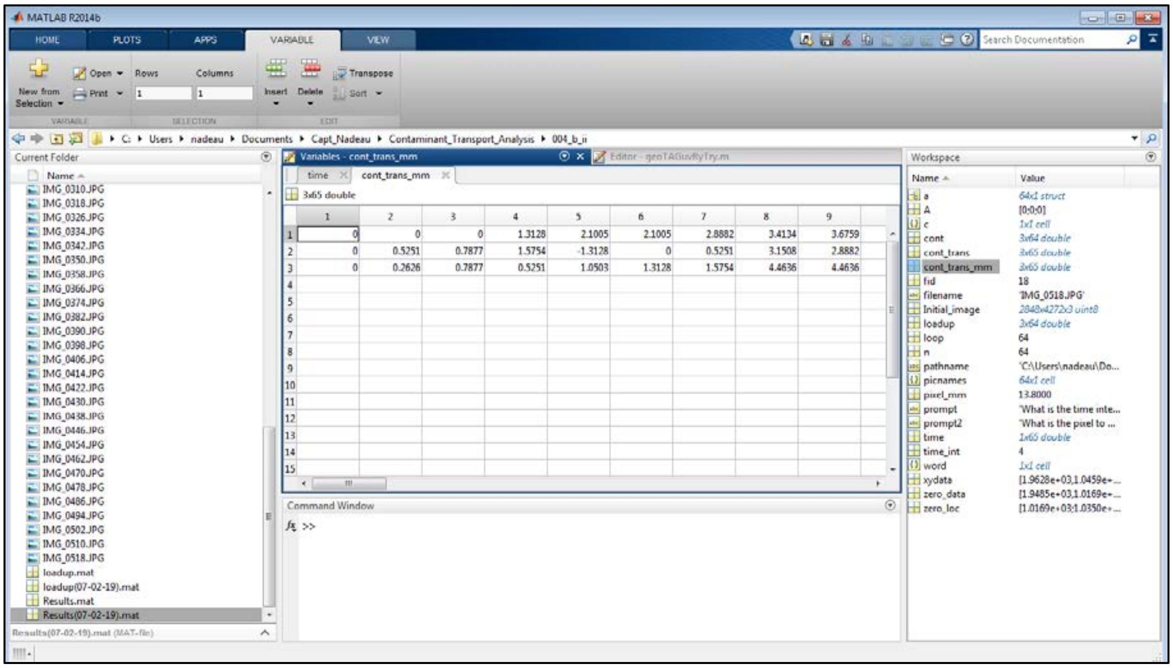

C: ▸ Users ▸ nadeau ▸ Documents ▸ Capt_Nadeau ▸ Contaminant_Transport_Analysis ▸ 004_b_ii

3x65 double

	1	2	3	4	5	6	7	8	9
1	0	0	0	1.3128	2.1005	2.1005	2.8882	3.4134	3.6759
2	0	0.5251	0.7877	1.5754	-1.3128	0	0.5251	3.1508	2.8882
3	0	0.2626	0.7877	0.5251	1.0503	1.3128	1.5754	4.4636	4.4636

Figure G-10: Depth of oil front data from the workspace.

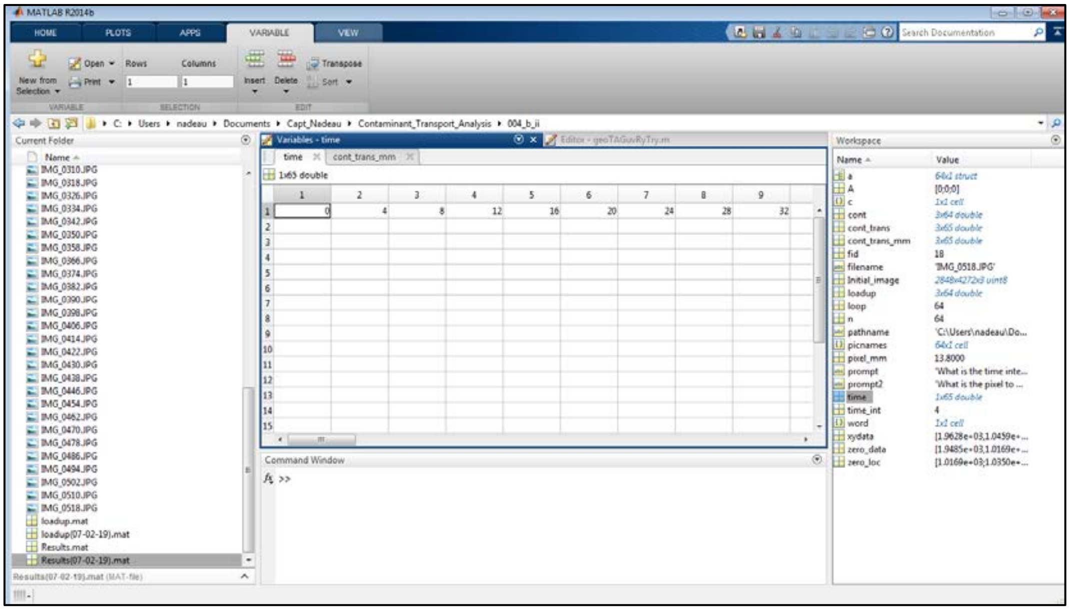

Name
IMG_0310.JPG
IMG_0318.JPG
IMG_0326.JPG
IMG_0334.JPG
IMG_0342.JPG
IMG_0350.JPG
IMG_0358.JPG
IMG_0366.JPG
IMG_0374.JPG
IMG_0382.JPG
IMG_0390.JPG
IMG_0398.JPG
IMG_0406.JPG
IMG_0414.JPG
IMG_0422.JPG
IMG_0430.JPG
IMG_0438.JPG
IMG_0446.JPG
IMG_0454.JPG
IMG_0462.JPG
IMG_0470.JPG
IMG_0478.JPG
IMG_0486.JPG
IMG_0494.JPG
IMG_0502.JPG
IMG_0510.JPG
IMG_0518.JPG
loadup.mat
loadup(07-02-19).mat
Results.mat
Results(07-02-19).mat

time | cont_trans_mm

1x65 double

	1	2	3	4	5	6	7	8	9
1	0	4	8	12	16	20	24	28	32
2									
3									
4									
5									
6									
7									
8									
9									
10									
11									
12									
13									
14									
15									

Name	Value
a	64x1 struct
A	[0;0;0]
c	1x1 cell
cont	3x64 double
cont_trans	3x65 double
cont_trans_mm	3x65 double
fid	18
filename	'IMG_0518.JPG'
Initial_image	2848x4272x3 uint8
loadup	3x64 double
loop	64
n	64
pathname	'C:\Users\nadeau\Do...
picnames	64x1 cell
pixel_mm	13.8000
prompt	'What is the time inte...
prompt2	'What is the pixel to ...
time	1x65 double
time_int	4
word	1x1 cell
xydata	[1.9628e+03,1.0459e+...
zero_data	[1.9485e+03,1.0169e+...
zero_loc	[1.0169e+03;1.0350e+...

Figure G-11: Time data from the workspace.

11. The graph, results and loadup data should be renamed to have a time stamp in the file name. This will ensure that they are not overwritten if the code is run for the same experiment more than once.

12. To calculate the infiltration rate for the oil, the slope of the depth of oil front versus time can be calculated in Excel. The slope shall only be calculated for the data when infiltration is occurring.